Dissertation presented to the Instituto Tecnológico de Aeronáutica and the University of Twente, in partial fulfillment of the requirements for the double degree programme of Master of Science in the Graduate Program of Engenharia da Aeronautica (ITA) and Mechanical Engineering (UT), Field of Aeronautical Design, Structures and Aerospace Systems (ITA) and Aeronautics (UT).

Nikolaj Angel Peter Even

PARAMETRIC STUDY OF AERODYNAMIC INTERFERENCE ON GLOBAL PROPELLER PERFORMANCE USING OPENVSP

Dissertation approved in its final version by signatories below:

Prof. Dr. Roberto Gil Annes da Silva
Advisor

Dr. Ir. Arne van Garrel
Co-advisor

Prof. Dr. André Valdetaro Gomes Cavalieri
Pro-Rector of Graduate Courses - ITA

UT Graduation Number: 459

Campo Montenegro
São José dos Campos, SP - Brazil
2024

Cataloging-in Publication Data
Documentation and Information Division

Even, Nikolaj Angel Peter
Parametric study of aerodynamic interference on global propeller performance using OpenVSP / Nikolaj Angel Peter Even.
São José dos Campos, 2024.
149f.

Dissertation of Master of Science – Course of Engenharia da Aeronautica. Area of Aeronautical Design, Structures and Aerospace Systems – Instituto Tecnológico de Aeronáutica, 2024. Advisor: Prof. Dr. Roberto Gil Annes da Silva. Co-advisor: Dr. Ir. Arne van Garrel.

1. Propeller. 2. Panel Method. 3. Aerodynamic Interference. I. Instituto Tecnológico de Aeronáutica. II. Parametric study of aerodynamic interference on global propeller performance using OpenVSP.

BIBLIOGRAPHIC REFERENCE

EVEN, Nikolaj Angel Peter. **Parametric study of aerodynamic interference on global propeller performance using OpenVSP**. 2024. 149f. Dissertation of Master of Science – Instituto Tecnológico de Aeronáutica, São José dos Campos.

CESSION OF RIGHTS

AUTHOR'S NAME: Nikolaj Angel Peter Even
PUBLICATION TITLE: Parametric study of aerodynamic interference on global propeller performance using OpenVSP.
PUBLICATION KIND/YEAR: Dissertation / 2024

Nikolaj Angel Peter Even
Hogeboekelweg 77 - Losser
7582PP – The Netherlands

PARAMETRIC STUDY OF AERODYNAMIC INTERFERENCE ON GLOBAL PROPELLER PERFORMANCE USING OPENVSP

Nikolaj Angel Peter Even

Thesis Committee Composition:

Prof. Dr.	André Fernando de Castro da Silva	Chairman	-	ITA
Prof. Dr. Ir.	Cornelis Henricus Venner	Chairman	-	UT
Prof. Dr.	Roberto Gil Annes da Silva	Advisor	-	ITA
Dr. Ir.	Arne van Garrel	Co-advisor	-	UT
Prof. Dr.	Vitor Gabriel Kleine	Member	-	ITA
Dr.	Yashar Hajimolana	Member	-	UT

ITA

Acknowledgments

When I started with my master's, I never expected it to become such as large adventure as it turned out to be. I had so many different experiences during my time, both in Brazil and back home in the Netherlands, and I truly feel that I did not only learn a lot, but that I have also grown as a person. This thesis is the final product of my study and I could not have created it all by myself. I would like to express my sincere gratitude to everyone who made this possible.

A few individuals should be mentioned. First of all, I would like to thank my supervisor from ITA, Prof. Gil for his supervision, and limitless enthusiasm for my research topic. I appreciate your help for finding resources to progress my research and for helping me with the organization of my master at ITA. I would also like to thank you for providing the Portuguese version of the abstract.

Secondly, I would like to thank my supervisor from UT, Dr. Arne van Garrel for his patience, dedication and support for my research. Every meeting I learned something new from you, whether it be about aerodynamics or panel methods and your feedback throughout the whole process has been invaluable. I could not have done this without you and I sincerely appreciate the time you set aside for me.

Aside from my supervisors, I would like to thank Prof. Kees Venner for the possibility to participate in the double degree programme. The experience has truly been a privilege and I would like to thank you for your confidence in me. In the same vein, I would like to thank Prof. Mariano Arbelo for helping me get settled in Brazil and the general organization of my master at ITA.

A special mention goes to Dr. Leandro de Santana for encouraging me to apply for the double degree programme in the first place. Before your suggestion I never even considered the possibility to apply, but you motivated me to go ahead and try anyway. I am really glad about how everything turned out and how memorable my time as a master's student turned out to be.

> *"Remember that all models are wrong;*
> *the practical question is how wrong do they have to be to not be useful."*
> — George E. P. Box

Abstract

Electric motor and battery technologies have advanced to the point where electric aircraft with a payload in the order of hundreds of kilograms start to become viable. Compared to gas turbine engines, the efficiency of electric motors is less dependent on the size of the power unit. This offers a higher degree of freedom for the layout of an electric aircraft concept. To quickly discard preliminary design concepts with low potential and focus on concepts with promising performance characteristics, it is highly desirable to have medium-fidelity analysis tools that can relatively quickly assess the viability of a broad range of different configurations. In a later stage of the design process only the most viable design(s) will then need to be analyzed in detail with (expensive) high-fidelity computational and/or experimental methods. The current work focuses on the aerodynamic interference between propellers and wings. This interference will be studied using the panel method in VSPAero, a potential flow solver that is part of the OpenVSP software suite.

For the isolated propeller or wing, it was possible to obtain results that agreed reasonably well with literature, though some clear shortcomings in the VSPAero solver were observed. While some of these shortcomings were expected due to the assumptions and simplifications underlying the governing equations, there were a few limitations with unclear causes as well. When the combined geometry was simulated, it was found that while the results for the propeller were plausible, the results for the wing were sometimes highly irregular, casting significant doubt on the accuracy of the propeller results as well due to the two-way interaction between the geometries.

Resumo

As tecnologias de motores elétricos e baterias avançaram a ponto de viabilizar aeronaves elétricas com carga útil da ordem de centenas de quilogramas. Em comparação com os motores de turbina a gás, a eficiência dos motores elétricos é menos dependente do tamanho da unidade de potência, o que oferece maior flexibilidade para o layout da integração aeropropulsiva de um conceito de aeronave elétrica. Para descartar rapidamente conceitos de projeto preliminares com baixo potencial, e concentrar-se em conceitos com características de desempenho aeropropulsivo promissoras, é altamente desejável ter ferramentas de análise de média fidelidade que possam avaliar com relativa rapidez a viabilidade de uma ampla gama de configurações diferentes. Em um estágio posterior do processo de projeto, apenas o projeto mais viável passará a ser analisado detalhadamente com métodos computacionais e/ou experimentais de alta fidelidade o que implica em alto custo computacional. O presente trabalho concentra-se na interferência aeropropulsiva, sob o aspecto aerodinâmico, entre hélices e asas. Estes aspectos físicos relacionado às interferências serão estudados empregando um método de painéis implementado no software VSPAero, um código de solução aerodinâmica potencial que faz parte do software OpenVSP.

Para a hélice ou asa isolada, foi possível obter resultados que concordaram razoavelmente bem com a literatura, embora tenham sido observadas algumas deficiências claras nos resultados obtido por VSPAero. Embora algumas dessas deficiências fossem esperadas devido às suposições e simplificações subjacentes às equações governantes, também houve algumas limitações com causas associadas e aspectos não identificados neste trabalho. Quando a geometria combinada hélice e asa foi simulada, verificou-se que, embora os resultados para a hélice fossem plausíveis, os resultados para a asa eram, às vezes, altamente irregulares, lançando dúvidas significativas sobre a precisão dos resultados da hélice também devido à interação mútua entre as geometrias.

List of Figures

List of Tables

List of Abbreviations and Acronyms

BEM	Blade Element Momentum
CAD	Computer Assisted Design
CFD	Computational Fluid Dynamics
CPU	Central Processing Unit
CPC	Carlson's Pressure Correlation
eVTOL	Electric Vertical Take-Off and Landing
FFT	Fast Fourier Transform
GMRES	General Minimised Residual
GPU	Graphics Processing Unit
IU	Inboard Up
NURBS	Non-Uniform Ration Basis Spline
OU	Outboard Up
P/W	Propeller-Wing
PCHIP	Piecewise Cubic Hermite Interpolating Polynomial
RAM	Rapid Aircraft Modeler / Random Access Memory
RANS	Reynolds-Averaged Navier-Stokes
TE	Trailing Edge
VLM	Vortex Lattice Method
VSP	Vehicle Sketch Pad
Comp.	Complete
Conv.	Conventional
Corr.	Correction
Exp.	Experiments
Pot.	Potential flow

List of Symbols

a	Axial induced velocity	(m/s)
a'	Radial induced velocity	(m/s)
A	Area	(m^2)
AR	Aspect ratio	s^2/S
$\tilde{A}$	Normalized section area	A_{sec}/A_{tot}
$\mathbf{A}$	Influence coefficient matrix	
b	Semispan	(m)
c	Chord	(m)
C_d	Drag coefficient, 2D	$D/(0.5\rho V^2 c)$
C_D	Drag coefficient, 3D	$D/(0.5\rho V^2 A)$
C_f	Friction coefficient	(-)
C_l	Lift coefficient, 2D	$L/(0.5\rho V^2 c)$
C_L	Lift coefficient, 3D	$L/(0.5\rho V^2 A)$
C_m	Moment coefficient, 2D	$D/(0.5\rho V^2 c)$
C_M	Moment coefficient, 3D	$D/(0.5\rho V^2 A)$
C_p	Pressure coefficient	(-)
C_P	Power coefficient	$P/(\rho n^3 D^5)$
C_T	Thrust coefficient	$T/(\rho n^2 D^4)$
dt	Timestep size	(s)
D	Diameter	(m)
F	Force	(N)
J	Advance Ratio	$V_\infty/(nD)$
M	Mach number	(-)
n	Rotation speed	(1/s)
$\vec{n}$	Normal vector	
P	Power	(J/s)
r	Euclidean distance (§3.2.1 and §3.2.2)	(m)
r	Residual (§3.2.3)	
r	Propeller radial position (§4 and later)	(m)
R	Propeller radius	(m)
Re	Reynolds number	$\rho u L/\mu$
s	Span	(m)
S	Wing surface area	(m^2)

t	Thickness	(m)
T	Thrust	(N)
$\vec{u}$	Velocity vector	(m/s)
V	Speed	(m/s)
$\vec{x}$	Position vector	(m)
α	Angle of attack	(°)
β	Propeller twist angle at 0.75 r/R (§2 and §4)	(°)
β	Prandtl-Glauert factor (§3.2.2)	$\sqrt{1-M^2}$
γ	Vortex strength	(m^2/s)
γ	Heat capacity ratio (§3.2.7)	(-)
$\Delta\theta_t$	Propeller rotation per timestep	(°)
η_P	Propeller efficiency	$J\,C_T/C_P$
θ	Circumferential propeller angle	(°)
ρ	Density	(kg/m^3)
ϕ	Flow potential	(m^2/s)
subscripts:		
c	Chord(wise)	
cref	Value at reference chord	
eff	Effective	
fric	Friction	
∞	Freestream	
loc	Local	
max	Maximum	
p	Point	
pnl	Panel	
prop	Propeller	
ref	Reference	
s	Span(wise)	
sec	Section	
sing	Singularity	
stall	Stall	
tip	Tip	
tot	Total	
visc	Viscous	
wake	Wake	
wet	Wetted	
wing	Wing	

Contents

1 Introduction

In the last two decades, electric motor and battery technologies have advanced to the point where electric aircraft with payloads of hundreds of kilograms can be produced. Although it may not yet be economically or technically viable to produce an electric aircraft on the scale of a large passenger jet, it is inevitable that the exhaustion of naturally occurring fossil fuel reserves or increasingly stringent environmental regulations will motivate the aeronautical industry to look for more environmentally conscious forms of aircraft propulsion. There are currently many electric general aviation projects ongoing which have already resulted in flying prototypes. These range from completely new designs, such as the Airbus A3 Vahana (shown in Figure 1.1) (AIRBUS, 2024), Eviation Alice (EVIATION, 2024), or the Lilium Jet (LILIUM, 2024), to electrified existing designs, such as the NASA X-57 (NASA, 2024), Cellsius E-sling (CELLSIUS, 2024), or Pipistrel Velis Electro (PIPISTREL, 2024). The latter in particular is a milestone, as it the first electric aircraft that is being commercially sold. One common factor among all of these new aircraft is that they all feature propellers as their propulsion mechanism, meaning that the trend towards electric aircraft is coupled with increased research interest into propellers. Electric aircraft have several different advantages and disadvantages compared to fossil fuel powered aircraft, but one quite distinctive advantage for electric aircraft is the configuration flexibility: Jet-powered aircraft have become more efficient in no small part due to the increase of the bypass-ratio of turbofan engines (KUROPATWA *et al.*, 2022). While high-bypass ratio turbofan engines are efficient, this efficiency comes at the cost of a large engine diameter and weight, which limits potential mounting locations for the engine. A typical modern jet aircraft has two turbofan engines mounted on pylons under the wing, a configuration referred to as ‘tube with wings’.

FIGURE 1.1 – The Airbus A3 Vahana, a quad tiltwing eVTOL demonstrator aircraft (sUAS News, 2019).

The efficiency of electric motors is not as strongly dependent on their size, which gives fewer constraints for the placement of the propulsion systems and even allows for a distributed propulsion system, or vertical take-off and landing capabilities (eVTOL). However, the increased amount of possibilities makes the design phase challenging, as analyzing all feasible configurations will be very time consuming and costly if performed to the same level of detail as a 'conventional' aircraft. This is not practical and raises the question whether it would be possible to do a prelinary design analysis of various possible propulsion configurations in a way that is less time consuming. A possible answer to this question would be to use a lower fidelity analysis tool, such as a panel method solver instead of a Reynolds-Averaged Navier-Stokes (RANS) solver for example. Especially during preliminary or conceptual stages of aircraft development, using a medium fidelity solver is likely beneficial, as it could result in significant time savings, while still yielding solutions that have acceptable accuracy for engineering purposes.

A particular area of interest is the aerodynamic interference effect between a propeller and a wing: a two-way interaction that affects the performance of both components. This interaction depends primarily on fluid parameters, geometry and the performance of the propeller and wing. From an integration point of view it is not immediately obvious which configurations are viable. It would be interesting if the aerodynamic interference between a propeller and wing could be analyzed with sufficient accuracy with a medium-fidelity solver. Especially for an electric aircraft with fully blown wings featuring distributed propulsion, or a tiltwing eVTOL concept, understanding and characterizing the aerodynamic interference early in the aircraft design process is very important for the selection of safe and efficient aircraft configurations.

Although there have already been various studies performed regarding the aerodynamic interference between a wing and a propeller, these are (with few exceptions) focused on the wing, not the propeller. This research will focus on how the propeller-wing interaction influences the performance of a propeller using a medium-fidelity numerical method. Simulations will be performed with VSPAero: a medium-fidelity panel-method solver included as part of the OpenVSP software suite. The goal of this study is to determine the feasibility of a medium-fidelity solver such as OpenVSP for the analysis of the propeller-wing aerodynamic interference effects. As follow up studies, similar research can be performed for other aspects of conceptual aircraft design. For example: in many electric aircraft concepts involving intra-urban transportation, noise pollution becomes a major design consideration as noise regulations are stricter near populated areas. Since panel method solvers can be used to compute pressure distributions, the fluctuations in these distributions could be analyzed and correlated to noise emissions.

Another design consideration due to the additional design freedom offered by electric propulsion is the load-bearing structure of the aircraft, as a tilt-wing setup or fully-distributed propulsion system is a significantly more complex load case than a typical aircraft design. Especially if lighter, less stiff materials are used, the aeroelastic behavior of the lifting structures of these aircraft should already be accounted for in the preliminary design phase.

1.1 Research Goals

The goal of this study is to determine the feasibility of the medium-fidelity solver VSPAero for the analysis of the propeller-wing aerodynamic interference effect. The intermediate objectives of this research are twofold: first, an understanding of the flow physics that are relevant for aerodynamic and how these can be modeled numerically will be discussed in Section 2. Secondly a good understanding of the capabilities of VSPAero is necessary as well: An analysis of the governing equations and the solver implementation in VSPAero is performed, which is treated in Section 3. As VSPAero offers several settings potentially which affect the accuracy of the solution, it will be investigated how changes in these settings propagate into the solution. The convergence behavior and accuracy of the solution is investigated with a series of test cases of increasing complexity, which are discussed in Sections 5 and 6, respectively. This will build confidence in the solution and show where potential weaknesses in the solver are present. Afterwards, an experimental study on propeller-wing aerodynamic interference by (SINNIGE *et al.*, 2019) will be recreated. The modeling of the experimental geometry is discussed in Section 4 and VSPAero simulation results for this geometry are discussed in Section 7. Lastly, the suitability of the OpenVSP software suite for simulating the aerodynamic interference effect and whether the results obtained for the global propeller performance are of acceptable accuracy for a preliminary design study is discussed in Section 8.

2 Propeller-Wing Aerodynamic Interference

To have a better understanding of the influence on propeller performance due to propeller-wing aerodynamic interference, earlier studies on the aerodynamic interference effect will be discussed. Unfortunately, most experimental works mainly focus on the effect of aerodynamic interference on a wing. However, this still provides valuable insights, as this data can be used as a reference for the numerical results obtained in this research. If the numerical results obtained for a wing disagree with the predicted results from literature, the results for the propeller will be untrustworthy as well.

To complement the experimental studies, numerical studies have been analyzed as well, as these often do include the results for the propeller. Research regarding the use of OpenVSP is of particular interest, as this gives an indication of the expected accuracy of the results, and points out important remarks for OpenVSP specifically, which can be incorporated into the simulation strategy.

The main theory regarding aerodynamic interference are the compiled works by (VELDHUIS, 2005). Although the details of the aerodynamic interference are complex, due to the two-way interaction between the propeller and wing, it is possible to express the induced axial and radial velocities at the propeller as a function depending on the general propeller geometry and setting, operating conditions, effective angle of attack and the interference effect, which (VELDHUIS, 2004) stated as follows:

$$a(x_{prop}, r) = f_a(G, \beta, J, \alpha_{prop,eff}, I_{wing}) \tag{2.1}$$

$$a'(x_{prop}, r) = f_t(G, \beta, J, \alpha_{prop,eff}, I_{wing}) \tag{2.2}$$

For any given quasi-steady condition, the geometry, twist angle and operating conditions (G, β, J) are all constant, leaving the induced velocities only dependent on the propeller angle of attack and the interference effect. As a simplification, it is possible to ignore the interference effect on the propeller outright and only consider the one-way interaction from the propeller on the wing, known as the single interaction model (SIM). While simpler, the SIM approach is more restrictive for considering different aircraft configurations, even for steady-state cases (VELD-

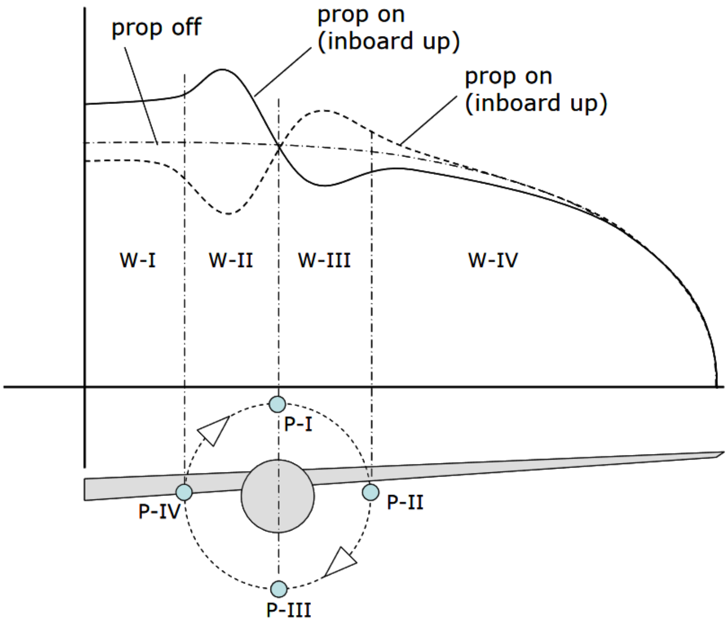

FIGURE 2.1 – Influence regions for aerodynamic interaction between propeller and wing, as well as theoretical change in lift distribution (VELDHUIS, 2004). Image shows the front view of the port size wing, with a propeller rotating in the inboard up (IU) direction.

HUIS, 2004). A more complete approach would be to model the two-way interaction between the propeller and wing, known as the full interaction model (FIM). While more accurate than SIM, the obvious drawback of using the FIM approach is the increased complexity and computation time required to model the two-way interaction effects.

As pointed out by (VELDHUIS, 2005), in the context of propeller-wing aerodynamic interference, is possible to define four regions on the wing and four points on the propeller to characterize the effects of aerodynamic interference between these components. These regions are shown in Figure 2.1. It should be noted that the flow properties between these points and regions change continuously.

For the four regions on the wing, the influence due to the propeller can be characterized as follows: W-II and W-III are directly in the wake of the propeller and experience the greatest aerodynamic interference. The influence of the propeller on the wing inflow is an increase in flow velocity in the wake of the propeller and a change in the local wing section angle of attack due to the propeller adding swirl velocity. The first effect will result in a net lift coefficient increase in both W-II and W-III due to the increased flow velocity. The propeller wake swirl velocity influences the local angle of attack which is increased in W-II and decreased in W-III. The magnitude of these effects varies depending on the exact position in the region, as can be seen in Figure 2.1, and depends on the relative blade load on the radial stations of the propeller. In regions W-I and W-IV the influence of the propeller is still present. Despite the fact that these regions are outside the propeller wake, the distortions to the flow field due to the propeller are still propagated into W-I and W-IV in the form of distorted vorticity sheets (VELDHUIS, 2005).

On the propeller side, the upwash of the wing influences effective angle of attack and flow velocity differently for the points P-I through P-IV. For the whole propeller, the effective angle of attack is increased due the upwash effect of the wing, known as the blockage effect (SEO *et al.*, 2022). Additionally, for point P-II there is an increase in the local angle of attack due to the upwash of the wing, resulting in a greater thrust generation. The opposite effect applies to P-IV, where the upwash of the wing reduces the local angle of attack and thrust instead. Note that this applies for a propeller rotating in the IU direction as shown in Figure 2.1, and the effect is reversed for a propeller spinning in the opposite direction. Furthermore, in points P-I and P-III, the axial induced velocity is increased and decreased, respectively, due to the wing circulation effect inducing a downwash in P-I and upwash in P-III (VELDHUIS, 2004) (SEO *et al.*, 2022).
Furthermore, the propeller wake swirl velocity is significantly decreased due to the presence of a wing in general, improving propeller efficiency.

Additionally, including the propeller nacelle in the simulation geometry increased the axial velocity in all marked points on the propeller, though this was a very minor effect (VELDHUIS, 2004).

2.1 Experimental Studies

The primary foundation of the current research is the study performed by (VELDHUIS, 2005), as well as assorted papers from (SINNIGE *et al.*, 2019), (SINNIGE *et al.*, 2018) and (STOKKERMANS *et al.*, 2019). In particular, the propeller geometry used in these studies, will be used in this research as well, which will be discussed in detail in Section 4.1.

In their research, (SINNIGE *et al.*, 2019) focused on the benefits of using a tip-mounted propeller to counteract losses due to tip vortices, and found that the complete system performance improved for the tip-mounted configuration compared to the conventional layout with the propeller relatively close to the wing root. Unfortunately, most results from (SINNIGE *et al.*, 2019) were for the effect on the wing. It was observed that the local lift distribution was modified due to the propeller, in accordance with the observations made by (VELDHUIS, 2005).

Another experimental study was performed by (FEI *et al.*, 2018), which focused on the aerodynamic interference effect for a distributed propulsion system by performing a parametric study for a propeller-wing geometry similar to the setup used by (SINNIGE *et al.*, 2019). Again, most of the results obtained describe the loading on the wing, rather than the propeller, though the sheer amount of parameters tested gives a broad overview of the relevant variables of the propeller-wing interference. The main observation made is the apparently linear relation between the wing lift coefficient and the height difference between the propeller thrust line and wing chord line. Additionally, it was noted that, for wing angles of attack in the linear lift region, the lift increase is proportional to propeller thrust generated. However, it was also noted that these behaviors were not always observed, as in certain cases the wing lift coefficient was not affected significantly or at all by the propeller inclination angle.

2.2 Numerical Studies

In the 1970's, the first practical panel method code was used extensively during the design process of an aircraft, when a code was developed by Boeing engineers to assist in the design of the Boeing 727 aircraft (RUBBERT; SAARIS, 1972). However, it took until the 1980's before any practical panel method codes were developed for simulating rotating propeller blades, as opposed to modeling the propeller as an actuator disk. Allegedly, the first panel method to simulate rotating blades was developed by (HESS; VALAREZO, 1985) during the development process of the ill-fated McDonnell-Douglas MD-94X propfan concept plane, which is shown in Figure 2.2. The method devised by (HESS; VALAREZO, 1985), only considers the axisymmetric steady state propeller flow, which is a step-up over using an actuator disk model. A difficulty encountered by (HESS; VALAREZO, 1985) regards the treatment of the trailing wake, as the authors point out the trailing wake should be modeled sufficiently far downstream of the propeller, such that increasing the wake length further does not significantly change the induced velocities at the simulated geometries, which is still a relevant problem. As the required wake distance was too large to simulate, (HESS; VALAREZO, 1985) approximated the wake with the semi-infinite wake of an actuator disk. This approximation yielded very accurate blade loads, especially for propellers with increasing blade numbers. Furthermore, the authors performed an advance ratio sweep using their panel method and compared the thrust and power coefficients against experimental measurements. It was found that the panel method consistently overpredicted both thrust and power compared to the experiments, yet similar efficiencies were obtained for most of the propeller operating range. Only for advance ratios approaching $J = 1$ and beyond, did the predicted efficiency start to diverge significantly from the measurements.

In a later study based on the work by (HESS; VALAREZO, 1985), an extension to the original method was devised to simulate multirotor setups (VALAREZO, 1991). One of the main challenges addressed by (VALAREZO, 1991) is the impingement of the wake of the first rotor into the second, which uses the same principle as discussed by (HESS; VALAREZO, 1985). It was found by the author that the time-averaged results for the steady-state case showed good agreements with experimental data, though no comment is made regarding the accuracy of the time-series results. Additionally, (VALAREZO, 1991) simulated an equivalent single-rotor case to evaluate whether the rotor-to-rotor interference effects can be reduced to a simple correction on a single-rotor case and whether significant savings in computational time could be obtained. It was found that, while it was possible to obtain reasonable results with the equivalent single rotor approach, (VALAREZO, 1991) recommended using the real double rotor geometry as the interaction effect on the downstream body pressure distribution is too significant to capture with a single rotor approach.

Another study describing the development of panel codes, specifically for modeling propeller-

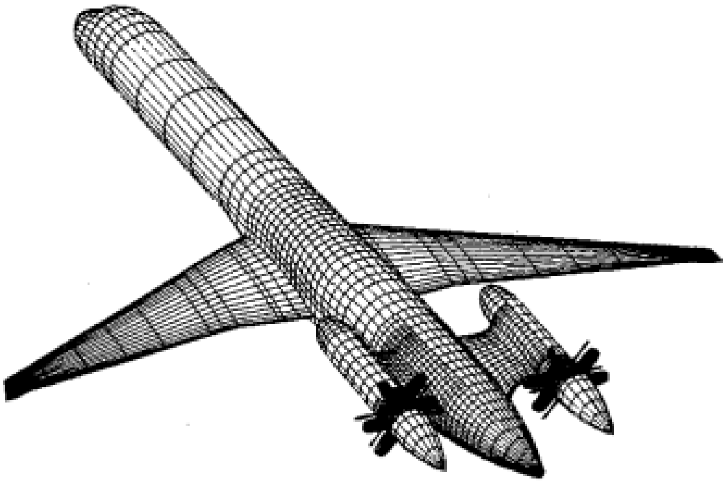

FIGURE 2.2 – Mesh of the MD-94X propfan concept aircraft, shown without the vertical stabilizer. Original figure by (VALAREZO, 1991).

airframe interaction, was performed by (SCHIPHOLT *et al.*, 1993), who suggest that the optimal operating condition for the combined wing-propeller geometry is different from the optimum of the individual components, emphasizing the need for accurately simulating the aerodynamic interference effects. The panel code was compared to experiments, and it was found that the global propeller parameters agreed well, though the panel code underpredicted the power coefficient. Furthermore, it was noted that in some cases, the induced velocities in the wake were not quite predicted correctly, showing the same trend as the experiments, but with the incorrect magnitude.

2.3 OpenVSP Studies

Several studies have been performed using OpenVSP as the numerical software suite of choice, ranging from verifications of isolated lifting geometries to validations of complete aircraft concepts. A report that is particularly relevant to this thesis was composed by (SHERIDAN *et al.*, 2021), who investigated the capabilities of VSPAero to simulate propeller-blown wing configurations. However, (SHERIDAN *et al.*, 2021) primarily focused on the results of the blown wing, rather than the propeller. As such, in most cases the simpler actuator disk model was used which is unable to model aerodynamic interference effects, as properties of the actuator disk in VSPAero are prescribed by the user. Furthermore, the authors used the VLM mode of VSPAero for all simulations, rather than the panel mode, thus all geometric thickness effects have not been accounted for. However, despite the fact that a simpler set of test cases was used, the results obtained served as good reference for the expected results of this study. Additionally, the results obtained with VSPAero were compared to a Reynolds-Averaged Navier-Stokes (RANS) solver. A relatively simple convergence study was carried out by (SHERIDAN *et al.*, 2021), which suggested that the results obtained by VSPAero are not completely grid-independent, though the authors did not elaborate much on this observation. Furthermore, despite the fact that any detailed calculations regarding the convergence behavior were missing, the authors showed that the convergence of the results in VSPAero was not particularly consistent, with large fluctuations present in the result for increasingly finer grids in nearly all cases discussed. Compared to the RANS results,(SHERIDAN *et al.*, 2021) found that for a fixed wing, the inviscid solution obtained with VSPAero agreed well with the RANS solver, with the difference between the results being in the order of percents. However, with VSPAero being an inviscid solver at its core, it was found that the viscous solutions differed more from RANS. An odd result that the authors obtained is that the result seemed slightly asymmetric for a symmetric wing, which is not elaborated upon. It is hypothesized that this might be due to asymmetries in the panel agglomeration. For an isolated propeller, results with the same order of accuracy as the wing results were found. Lastly, for the combined geometry, (SHERIDAN *et al.*, 2021) found better agreement between the RANS results and the VSPAero results using an actuator disk, compared to simulating rotating blades. For both cases, the difference compared to RANS was in the order of 10 %. Hence, the authors concluded that VSPAero could be useful for preliminary design phases, where it is more important that the global performance parameters are in the correct order of magnitude, rather than being completely correct. This was corroborated by pointing out that the computation time compared to the RANS solution was at least a full order of magnitude less when simulating rotating blades in VSPAero, and at least two to three when replacing the rotating blades with an actuator disk.

Another study in OpenVSP regarding propeller-wing aerodynamic interference was carried out by (GONÇALVES, 2024), using the same propeller and wing geometry as discussed in the works from TU Delft. While these simulations used the VLM simulation mode, the obtained results are still relevant, as the same flow conditions and geometry was used as in this research. It was pointed out that care must be taken regarding the discretisation of the geometry near the propeller tips, as this significantly affects the convergence behavior of the solver. Similarly to the work by (SHERIDAN *et al.*, 2021), simulations were performed for the propeller and wing geometries separately as well as the complete geometry including nacelle. It was found that for the isolated wing, the lift slope predicted by VSPAero was lower than was observed in the measurements, and the drag behavior was rather inconsistent: for positive angles of attack, the total drag predicted by VSPAero was higher than the experiments, while the opposite was true for negative angles of attack. For the isolated propeller analysis, a performance map was created and compared to real measurements. It was found that VSPAero overpredicted both the thrust and power coefficients compared to the experiments, though the overall efficiency figures were reasonable close for lower advance ratios. Lastly, for the complete geometry, it observed that the lift slope for the wing unexpectedly showed highly oscillatory behavior. However, the overall trend behavior of the lift slope still corresponded somewhat to the experimental results, with a linear regression showing that the experimental lift slope was somewhat higher than predicted by VSPAero.

A comparison study by (PERDOLT *et al.*, 2021) was performed with multiple solvers of different fidelity levels, including VSPAero, to evaluate the suitability of analyzing rotors and eVTOL aircraft. As the reference geometries, the ubiquitous Caradonna-Tung rotor, shown in Figure 2.3,

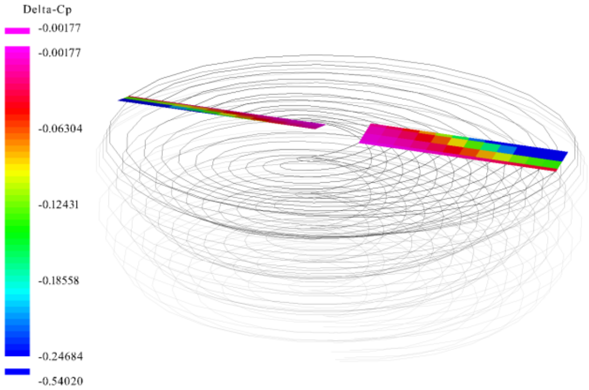

FIGURE 2.3 – Snapshot of the Caradonna-Tung rotor in hover, simulated in VSPAero. Original figure by (PERDOLT *et al.*, 2021)

was used as a benchmark for the isolated rotor comparisons and the Airbus A3 Vahana served as the comparison for a complete eVTOL geometry. Out of all solvers considered by (PERDOLT *et al.*, 2021), VSPAero was the simplest, yet was able to achieve similar global results to the other solvers for the isolated rotor benchmarks performed, though clear differences were observed for the load distribution. Furthermore, stability issues were noted for certain cases in VSPAero and it was remarked that the panel method in VSPAero was completely unusable, though at the time of writing, this issue seems to have been addressed. In general, (PERDOLT *et al.*, 2021) acknowledges the potential benefit of using OpenVSP for quick analyses with reasonable accuracy, though the limitations of the program must be kept in mind.

At the Hamburg University of Applied Sciences, several studies have been performed on modeling and analysis with OpenVSP (MARIËN, 2021) (FERNÁNDEZ, 2023). While both of these works have an emphasis on the analysis of fixed-wing aircraft, both the VLM and panel mode are used, rather than just the VLM mode as is common. Several tests were performed, starting with an angle of attack sweep for a straight and tapered wing with a thin airfoil. (MARIËN, 2021) found good agreement between both the VLM and panel mode results, as well as theoretical results. Furthermore, (MARIËN, 2021) showed that VSPAero is capable for analyzing unconventional configurations, as the numerical results for a box wing obtained with VSPAero for both VLM and panel mode matched well with experiments. In the research from (FERNÁNDEZ, 2023), a parametric design study was performed, varying the engine placement and quantity, with an Airbus A320 geometry as the baseline. While the engines were modeled as actuator disks enclosed in a body of revolution to represent the nacelle, it showed that VSPAero is at least capable for SIM modeling, though this capability was available approximately 50 years ago already. Another observation made by (FERNÁNDEZ, 2023) is the wiggly spanwise drag distribution, which unfortunately is not elaborated upon any further. While it could be seen that a low chordwise grid resolution was used, it is not clear if this is the cause for the drag wiggles. Nevertheless, both authors conclude that for relatively simple analyses, OpenVSP is a valuable tool, as it is possible to quickly create and analyses a geometry from nothing.

From general literature review, there appears to be a distinct lack of studies performed using the panel method in VSPAero, as nearly all publications seem to exclusively use the VLM mode. For geometries with thin airfoils, this would be appropriate and even preferable, as the VLM mode is typically approximately twice as fast as the panel mode (KINNEY, 2020). However, for relatively thick airfoils, the assumptions behind the thin airfoil theory that serves as the basis of the VLM method start to break down. Furthermore, most publications on OpenVSP typically use the actuator disk simulation mode, rather than simulating the actual blade geometry. The actuator disk mode is much quicker to simulate, but highly-simplified representation of a propeller and in the context aerodynamic interference, the actuator disk representation is a SIM model, making it completely inappropriate for the purposes of this research. As publications using the panel mode in OpenVSP or the rotating blade mode are quite rare, it is hardly surprising that the amount of publications where both of these settings are used is basically non-existent. Thus, this research is likely one of the first to use both settings and will hopefully plug an apparent gap in the knowledge base on aerodynamic interference modeling with panel methods.

3 Theoretical Background of OpenVSP

This section will give a brief overview of the OpenVSP software suite, with particular emphasis on VSPAero, the potential flow solver included with this package. While other solvers are bundled as well, these serve different purposes and are outside of the scope of this research.

3.1 OpenVSP

OpenVSP is an open-source software suite for parametric aircraft geometry design and analysis developed by NASA. At its core, OpenVSP is a geometry design tool that allows the user to design a computer assisted design (CAD) model from engineering parameters relatively quickly (MCDONALD *et al.*, 2012) (MCDONALD; GLOUDEMANS, 2022). While the focus of OpenVSP is on designing aircraft, non-aircraft geometries can be created as well. OpenVSP was released as an open-source software suite in 2012, though predecessors of the program have been developed since the 1990's, and were not available for public in open-source form (GLOUDEMANS *et al.*, 1996) (HAHN, 2010).

Aside from featuring geometry designing functionality, OpenVSP comes packaged with a variety of analysis tools that allow the user to perform various aeronautical analyses, ranging from basic aerodynamic performance analysis, to stability or aerostructural analyses. The aerodynamic analysis tool, called VSPAero, is of particular interest for this study and will be described in more detail in Section 3.2.

When this research was started, the newest version available is OpenVSP 3.39, which was obtained from the downloads page on the official OpenVSP website (MACDONALD *et al.*, 2024). This version was used for the entirety of the research outlined in this report. At the time of writing, the latest version is OpenVSP 3.41, though the changelogs suggest that VSPAero has not received any significant changes since the version used in this report.

In addition to the official website, the OpenVSP team manages a forum regarding the use of OpenVSP (OpenVSP Google Group, 2024), seemingly meant for questions regarding the modeling process and integration with other software, rather than detailed questions about the working principles of OpenVSP and VSPAero. Additionally, the complete source code of OpenVSP is available on Github (MCDONALD, 2024), which is the most complete, yet very cumbersome source of information on the inner workings of OpenVSP. It should be emphasized that no theory manual or detailed description of VSPAero is available.

While the author attempted to obtain as much information as possible from the combination of available sources on OpenVSP: the documents related to OpenVSP workshops found on the main site, the papers from the OpenVSP team as well as other authors about the program, the source code repository, and to a very minor extent the forum, not all details on the inner workings of OpenVSP are known unfortunately, which is reflected in the description in this report.

3.1.1 Geometry Design

The geometry designer in OpenVSP is a flexible design tool for creating aircraft. Rather than requiring the user to exactly specify all geometric details, OpenVSP contains a small selection of pre-defined geometries which can be tailored to the user requirements by means of parametric modeling. The main distinction between these components is whether these are considered to lift-generating, such as the wing or propeller, or non-lifting, such as the pod or fuselage to name a few examples. The main distinction between these two geometry types only applies for the numerical solution process, as only the lifting geometries shed a trailing wake. From a purely geometric perspective, there is in principle almost enough freedom for the user to create any geometry type with a completely different class. This is because all basic shapes are made constructed by defining multiple cross-sections consisting from canonical curves, which are then stitched together with non-uniform rational basis splines (NURBS) to create three-dimensional geometries (MCDONALD; GLOUDEMANS, 2022). Although there is no limitation for which type of cross-section shapes can be used for which type of geometry, there is a clear difference in the intent for certain cross-section shapes. For non-lifting surfaces, the circular, elliptic and rounded rectangle cross-sections are recommended and for lifting surfaces, OpenVSP contains a large library of airfoils including a large selection of different NACA series airfoils, as well as a few other airfoil types. Furthermore, it is possible to create a user-specified curve from different types of spline sections, such a cubic Bézier curves or piecewise cubic hermite interpolating polynomial (PCHIP) splines. It should however be noted that this geometric freedom may be limited by certain solver requirements. For example: many panel codes require a sharp trailing edge to enforce the Kutta condition.

As discussed, all basic geometries in OpenVSP are can be parametrically customized, though depending on the geometry, different parameters are available. For example: for the wing it is possible to define the tip and root chord, average chord, taper ratio, span, area, aspect ratio (AR) and sweep. It is not necessary to define all of these parameters, only three have to be specified, from which all other parameters are derived. Furthermore, it is possible to split into wings different nominally trapezoidal sections to create more complex lifting surfaces, and there are several options for creating caps on the extremities of the wing.

As it is a particularly component for this study, the propeller component will be described in some detail as well. The propeller is by far the most complex component available in OpenVSP, as it has the greatest amount of free parameters. There are three other features that make the propeller unique: firstly, the propeller can be toggled to be rendered and simulated as specified, or render and behave as a simplified actuator disk. Secondly, the propeller is the only component where its parameters can be defined continuously along the radius, rather than defining these at several discrete stations. Lastly, the propeller is the only shape in OpenVSP that can be simulated as a rotating component.

Although there are a lot of parameters available to the user for designing a geometry, this section will mainly discuss the parameters that directly affect the resulting mesh of a geometry, as this has a direct impact on the detail of the model and the computational time of any analyses.

The main parameters that influence the model detail are the number of cross-sections in the chordwise and spanwise directions, which are referred to in OpenVSP as U-tesselation and W-tesselation, respectively. These settings directly influence the amount and the size of the panels in VSPAero, as the panels are bounded by the cross-section lines. The amount of panels in the resulting geometry can be derived from the tesselation settings with the following equations:

$$N_{pnl,tot} = N_{pnl,c} \cdot N_{pnl,s} + N_{pnl,c} \cdot N_{pnl,tip} \tag{3.1}$$

$$N_{pnl,c} = W - 1 \tag{3.2}$$

$$N_{pnl,s} = U - 1 \tag{3.3}$$

$$N_{pnl,tip} = T - 1 \tag{3.4}$$

The amount of spanwise panels can be chosen freely in OpenVSP, whereas the amount of chordwise panels can only be increased in steps of two, as adding a chordwise section splits both the top and bottom surfaces of an airfoil, which increases the panel count on both sides. Furthermore, the amount of spanwise panels on the tip cap is defined separately from the rest of the lifting geometry, though the amount of the chordwise panels is shared.

Aside from setting the amount and size of the panels, OpenVSP offers the user the possibility to cluster panels together at the extremities of the geometry, such as the leading or trailing edge, root and tip of the wing. This can be very convenient, as it allows for the creation of a grid where the nodes are clustered near regions of interest, such as near large pressure gradients, while not having an unnecessary amount of detail elsewhere in the geometry. The clustering is controlled by the appropriately named clustering parameters, which are used as the inputs for the stretched hyperbolic tangent algorithm to determine the spacing of the nodes. A low value for the clustering parameter indicates that the nodes are spaced closer together, whereas a high value results in the nodes being spaced further apart. Setting the clustering to exactly one, results in equidistant node spacing. The exact clustering algorithm used by OpenVSP is the stretched hyperbolic tangent algorithm (THOMPSON *et al.*, 1985) (VINOKUR, 1983), which clusters the nodes based on the relative node spacing set at the endpoints. An example of the node distribution that can be obtained with the hyperbolic tangent stretching function is shown in figure 3.1, where the nodes are simply symmetrically clustered near the extrema of the interval.

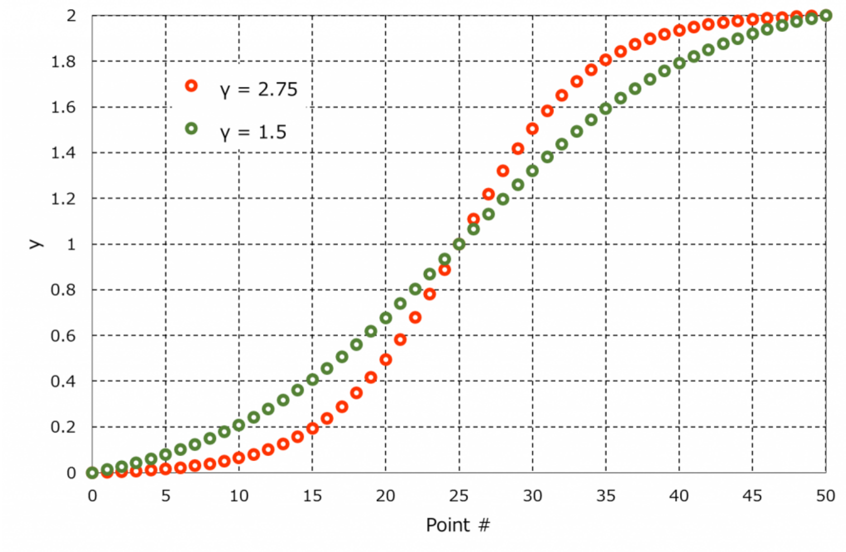

FIGURE 3.1 – Example of the node distribution obtained with hyperbolic tangent stretching, mapping 50 nodes on the interval $0 \leq y \leq 2$. Original figure taken from (ABE *et al.*, 2001).

3.2 VSPAero

VSPAero is the built-in aerodynamic analysis tool included with OpenVSP and as such, it is able to analyze nearly every geometry produced with OpenVSP. It is also possible to import geometries created with other methods as well, the exact shape of the panels does not matter too much, as the program is not only able to work with triangular or rectangular panels, but polygons of arbitrary shape as well (KINNEY, 2020).

VSPAero is solves potential flow field, which is a highly simplified form of the Navier-Stokes equations, as shown in Appendix A. Potential flow theory assumes that the flow is incompressible, inviscid, and irrotational. Commonly, it is assumed that the flow is steady as well, though this assumption would make the unsteady analysis of propellers impossible. Under these assumptions, the mass conservation equation simplifies to the form shown in equation 3.5, which is solved by introducing the flow potential as shown in equation 3.6 (DRELA, 2014).

$$\nabla \cdot \vec{u} = 0 \tag{3.5}$$

$$\vec{u} = \nabla \phi \tag{3.6}$$

The main benefits of using a flow potential in this manner is that the irrotational flow condition is automatically satisfied, as the curl of a gradient is by definition zero (HASS *et al.*, 2018), as shown in equations 3.7 and 3.8. Additionally, a single scalar function can be used to describe the whole velocity field, which can be preferable over using the velocity vectors explicitly.

$$\nabla \times \vec{u} = \vec{0} \tag{3.7}$$

$$\nabla \times \nabla\phi = \vec{0} \tag{3.8}$$

Equations 3.5 and 3.6 can be combined to yield equation 3.9, which can be recognized as the Laplace equation, meaning that the linear superposition principle holds and an almost arbitrary combination of fundamental potential flow solutions can be used to model the flow field under the assumptions taken.

$$\nabla^2\phi = 0 \tag{3.9}$$

There are a few different fundamental solutions for the potential flow equation, namely: the uniform flow, the source, the sink, the vortex and the doublet. The last two solutions in particular are important, as these are the only fundamental solutions with non-zero circulation, which is a prerequisite for generating lift in potential flow theory (ANDERSON, 2016).

VSPAero has two simulation modes: the Vortex Lattice Mode (VLM) and the panel mode. These simulation modes are very similar, both solving a potential flow field by distributing fundamental solutions on the surface of the (lifting) body in the flow. The primary difference between these modes is that for the panel mode, the full thickness of the geometry is considered, whereas the VLM mode degenerates the geometry down to its camber surface. The advantage of using VLM over the panel mode is that is typically saves significant computation time compared to the panel mode, while offering similar accuracy for thin lifting surfaces. However, for thick lifting bodies, it is preferable to use the panel mode instead. Furthermore, when simulating non-lifting bodies, such as nacelles, there is only a contribution to the moment in the VLM mode, whereas the complete influence of non-lifting bodies is considered for the panel mode. As this work focuses on the panel mode of VSPAero, the theoretical background discussed will primarily focus on this mode, with occasional remarks being made about VLM where relevant.

3.2.1 Boundary Conditions

From the linear superposition principle, it follows that a complex potential flow field can be built up from an almost arbitrary combination of elementary solutions. However, this might give rise to the question of how a physically realistic flow field is constructed.

If a solid object is in a flow field, the flow would go around the object, rather than through it. At the surface of the solid object, the velocity of the flow is completely parallel to the object itself, or in other words: the velocity vector is perpendicular to the normal vector of the object. the velocity vector is perpendicular to the normal vector of the object, which can be expressed mathematically by taking the dot product between the velocity vector at the surface and the corresponding normal vector, and setting this to zero, as shown in equation 3.10.

$$\vec{u} \cdot \vec{n} = 0 \tag{3.10}$$

For potential flow methods, there are two different ways to implement the no-penetration condition numerically, which will briefly be covered here for the sake of completeness. For more detailed explanations, the author recommends the descriptions given by (HOEIJMAKERS, 1992), (KATZ; PLOTKIN, 2001) and (VAN GARREL, 2016) as excellent sources of further reading.

The no-penetration condition can be enforced explicitly at the collocation points of the outer surface of the body, which makes the most intuitive physical sense and is mathematically equivalent to prescribing the gradient of the potential on the surface ($\partial\phi/\partial\vec{n} = 0$). This boundary condition is known as the Neumann boundary condition. Assuming that there is some arbitrary point p on the outer surface of the lifting body, the induced velocity at that point due to the contributions of all source (σ) and doublet (μ) elements on the surface (y) can be described as follows:

$$\vec{u}(\vec{x_p}) = \frac{1}{4\pi}\left(\iint \sigma_y \nabla\left(\frac{1}{r}\right) dS + \iint \mu_y \nabla\left(\frac{\vec{n}\cdot\vec{r}}{r^3}\right) dS\right) \tag{3.11}$$

$$\vec{r} = \vec{x}_p - \vec{x}_{sing} \tag{3.12}$$

$$r = \sqrt{\vec{r}\cdot\vec{r}} \tag{3.13}$$

To enforce the Neumann boundary condition on the outer surface of the body, the dot product between the normal vector and velocity vector at every collocation point should be equal to zero. This results in a linear system of equations that can be solved for the strength of the sources and doublets in equation 3.11. As a remark outside of the scope of this work: it is also possible to enforce that $\vec{u} \cdot \vec{n}$ is equal to a positive non-zero value at the collocation points to model viscous losses, known as the wall transpiration model (DRELA, 2014).

The Neumann boundary condition only prescribes the behavior of the flow on the outer surface of the body. Whatever happens inside of the body is in principle arbitrary, as the potential can be discontinuous over the surface. The only requirement for the inner potential is that the Laplace equation (3.9) is satisfied, like for the rest of the flow field.

Alternatively, it is possible to take advantage of the fact that there can be a discontinuity in the normal velocity between the outer surface and the inner surface of the body in the flow field to enforce the no-penetration condition. In this case, an internal potential is prescribed inside of the body. As this internal potential does not necessarily have to match the freestream potential, there can be a flow velocity discontinuity through the surface of the body. The magnitude of these discontinuities depends on the strength of the elementary solutions on the surface, with the discontinuity in the normal direction being dependent on the source strength and the discontinuity in tangential direction depending on the doublet strength. Thus, by prescribing an inner potential, an inner normal velocity is prescribed at every collocation point, which will always have a unique source strength such that the outer normal velocity is zero on the other side of the discontinuity. However, as adding source elements on the surface of the body influences the potential on the inside as well, vortex elements must be added to maintain the same magnitude over the discontinuity, while ensuring that the internal potential is as prescribed, with the governing equation for this balance being given by equation 3.14.

$$\phi^*(\vec{x_p}) = \frac{1}{4\pi}\left(\iint \sigma_y \left(\frac{1}{r}\right) dS + \iint \mu_y \left(\frac{\vec{n}\cdot\vec{r}}{r^3}\right) dS\right) \tag{3.14}$$

While there is no unique way to prescribe the internal potential $\phi*$, as every prescribed Dirichlet boundary condition will automatically satisfy the Neumann boundary condition as well, two common choices are to prescribe either $\phi^* = 0$, or $\phi^* = \phi_\infty$, with the former choice resulting in a completely stagnant inner flow field, and the latter resulting in an inner flow field that matches the freestream infinitely far away from the body. Both of these choices have interesting consequences: By setting $\phi^* = 0$, it follows that the source strengths at all collocation points have to be equal to $\sigma = \vec{u}_\infty \cdot \vec{n}$, whereas prescribing $\phi* = \phi_\infty$ means that the source strength at every point has to be zero and thus, a solution with only doublet elements can be obtained.

Although both of these boundary conditions are similar, the fundamental difference in the implementation is that for the Dirichlet boundary condition, the body in the flow must have a non-zero volume, meaning that for VLM, only Neumann boundary conditions can be prescribed, whereas for the panel method, both types can be used interchangeably and even concurrently in the same problem.

In VSPAero, it seems that the Neumann-type boundary condition is used as in the source code, equation 3.10 is enforced explicitly, rather than specifying an internal potential.

Regardless of whichever boundary condition type is used, no unique solution for the strengths of the singularities on the surface exists, as any proportional scaling of the singularity strengths obtained from the no penetration condition will result in a mathematically valid flow field, though not necessarily a physically valid flow field. To address both of these problems, another boundary condition is necessary, namely: the Kutta condition (KUETHE; SCHETZER, 1959). The need for the Kutta condition stems from the assumptions taken for a potential flow, and is related to the locations of the stagnation points: for potential flow, it is mathematically possible to have the two stagnation points be anywhere on the lifting body. For the upstream stagnation point this is not a problem, as its location depends on the angle of attack. However, the location of the downstream stagnation point is more restricted, as a physically realistic flow cannot pass over the trailing edge due to viscous effects. Hence, the flow field must have a circulation such that the downstream stagnation point is always located on the trailing edge, which can be enforced by considering the trailing edge and the two panels that are attached to it. Both of these panels are bounded by vortex lines, likely with differing strengths. To balance the circulation over the trailing edge to be equal to zero, a shed vortex element is added such that no discrete vortex exists at all trailing edge nodes:

$$\gamma_{TE,upper} + \gamma_{TE,lower} + \gamma_{wake} = 0 \tag{3.15}$$

3.2.2 Solution Procedure

Now that the boundary conditions necessary to obtain a physically realistic flow field have been discussed, we will discuss the solution process used in VSPAero to obtain this flow field. First, the geometry of the lifting body is discretized into panels. Around these panels, bound vortex loops are placed with a certain circulation strength γ. For a given strength of γ, the induced velocity of a bound vortex loop can be computed at an arbitrary point in the flow using the Biot-Savart law, as given in equation 3.16 (KINNEY, 2020) (ANDERSON, 2016). The exact formulation of the Biot-Savart law used by VSPAero includes a linear compressibility correction term K, which can be computed using either the Prandtl-Glauert or Karmán-Tsien rule, as will be discussed in Section 3.2.7. Additionally, a Prandtl-Glauert transformation is applied as well, as prescribed by hyperbolic distance equation 3.18 (ERICKSON, 1990) (DRELA, 2014).

$$\vec{u}_p = \frac{-\beta}{2\pi K} \int_1^2 \frac{\vec{\Gamma} \times (\vec{r} - \vec{r}')}{r_\beta^3} ds \tag{3.16}$$

$$\beta^2 = 1 - M_\infty^2 \tag{3.17}$$

$$r_\beta^2 = (x - x_p)^2 + \beta^2 \left[(y - y_p)^2 + (z - z_p)^2\right] \tag{3.18}$$

Equation 3.16 describes the induced velocity in some arbitrary point p not on a vortex loop, by a vortex filament, which has 1 as its starting point and 2 as its endpoint. For incompressible flows, equation 3.18 reduces to the geometric distance between the vortex filament and point p.

Since VSPAero places a vortex loop around every panel the principle of superposition can be applied to compute the induced velocity at any arbitrary point p not on a vortex loop by summing the contributions from every vortex loop. Furthermore, since the no penetration condition has to be satisfied on every panel, this induced velocity computation is evaluated on the centroid of all panels in the geometry. Additionally, the induced velocity from the shed wakes had to be taken into account as well, resulting in the following sum for the induced velocity at point p (KINNEY, 2020):

$$\vec{u}_p(\vec{x}_i) = \sum_{j=1}^{n_{p,body}} \vec{A}_{ij}\gamma_j + \sum_{j=1}^{n_{p,wake}} \vec{A}_{ij}\gamma_j + \vec{u}_\infty = (\vec{A}\gamma)_{body} + (\vec{A}\gamma)_{wake} + \vec{u}_\infty \tag{3.19}$$

In equation 3.19, the first sum contains the influence of all vortex loops, including those on other lifting bodies in the domain, such as propellers, the second sum contains the influence from all shed vortex wakes and lastly, the $\vec{u}_\infty$ is the influence due to the freestream velocity. The induced velocities depend on the distance between point p and the loop, as well as strength of each vortex loop. Furthermore, as the boundary condition (equation 3.10) is enforced on the panel centroids is a scalar equation, equation 3.19 can be rewritten as a system of linear equations for every collocation point p by combining equation 3.19 with the no-penetration condition. In the context of VSPAero, which uses vortex loops of constant strength γ, this yields equation 3.20, which can be rewritten to isolate the unknown vortex loop strengths present on the discretized body on the left-hand side (equation 3.21) and can then be rewritten as a system of linear equations of the form shown in equation 3.22 to be solved for the unknown body vortex strengths γ to obtain the flow field.

$$\vec{u}_p(\vec{x}_i) \cdot \vec{n}_i = \sum_{j=1}^{n_{p,body}} \left(\vec{A}_{ij} \cdot \vec{n}_i\right) \gamma_j + \sum_{j=1}^{n_{p,wake}} \left(\vec{A}_{ij} \cdot \vec{n}_i\right) \gamma_j + \vec{u}_\infty \cdot \vec{n}_i = 0 \tag{3.20}$$

$$\sum_{j=1}^{n_{p,body}} \left(\vec{A}_{ij} \cdot \vec{n}_i\right) \gamma_j = - \sum_{j=1}^{n_{p,wake}} \left(\vec{A}_{ij} \cdot \vec{n}_i\right) \gamma_j - \vec{u}_\infty \cdot \vec{n}_i \tag{3.21}$$

$$\mathbf{A}x = b \tag{3.22}$$

It should be noted that, although the strength of the shed wake vortices is included in the no penetration condition at all panels, the strength of the wake vortices attached to the trailing edge is determined by enforcing the Kutta condition at the trailing edge points.

3.2.3 Iterative Procedure

In order to compute the flow field, the linear system of equations 3.22 needs to be solved. Matrix A has as many entries on the rows and on the columns as there are unknown vortex strengths, meaning that it will grow very quickly for complex models. Thus, directly solving for A is too expensive in practice and instead, iterative solution methods are used typically used in these cases. VSPAero solves for this system iteratively using the GMRES method (SAAD; SCHULTZ, 1986), which will briefly be explained in this report. It should be noted that there are many different iterative solution algorithms available and in use by other solvers. Based on the linear system described by equation 3.22, it is possible to define the residual vector r of the linear system as follows:

$$r = b - \mathbf{A}x \tag{3.23}$$

From equation 3.23 it follows that the linear system is solved exactly if $r = 0$. However, as the problem is being solved iteratively, the residual vector will never exactly go to zero in practice and only as many iterations are made as necessary to reach a residual vector that is deemed sufficiently small. In VSPAero, it is not possible for the user to specify the iteration limit or convergence criteria without modifying the code. To determine whether a solution is converged, VSPAero considers two criteria:

1. Is the current residual lower than the prescribed tolerance?
2. Is the current residual an order of magnitude smaller than the residual after the first iteration?

Additionally, if the amount of iterations exceeds the hard-coded limit in VSPAero, the solver will continue on to the next calculation step, even though the result has not converged.

To evaluate whether the two convergence criteria are met, the norm of the residual is evaluated after every iteration as shown in equation 3.24.

$$||r|| = \sqrt{\sum_{i}^{n} r_i^2} \tag{3.24}$$

VSPAero evaluates whether the two convergence criteria are met as follows: First, the residual is compared against the tolerance residual $r_{tol} = 0.1 \cdot V_{ref}$ by evaluating if $r_i < r_{tol}$ is true. Secondly, the residual is compared to the residual after the first iteration r_1 by evaluating if $log(r_i/r_1) < -1$. For the cases where a fixed wake is simulated, the second convergence criterion is modified to be $log(r_i/r_1) < -3$ instead.

The GMRES algorithm performs its iterative calculations by first preconditioning the linear system in equation 3.22 by pre-multiplying both sides of the equation with matrix $\mathbf{P}^{-1}$:

$$\mathbf{P}^{-1}\mathbf{A}x = \mathbf{P}^{-1}b \tag{3.25}$$

There is some freedom for choosing the matrix $\mathbf{P}^{-1}$. For example, if $\mathbf{P}^{-1}$ is chosen such that $\mathbf{P} = \mathbf{A}$, then equation 3.25 simplifies as follows:

$$\mathbf{A}^{-1}\mathbf{A}x = \mathbf{A}^{-1}b \tag{3.26}$$

$$x = \mathbf{A}^{-1}b \tag{3.27}$$

As can be seen in equation 3.27, using the choice $\mathbf{P} = \mathbf{A}$ gives the direct solution for the linear system. However, it requires the direct computation of the inverse of matrix $\mathbf{A}$, which will become computationally expensive very quickly. Therefore, VSPAero chooses $\mathbf{P}$ such that it approximates the matrix $\mathbf{A}$ and that the action of $\mathbf{P}^{-1}$ on a vector can be computed efficiently. VSPAero offers three built-in preconditioning options:

- Jacobi Iteration, where $\mathbf{P}$ is chosen to be the diagonal of $\mathbf{A}$.

- Gauss-Seidel (Successive Over) Relaxation, where **P** is chosen to be a linear combination of the upper and lower triangular decompositions of **A**.
- Matrix, where **P** is chosen to be an approximate Lower-Upper (LU) decomposition of **A**. This option is set by default and was used for all simulations in this report. Crout's algorithm is used to compute the approximate LU decomposition (PRESS *et al.*, 1992).

3.2.4 Vortex Loop Agglomeration

Aside from the iterative solution procedure, VSPAero uses another technique to reduce the computation time. As a large computational effort is required to compute the sum of all induced velocities for all control points (equation 3.19), a significant speed increase can be gained if this calculation can be simplified. VSPAero uses vortex-ring agglomeration by recursively creating several courses panel grids where neighboring vortex loops are merged together, creating multiple levels of coarsening. Whenever the induced velocity at a point is computed, these increasingly coarsened approximations are used to compute the induced velocity from more distant vortex loops, which is essentially a far-field approximation. An example of the agglomeration process is shown in figure 3.2.

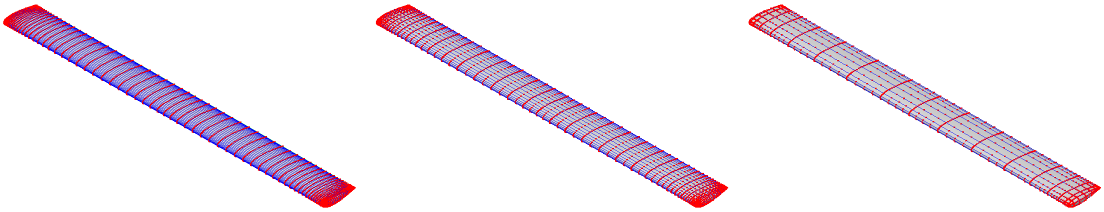

(a) Level 1 (user specified mesh). (b) Level 2. (c) Level 3.

FIGURE 3.2 – Example of grid agglomeration levels, shown for a straight wing.

For the coarser grid levels, the vortex loop agglomeration scheme takes an area-weighted average of the merged loops to determine the vortex strength at the coarser grid levels, and applies direct injection whenever the coarse grid solution is interpolated back onto the finer grid levels. Furthermore, during the agglomeration procedure, the algorithm attempts to merge the vortex loops using the following rules wherever possible:

- Get rid of panels with AR > 10 as much as possible.
- Merge triangular panels together into quadrilaterals.
- When merging loops, try to merge panels with similar aspect ratios together (as long as AR < 10).
- Per agglomeration level, apply no more than one level of panel merging.
- Merge collinear edges together.

3.2.5 Wake Calculation

In VSPAero, all lifting surfaces shed wakes from their trailing edges, modeled as vortex filaments. Wake segments are only shed at the collocation points where the Kutta condition is enforced and are referred to as Kutta nodes.

The user can specify the amount of wake nodes, the wake far-field distance and for steady simulations only, the number of iterations for the wake relaxation process. The number of wake nodes determines in how many strips each wake vortex filament is divided. The far-field distance determines the cut-off length of the wake. The number of wake iterations determines how many wake relaxation iterations are performed for the steady simulation case. For the unsteady case, no wake relaxations are performed. Due to this difference, the wake calculations are performed slightly differently between steady and unsteady simulations.

For steady simulations, after the body vortex loop strengths have been computed, the first wake is convected in the direction of the freestream with constant vortex strengths over the entire length of each trailing wake segment such that the Kutta condition as given by equation 3.15 is enforced. The length of this wake is cut-off at the far-field distance. Due to the addition of the trailing wakes, the original body vortex strength distribution no longer satisfies the no-penetration condition. Hence, these will be computed again as described in Section 3.2.3, but this time, the induced velocities from the first wake iteration are incorporated into the right-hand side of the system of linear equations as well. After re-computing the body vortex strengths, the wake positions and strengths are updated to enforce the Kutta condition again. The combination of first computing the vortex loop strengths on the body panels and then iterating on the wake is called a wake iteration. The goal of this iterative wake scheme is to make the wakes converge to follow the streamlines of the flow field.
Additionally, VSPAero offers the option to simulated ‘fixed wakes’ by only convecting the wake in the freestream direction after iteratively solving the body vortex loop strengths once.

For unsteady simulations, rather than convecting the entire wake at once, every timestep a single strip of shed wake vortices is added at all Kutta nodes and any existing wake segments are convected with the local flow velocity at every timestep. Thus, for unsteady simulations, the wakes are incrementally growing over time. If the number of wake nodes is specified to be lower than the number of timesteps, the oldest wake segments are truncated whenever the maximum number of wake nodes is exceeded. According to comments in the source code, there is allegedly a limiter in place to prevent unrealistic wake propagation speeds, though it was not clear how this was implemented.

3.2.6 Drag Calculation

Although a pure potential flow model fundamentally does not include viscous drag effects, VSPAero includes a relatively simple viscous drag correction method to provide an estimate of the viscous drag. Despite the simplicity of this correction in VSPAero, it at least offers an engineering-accurate estimate for preliminary design stages, which is more or less in line with the accuracy that can reasonably be expected from VSPAero.

Although no clear mention could be found in any publication, nor in the comments in the source code, VSPAero uses a Schlichting-type viscous correction, where a distinction is being made for lifting and non-lifting bodies. For lifting bodies, a local friction coefficient is defined as shown in equation 3.28, with the definition of the local Reynolds number Re_{loc} following in equation 3.29 (SCHLICHTING; GERSTEN, 2017):

$$C_f = \frac{1.037}{log(Re_{loc})^{2.58}} \tag{3.28}$$

$$Re_{loc} = Re_{c_{ref}} \cdot \frac{V_{loc}c_{loc}}{V_{ref}c_{ref}} \tag{3.29}$$

Based on the friction coefficient in equation 3.28, the friction force is computed as follows:

$$F_{fric} = 0.5 \cdot C_f \cdot \rho \cdot V_{loc}^2 \cdot A_{loc} \tag{3.30}$$

An important remark regarding the user-specified $Re_{c_{ref}}$: although the user is free to specify any reference value for the Reynolds number, this value is clamped to a maximum of $Re = 10^{12}$, meaning that the friction coefficient is always at least equal to $C_f = 0.0017$, assuming $Re_{loc} \approx Re_{c_{ref}}$. Setting $Re_{c_{ref}} = 0$ does not disable the correction either as the solver is hard-coded to set $Re_{loc} = 1000$ whenever a value of Re_{loc} smaller than 1000 is computed. However, as specifying $Re_{c_{ref}} = 10^{12}$ essentially disables the viscosity correction, this setting will be referred to as inviscid for the purposes of this research.

In addition to the friction drag correction, a '2D drag due to lift' correction is added, which according to comments in the source code is allegedly based on a curve fit to unspecified data of NACA 0012 and NACA 2412 airfoils. This correction is calculated as follows:

$$F_{l,2d} = 0.5 \cdot f_{comp} \cdot 0.00625 \cdot \left(\frac{c_{n,loc}}{(V_{loc}/V_{ref})^2} \right)^2 \cdot V_{loc}^2 \cdot A_{loc} \tag{3.31}$$

Where f_{comp} is a compressibility-related factor that is set as $f_{comp} = 1$ for $M_{loc} < 0.6$, and is computed with equation 3.32 for $0.6 \leq M_{loc} \leq 0.95$. Any local Mach numbers that would exceed 0.95 during this calculation are clamped at $M_{loc} = 0.95$.

$$f_{comp} = 1 + 0.5 \cdot (M_{loc} - 0.6)^2 \tag{3.32}$$

The total viscous correction is then obtained by summing the contributions from equations 3.30 and 3.31:

$$F_{visc} = F_{fric} + F_{l,2d} \tag{3.33}$$

$$\vec{F}_{visc} = F_{visc} \cdot \frac{\vec{u}_{loc}}{V_{loc}} \tag{3.34}$$

As a final step, a crude flow reversal model is applied, which checks if $\vec{u}_{loc} \cdot \vec{u}_{\infty} < 0$ is true, and multiplies F_{visc} from equation 3.33 by two.

For non-lifting bodies, an even simpler drag model is applied, consisting of only a friction drag component, where the friction coefficient is computed as shown in equation 3.35.(SCHLICHTING; GERSTEN, 2017).

$$C_f = \frac{0.455}{log(Re_{loc})^{2.58}} \tag{3.35}$$

With the friction coefficient, an incremental drag coefficient can be computed for every non-lifting panel using equation 3.36. The factor 1.25 represents a 25 % increase in drag due to 'miscellaneous' contributions, as commented in the source code. The total friction force on a non-lifting body is computed by taking the sum of the friction drag contributions over all panels, as shown in equation 3.37:

$$dC_D = 1.25 \cdot C_f \cdot A_{wet} \tag{3.36}$$

$$F_{fric} = \sum dC_D \cdot 0.5 \cdot \rho \cdot V_{ref}^2 \tag{3.37}$$

3.2.7 Compressibility Correction

As briefly discussed already in Section 3.2.2, VSPAero can be configured to use two different types of compressibility correction: the Prandtl-Glauert correction, and the Karmán-Tsien correction. The former compressibility correction essentially corrects the flow coefficients according to the following rule:

$$C_p = \frac{C_{p,0}}{\sqrt{1 - M_{loc}^2}} \tag{3.38}$$

Where $C_{p,0}$ is the pressure coefficient for a completely incompressible flow ($M_{\infty} = 0$).

As an alternative, VSPAero offers the Laitone's form of Karmán-Tsien correction as well, given in equation 3.39. This is the default compressibility correction setting, in VSPAero and was used for all simulations during this research when the compressibility correction was applied.

$$C_p = \frac{C_{p,0}}{\sqrt{1 - M_{loc}^2} + C_{p,0}\left(\frac{M_{loc}^2(1+0.5\cdot[\gamma-1]M_{loc}^2)}{2\sqrt{1-M_{loc}^2}}\right)} \tag{3.39}$$

For the specific heat ratio γ, VSPAero uses the constant value of $\gamma = 1.4$.

3.2.8 Stall Models

Although the assumptions taken for the potential flow model do not permit detached flows, and therefore no stall behavior, VSPAero offers two correction models that can be applied to spanwise load distributions of lifting bodies as a post-processing step to mimic stalling behavior. The two models available are the 2D CLmax model and Carlson's Pressure Correlation (CPC).

3.2.8.1 2D CLmax

The 2D CLmax model works by locally limiting the lift force to the maximum value that can be obtained for the two-dimensional cross-section at that station. As an additional input for this model, the user must specify the value for $C_{l,max,2D}$, which can be obtained either from literature or 2D flow solvers such as XFoil (DRELA, 2013).

The stall correction factor is computed and is applied as a post-processing step to the spanwise load distribution, shown for the lift coefficient in equation 3.40 as an example, though this applies for all forces except the drag, which is corrected according to equation 3.41. For both equations, the corrections are independently applied for all spanwise stations.

$$C_L = f_{stall} \cdot C_{L,0} \tag{3.40}$$

$$C_D = f_{stall} \cdot C_{D,0} + 0.25 \cdot (1 - f_{stall}) \cdot |C_{n,0}| \tag{3.41}$$

The stall correction factor f_{stall} is computed using the relation between the normal coefficient and the user-specified maximum 2D lift coefficient, corrected using the local flow speed, as shown in equations 3.42 and 3.43.

$$f_{stall} = \frac{|min(|c_{N,0}|, c_{l,2d})|}{|c_{N,0}|} \tag{3.42}$$

$$C_{l,2D} = C_{l,max,2D} \cdot max\left(1, \left(\frac{V_{loc}}{V_{ref}}\right)^2\right) \tag{3.43}$$

3.2.8.2 Carlson Pressure Correlation

The Carlson Pressure Correlation model does not require any additional user input though it should be noted that this stall correction does not work if the flow is incompressible. The CPC model works by predicting a critical sonic pressure coefficient, and assumes that a shockwave occurs that causes boundary layer separation if exceeded. Although this effect is not modeled physically in VSPAero, the effects of such behavior are approximated with the CPC model (VALAREZO; CHIN, 1994).

At the basis of the CPC model is the local minimal pressure coefficient, which is the critical point when the flow speed locally becomes sonic. The critical pressure coefficient for this to occur uses the method from (VALAREZO; CHIN, 1994) and is given by equation 3.44, which is then modified according to equation 3.45 to incorporate Carlson's pressure correlation.

$$C_{p.min} = \frac{\left(\frac{1+0.2M_{loc}^2}{1.2}\right)^{3.5} - 1}{0.7M_{loc}^2} \tag{3.44}$$

$$C_{p.min,CPC} = C_{p.min} \cdot \left(\frac{c_1}{c_2}\right)^{c_3} \tag{3.45}$$

The coefficients c_1, c_2 and c_3 in equation 3.45, are given by equations 3.46-3.48.

$$c_1 = \frac{Re_{loc}}{10^6} \tag{3.46}$$

$$c_2 = \frac{Re_{loc}}{10^6} + 10^{4-3M_{loc}} \tag{3.47}$$

$$c_3 = 0.05 + 0.35 \cdot (1 - M_{loc}^2) \tag{3.48}$$

Once the sonic pressure coefficient has been computed for every spanwise station, a check is done to see if the local minimum pressure coefficient is lower. If that is the case, then the stall correction factor is applied in a similar fashion as shown in equations 3.40 and 3.41, but with the stall factor f_{stall} being computed using equation 3.49 instead of equation 3.42.

$$f_{stall,CPC} = \frac{\frac{|C_{p,loc}|}{|C_{p.min,CPC}|} - \frac{V_{loc}}{V_\infty}}{\left(\frac{V_{loc}}{V_\infty}\right)^6} \tag{3.49}$$

3.2.9 Time Integration

So far, a description has been given of the calculations performed by VSPAero for a steady simulation. While this description is valid for individual timesteps of simulations as well, a time integration must be applied to resolve the temporal aspect of the simulation. VSPAero performs this calculation by decomposing the potential solution into a steady part and an unsteady part, where the steady part is computed for every timestep independently, and the unsteady part is calculated based on information from previous timesteps.

The pressure coefficient on every panel is computed in VSPAero as shown in equation 3.50, where it can be seen that it consists of a steady part, given by $\vec{U} \cdot \vec{U}$, which is the steady panel velocity and $\frac{d\gamma}{dt}$, which is the unsteady panel velocity, which is an approximation of the time derivative of the vortex strength of the panel.

$$C_p = \frac{1 - (\vec{u} \cdot \vec{u}) - \frac{d\gamma}{dt}}{\frac{1}{2} V_{ref}^2} \tag{3.50}$$

The approximation of $\frac{d\gamma}{dt}$ is computed in VSPAero according to equation 3.51, which takes the vortex ring strength at the current and previous two timesteps for the approximation. While this method is not explicitly cited in the source code, it can be recognized as variation of the Adams-Bashford method, which is an explicit linear multistep time integration scheme (BUTCHER, 2003). The specific formulation used by VSPAero has second-order accuracy.

$$\left.\frac{d\gamma}{dt}\right|_t = \frac{3\gamma_t - 4\gamma_{t-1} + \gamma_{t-2}}{2dt} \tag{3.51}$$

Since the Adams-Bashford method requires information at two previous timesteps, a problem arises whenever the first timestep is calculated, as there is not enough information available to perform this calculation. Thus, for the first timestep, VSPAero applies an explicit Euler step, as shown in equation 3.52.

$$\left.\frac{d\gamma}{dt}\right|_{t_1} = \frac{\gamma_{t_1} - \gamma_{t_0}}{dt} \tag{3.52}$$

4 Simulation Geometry and Strategy

This section will discuss the testing methodology for quantifying the aerodynamic interference between the propeller and wing. First, an overview will be given of the geometry that will be used for the parametric study for the quantification of the interference effect. Secondly, the simulation test cases, the relevance of the parameter being studied, and the expected result will be explained.

4.1 Simulation Geometry

The main geometry that was used for the parametric study is the PROWIM propeller from TU Delft, which is a four-bladed propeller using the blade geometry from the DHC-2 Beaver (SINNIGE *et al.*, 2020) (SINNIGE *et al.*, 2020). This propeller has been chosen for several reasons: windtunnel measurement and CFD datasets are available, which allows for verification of the results obtained in this thesis against real data. Secondly, the propeller is a relatively simple design and is therefore easy to recreate in OpenVSP. Lastly, nearly all electric airplane prototypes are of a similar size as the DHC-2 Beaver aircraft, meaning that the operating conditions will likely be similar as well, which makes the PROWIM a suitable testing geometry. The PROWIM was recreated in OpenVSP using the technical drawings and descriptions discussed in several reference papers from TU Delft (SINNIGE *et al.*, 2018) (STOKKERMANS *et al.*, 2019) (SINNIGE *et al.*, 2019), and is shown in Figure 4.1, where both a front view and angled view are shown. The former gives a clearer view of the chord distribution, whereas the latter better shows the twist and thickness distribution. The pitch, thickness and chord distributions are shown in Figures 4.4a, 4.4b and 4.4c, respectively.

The propeller has been used in several different wing and pylon mounting configurations, but for this specific study, the geometry used by (STOKKERMANS *et al.*, 2019) and (SINNIGE *et al.*, 2019) was used, which pairs the propeller with an untapered rectangular wing, using a NACA 64_2A615 profile over the whole span. The nacelle housing the propulsive assembly could be mounted either on the tip, or approximately at the midspan, as the wing was designed as two interchangeable sections. Photos of the real test set-up was used as the reference geometry for this study is shown in Figure 4.2, with the recreation of the geometry in OpenVSP being shown in Figure 4.3. The recreation of the model was based on the technical drawings included in the report from (SINNIGE *et al.*, 2019). However, some changes had to be made to the geometry due to some simulation issues, which will be discussed in detail in Sections 4.1.1 and 4.1.2.

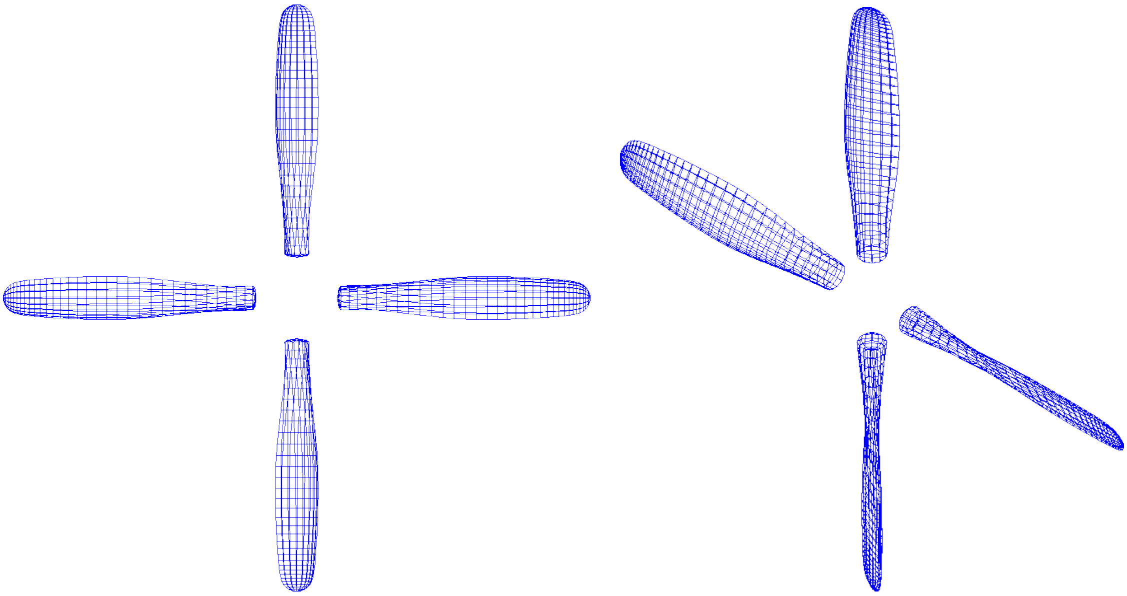

(a) Front view.

(b) Left isometric view.

FIGURE 4.1 – Overview of the PROWIM propeller geometry, recreated in OpenVSP. Grid has been adjusted for improved view clarity, and is not optimized for computations.

In addition to these major changes, the model was modified where necessary according to the suggestions outlined by (LITHERLAND, 2021).

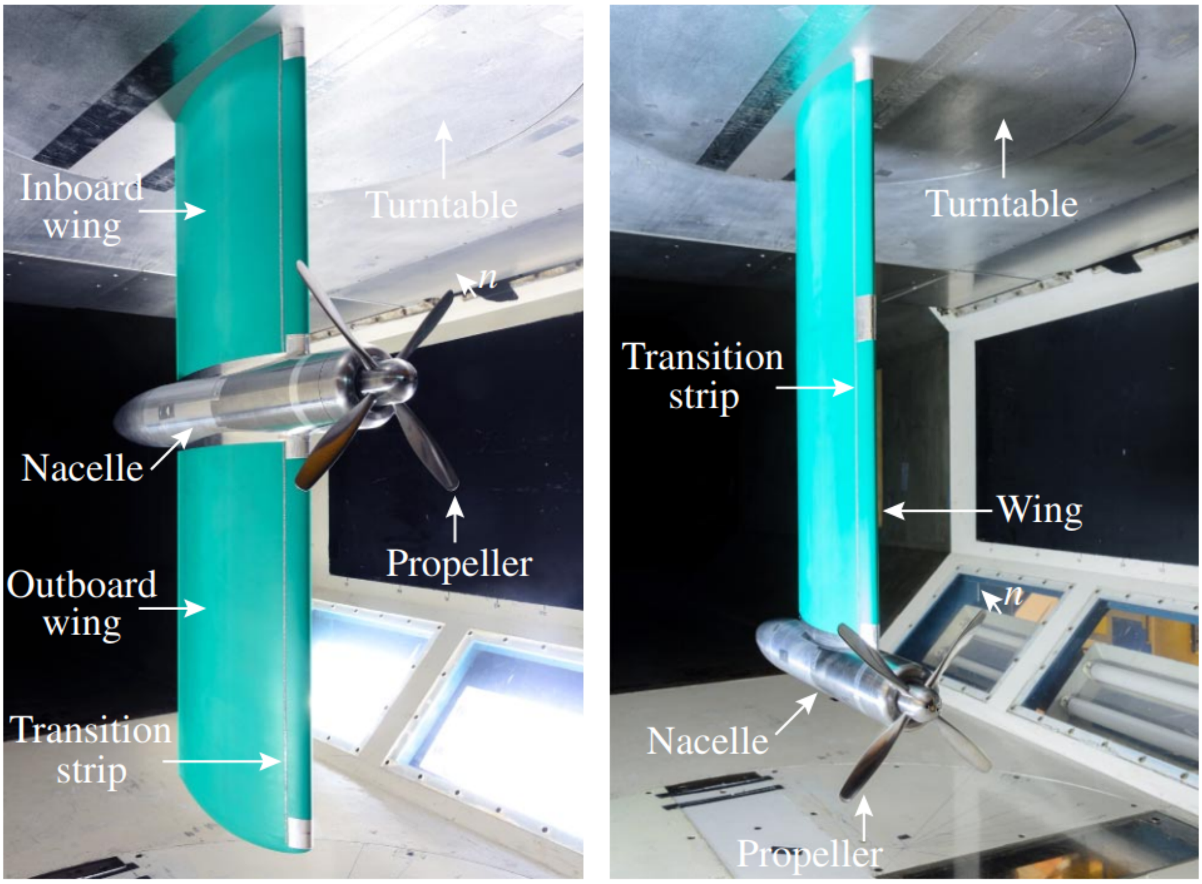

FIGURE 4.2 – Overview of the two possible configurations of the complete geometry (SINNIGE *et al.*, 2019). Left image shows the conventional layout and the right image shows the tip-mounted layout.

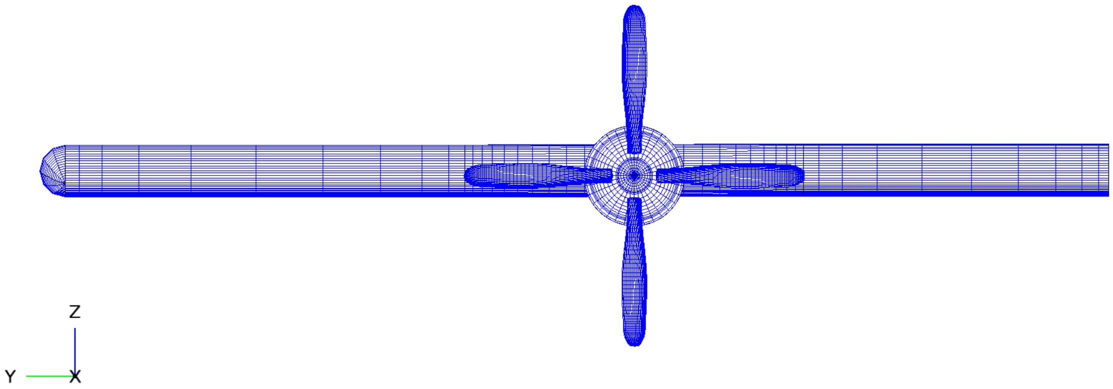

(a) Conventional layout, front view.

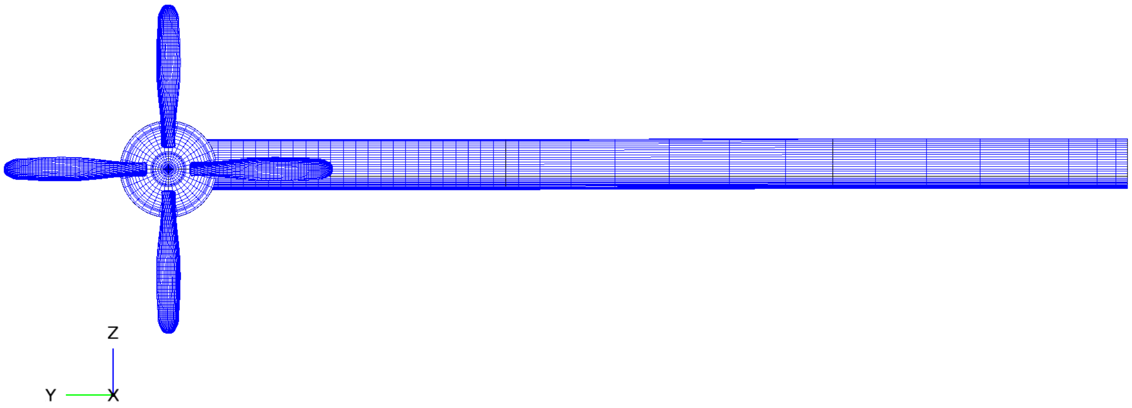

(b) Tip-mounted nacelle, front view.

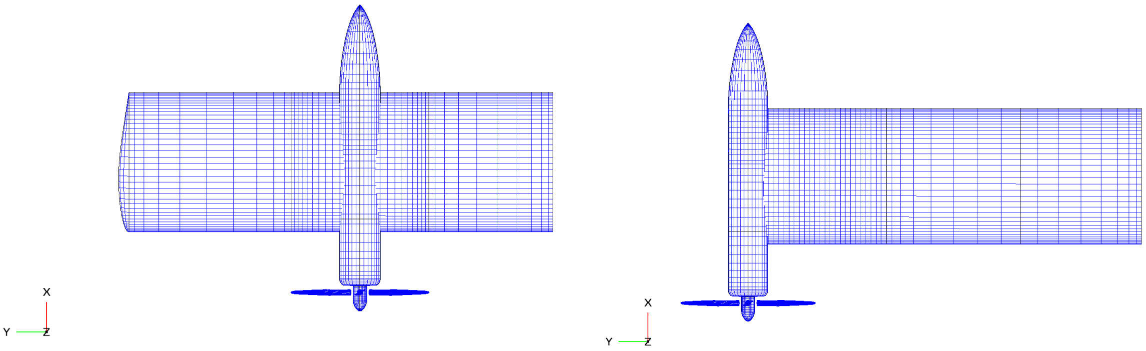

(c) Conventional layout, top view.

(d) Tip-mounted nacelle, top view.

FIGURE 4.3 – Overview of the complete testing geometry, based on the geometry used by (SINNIGE *et al.*, 2019).

4.1.1 Propeller Redesign

Unfortunately, it was found that the geometry near the tip of the propeller blades proved to be problematic during the grid sensitivity study as unresolvable errors would be encountered for grids with 24 or more chordwise panels. This was found to be due to the panels on the tip cap being excessively fine. Therefore, the tip geometry was redesigned slightly, by increasing the chord of the tip compared to the original geometry. This change allowed for significantly greater chordwise grid resolutions to be used and had a relatively minor impact on the performance of the propeller. Furthermore, as discussed in Section 5, the modified geometry results in a more realistic load distribution on the propeller as well.

The comparison between the two chord distributions can be seen in Figures 4.4c and 4.4d, where the latter figure is zoomed in onto the tip to show the difference between the two geometries. Figure 4.5 shows the difference between the original and modified geometry. The data shown 4.4 can also be found in Tables C.1 and C.2.

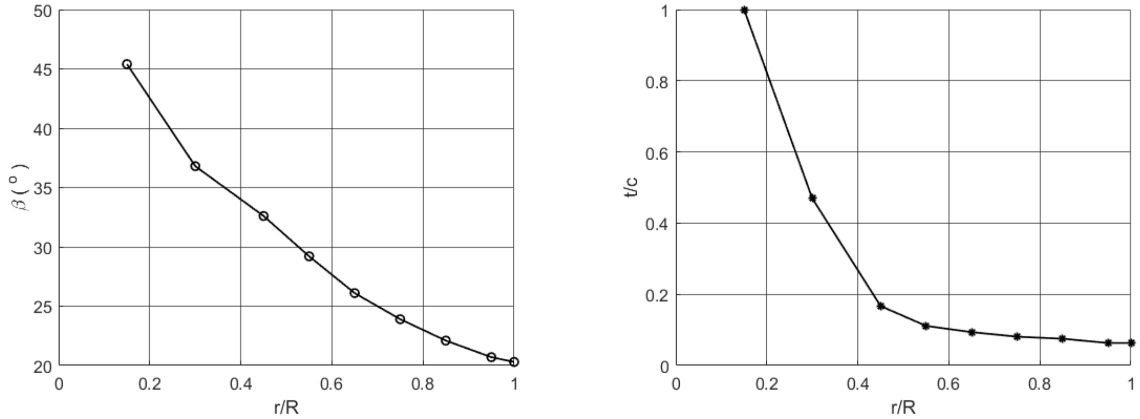

(a) Pitch angle distribution. (b) Thickness distribution.

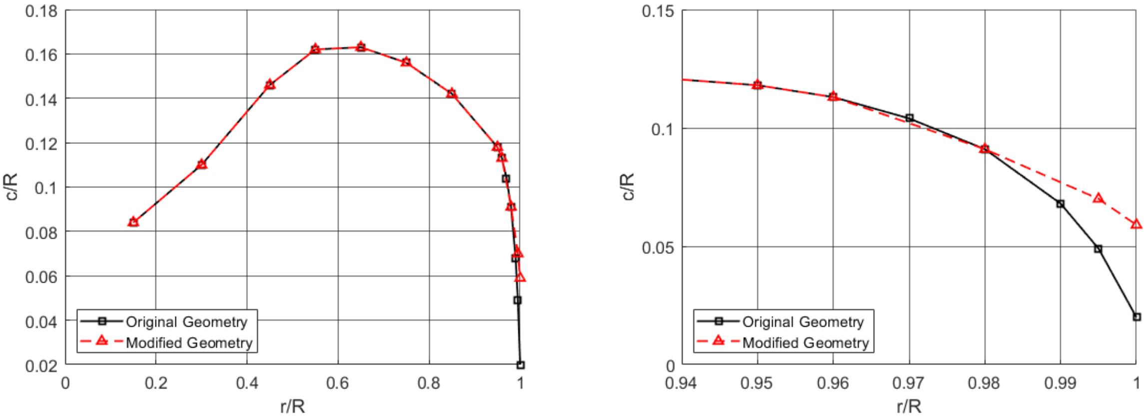

(c) Chord distribution. (d) Zoomed in view of the chord distribution on the tip.

FIGURE 4.4 – Radial distribution of the design parameters of the PROWIM.

In addition to the tip redesign, more changes were required, as the propeller rotation speeds used in the reference studies resulted in exploding 'tumbleweed' wakes, which is not physically correct behavior. Simply reducing the rotation speed would alter the flow characteristics, making it impossible to compare the simulated results to the measurements. However, if the Reynolds and Mach numbers of the flow, as well as the advance ratio of the propeller can be matched for both cases, flow similarity rules will be satisfied and the results of both cases can be compared. Since it is possible to specify the Reynolds and Mach number freely in VSPAero, can be matched to the measurements. However, to match the advance ratios for a reduced propeller rotation speed, either the freestream velocity should be reduced, or the propeller diameter should be increased, both proportionally to the rotation speed reduction. Both of these choices are equally

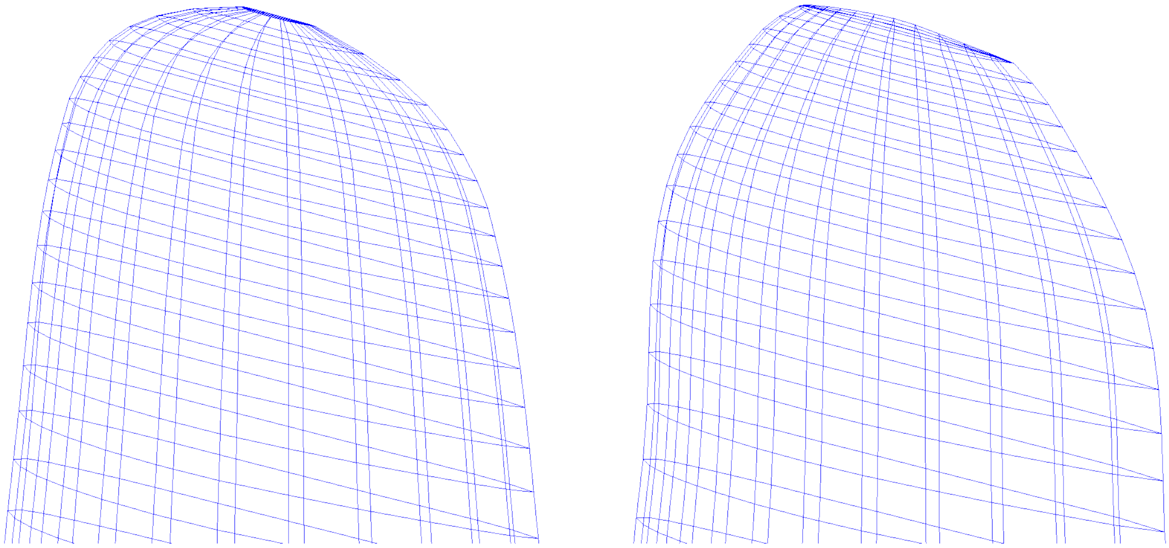

(a) Original tip geometry.

(b) Modified tip geometry.

FIGURE 4.5 – Comparison between the original and modified tip geometry of the PROWIM propeller, zoomed in on approximately the outer 10 % of the radius of the propeller.

valid, and should both give the same result. For this work, it has been chosen to increase the propeller diameter by a factor of five, from 0.237 m, to 1.185 m. Increasing the propeller size by a factor of five, means that the rest of the geometry must be increased in scale by the same factor as well.

4.1.2 Hub Redesign

In the testing geometry shown in Figure 4.3, it can be noticed that the diameter of the spinner seems to be too small, as the propeller blades are not actually attached to the spinner. The diameter of the spinner was decreased on purpose, due to an apparent limitation in OpenVSP for simulating rotating geometries, as only the propeller can be simulated as a rotating component, but not the spinner. This restriction presented a problem during the meshing process, as the mesh of the spinner would have cutouts where the propeller blades would intersect it. However, once the propeller blades would start to move on the next timestep, the holes in the mesh of the spinner remained in the original location, which resulted in a distorted flow field around the spinner, rendering the simulation unusable as a result. To overcome this problem, a few different solutions were tried.

The first solution that was attempted was to modify the cut-in radius of the propeller, such that the roots of the propeller blades would ‘float’ over the surface of the spinner. While this approach removed the holes from the spinner mesh, it resulted in very large pressure coefficients at the propeller blade root and the spinner and unrealistic blade load distributions with large thrust peaks at the root. As this approach yielded physically unreasonable results, it was abandoned.

The second solution that was attempted was to forgo the inclusion of the spinner altogether and to extend the propeller blade roots such that these all meet in the middle of the propeller, to create a cruciform propeller shape. The reasoning behind this approach is that the blockage effect around the center of the propeller that is normally caused by the spinner would still be accounted for. Unfortunately, this approach did not work either, as OpenVSP seemed to have difficulty merging the propeller geometries at their intersecting roots, which resulted in unusable simulations with 'exploded' wakes.

The last solution was very similar to the first: both the spinner and propeller were included in the geometry, but instead of modifying the cut-in radius of the propeller blades, the spinner diameter was decreased instead. Furthermore, a larger gap was left between the spinner and the propeller blades, which was achieved by reducing the spinner diameter by 33.33%, though it should be remarked that other values may work as well. This method has the benefit of maintaining a consistent propeller geometry across all simulations, which is highly desirable as the propeller is the main focus of this research. Fortunately, this solution yielded simulations without exploding wakes, nor without physically unrealistic load distributions. Therefore, the decreased spinner diameter was maintained for all simulations where the complete geometry was used.

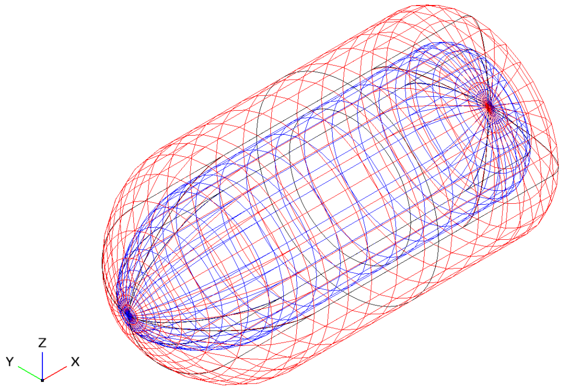

FIGURE 4.6 – Size comparison between the original spinner geometry shown in red, and the modified geometry with a reduced diameter shown in blue.

4.2 Simulation Strategy

To gain confidence and understand the limits of VSPAero, a set of test cases of increasing complexity are simulated and analyzed. Therefore, before considering the complete geometry as shown in Figure 4.3, a grid sensitivity study will be performed first on an isolated rectangular wing to evaluate the consistency of the results obtained with VSPAero and determine the level of grid-dependence in the solutions. This grid refinement study will also investigate the influence of the VSPAero wake settings on the results. The goal of this set of simulations is to determine which spatial grid and wake settings yield consistent simulation behavior.

Next, an isolated propeller will be investigated, using the spatial grid settings found for the isolated wing. As the propeller is an unsteady simulation, a temporal refinement study will be performed to determine the effect of the timestep on the results, in addition to the effect of the spatial grid.

For the last part of the grid sensitivity study, the combination of the propeller and wing geometries will be investigated, to emulate a simplified version of the geometry discussed in Section 4.1. With this geometry, a short spatial and temporal refinement procedure will be performed, to verify whether the aerodynamic interference affects the convergence behavior observed for the two separate geometries. Additionally, during all phases of the grid sensitivity study, the computation time for all simulations was tracked. Aside from accuracy, the computation time requirement is an important consideration for any numerical method. Hence, the goal of the last phase of the grid sensitivity study is to determine which spatial and temporal resolution yields acceptable accuracy for the cases considered in this report, while not being too computationally expensive.

In addition to a grid sensitivity analysis, a few additional simulations were performed to evaluate the simulation capabilities of VSPAero. Similarly to the grid sensitivity study, these simulations are set-up in order of increasing complexity. First, a quasi-2D, incompressible and inviscid test case will be compared against XFoil to evaluate how accurate the fundamental potential flow solution process from VSPAero is. Secondly, the accuracy of two stall correction models included with VSPAero will be compared against wind tunnel measurements. Thirdly, the redesigned propeller geometry from Section 4.1.1 will be simulated and compared to the original geometry. Lastly, the simplest non-axisymmetric propeller load case will be investigated, by comparing the simulation results for a propeller which has its thrust axis aligned with the freestream and a propeller placed under a 10 degree angle of attack. As the main topic of this research involves a significantly non-uniform propeller inflow, this case will serve as the prelude to the main research goal.

After the grid sensitivity and accuracy studies had been completed, the main research simulations were carried out in three distinct phases of increasing complexity:

1. Isolated propeller.
2. Propeller and wing without nacelle or spinner.
3. Complete geometry.

Aside from applying the strategy of increasing complexity, each of these three phases had different research objectives. For the first phase, the main objective is to establish the baseline performance of the propeller by performing an advance ratio sweep and angle of attack sweep. Additionally, this baseline will be compared to experimental results and numerical results obtained with the VLM mode in VSPAero to compare how the results between these three methods differ.

For the second phase, the goal is to evaluate whether the aerodynamic interference can be accounted for in VSPAero by performing a similar advance ratio and angle of attack sweep as in phase 1 and comparing the results to the baseline and experiments. Additionally, difference in the aerodynamic interference effect of mounting the propeller on the midspan or tip will be investigated.

Lastly, for the third phase, the goal is to evaluate how accurate the complete geometry can be simulated and how the results differ from the experiments.

5 VSPAero Grid Sensitivity Study

Before analyzing the propeller-wing interference with VSPAero, a grid sensitivity study is performed to verify that the simulations converge to the same solution for finer grids and to quantify the numerical error. This is an important step required for interpreting the results correctly, since any simulation is wrong if the numerical error cannot be quantified. Additionally, the grid refinement study will give insights to the scaling of the computational time with respect to the complexity of the simulation. Understanding the relation between the simulation time and simulation complexity is practical for several reasons, as it facilitates planning simulations, estimating the simulation time for untested settings and even for knowing when to switch to a different numerical method, as at some point increasing the level of detail in a simulation yields diminishing returns.

In VSPAero, there are many different simulation settings that can potentially affect the convergence behavior of the simulations. Aside from the number of panels, the aspect ratio and tesselation of the panels could play a role. Furthermore, the amount of wake nodes and wake iterations can significantly impact the convergence and accuracy of the simulations as well. Although there is no standardized procedure for performing a grid sensitivity study, the goal is to verify whether the solution produced by the numerical solver is grid-independent. Thus, for increasingly finer grids, the differences between the solutions should become increasingly smaller and converge to the same solution in the limit of an infinitely fine grid (HAGMEIJER, 2008). It should be noted however, that a converged solution may not be the exact solution, as the numerical method likely contains assumptions, simplifications, and errors that result in a difference with respect to the exact solution.

A strategy for the sensitivity study was created based on earlier works involving OpenVSP by (SHERIDAN *et al.*, 2021), (MARIËN, 2021) and (REDDY, 2023), as well as more general sources on numerical methods (VAN DER WEIDE, 2021) (VENNER; LUBRECHT, 2000) and modeling recommendations by the OpenVSP team (LITHERLAND, 2021). The grid refinement process was performed with a simplified geometry and was divided into three broad steps:

1. Refinement of an isolated wing.
2. Refinement of an isolated propeller.
3. Refinement of a wing-propeller combination.

Each of these steps has a different goal: With the isolated wing refinement, the focus is on the spatial grid and wake properties, as this is a steady simulation and time refinement is not applicable. The objective of the wing refinement is to determine which spatial grid settings produce good convergence behavior, which will serve as the grid settings for the research geometry. For the isolated rotor refinement, the grid settings found in the previous step will be used, and a time refinement study will be done to determine which time integration settings are necessary to show good convergence behavior. Lastly, the refinement with the combined geometry will serve as a verification step to see if convergence behavior is found for a simulation with the same characteristics as the research geometry.

Since VSPAero has a lot of settings for the spatial grid, the refinement process for the isolated wing was performed by doing several simulation runs where every time a different parameter is changed. The refinement sweeps were performed as follows:

1. Clustered panels with the default VSPAero settings.
2. Wake detail, to see how the wake affects to solution.
3. Different panel aspect ratios.

With these sweeps, a grid configuration could be found in the end that showed good convergence behavior, which gives confidence in the accuracy of the numerical solution.

5.1 Isolated Wing

In this section, a summary of the findings from the grid sensitivity study for the isolated wing will be shown. A straight wing with a NACA0018 profile over the whole span and an aspect ratio of ten was used. Rounded caps were applied on the wing tips. A geometric overview is given in Figure 5.1 and Table 5.1. For all cases, the global lift, drag and moment coefficients, as well as change of these parameters will be tracked to evaluate the convergence behavior. The differences in the parameters between runs are expressed in two ways: the L_2 norm of the difference between subsequent simulations and the percentage difference of the results with respect to the finest grid setting tested for a given set of simulations. Additionally, the spanwise distribution of these coefficients has been compared as well.

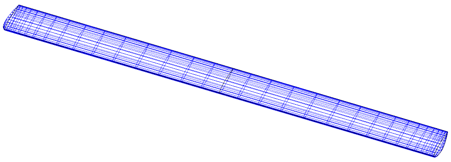

FIGURE 5.1 – Overview of the isolated wing geometry.

TABLE 5.1 – Geometric properties of the wing.

c - wing chord (m)	0.68065
s - wing span (m)	6.8065
S - wing surface area (m^2)	4.6328
AR - wing aspect ratio (-)	10

5.1.1 Simulation Settings

For all grid refinement simulations with only the isolated wing, the wing was set at an angle of attack of five degrees, with the following freestream properties: $Re = 700000$ and $M = 0$. Furthermore, the side-slip angle of the flow was set to zero degrees and no stall model was enabled.

Furthermore, unless otherwise specified, the default simulation settings from VSPAero were used, which are listed in Table 5.2.

TABLE 5.2 – Default VSPAero simulation settings.

Setting	Default	Explanation
Preconditioner type	Matrix (LU)	Matrix preconditioning setting for the solver.
Wake type	Free	Toggle for wake solution mode.
Wake iterations	10	Number of wake relaxation iterations, does not apply for fixed wakes.
Wake nodes	64	Number of nodes for the wake curvature.
Far-field distance	One semispan	Maximum trailing wake length.

5.1.2 Panel Count

For the first run of the grid sensitivity study, the influence of increasing the panel count on the solution was investigated. The wing was discretized using a quasi-cosine clustering scheme, with the tip cap paneling being adjusted to ensure that neighboring panels were of similar size and aspect ratio. Many studies performed with VSPAero often used ‘VLM-style’ grids with equidistant panel spacing. This is a poor discretization of the leading edge of the wing, as the geometry is captured poorly and the suction peak near the leading edge is easily miscalculated. Therefore, no such discretization is used in this report.

In addition to the increasing panel count, the amount of wake nodes was increased from the default value of 64 to 128. To show the panel distribution, the coarsest grid setting is shown in Figure 5.2. It can be seen that the panels are clustered near the edges of the wing, particularly near the tips due to the larger amount of spanwise panels than chordwise panels. The summary of grid settings used is shown in Table 5.3.

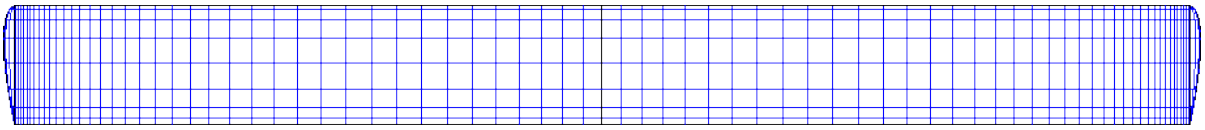

(a) Top view.

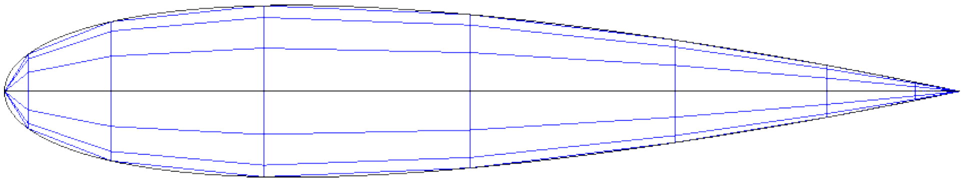

(b) Side view.

FIGURE 5.2 – Coarsest grid used for the first run of the isolated wing grid sensitivity study.

TABLE 5.3 – Grid settings tested for the first refinement run, including the total panel counts. *Not including tip caps.

Spanwise panels*	Chordwise panels*	Total panels without caps	Total panels
40	16	640	704
50	20	1000	1080
60	24	1440	1560
70	28	1960	2128
80	32	2560	2752
90	36	3240	3492
100	40	4000	4320
110	44	4840	5192
120	48	5760	6144
130	52	6760	7228
140	56	7840	8400
150	60	9000	9660
160	64	10240	11008

5.1.2.1 Global Coefficients for Panel Counts

The obtained results for the evolution of the global coefficients are shown in Figure 5.3a and Table 5.4. It can be seen that generally, the coefficients do not change much for increasingly finer grids, as can be seen in Figure 5.3a. However, when considering the difference between the results for increasingly finer grids, shown in Figure 5.3b that there is no downward linear in the L_2 norm of subsequent simulation results, indicating poor convergence behavior. Figure 5.3c, shows that relative to the finest grid, the difference between the results seems to decrease for finer grids, though it should be kept in mind that there is no indication that the result for the finest grid can be considered as sufficiently converged to use as a reference.

TABLE 5.4 – Global coefficients obtained during the first refinement run.

Total panels	704	1080	1560	2128	2752	3492	4320	5192	6144	7228	8400	9660	11008
C_L	0.4746	0.4793	0.4747	0.4668	0.4647	0.4619	0.4649	0.4621	0.4630	0.4557	0.4580	0.4550	0.4592
C_D	0.0210	0.0214	0.0214	0.0214	0.0212	0.0213	0.0214	0.0215	0.0215	0.0218	0.0216	0.0217	0.0217
C_M	-0.1108	-0.1148	-0.1142	-0.1120	-0.1120	-0.1118	-0.1137	-0.1133	-0.1140	-0.1123	-0.1128	-0.1121	-0.1139

TABLE 5.5 – L2 norms of the coefficients with respect to the previous grid setting.

Total panels	704	1080	1560	2128	2752	3492	4320	5192	6144	7228	8400	9660	11008
C_L	n/a	$4.6649 \cdot 10^{-3}$	$4.5412 \cdot 10^{-3}$	$7.8886 \cdot 10^{-3}$	$2.1761 \cdot 10^{-3}$	$2.7739 \cdot 10^{-3}$	$3.0405 \cdot 10^{-3}$	$2.8694 \cdot 10^{-3}$	$9.227 \cdot 10^{-4}$	$7.2671 \cdot 10^{-3}$	$2.2854 \cdot 10^{-3}$	$3.016 \cdot 10^{-3}$	$4.184 \cdot 10^{-3}$
C_D	n/a	$3.9579 \cdot 10^{-4}$	$4.3299 \cdot 10^{-5}$	$3.1059 \cdot 10^{-5}$	$1.812 \cdot 10^{-4}$	$1.6293 \cdot 10^{-4}$	$9.5552 \cdot 10^{-5}$	$8.472 \cdot 10^{-5}$	$5.2425 \cdot 10^{-6}$	$2.8578 \cdot 10^{-4}$	$2.1781 \cdot 10^{-4}$	$8.1948 \cdot 10^{-5}$	$1.3881 \cdot 10^{-7}$
C_M	n/a	$4.013 \cdot 10^{-3}$	$6.5804 \cdot 10^{-4}$	$2.1656 \cdot 10^{-3}$	$5.9512 \cdot 10^{-5}$	$1.6984 \cdot 10^{-4}$	$1.9478 \cdot 10^{-3}$	$4.3453 \cdot 10^{-4}$	$7.4178 \cdot 10^{-4}$	$1.7685 \cdot 10^{-3}$	$4.9001 \cdot 10^{-4}$	$7.1431 \cdot 10^{-4}$	$1.8204 \cdot 10^{-3}$

5.1.2.2 Spanwise Distribution for Panel Counts

The spanwise distributions of the three coefficients are shown in Figure 5.4. For the lift distribution shown in 5.4a, it can be seen that the same general shape is obtained for all grid settings, where the most lift is generated at the midspan of the wing and a large reduction close to the wingtips due to tip losses. However an unexpected asymmetry can be observed for the distribution obtained for 7228 panels. It is possible that this is a recurring issue with VSPAero, as (SHERIDAN *et al.*, 2021) noted strange results for an isolated wing with a similar grid settings,

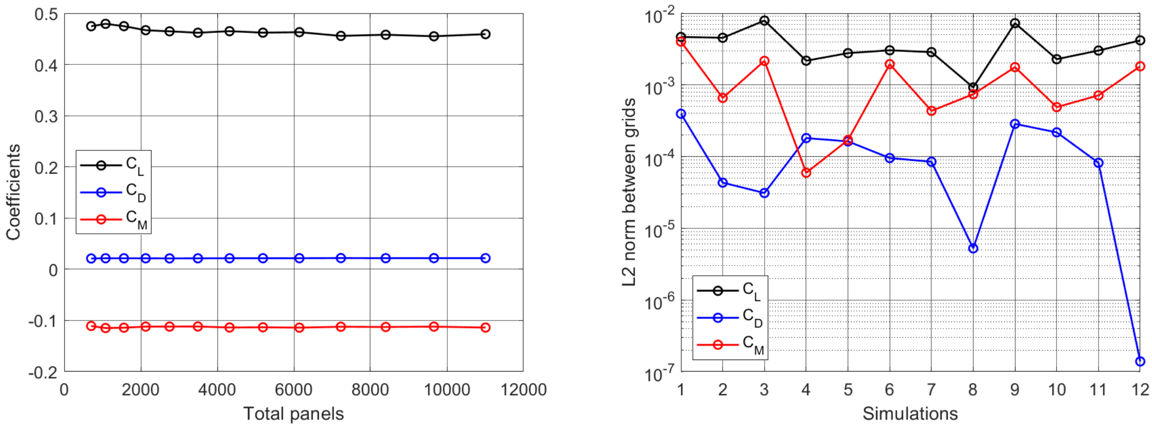

(a) Evolution of the global coefficients.

(b) L2 norms of the global coefficients.

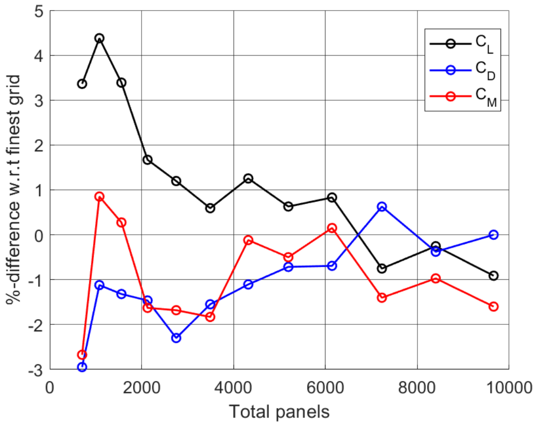

(c) Percentage difference for all simulations with respect to the finest grid tested.

FIGURE 5.3 – Global wing coefficient results for grids with increasing panel counts.

where unexpected results were obtained with a U-tesselation setting of 133, and the authors recommended to not use a U-tesselation similar to this value. Since the 7228 panel grid uses a U-tesselation of 131, it might suffer from the same issue.

The drag distribution shown in Figure 5.4b shows rather bizarre results, as rather large oscillations can be seen, especially for the coarsest and finest grids considered. It is highly unlikely that this is caused by the viscous drag correction, as that is a post-processing step based primarily on the local velocity. Hence, the drag results seem to indicate that a potential grid-dependent instability is present in the velocity calculations of VSPAero. If the drag oscillations are ignored, the general shape of the drag distributions is more or less as expected.

Lastly, for the moment distribution shown in Figure 5.4c, it can be seen that there is very little difference for finer grids, though some odd behavior can be observed for the coarsest grid near the wingtips. The overall shape of the moment distribution is roughly the inverse of the lift distribution as expected.

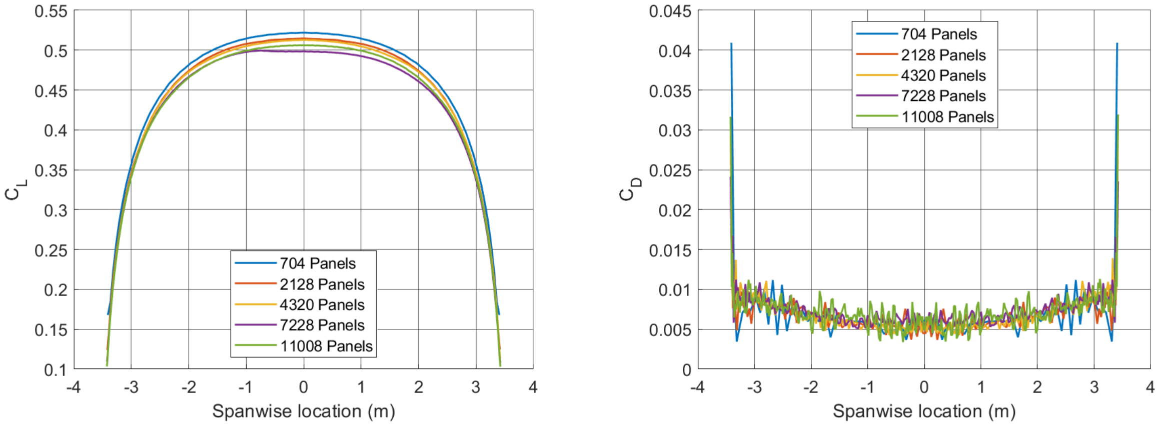

(a) Lift distributions.

(b) Drag distributions.

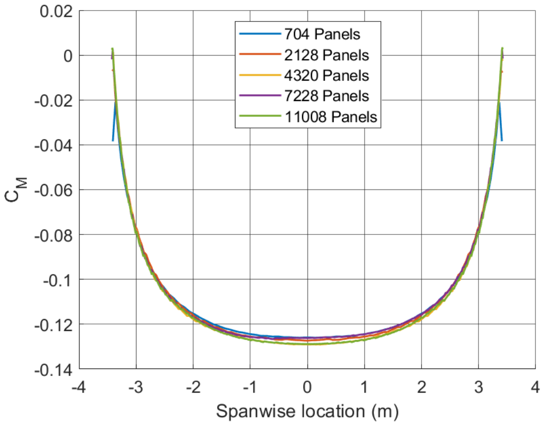

(c) Moment distributions.

FIGURE 5.4 – Comparison between spanwise load distributions for increasing amounts of wing panels.

5.1.2.3 Computation Time Dependency on Panel Count

The relation between the computation time and the total amount of wing panels is plotted in Figure 5.5. A fit with a slope of 1.30 can be fitted through the data points, whereas typical solvers for systems of linear equations have quadratic or even cubic time complexity.

5.1.2.4 Conclusion for Increasing Panel Counts

It was seen that only increasing the panel count is apparently not sufficient to obtain converging results in VSPAero. However, it is possible that the default wake settings result in wakes of insufficient detail relative to the finer grids. Thus, the numerical error on the grid might be reduced, but the error in the wake could be dominant, making the error reduction from a finer grid irrelevant. This will be investigated in Section 5.1.3.

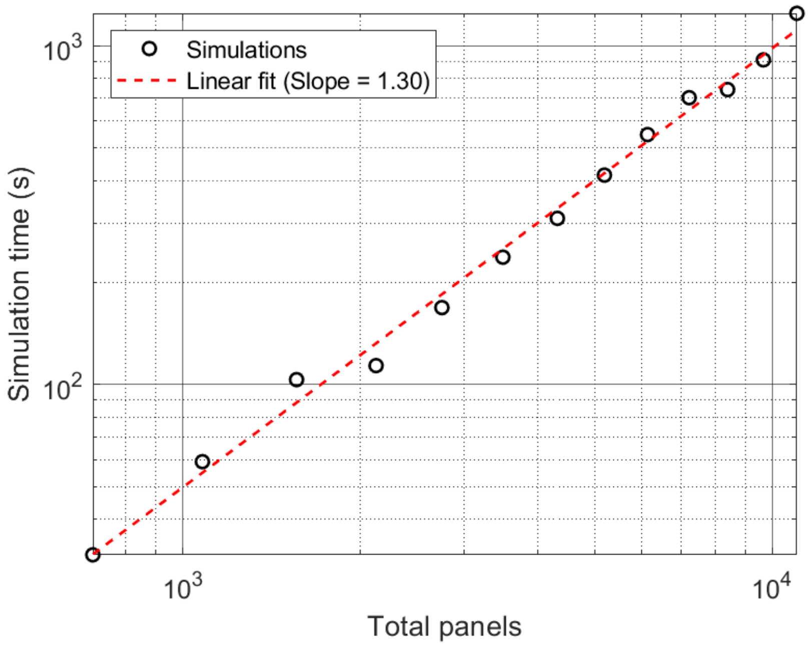

FIGURE 5.5 – Relation between computation time and panel count.

5.1.3 Wake Refinement

For wake refinement study, the grid of the wing was kept unchanged and the amount of wake iterations was increased in steps of five up to 50 total iterations. Additionally, the 'fixed wake' setting was tested as well, which will perform no iterative process to determine the wake shape, and instead align it with the exit streamline of the trailing edge. All other settings were kept the same as stated in Section 5.1.2.

Compared to the meshes used in Section 5.1.2, a mesh with greater chordwise detail was used to attempt to capture the suction peak better. The mesh uses 40 spanwise and 120 chordwise panels. A factor four coarsened version of the mesh is shown in Figure 5.6.

(a) Top view.

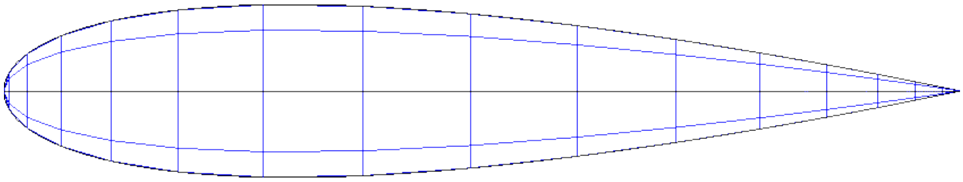

(b) Side view.

FIGURE 5.6 – Grid used for the wake refinement study. Coarsened by a factor of four for clarity.

5.1.3.1 Global Coefficients for Wake Refinement

The obtained results for the global coefficients are plotted in Figure 5.7 and Table 5.6. Compared to the results obtained for increasing the panel count, it can be seen in Figure 5.7a that the global coefficients are significantly less sensitive to changes in the amount of wake iterations compared to changes in the panel count. It can be seen that the convergence behavior up to approximately 25 wake iterations shows a consistent downward linear trend for the lift and moment coefficient, as can be seen in Figure 5.7b, though beyond this point the convergence behavior seems to become inconsistent. The drag convergence exhibits oscillatory behavior in the convergence plot, though a general downward trend can be observed. Furthermore, Figure 5.7c shows that the variations between runs are quite small to begin with, and decrease consistently as well, with differences lower than 0.2% being achieved for ten or more wake iterations. In general, it appears that the results are less sensitive to the amount of wake relaxations than the number of panels.

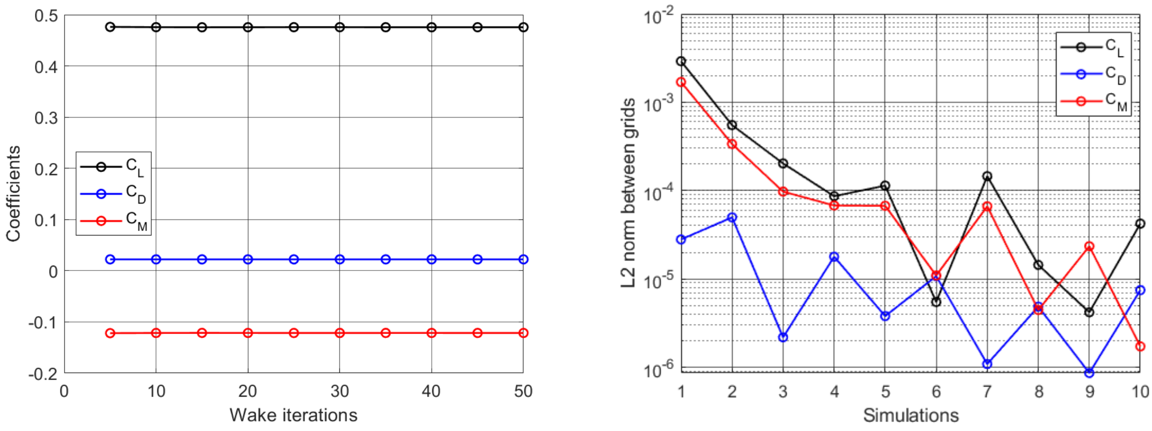

(a) Evolution of the global coefficients for different amounts of wake iterations.

(b) L2 norms of the global coefficients for increasing wake iteration amounts.

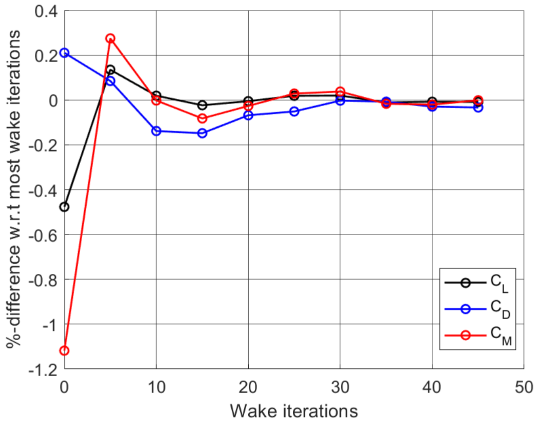

(c) Percentage difference for all simulations with respect to the most wake iterations tested.

FIGURE 5.7 – Results of the global coefficients from the wake refinement run.

TABLE 5.6 – Global coefficients obtained during the wake refinement run.

Wake Iterations	Fixed	5	10	15	20	25	30	35	40	45	50
C_L	0.4733	0.4762	0.4757	0.4754	0.4755	0.4756	0.4757	0.4755	0.4755	0.4755	0.4756
C_D	0.0223	0.0223	0.0222	0.0222	0.0222	0.0222	0.0222	0.0222	0.0222	0.0222	0.0222
C_M	-0.1202	-0.1219	-0.1216	-0.1215	-0.1215	-0.1216	-0.1216	-0.1215	-0.1215	-0.1216	-0.1216

TABLE 5.7 – L2 norms of the coefficients with respect to the previous wake setting.

Wake Iterations	Fixed	5	10	15	20	25	30	35	40	45	50
C_L	n/a	$2.9084 \cdot 10^{-3}$	$5.5087 \cdot 10^{-4}$	$2.0273 \cdot 10^{-4}$	$8.6269 \cdot 10^{-5}$	$1.1362 \cdot 10^{-4}$	$5.4697 \cdot 10^{-6}$	$1.4537 \cdot 10^{-4}$	$1.4385 \cdot 10^{-5}$	$4.1852 \cdot 10^{-6}$	$4.2212 \cdot 10^{-5}$
C_D	n/a	$2.7929 \cdot 10^{-5}$	$4.9650 \cdot 10^{-5}$	$2.1809 \cdot 10^{-6}$	$1.7814 \cdot 10^{-5}$	$3.7902 \cdot 10^{-6}$	$1.0731 \cdot 10^{-5}$	$1.0867 \cdot 10^{-6}$	$4.8507 \cdot 10^{-6}$	$8.5971 \cdot 10^{-7}$	$7.4653 \cdot 10^{-6}$
C_M	n/a	$1.6924 \cdot 10^{-3}$	$3.3661 \cdot 10^{-4}$	$9.7226 \cdot 10^{-5}$	$6.7689 \cdot 10^{-5}$	$6.7113 \cdot 10^{-5}$	$1.0917 \cdot 10^{-5}$	$6.6225 \cdot 10^{-5}$	$4.4402 \cdot 10^{-6}$	$2.3411 \cdot 10^{-5}$	$1.7195 \cdot 10^{-6}$

5.1.3.2 Spanwise Distribution for Wake Refinement

The spanwise loads are shown in Figure 5.8. It can be seen that in general, the amount of wake relaxation iterations does not seems to affect the spanwise distributions significantly. For the drag distribution shown in Figure 5.8b, the fixed wake results show a significant asymmetry in the drag distribution. This is likely caused by slight asymmetry in the wing panel agglomeration, which results in an asymmetric velocity field over the wing and wake shedding. Additionally, compared to the drag distribution seen in Section 5.1.2.2, it can be seen that the drag distribution is significantly less jagged. This is likely due to the greater chordwise panel count, which seems to the pressure-integration results significantly. The amount of wake relaxation iterations does not appear to affect the drag distribution, all results except those for the fixed wake coincide.

5.1.3.3 Computation Time for Wake Refinement

The relation between the number of wake iterations and the computation time is shown in Figure 5.9. The necessity to account for run-to-run variation can be seen, as there are two points where an increase in wake iterations requires less simulation time, and the computation times for 25 to 40 wake iterations seem disproportionally lower than the others, though it is more likely that the other simulations took longer to finish than expected, due to other programs working in the background. To create the linear fit, the results from 25 to 40 iterations were not taken into account, resulting in a slope of 0.91. If all point were used, the slope would be 0.82. In both cases, this is a slope lower than one, suggesting that the amount of computation time grows proportionally slower than the amount of wake iterations. However, it is hard to claim with certainty that this is correct, as this is unexpectedly efficient and the actual computation times did behave strange at times.

5.1.3.4 Conclusion for Wake Refinement

From the results obtained with the wake refinement process, it could be seen that increasing the amount of wake iterations from the default value of 10 and the increase in chordwise paneling could increase the consistency of the numerical results. Therefore, for subsequent refinement runs, the amount of wake iterations was increase to 25, in accordance with Figure 5.7b and the higher chordwise resolution was maintained as well.

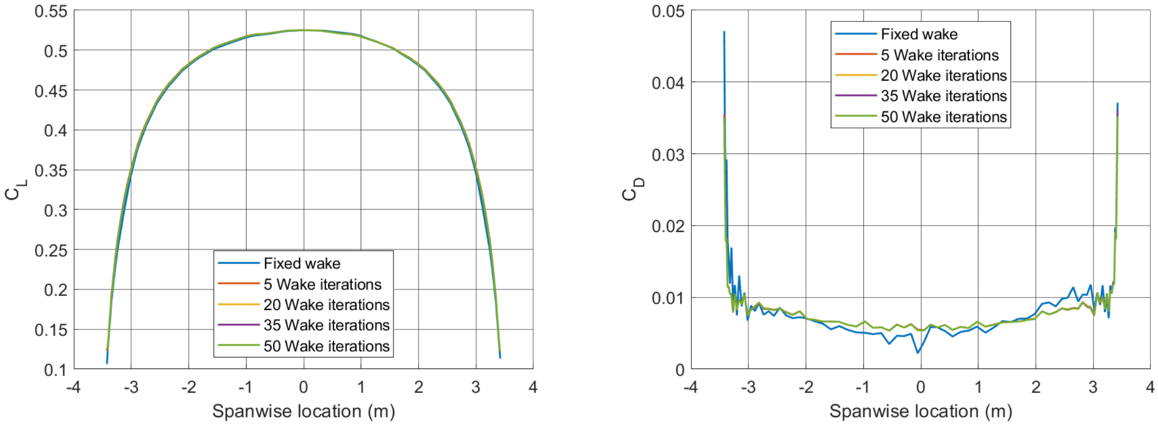

(a) Comparison of lift distributions.

(b) Comparison of drag distributions.

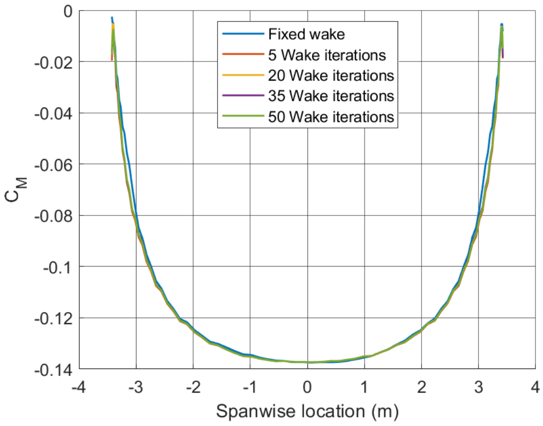

(c) Comparison of moment distributions.

FIGURE 5.8 – Results of the spanwise load distributions from the wake refinement simulations.

5.1.4 Final Grid Settings

For the final grid refinement run, the wake settings discussed in the previous sections were used and the amount of wake nodes was increased from 128 to 256. Furthermore, the far-field distance setting, which influences trailing wake length, was set to ten wingspans. A similar chordwise to spanwise panel ratio was used as in Section 5.1.3. The coarsest grid is shown in Figure 5.10. The summary of grid settings used is shown in Table 5.8.

TABLE 5.8 – Grid settings tested for the final refinement run, including the total panel counts. *Not including the tip caps.

Spanwise panels*	Chordwise panels*	Total panels without caps	Total panels
8	16	128	240
16	32	512	736
24	48	1152	1488
32	64	2048	2496
40	80	3200	3760
48	96	4608	5280
56	112	6272	7056

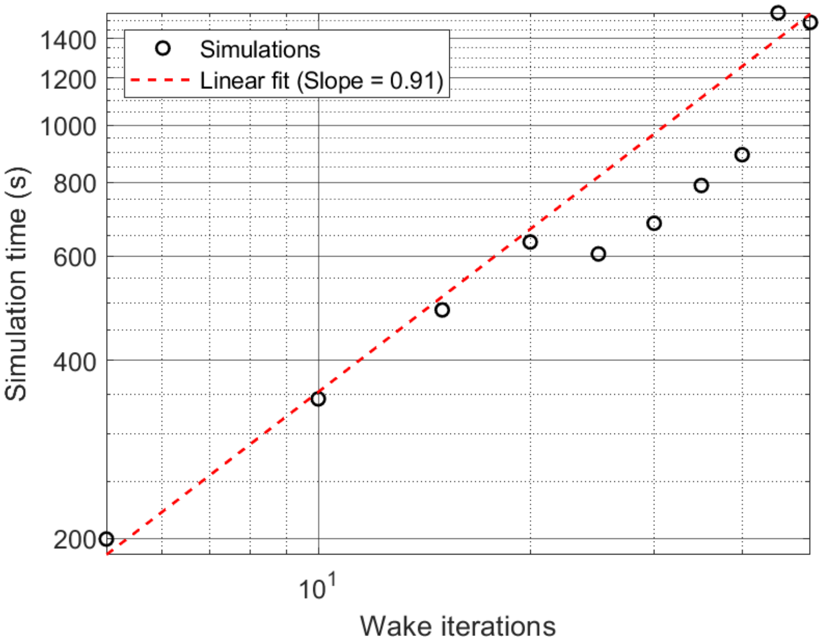

FIGURE 5.9 – Relation between computation time and wake iteration count.

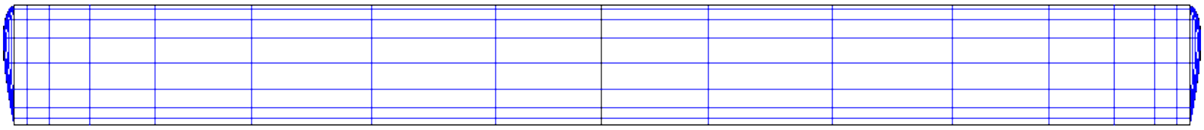

(a) Top view.

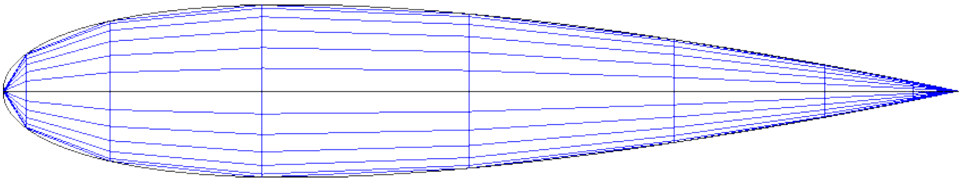

(b) Side view.

FIGURE 5.10 – Coarsest grid used for the last run of the isolated wing grid sensitivity study.

5.1.4.1 Global Coefficients for the Final Grid Settings

The obtained results for the evolution of the global coefficients are shown in Figure 5.11a and Table 5.9. When comparing Figure 5.11a to Figure 5.3a, it can be seen that the variation between the global coefficient for grid levels is lower for the final set analyzed. Furthermore, when looking at the L2 norms between grids as seen in Figure 5.11b and Table 5.10, it can be observed that the L2 norm shows a somewhat consistent linear decrease for finer grids, especially compared to the convergence behavior seen in Section 5.1.2. This trend can be observed in Figure 5.11c as well, as the differences between increasingly finer grids become smaller than 0.01%, which is a remarkably good result. Especially when compared to Figure 5.3c, where it can be seen that the difference in the results compared to the finest grid setting is at least two orders of magnitude greater.

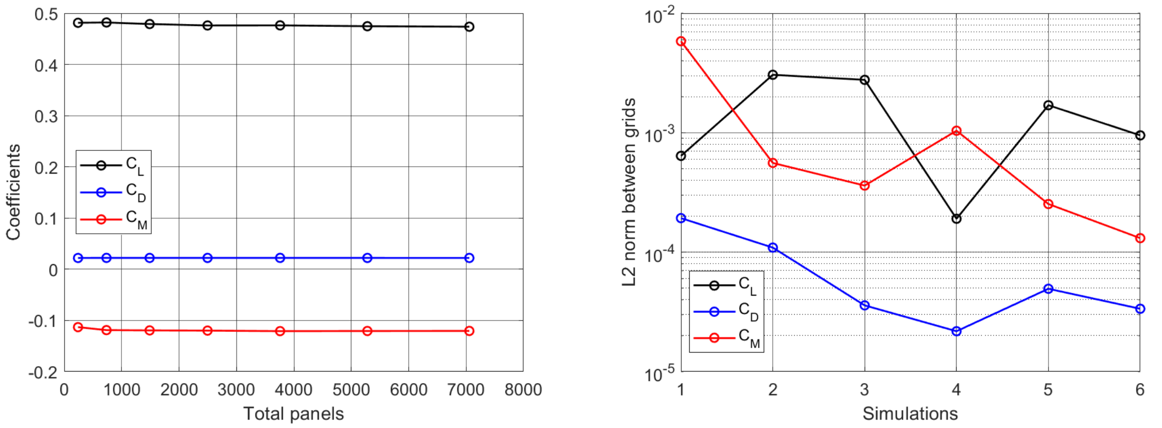

(a) Evolution of the global coefficients between different grid sizes.

(b) L2 norms of the global coefficients between subsequent grid sizes.

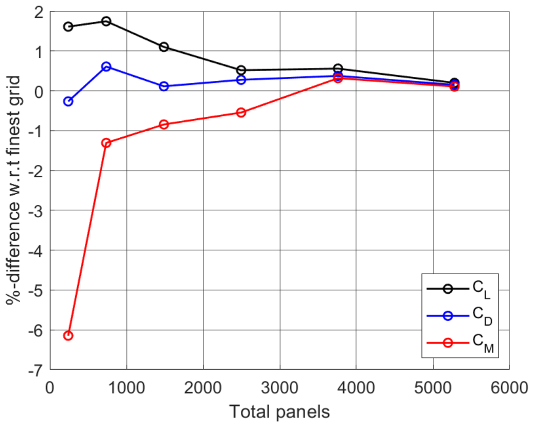

(c) Percentage difference for all simulations with respect to the finest grid tested.

FIGURE 5.11 – Global coefficient results for the final isolated wing grid sensitivity run.

TABLE 5.9 – Global coefficients obtained during the final isolated wing grid sensitivity run.

Total panels	240	736	1488	2496	3760	5280	7056
C_L	0.4813	0.4819	0.4789	0.4761	0.4763	0.4746	0.4736
C_D	0.0220	0.0222	0.0221	0.0221	0.0221	0.0221	0.0221
C_M	-0.1130	-0.1189	-0.1194	-0.1198	-0.1208	-0.1206	-0.1204

TABLE 5.10 – L2 norms of the coefficients with respect to the previous grid setting.

Total panels	240	736	1488	2496	3760	5280	7056
C_L	n/a	$6.3943 \cdot 10^{-4}$	$3.0522 \cdot 10^{-3}$	$2.7679 \cdot 10^{-3}$	$1.9044 \cdot 10^{-4}$	$1.6981 \cdot 10^{-3}$	$9.5007 \cdot 10^{-4}$
C_D	n/a	$1.9276 \cdot 10^{-4}$	$1.0922 \cdot 10^{-4}$	$3.5866 \cdot 10^{-5}$	$2.1800 \cdot 10^{-5}$	$4.9399 \cdot 10^{-5}$	$3.3595 \cdot 10^{-5}$
C_M	n/a	$5.8293 \cdot 10^{-3}$	$5.5824 \cdot 10^{-4}$	$3.6079 \cdot 10^{-4}$	$1.0390 \cdot 10^{-3}$	$2.5300 \cdot 10^{-4}$	$1.3102 \cdot 10^{-4}$

5.1.4.2 Spanwise Distribution for the Final Grid Settings

The spanwise load distributions are shown in Figure 5.12. It can be seen that the spanwise distributions seem to converge to the same distribution for increasingly finer grids. Additionally, when comparing the drag distribution from Figure 5.12b to figure5.4b, it can be seen that the spanwise drag oscillations are not as significant. Unfortunately, they are still present and it is likely that it the only solution to completely eliminating the drag oscillations is to use an excessively coarse grid, which is undesirable. It can be seen that the coarsest grid setting is too coarse, as it is the only setting where the lift distribution and especially moment distribution diverges significantly from the other results.

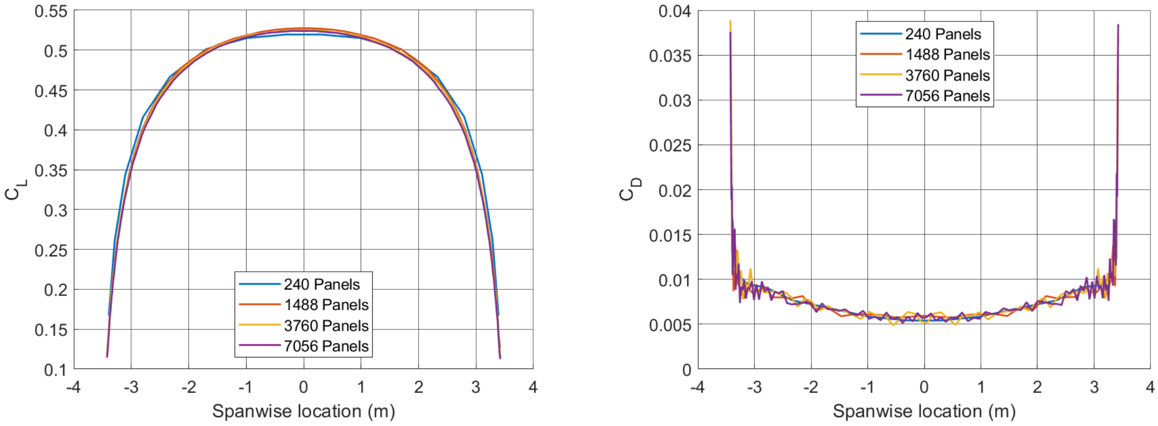

(a) Comparison of lift distributions.

(b) Comparison of drag distributions.

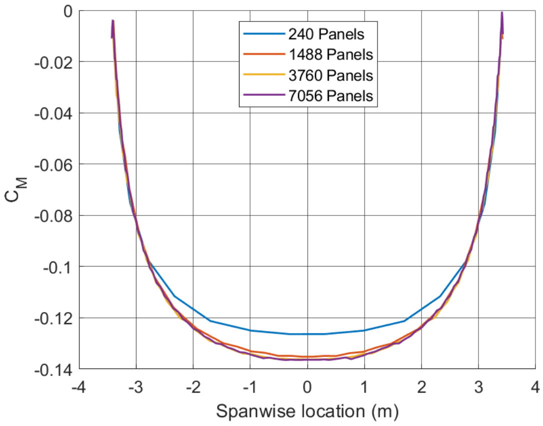

(c) Comparison of moment distributions.

FIGURE 5.12 – Results of the spanwise load distributions from the final isolated wing grid sensitivity run.

5.1.4.3 Computation Time for the Final Grid Settings

The computation time evolution of the final run is shown in Figure 5.13. It can be seen that the slope is similar to the one observed in Section 5.1.2. The overall computation time has increased due, most likely due to the increased amount of wake iterations and wake nodes.

5.1.4.4 Conclusion for the Final Grid Settings

The final set of grid refinement simulations has shown that with some adjustment of the simulation settings, it is possible to achieve quite decent convergence behavior with VSPAero for steady simulations. The final grid settings used in this section will be used as the starting point for the propeller grid for the sensitivity studies for the propeller and propeller-wing models, as

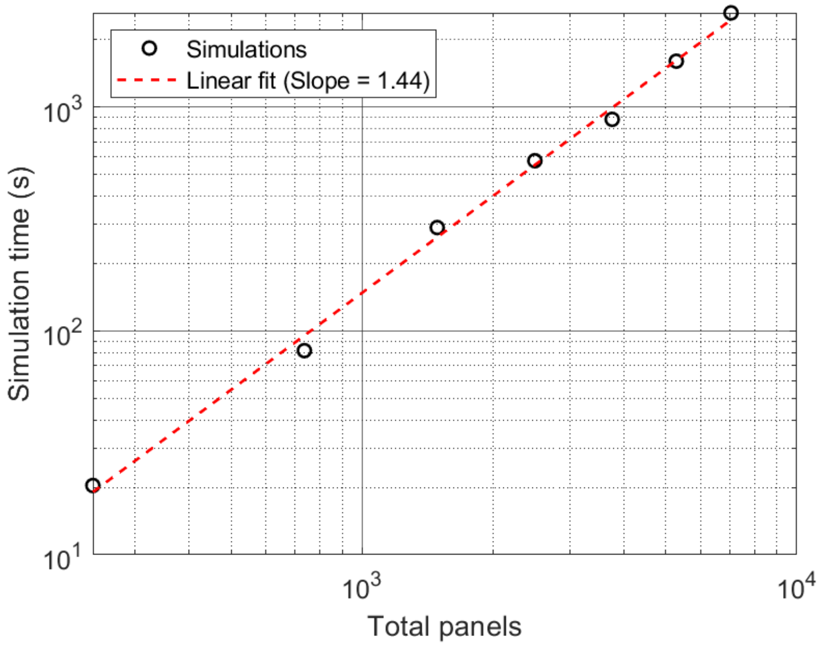

FIGURE 5.13 – Relation between computation time and panel count.

well as the validations discussed in Section 6 and are listed in Table 5.11, together with the default setting as a reference.

TABLE 5.11 – Simulation settings used for the remaining simulations in this research, compared to the default settings.

Setting	Specified	Default
Preconditioner type	Matrix (LU)	Matrix (LU)
Wake type	Free	Free
Wake iterations	25	10
Wake nodes	256	64
Far-field distance	10 spans widths	1 semispan

5.2 Isolated Propeller

For the next step in the grid sensitivity study, the analysis of an isolated propeller was performed. The primary difference compared to the isolated wing, is that the isolated wing is an unsteady simulation and the temporal resolution of the simulations must be considered in addition to the spatial discretization. As the spatial and wake settings have already been discussed in Section 5, the focus for the isolated propeller will be the temporal resolution sensitivity study, though the relation between and the relation between the temporal and spatial resolution of the simulations will be investigated as well.

5.2.1 Simulation Settings

Unless otherwise indicated, the modified propeller geometry as described in Section 4.1.1 was used during the refinement study. Furthermore, the freestream velocity, Reynolds number and

Mach number were set to $V_\infty = 20m/s$, $Re = 500000$ and $M = 0$, respectively. The propeller was set to have a rotation speed of 1200 rpm, corresponding to an advance ratio of $J = 0.844$. Five full propeller rotations were simulated in all cases.

For nearly all cases, five different timestep sizes were used. By default, VSPAero used a timestep corresponding to $\Delta\theta_t = 18°$ of propeller rotation per timestep, as is the recommendation by the developers (LITHERLAND, 2021). This starting timestep was doubled and halved twice, to obtain a range from $\Delta\theta_t = 72°$ per timestep as the largest timestep to $\Delta\theta_t = 4.5°$ as the finest. Since the same propeller rotation speed was used during all grid sensitivity simulations, the same timestep size for all cases could be derived, as listed in Table 5.12.

TABLE 5.12 – Correspondence between timestep resolution defined in $\Delta\theta_t$ and dt, for a propeller spinning at 1200 rpm.

Total timesteps	25	50	100	200	400
Timesteps per rotation	5	10	20	40	80
$\Delta\theta_t$	72°	36°	18°	9°	4.5°
dt	0.01 s	0.005 s	0.0025 s	0.00125 s	0.000625 s

Four grids were analyzed, where the chordwise resolution in particular was varied, as this has the greatest influence on the result of the pressure integral over the lifting surface. The grid settings used are listed in Table 5.13. For the panel clustering, the same settings were used as discussed in Section 5.1.4. For the naming convention, the grids will be referred to by the amount of chordwise and spanwise panels, using the *xxcyys* format, where *xxc* represents the chordwise panel count and *yys* represents the spanwise panel count, both excluding tip panels.

TABLE 5.13 – Spatial grids used for the isolated propeller grid sensitivity study.

Grid Name	Chordwise Panels Per Blade Without Caps	Spanwise Panels Per Blade Without Caps	Total Panels Per Blade, Without Caps	Total Panels Per Blade, With Caps	Total Panels Complete Geometry
4x 24c48s	24	48	1152	1224	4896
4x 48c48s	48	48	2304	2448	9792
4x 80c48s	80	48	3840	4160	16640
4x 112c58s	112	58	6496	6944	27776

Due to the large amount of combinations possible for the timestep and grid settings, it naturally follows that a large amount of results is available. As it is not possible, nor desirable, to discuss all results of the grid sensitivity study for the propeller in detail, this section will only show and discuss the most relevant results.

5.2.2 Global Propeller Performance Time History

To show the global propeller performance in a sensible manner, it is possible to group the results for the same temporal resolution or same spatial resolution. Grouping the results by same timestep will show the differences due to the different grid resolutions more clearly, whereas showing the results grouped by the same grid settings, will show the differences due to the differing time resolutions. As Section 5.1 discussed the grid sensitivity results in detail already, this section will emphasize the influence of the timestep resolution on the results, hence the figures will primarily be grouped for the same spatial grid.

Figure 5.14 shows the time history of the thrust coefficient for all combinations of grid resolution and timestep size, grouping the results for the same grid together in one subfigure. When comparing the results, it can be seen that globally, the same behavior is obtained, regardless of temporal or spatial resolution: Initially, the propeller experiences a thrust peak upon start-up, which dissipates over the first rotation. The duration and amplitude of this thrust peak is clearly dependent on the timestep size, as smaller timesteps result in a narrower and taller peak. Afterwards, the propeller gradually reaches its steady operating state, as can be seen by the flatlining thrust outputs. This initial thrust peak is likely a numerical artifact caused by the Euler step performed at the beginning of the time integration procedure. Since the propeller is stationary on the first timestep, the unsteady term in equation 3.52 reduces to $\frac{\gamma_{t_1}}{dt}$ which grows for decreasing values of dt.

A few differences can be spotted in the results: First, for increasingly finer grids, the steady state thrust output becomes more sensitive to the timestep resolution, especially for the coarsest timestep of $dt = 0.01s$. However, it is believed that this timestep is too coarse to produce accurate results, as the wake geometry is represented too crudely at this timestep, resulting in nearly square wakes.

Secondly, when only considering the results for the finer timesteps, it can be seen that the steady state thrust level does vary somewhat depending on the exact grid configuration and timestep size, which can be more clearly seen in Figure 5.14. There seems to be no clear correlation between the steady-state thrust level reached and the spatial grid settings, but in all cases tested a steady state C_T between 0.08 and 0.086 was obtained for all timesteps except $dt = 0.01s$. Furthermore, the difference in the steady-state thrust level seems to be somewhat consistent across different grids for the same timestep resolution. Additionally, when considering the same timestep size across different grid, it seems that the variation in the steady state thrust level for the finer timesteps is lower than for the coarser timesteps.

Lastly, it can be very clearly observed that for the finest two timesteps in particular, there is a clearly noticeable wiggle in the steady-state thrust output. It is suspected that this is a consequence of modeling the strips of shed wake elements as vortex lines with constant strength, resulting in jumps in the velocity potential between wake strips. Especially for smaller timesteps and therefore shorter wake elements, it may very well be that these vortex strength discontinuities result in numerical difficulties in enforcing the Kutta condition at the trailing edge. Furthermore, it has been shown that for shed vortex elements of constant strength, the ratio between the length of a vortex segment shed in a single timestep and the size of the panels near the trailing edge significantly affects the strengths of the vortex elements on the body. This undesirable behavior could potentially be resolved by using wakes with linear rather than constant vortex strengths, as this makes the results independent from the timestep size (HSIN,

1990) (KINNAS; HSIN, 1992).

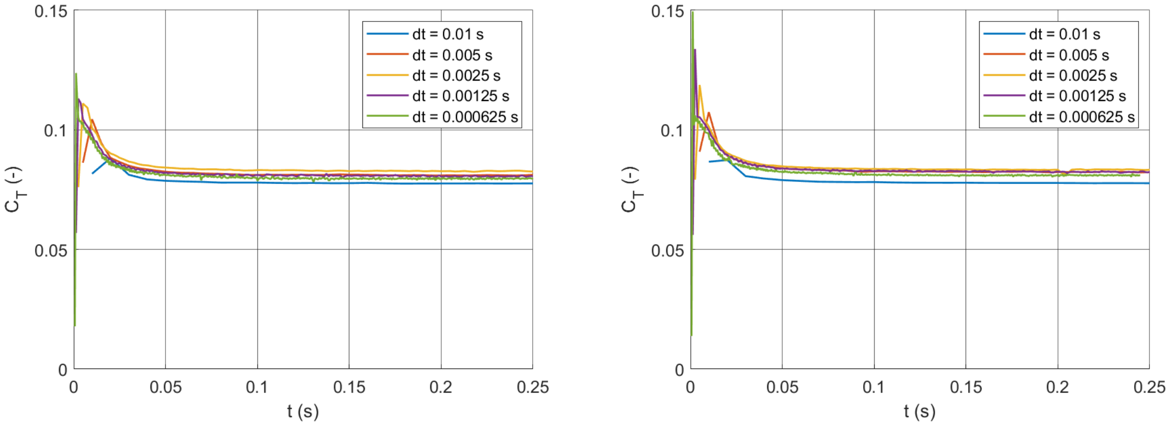

(a) 4x 24c48s grid.

(b) 4x 48c48s grid.

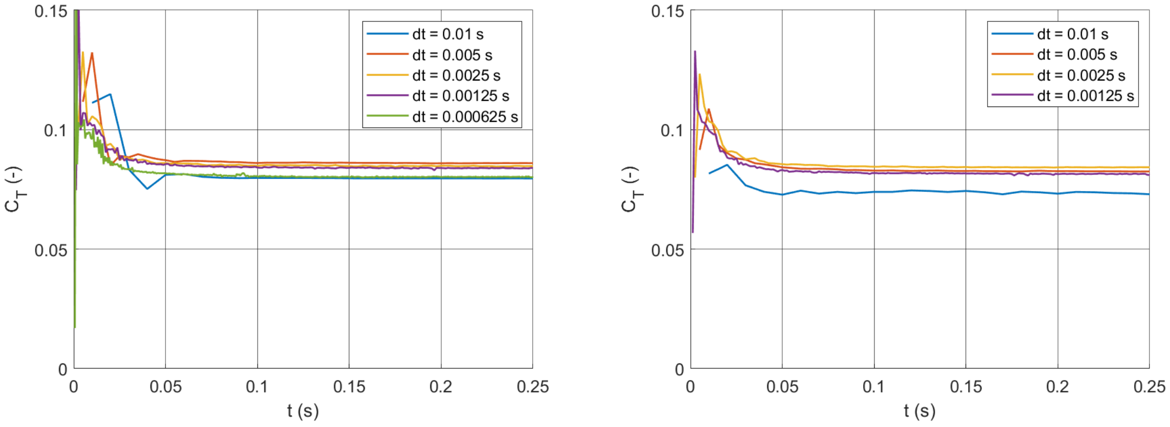

(c) 4x 80c48s grid.

(d) 4x 112c58s grid.

FIGURE 5.14 – Time history of the thrust coefficient for all grids and timesteps tested, grouped by grid.

Based on the results from the last rotation, the global C_T, C_P and η_P were computed by taking the average of these values over the last rotation. These are shown in figures 5.16a and 5.16b. The difference of these values with respect to those corresponding to the finest timestep are shown in Figure 5.17. It can be seen in the results for the thrust coefficient, that the spread between spatial grids tends to reduce for smaller timesteps, which was also observed in Figure 5.14. When considering the evolution of the power coefficient, it can be seen that there is significantly more spread between the different spatial grids tested compared to the thrust coefficient, although for both coefficients the spread seems to reduce for increasingly finer timesteps. A clear outlier in this regard is result for the 4x 112c58s grid, as the power coefficient obtained is significantly lower than for all other grids, whereas the thrust coefficient seems more in line with the other grids. The result of this effect can be seen in Figure 5.16b, as the efficiency of the finest spatial grid is a clear outlier.

Lastly, to get an indication of the convergence behavior for the different grids, the difference between the results relative to the finest timestep was computed, which is shown in Figure 5.17. While the amount of data points along the x-axis of the figure is somewhat lacking to draw any definitive conclusion, it can be seen that a similar trend in the evolution of the results can

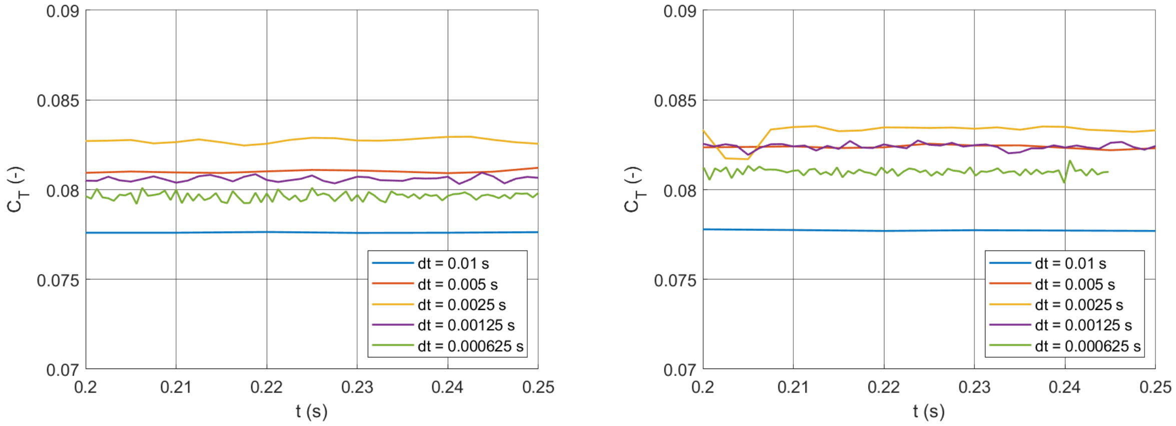

(a) 4x 24c48s grid.

(b) 4x 48c48s grid.

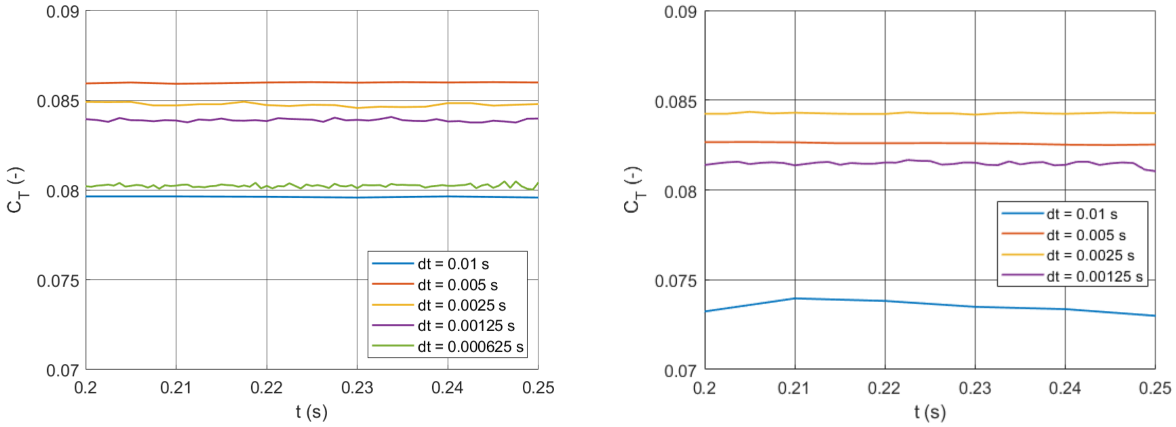

(c) 4x 80c48s grid.

(d) 4x 112c58s grid.

FIGURE 5.15 – Time history of the thrust coefficient for all grids and timesteps tested, grouped by grid, zoomed into the steady-state reached at the final rotation.

be seen as for the final grid refinement set for an isolated wing, as seen in Figure 5.11c, which seems to indicate that the results are converging, assuming that a significantly finer timestep size is used. Additionally, it can be observed in general, the results obtained on the coarser grids are less dependent on the timestep size, possibly due to the control points being further away from vortex rings in the body and the shed wake and therefore less sensitive to changes in the strengths of these vortex rings.

5.2.3 Radial Load Distribution

The radial load distributions are shown in figures 5.18 and 5.19, showing the C_T and $C_T/\tilde{A}$ distributions, respectively.

When looking at the results shown in Figure 5.18, it can be seen that the obtained load distributions are mostly similar for all cases tested. An oddity that is immediately apparent can be seen when comparing Figure 5.18d to the other subfigures, as it seems to suggest that for the 4x 112c58s grid, the magnitude of the radial loading is significantly lower than for the other grids

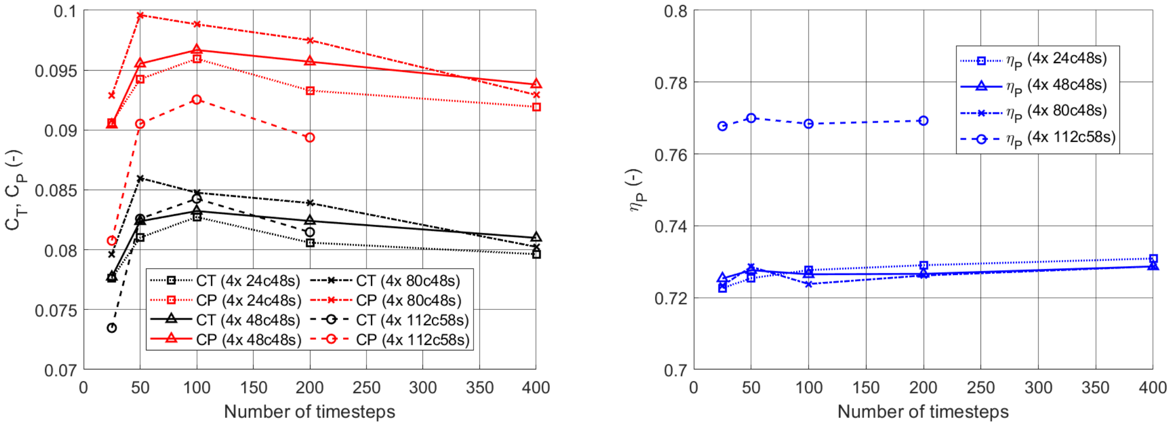

(a) Power and thrust coefficients.

(b) Propeller efficiency.

FIGURE 5.16 – Average global propeller parameters for the last rotation of every respective simulation.

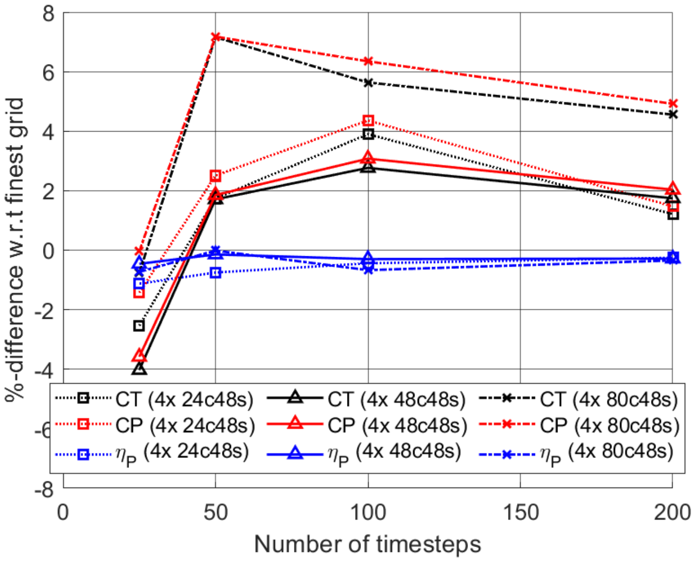

FIGURE 5.17 – Percentage difference between the results obtained relative to those for the smallest timestep ($dt = 0.000625s$). No results available for the 4x 112c58s grid, as the smallest timestep was not simulated on this grid.

tested, even though the global performance results discussed in the previous section did not show a significantly lower thrust level for this specific grid compared to the others. This apparent discrepancy is actually correct, as Figure 5.18 shows the thrust per radial station. Since the 4x 112c58s grid is the only grid with more radial stations than the others tested, and yet the same approximate is found for all grids; Ergo, the thrust on each spanwise station must be lower for the finest grid, as there are more panels to divide the total thrust level over. In the extreme cases where there is either a single spanwise panel or infinite spanwise panels, the thrust per spanwise station will be a quarter of the global thrust for the former case, and zero for the latter.

Aside from the apparent thrust level discrepancy, the load distributions seem to not differ significantly and make physical sense: most of the thrust is produced around $0.75r/R$, and the thrust tends to go to zero near the root and tip. However, in Figure 5.18c, it can be seen that the thrust goes up noticeably near the tip, which is not physically realistic. As this seems to occur for all timestep sizes, this seems to suggest that there is a problem with the discretization of the tip for this grid. A smaller wiggle can be seen near the tip in Figure 5.18a as well, likely due to the tip discretization as well.

In any case, what can be observed quite clearly is that the thrust level does seem to depend somewhat on the timestep size, as hypothesized in Section 5.2.2 (KINNAS; HSIN, 1992) with the largest timestep of $dt = 0.01s$ generally resulting in the lowest thrust distribution for any given grid. Additionally, the results for the other timestep sizes are generally closer together, which matches observations for the global C_T.

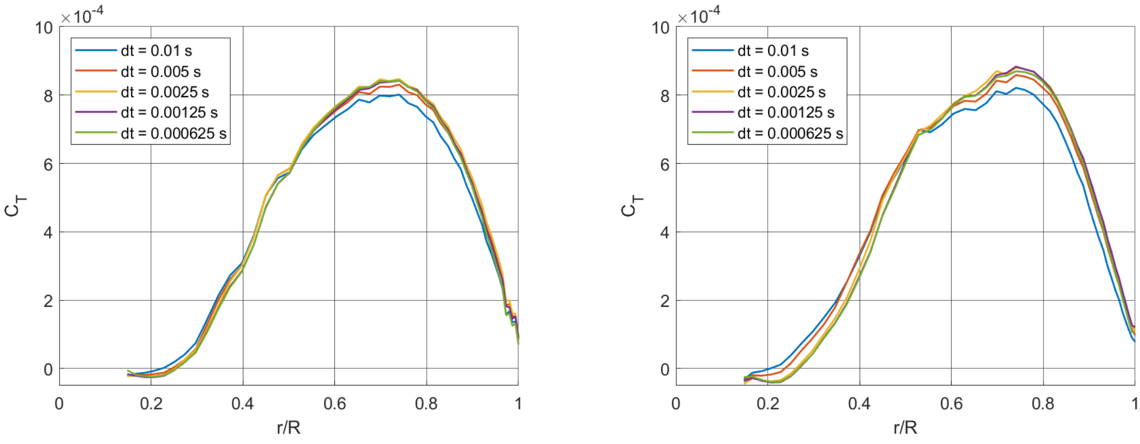

(a) 4x 24c48s grid.

(b) 4x 48c48s grid.

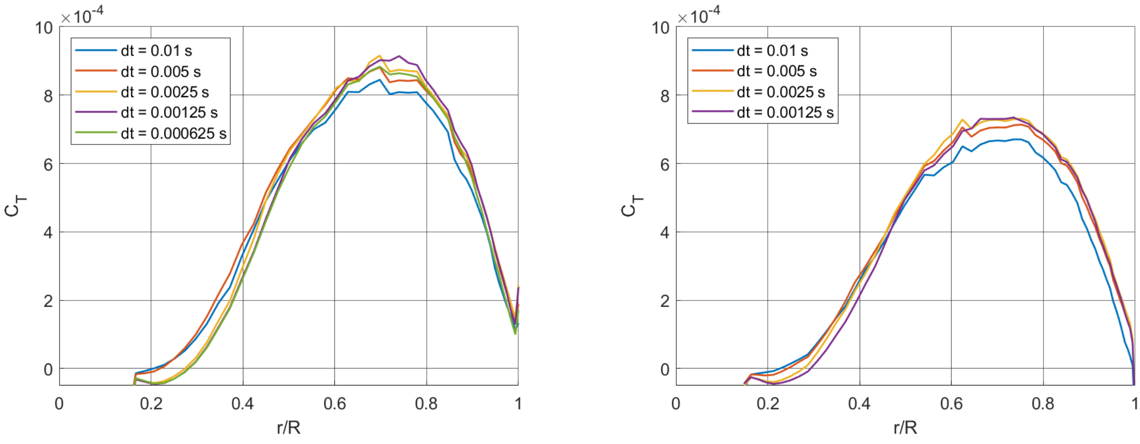

(c) 4x 80c48s grid.

(d) 4x 112c58s grid.

FIGURE 5.18 – Radial C_T distribution per spanwise blade station for all timestep and spatial grid combinations tested. Results shown are the averages over all four blades for the last rotation.

For the area-normalized thrust distributions in Figure 5.19, it can be seen that the thrust level per radial station is consistent across different grids, thus showing that this scaling is grid-independent. For all combinations of grid settings and timestep size, it can be seen that the nondimensionalized thrust per unit area is approximately linear over the radius, which matches the expected distribution (VERHOEFF, 2005). However, it can be seen that particularly near the tip, the results vary significiantly, especially between different grids. This is another indicator that VSPAero struggles with the relatively small panels at the tips of lifting bodies.

Out of the four grids considered, the 4x 112c58s grid shown in Figure 5.19d shows results that are the most physically plausible, as the load distribution is the smoothest near the tip and the load goes to zero at the furthest point of the tip, which is not observed for any of the other grids.

When comparing the remaining three grids, the results for the 4x 24c48s grid seen in Figure 5.19a makes the least physical sense, as it can be seen that, independent of the timestep, fluctuations start to occur at approximately $r/R = 0.9$, which increase in amplitude towards the tip. For the remaining two grids, the results are slightly better, though with similar problems near the tip.

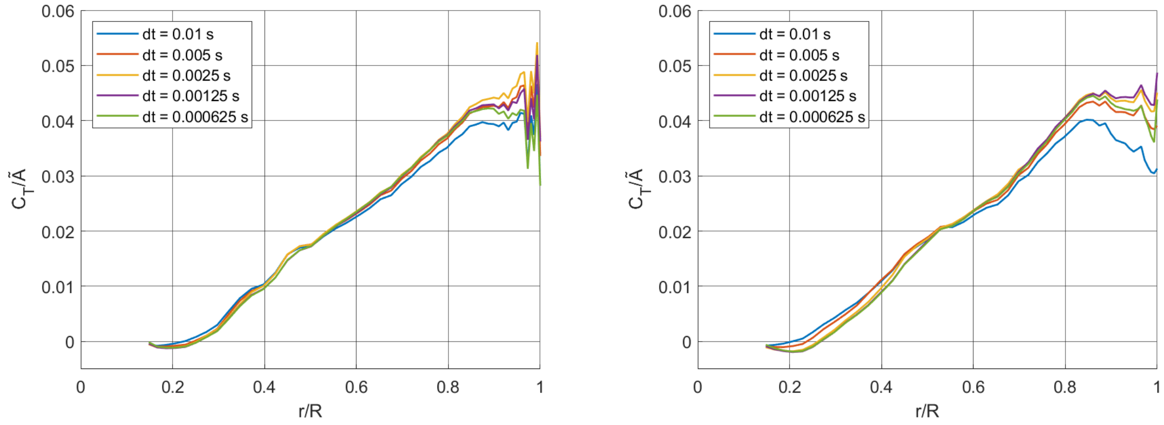

(a) 4x 24c48s grid.

(b) 4x 48c48s grid.

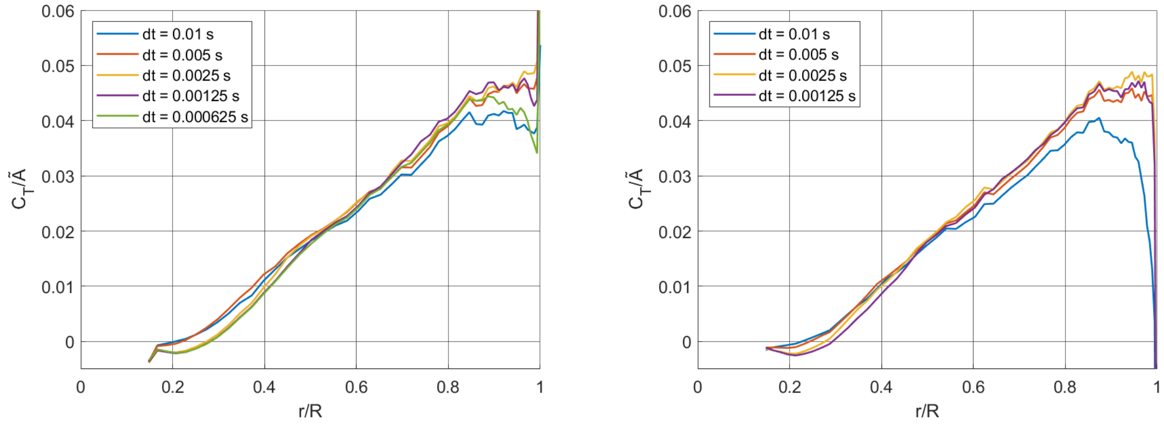

(c) 4x 80c48s grid.

(d) 4x 112c58s grid.

FIGURE 5.19 – Radial $C_T/\tilde{A}$ distribution per spanwise blade station for all timestep and spatial grid combinations tested. Results shown are the averages over all four blades for the last rotation.

As figures 5.18 and 5.19 show blade-averaged results, it should be verified whether the loads for the individual blades exhibit any significant differences, which should not be the case due to the uniform inflow conditions. For sake of brevity, the results for only a single timestep size will be discussed. To distinguish the individual blades, these will be numbered one to four, with blade one being the blade at the three 'o clock position when considering the front view of the propeller, counting up in a counterclockwise direction.

Figure 5.20 shows the percentage difference in blade loads, relative to blade one. It can be seen that for all grids, there are two regions where the difference between blades is relatively large: approximately around $r/R = 0.3$ and at $r/R > 0.95$, though even at these positions, the difference between blades is at most 1.5%. The difference between at the tips of the blades is very likely another symptom of VSPAero struggling with the tips of lifting surfaces, whereas the relatively large difference around $r/R = 0.3$ is due to the reference load for calculating the percentage difference being around $C_T = 0$ at this region, as can be seen in figures 5.18 and 5.19.

For the important middle region of the blades between $0.4 < r/R < 0.9$, it can be seen that the differences between the blade loads are in the order of 0.1%, which is in line with earlier accuracy observations of VSPAero. For the finest 4x 112c58s grid, the difference between the blades appears to be somewhat larger than for the other grids, though the differences are still within the same order of magnitude.

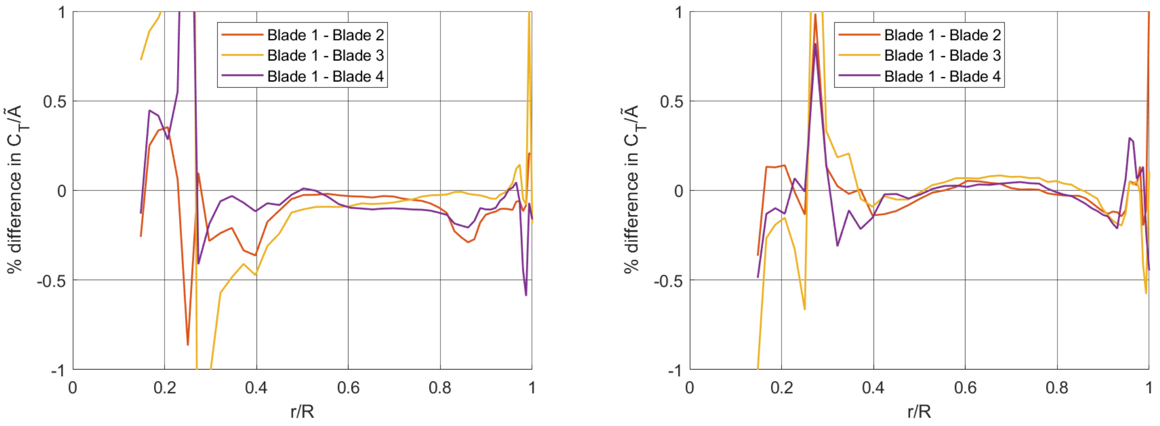

(a) 4x 24c48s grid.

(b) 4x 48c48s grid.

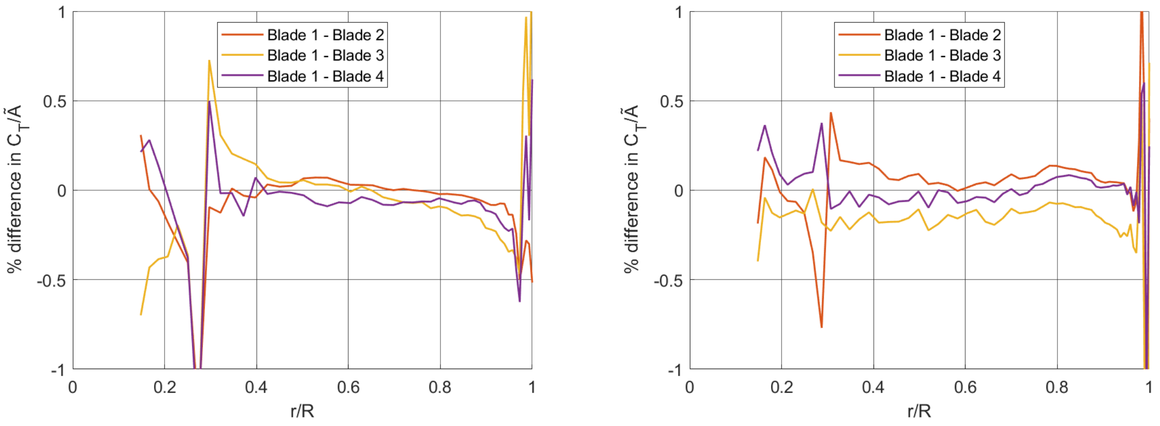

(c) 4x 80c48s grid.

(d) 4x 112c58s grid.

FIGURE 5.20 – Difference in the loads for the individual blades for all four grids tested. All percentage differences are relative to the load on blade 1.

5.2.4 Computation Time

Figure 5.21 shows the relation between the required computation time and number of timesteps, grouped for every grid. Aside from the actual results, a linear fit over all results for the same

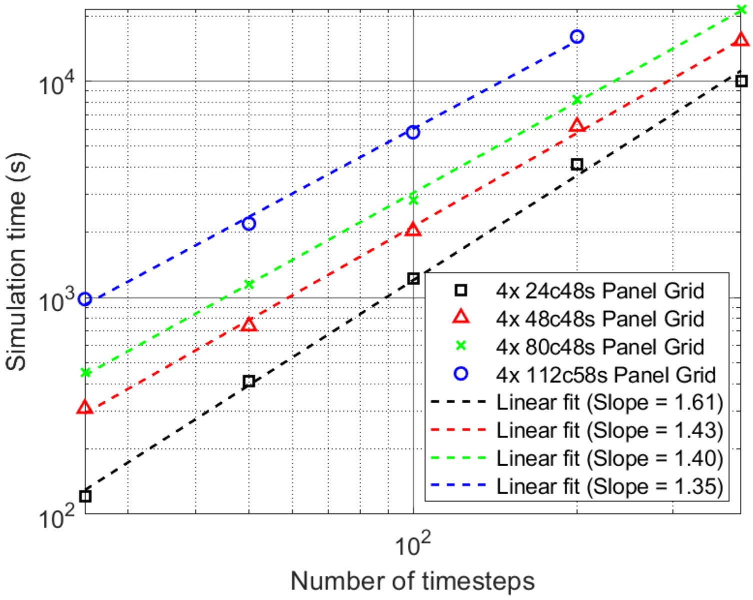

FIGURE 5.21 – Relation between the computation time, grid resolution and number of timesteps.

grid has been added to the figure. It can be seen that the obtained slopes for these fits are all very similar to those observed in Section 5.1. Interestingly, it seems that the computation time grows the quickest with more timesteps for the coarsest 4x 24c48s grid compared to the other, though it is possible that this is mainly due to the somewhat outlying computation time for this setting at 200 timesteps.

5.2.5 Conclusion

From the grid sensitivity study for an isolated propeller, it has been seen that generally, the performance of the propeller is not altered significantly whenever different grids or timestep settings are used, though some timestep dependence remained in the results. Particularly for very coarse timesteps, a significant difference in propeller performance was observed, which is likely the result of the inaccurate representation of the wake geometry and the shed vortex strips having constant strengths, resulting in different results for different ratios of the trailing edge panel length and shed vortex strip length. The global results for the finer timesteps were generally grouped closer together and it seems that acceptable convergence behavior can be reached for finer timesteps, though this could not be rigorously established. Furthermore, it was again seen that the tips of lifting surfaces are particularly sensitive to the spatial discretization settings, as the coarser grids tended to have a larger numerical disturbance at the blade tips. Aside from at the tips, the found radial load distributions were found to be realistic, and the difference between the different blades was found to be minimal. Lastly, the computation time dependence on the simulation settings was not unexpected and seemed in line with earlier results for the isolated wing.

Now that the sensitivity to the simulation settings has been tested for a wing and propeller separately, the last step of the sensitivity study will be to investigate the geometries together, as this is the most representative case for the main research objective.

5.3 Propeller-Wing Model Results

In Sections 5.1 and 5.2, the results of the grid sensitivity studies for isolated wing and propeller geometries have been discussed, which leaves this section for discussing the grid sensitivity study for the combined propeller-wing geometry. The combined geometry is shown in Figure 5.22, and consists of the propeller and wing discussed in Sections 4.1 and 5.1. The propeller is placed 0.097 m, or one propeller chordlength upstream of the wing, centered at the wing midspan. The same conditions as discussed in Section 5.2.1 were used, and the geometry simulated at an angle of attack of $\alpha = 0°$.

5.3.1 Geometry and Simulation Settings

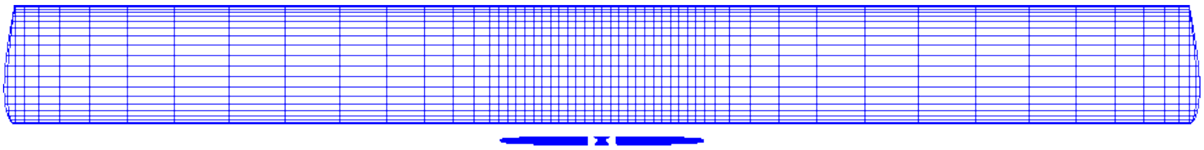

(a) Top view.

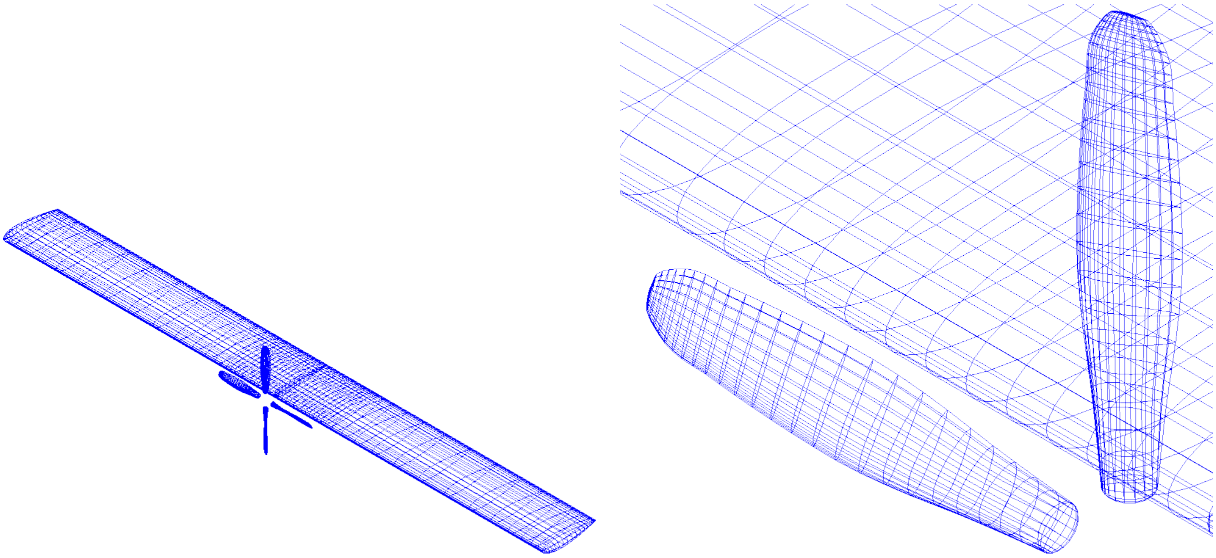

(b) Left isometric view.

(c) Closeup blade view.

FIGURE 5.22 – Overview of the propeller-wing geometry used for the grid sensitivity study. The grid setting shown is 4x 48c48s / 1x 80c42s, coarsened by a factor of two for clarity.

For the grid sensitivity study, two grid resolutions for the propeller and wing were used, resulting in four different grid settings in total, which are listed in Table 5.14. The selected grid settings for the individual components were taken from the sensitivity studies for the separate components, with a minor modification for the grid on the wing. Directly in the wake of the propeller, the wing panel density was increased significantly and the spanwise panel width in this region was set to be constant. Outside of the propeller wake region, the wing panels were clustered near the tip and near the wake region, as to not have large jumps in panel size or aspect ratio, as per developer recommendation (LITHERLAND, 2021). These grid changes can be seen most clearly in Figure 5.22a. For the timestep size, the same options were considered as listed in Table 5.12 in Section 5.2.1, except for the finest timestep.

TABLE 5.14 – Spatial grids tested for the grid sensitivity study with the propeller-wing geometry.

Grid Name	Total Panels Per Blade, Without Caps	Total Panels Per Blade, With Caps	Total Panels Wing Without Caps	Total Panels Wing With Caps	Total Panels Complete Geometry
4x 80c48s / 1x 112c58s	3840	4160	6160	6720	23360
4x 80c48s / 1x 80c42s	3840	4160	4400	4800	21440
4x 48c48s / 1x 112c58s	2304	2448	6160	6720	16512
4x 48c48s / 1x 80c42s	2304	2448	4400	4800	14592

5.3.2 Global Propeller Performance Time History

The time history of the thrust coefficient for all grid and timestep combinations is shown in Figure 5.23, grouped by grid. Unlike for case for the isolated propeller (Figure 5.14), it can be seen the propeller load has a very clear oscillatory load component, due to the aerodynamic interaction every time a propeller blade passes the wing. Furthermore, when considering the mean thrust coefficient, it can be seen that it is considerably higher in Figure 5.23 than in Figure 5.14, due to the wing blockage effect slowing the mean inflow velocity in the propeller plane resulting in greater propeller thrust.

When comparing the effects for the different timestep sizes, it is immediately apparent that the smallest two timesteps, $dt = 0.01s$ and $dt = 0.005s$, which correspond to $\Delta\theta_t = 72°$ and $\Delta\theta_t = 36°$, respectively, are inadequate to even capture the load oscillation frequency correctly. For the two finer timestep sizes, it can be seen that there are four full oscillations per rotation, as expected for a four-bladed propeller. For $dt = 0.01s$, it can be seen that the oscillatory part of load has only a single period per full rotation, and for $dt = 0.005s$, the load oscillations have two periods per full rotation. Interestingly, whereas the time history for a timestep of $dt = 0.01s$ shows a somewhat smooth curve, the result for $dt = 0.005s$ is very jagged. This is likely due to the motion simulated at $dt = 0.01s$ approximating a rotation in the opposite direction at $dt = 0.0025s$, hence resulting in a rather smooth load, though it is not clear why the result for $dt = 0.005s$ is as jagged as it is.

When considering the results for different grids using the finer timestep sizes, it can be seen that for the coarser propeller grid, shown in Figure 5.23c and 5.23d, the load over time follows a sinusoidal shape, with the average C_T being just slightly below $C_T = 0.1$. For the finer propeller grids in Figure 5.23a and 5.23b, the load appears to more closely resemble a triangle-like wave, and strangely, the oscillation amplitude for every other peak appears to be smaller, which cannot be explained. The average C_T for the finer grids seems to be a bit lower than for the coarser grids as well, mainly due to every other peak having a reduced amplitude.

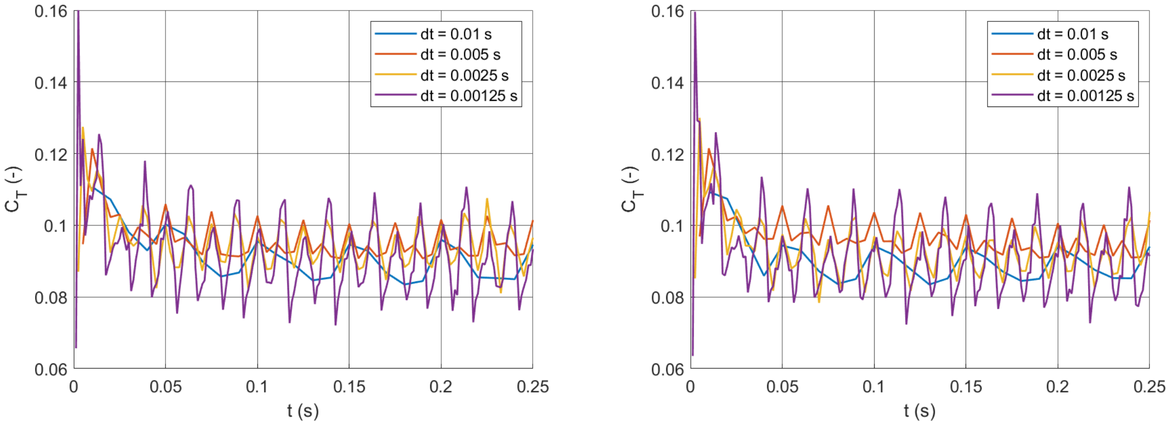

(a) 4x 80c48s/1x 112c58s grid. (b) 4x 80c48s/1x 80c42s grid.

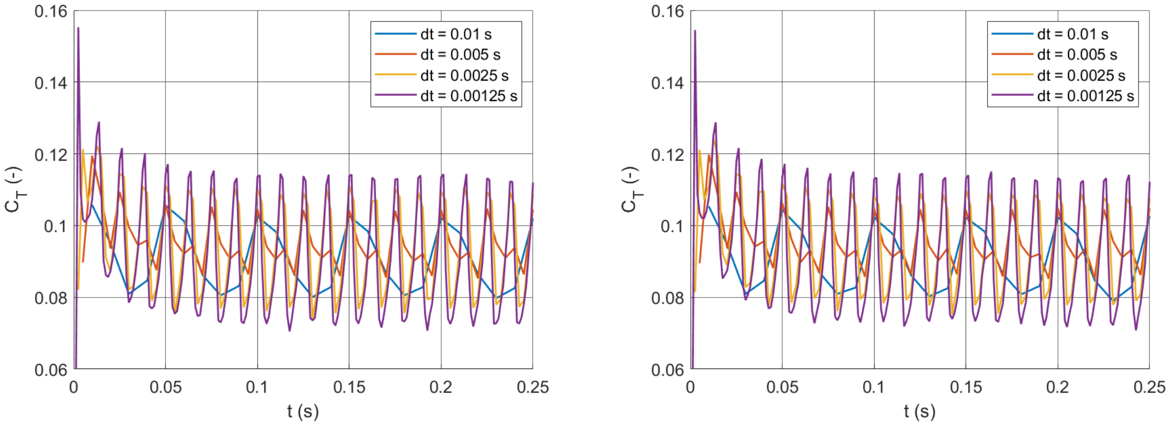

(c) 4x 48c48s/1x 112c58s grid. (d) 4x 48c48s/1x 80c42s grid.

FIGURE 5.23 – Time history of the thrust coefficient for all grids and timesteps tested, grouped by grid.

Since a clear oscillatory component is present in the load, the frequency content was analysed by applying a Fourier transform was to the time-series data using the built-in fast Fourier transform (FFT) algorithm in Matlab. The results are shown in Figure 5.24.

The Fourier transforms do indeed confirm the observations made for the results in the time domain: for $dt = 0.01s$ (Figure 5.24a), it can be seen that the main oscillatory component occurs at $20Hz$, which corresponds to the rotation speed set for the propeller. For all other timesteps, it can be seen that the largest peak occurs at a frequency of $80Hz$, which is four times the rotation speed and is the frequency of a blade passing in front of the wing. However, some particularly odd behavior can be observed for harmonics of the principal rotation speed, which will be discussed on a timestep-by-timestep basis. For $dt = 0.005s$, shown in Figure 5.24b, it can be seen that for the grids where the propeller is discretized at 4x 48c48s, there is a clear secondary peak present at $40Hz$, which agrees with the observations made in the time-domain representation of the results. However, this peak is absent for the cases where the propeller is discretized at the finer setting 4x 80c48s, and on top of that, the principal peak at $80Hz$ is lower compared to the coarser grid settings as well. On the contrary, for $dt = 0.0025s$ shown in Figure 5.24c, it can be seen that only on the fine grids, the lower frequency peak at $40Hz$ occurs, though for the coarser grids, the first overtone at $160Hz$ is clearly present. Again, the primary $80Hz$ peak is taller for the coarser spatial grids. Lastly, for the finest timestep shown in Figure 5.24d, the same observations can be made as for $dt = 0.0025s$, with an additional peak occurring at $120Hz$ for the finer grids only.

The behavior of the secondary peaks in the Fourier transforms is rather odd, as it appears that the propeller grid settings have an influence on the frequency content of the load, despite the fact that the operating conditions of the propeller were the same in all cases. The most likely hypothesis for the $40Hz$ peaks present in the FFT of the finest grids, is that this represents the frequency of the alternating peak magnitudes seen in figures 5.23a and 5.23b, as the peak magnitude alternates every other period. This hypothesis accounts for the $120Hz$ peak observed in Figure 5.24d as well, since this would be the third harmonic of the $40Hz$ base frequency. However, this hypothesis does not explain why the load magnitudes should alternate as seen in figures 5.23a and 5.23b in the first place, which remains unclear at the time of writing as well. Another potential cause for the odd behavior of the secondary peaks could be that these are an artifact of the FFT algorithm, though there is no evidence to substantiate this claim.

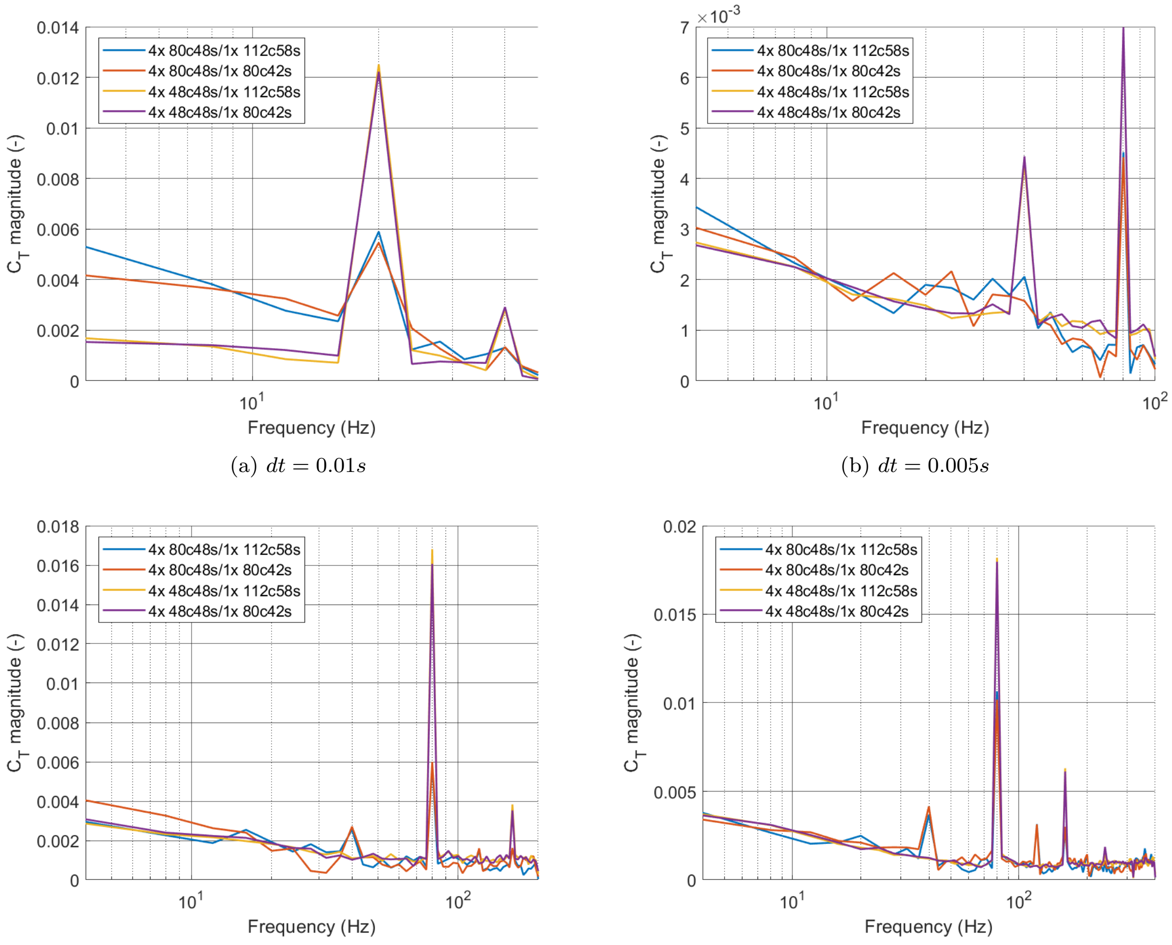

(a) $dt = 0.01s$

(b) $dt = 0.005s$

(c) $dt = 0.0025s$

(d) $dt = 0.00125s$

FIGURE 5.24 – Fourier transforms of the time history of the thrust coefficient, grouped by the same timestep as to match the resolution of the figures.

In addition to the complete time history, the average C_T, C_P and η_P were computed for all simulations, which are shown in Figure 5.25. It is remarkable how similar the results for different grid configurations are, especially when compared with the results for an isolated propeller shown in Figure 5.16. The spread in the coefficients due to changes in the timestep size appears to be two to three times larger than the spread due to different grid configurations. Furthermore, when comparing the efficiency shown in Figure 5.25b, it can be seen that the obtained efficiencies are all approximately $\eta_P \approx 0.765 \pm 0.0025$, aside from the outlying result obtained for the largest timestep with the 4x 80c48s/1x 80c42s. Again, this is a very tight grouping, as for the isolated propeller, the main grouping of efficiency results still spanned a band of approximately $\Delta\eta_P = 0.01$, excluding outliers (Figure 5.16b).

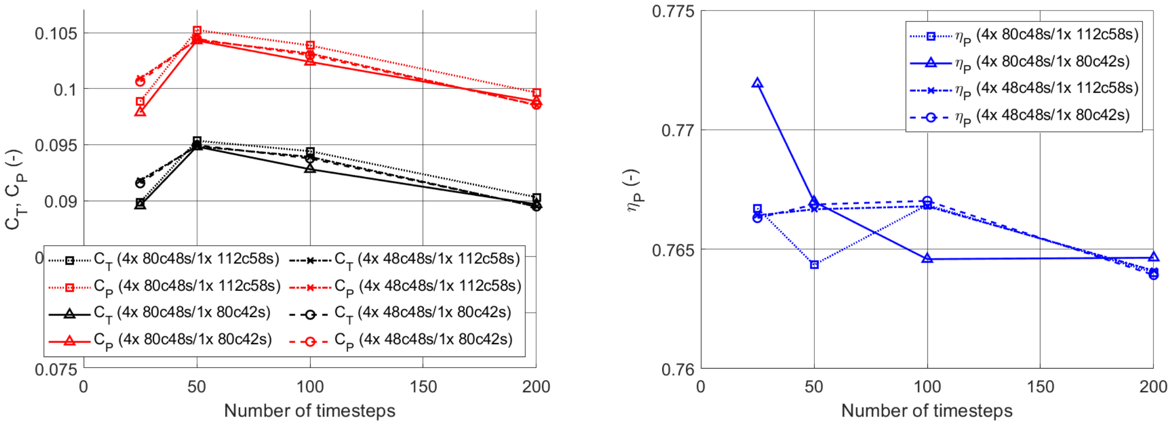

(a) Power and thrust coefficients.

(b) Propeller efficiency.

FIGURE 5.25 – Average global propeller parameters for the last rotation of every respective simulation.

To quantify the convergence behavior, the L2 norm was taken of the coefficient for increasingly smaller timesteps on the same grid, shown in Figure 5.26 and the percentage difference between the solutions was computed relative to the solution obtained on the finest timestep for each grid, shown in Figure 5.27.

When considering the evolution of the L2 norms for the thrust and power coefficients for all grids tested, it can be seen that that there is a clear downward trend in the difference between the results of the coefficients for increasingly finer timesteps, as should be expected of a consistent numerical method. The results for the 4x 80c48s/1x 80c42s grid in particular show surprisingly straight lines, and or all other grid settings, it can at the very least be said that the L2 norm between simulations does not increase, which is rather surprising compared to the poor convergence results observed in Section 5.1. Based on the observed trend for the limited amount of data points in Figure 5.26a, the convergence behavior seems encouraging.

The L2 norm of the efficiency between simulations was computed as well, which is shown in Figure 5.26b. Aside for the result for the 4x 80c48s/1x 80c42s grid, the efficiency does not seem to converge as clearly as the thrust- and power coefficients. However, as the efficiency is directly computed from these coefficients, it is sensitive to differences in their convergence behavior, hence it is not surprising that this could result in the observed behavior for the efficiency.

Furthermore, when considering the scale of the L2 norm differences for the finer timesteps, in combination with Figure 5.25b, it can be seen that the difference in the efficiency can be considered negligible for a preliminary study regardless.

From the percentage difference graphs shown in Figure 5.27, it can be seen that, although the percentual differences between results become smaller for increasingly finer timesteps, there is no clear damped harmonic-esque shape observed in the plots, though this is likely due to the lacking amount of data points.

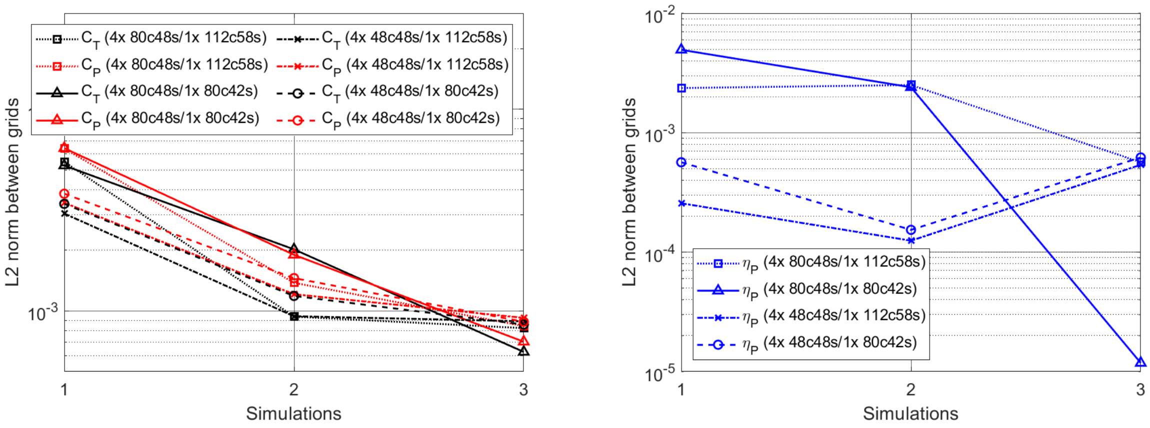

(a) Power and thrust coefficients.

(b) Propeller efficiency.

FIGURE 5.26 – Difference of the L2 norms for increasingly smaller timesteps for the same spatial grid.

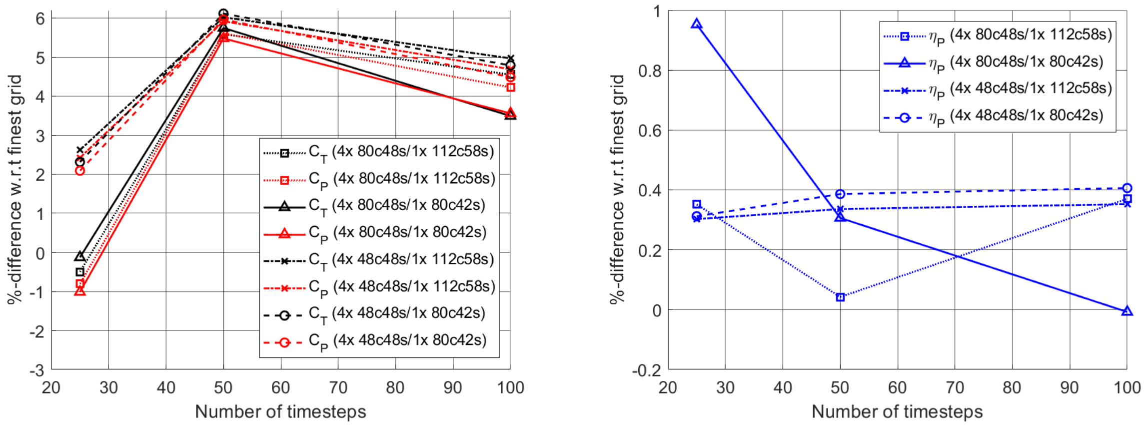

(a) Power and thrust coefficients.

(b) Propeller efficiency.

FIGURE 5.27 – Percentage difference between the results obtained relative to those for the smallest timestep ($dt = 0.00125s$).

5.3.3 Radial Load Distribution

The radial distribution of the thrust coefficient is shown in figures 5.28 and 5.29, grouped by grid and timestep size, respectively.

It can be seen in Figure 5.28, that the grid settings for the propeller geometry have a greater influence on the solution than the grid settings for the wing, as the results per grid are nearly unchanged for the grids with the same propeller discretization. Furthermore, it can be seen that the step size has a minor influence on the exact thrust distribution, with the clear outlier being the results for $dt = 0.01s$, which has a significantly lower load peak compared to the other settings.

Another observation is the small thrust spike at the tip observed for the finer two spatial grids, shown in Figure 5.28a and 5.28b, which is clearly not a physical phenomenon and is a continuation of the tip-related woes with VSPAero.

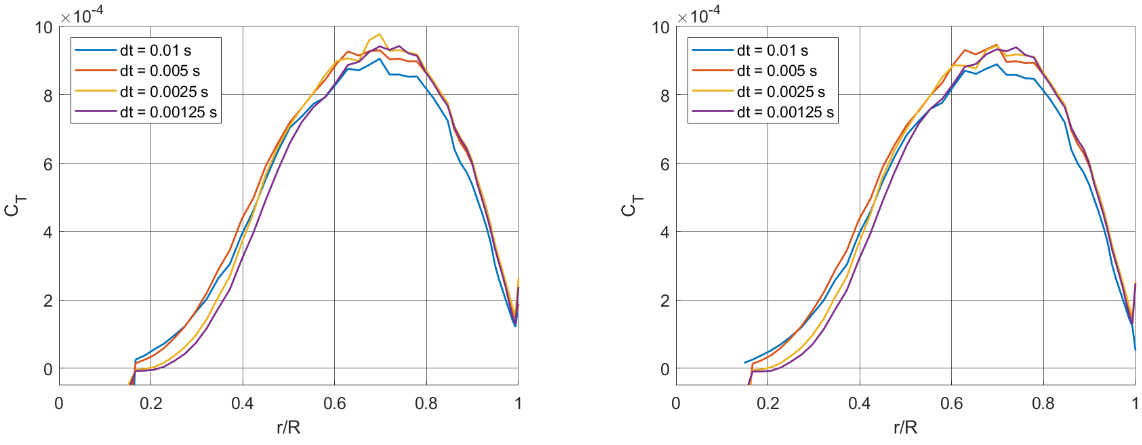

(a) 4x 80c48s/1x 112c58s grid.

(b) 4x 80c48s/1x 80c42s grid.

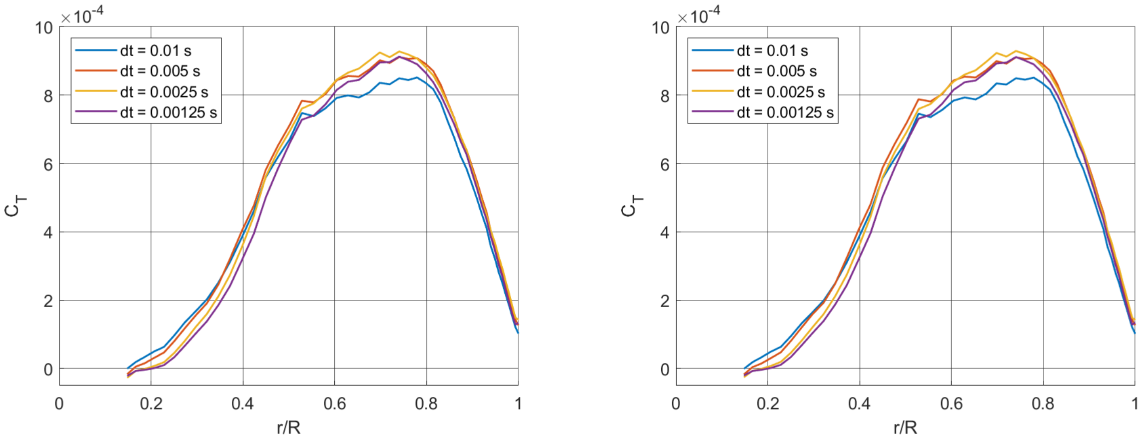

(c) 4x 48c48s/1x 112c58s grid.

(d) 4x 48c48s/1x 80c42s grid.

FIGURE 5.28 – Radial thrust distribution for all propeller-wing grid sensitivity study cases, grouped by grid.

The radial loads can be considered on a timestep-by-timestep basis as well, as shown in Figure 5.29. It can be seen for that for the same timestep size, the spatial grid settings do not influence the result significantly. There are some differences visible at the thrust peak for different grids, with the two finer grids generally predicting a larger thrust peak than the coarser two grids. Additionally, very minor differences can be observed for the load distribution at the root side of the blade.

For unclear reasons, the load for the finest two grids is quite jagged at the peak, as can be seen in Figure 5.29c, though it is not clear why this only occurs for this timestep size, as the thrust peak is smoother for both coarser and finer timesteps for these grid settings.

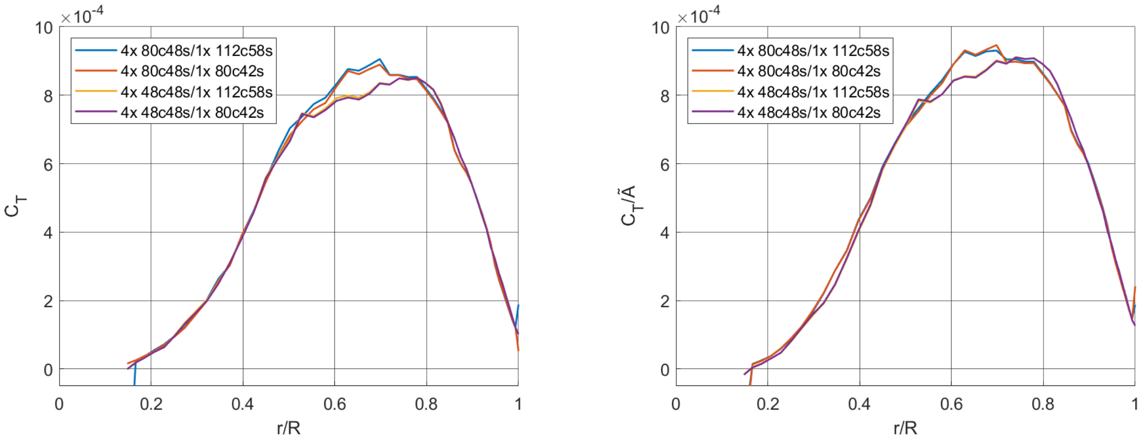

(a) $dt = 0.01s$ (b) $dt = 0.005s$

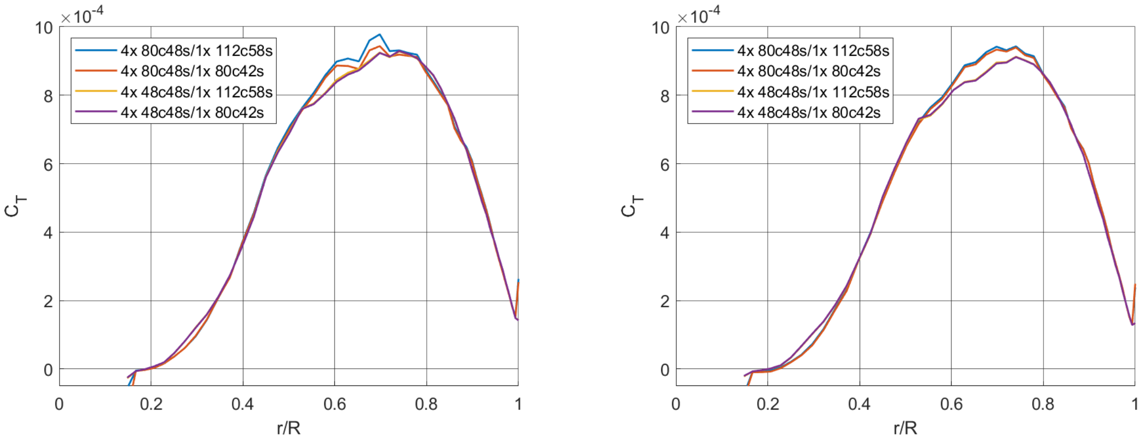

(c) $dt = 0.0025s$ (d) $dt = 0.00125s$

FIGURE 5.29 – Radial thrust distribution for all propeller-wing grid sensitivity study cases, grouped by timestep size.

5.3.4 Wing Loads

Although the main focus of this research is on the influence of aerodynamic interference on the propeller, it must be ensured that the results are consistent on the size of the wing was well. Thus, the lift distribution on the wing was analyzed as well, with the results being shown in Figure 5.30.

As the propeller was rotating counterclockwise from a front-view perspective, it is expected to the right of the midspan, a local increase in the lift coefficient is observed, whereas the opposite effect is expected on the left side of the midspan (SINNIGE *et al.*, 2019). However, even when only considering this effect, the lift distribution is not even consistent in this regard. For the largest and smallest timestep, it can at least be seen that the local modifications to the lift coefficient mostly agree with the expected shape of the lift distribution. For the timestep of $dt = 0.005s$, the coarsest grid seems to be a clear outlier, as it has a local lift peak on the opposite side than is expected. For a timestep of $dt = 0.0025s$, the lift distributions for two grids stand out: 4x 80c48s/1x 80c42s and 4x 48c48s/1x 112c58s. For the coarser grid, it can be seen that the distribution seems to be mirrored, similar to the observation made for the coarsest grid in Figure 5.30b. For the finer grid, it can be seen that there is only a disproportionally large lift deficit on the left side of the midspan, but no complementary peak on the other side.

In any case, not much useful information could be obtained from the wing data, which is rather disappointing, as an accurate representation of the wing loading is preferable for modeling the aerodynamic interference effect on the propeller, even if it is not the main topic of the study. As this data was not commonly included in other works, it is suspected that its omission was indeed due to the poor quality of the results.

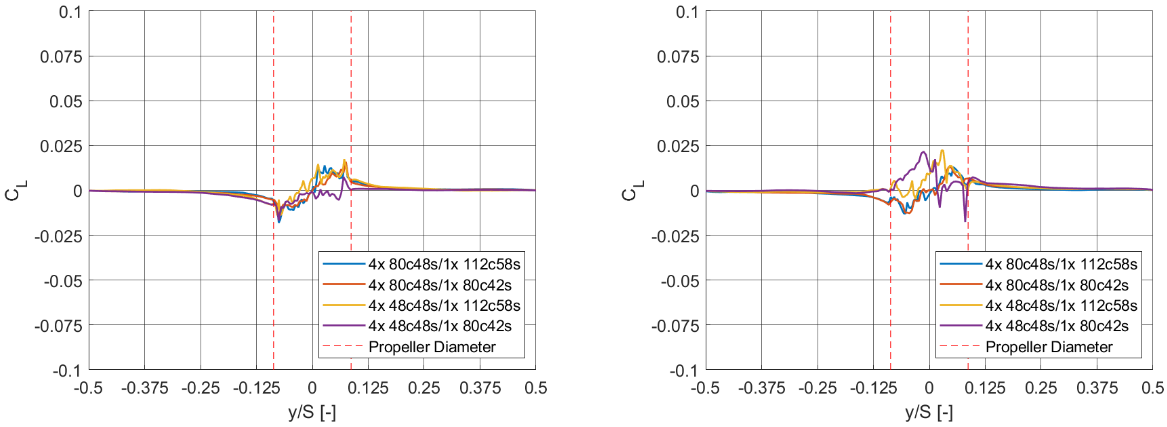

(a) $dt = 0.01s$ (b) $dt = 0.005s$

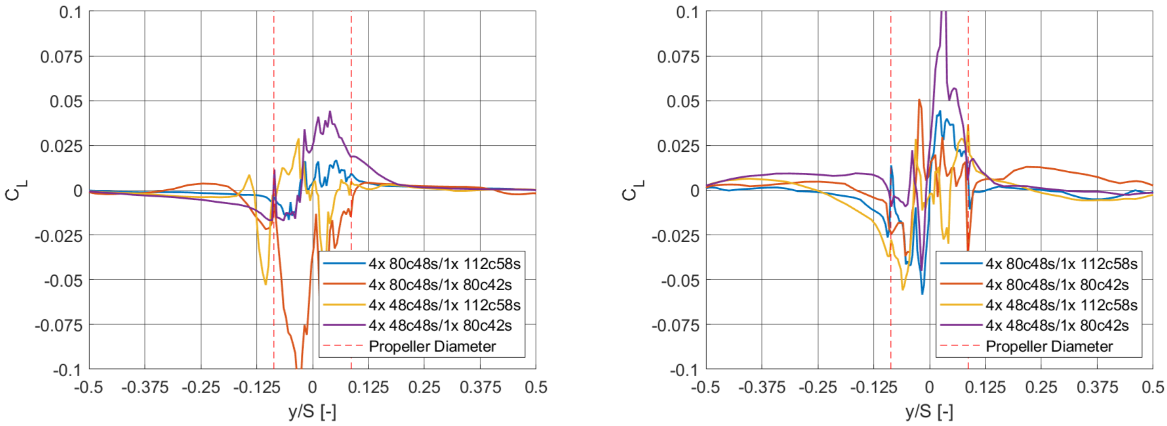

(c) $dt = 0.0025s$ (d) $dt = 0.00125s$

FIGURE 5.30 – Lift distribution of the wing, grouped by timestep size. The propeller diameter is marked with red dashed lines, to indicate the part of the wing located directly in the propeller wake.

5.3.5 Computation Time Dependence

As the last part of the grid sensitivity study, the computation time dependence on the configuration details was analyzed as well.

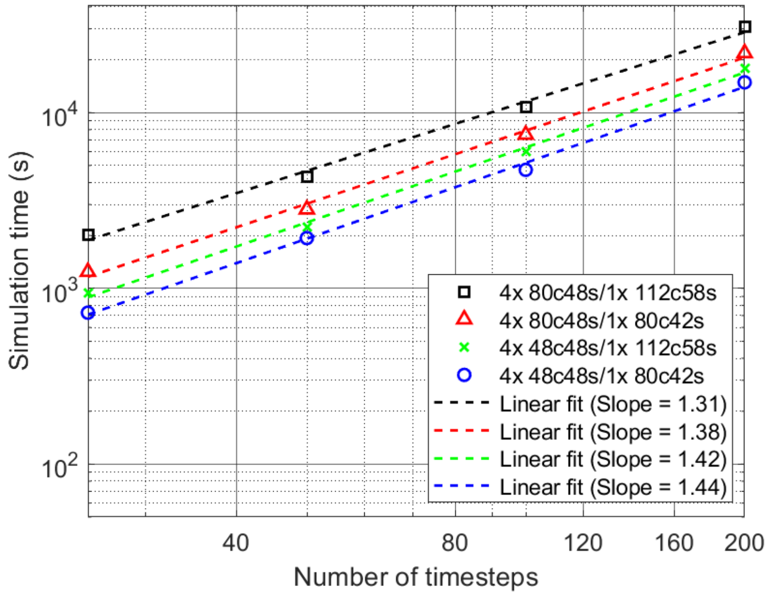

FIGURE 5.31 – Relation between the computation time, grid resolution and number of timesteps for the propeller-wing geometry.

Figure 5.31 shows the relation between the computation time for increasing amounts of timesteps, grouped by the same grid configuration, on a log-log scale. Linear fits have been computed for the plotted data, and similar slopes have been observed as for the isolated propeller and wing analyses. However, when comparing the computation time for the same propeller grids without wing in Figure 5.21, it can be seen that the addition of the wing actually resulted in an approximately threefold increase in computation time. As the amount of panels added due to the wing is a relatively small contribution to the computation time, it is likely that this increase is due to the increased amount of wake interaction calculations.

5.3.6 Conclusion

The grid sensitivity study for the combined propeller-wing geometry has yielded some interesting results. Based on the observations made for both the combined geometry as well as the separate wing and propellers, some observations can be made:

- For a propeller-wing model, the minimum timestep resolution lies between $\Delta\theta_t = 36°$ and $\Delta\theta_t = 18°$, as larger timesteps will misrepresent the propeller motion and wake geometry, producing inaccurate results in time and frequency domains. It should be noted that a truly time-independent solution seems to be impossible with VSPAero, likely due to the errors from the shed wake vortices.
- While difficult, it is possible to obtain somewhat consistent convergence behavior for increasingly finer grids or smaller timesteps, though one must be very elaborate regarding the settings used.

- Panels should be clustered near gradients, though care should be taken to ensure that the size of neighboring panels is not too dissimilar.
- The amount of wake relaxation iterations and the wake far-field distance setting can significantly affect the convergence behavior of the result, while having a relatively small impact on the computation time.
- For some unclear reason, VSPAero has a significant difficulties to obtain physically realistic load distributions at the tips of lifting bodies, as it was common to observe load spikes at propeller and wingtips, seemingly without rhyme or reason. This should always be kept in mind, especially considering how this could affect the solution.
- In most cases, the computation time scales with the number of panels and/or number of timesteps with $\mathcal{O}(n^{1.4})$-$\mathcal{O}(n^{1.6})$.

In addition to these observations, a choice was made for the grid and timestep settings for the main research simulations. The choice for the timestep setting was rather straight forward, as the lower bound was already established to be $\Delta\theta_t = 18°$. Regarding the upper bound, it was observed that there was some odd oscillatory behavior for $\Delta\theta_t = 4.5°$ compared to $\Delta\theta_t = 9°$, making the latter a safer choice. However, in addition to accuracy, computation time is an important consideration as well. Since lower-fidelity engineering methods, such as OpenVSP, are more commonly used during preliminary stages of the design process, it is not desirable to spend excessive time to obtain a more accurate solution, as the details are expected to be worked out later with more accurate methods. Considering the increase in computation time observed by halving the timestep resolution from $\Delta\theta_t = 18°$ to $\Delta\theta_t = 9°$, combined with the smaller change in the solution at that timestep decrease compared to larger timesteps, it was chosen to carry out the main research simulations using a timestep of $\Delta\theta_t = 18°$.

Aside from selecting a timestep size, a grid setting must be selected as well. For the propeller itself, the coarsest and finest two grids discussed in Section 5.2 are deemed not suitable. For the former, the concern is that the grid is too coarse to accurately represent the propeller geometry, whereas the results for the finest grids were significantly different from the other grids and on top of that, the computation time increase would be a major drawback as well. Between the 4x 48c48s and 4x 80c48s grids, the choice was made to use the 4x 48c48s grid, as the 4x 80c48s grid featured a physically incorrect tip load spike and especially in conjunction with a trailing wing, the computation time increase for the finer grid was hardly worth it, as aside from the tip peak, the results for these two grids were rather similar. Lastly, for the wing discretization, the coarsest setting discussed in this section was chosen, was the main focus of this study is the propeller, and other publications have significantly better results for the aerodynamic interference effect on the wing than could possibly be produced with OpenVSP. Additionally, having a wing grid that is too crude is not desirable either, as it will not save much computation time if the propeller grid is significantly finer than the wing grid, whereas the numerical error on the wing in particular is expected to be disproportionally large. Thus, the 1x 80c42s wing grid will be used for all further tests.

6 VSPAero Capabilities Assessment

Aside from the grid sensitivity study discussed in Section 5, a few tests were performed to assess the accuracy of the results obtained with the numerical methods implemented in VSPAero. These tests were built up gradually, ranging from a quasi-2D flow verified against XFoil, up to a test of an isolated propeller under an inflow angle. The objective of these evaluations was to determine whether the results of VSPAero can be considered reliable and accurate, or to point out inaccuracies in the solutions.

6.1 Quasi-2D Flow

For the first test, the simplest possible flow field was created with VSPAero to determine whether the core implementation of the panel method is correct. The compressibility and viscous corrections were disabled and a high aspect ratio elliptic wing was used to reduce the influence of the tip vortices, resulting in a quasi-2D flow field at the midspan of the wing. The exact elliptic wing geometry, is the same one as used in chapter four in (VAN GARREL, 2003), with the planform being shown in Figure 6.1 and the relevant parameters listed in Table 6.1.

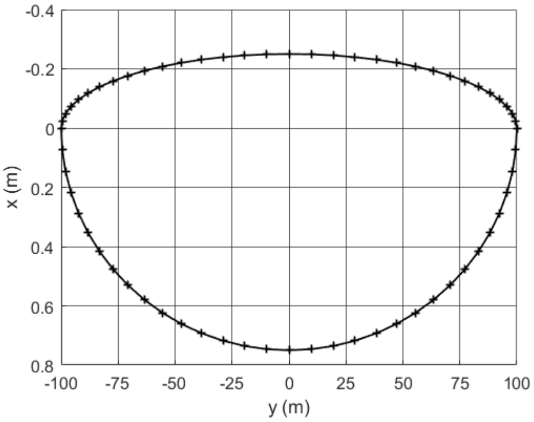

FIGURE 6.1 – Planform of the elliptic wing used. Plusses indicate start and endpoints of cross-sections. Please note that the axes are not to scale. (VAN GARREL, 2003)

TABLE 6.1 – Geometric properties of the elliptic wing.

c - wing chord $[m]$	1
s - wing span $[m]$	200
n_c - chordwise panels	128
n_s - spanwise panels	32
S - wing surface area $[m^2]$	156.8274
AR - wing aspect ratio [-]	255.0574

Furthermore, the elliptic wing features a NACA0018 airfoil as the cross-section over the entire span, which has been modified to feature a sharp trailing edge, as this is a prerequisite for the VSPAero panel mode to enforce the Kutta condition. The difference between the NACA0018 using the original geometry specification and the modification with the sharp trailing edge is shown in Figure 6.2. It can be seen that both geometries are nearly identical, with a minor difference in thickness over the chord after approximately $x/c = 0.25$. As the geometry with sharp trailing edge has been used for all simulations discussed in this report, it will for sake of convenience be simply referred to as 'NACA0018', unless otherwise specified.

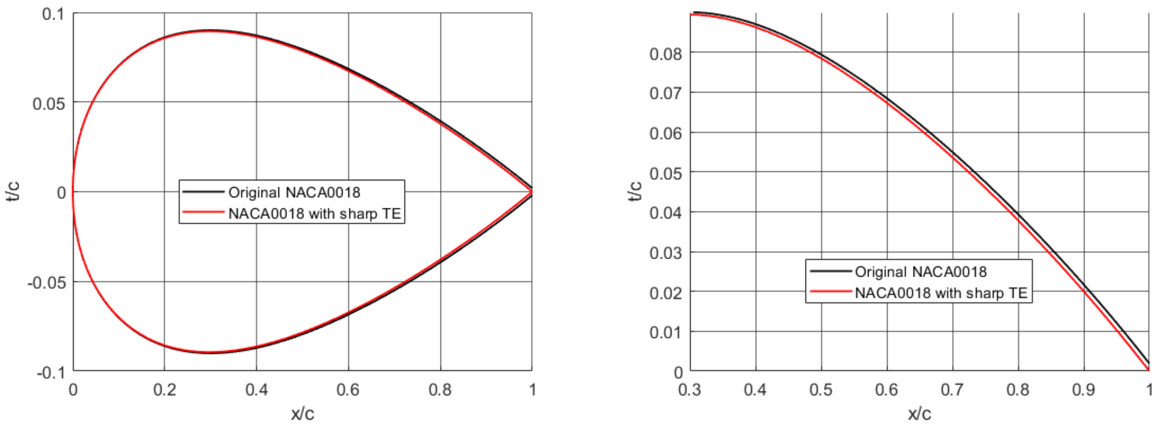

(a) Full view of both geometries.

(b) Zoomed in view of the top surfaces.

FIGURE 6.2 – Comparisons between the original NACA0018 and the NACA0018 with a sharp trailing edge. Please note that the axes are not to scale.

For comparison, the results obtained with VSPAero at the midspan of the elliptic wing were compared to an inviscid and incompressible XFoil simulation(DRELA, 2013). To correct for the fact that these methods inherently simulate flow fields differently, due to XFoil being a purely 2D method, whereas VSPAero is 3D, an angle of attack correction was applied to the XFoil results using equation 6.1 (VAN GARREL, 2016).

$$sin(\alpha_{3D} - \alpha_{0,3D}) = \frac{AR+2}{AR} sin(\alpha_{2D} - \alpha_{0,2D}) \tag{6.1}$$

Since the NACA0018 has a zero-lift angle of attack of $\alpha_0 = 0$, and the aspect ratio of the elliptic wing is known, equation 6.1 can be rewritten to obtain an equivalent 2D angle of attack for a given 3D angle of attack:

$$\alpha_{2D} = arcsin\big(0.9922\, sin(\alpha_{3D})\big) \tag{6.2}$$

In Table 6.2, the equivalent 2D angle of attack is listed for a few 3D angles of attack.

For the comparison between VSPAero and XFoil, an angle of attack sweep was performed to compare the lift slopes for both methods. Furthermore, the pressure distribution for $\alpha_{3D} = 0°$ and $\alpha_{3D} = 6°$ was compared as well. For VSPAero, the same settings as specified in Table 5.11 were used, except the amount of wake relaxation iterations was increased from 25 to 50.

Figure 6.3 shows the lift slopes obtained with both VSPAero and XFoil. In both cases, the lift

TABLE 6.2 – Equivalent 2D angles of attack for a few 3D angles of attack, for $AR = 255.0574$.

$\alpha_{3D}(°)$	0	3	6	9	12	15
$\alpha_{2D}(°)$	0	2.9766	5.9531	8.9294	11.9053	14.8806

slope obtained is linear as expected, although it can be seen that the lift slope of VSPAero is slightly lower than that of XFoil. This is a somewhat unexpected result, as a good effort has been made to reduce the variance between the two solvers. Since XFoil is a highly-regarded tool, the cautious conclusion will be made that VSPAero slightly underpredicts the 2D lift slope for an inviscid flow.

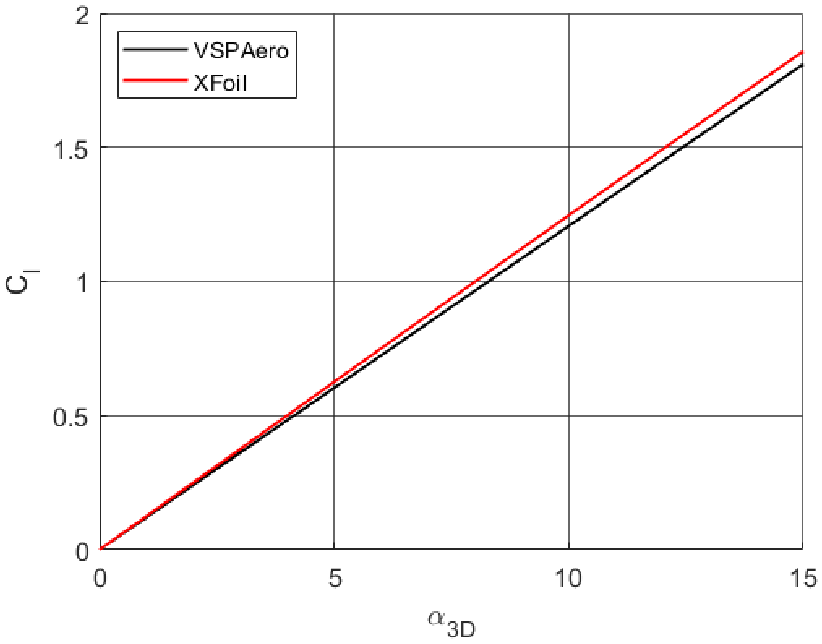

FIGURE 6.3 – Lift slopes obtained with VSPAero and XFoil.

Aside from the lift slope, the pressure distribution over the midspan was compared at two angles of attack: $\alpha_{3D} = 0°$ and $\alpha_{3D} = 6°$, shown in figures 6.4 and 6.5, respectively.
For $\alpha_{3D} = 0°$, it can be seen that both VSPAero and XFoil predict a symmetric pressure distribution, which is correct for a symmetric airfoil at zero angle of attack. However, it can be seen that VSPAero underpredicts the height of the pressure peak compared to XFoil. Furthermore, the VSPAero results show that there is apparently no stagnation point at the trailing edge, as the pressure coefficient decreases near the trailing edge. This seems to indicate that VSPAero apparently has a problem with enforcing the Kutta condition at the trailing edge.

For $\alpha_{3D} = 6°$, the pressure distributions are no longer symmetric, as the airfoil is generating lift in this configuration. It can again be seen that VSPAero has a smaller suction peak at the leading edge compared to XFoil and that the pressure coefficient decreases at the trailing edge. Furthermore, the pressure coefficient at the leading edge is less than one, indicating that there is likely a problem with both stagnation points.

Overall, the pressure distributions obtained with VSPAero are clos to those found with XFoil,

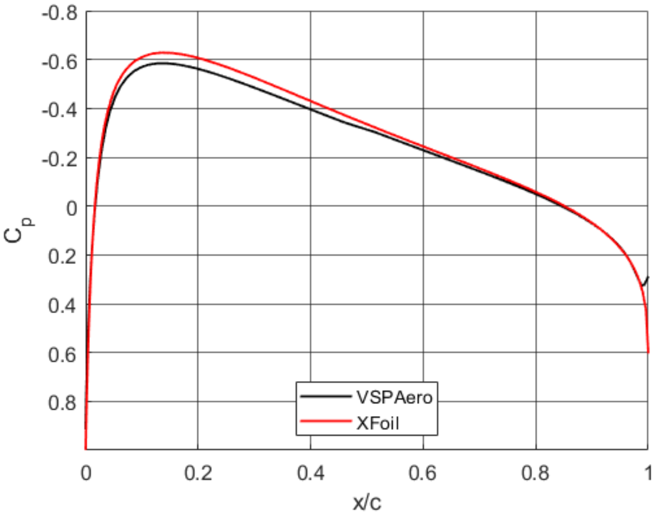

FIGURE 6.4 – Pressure distributions at $\alpha_{3D} = 0°$ obtained with VSPAero and XFoil.

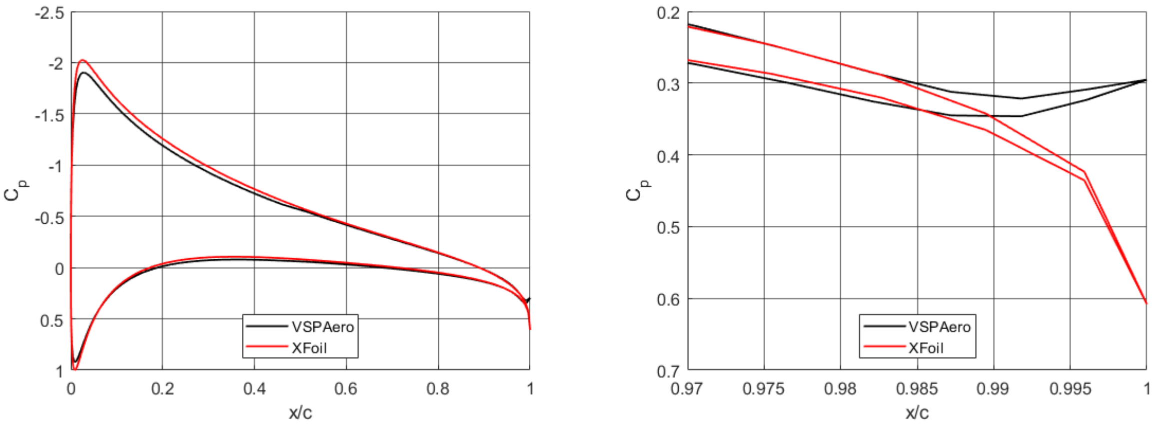

(a) Complete pressure distribution.

(b) Zoomed in view near the trailing edge.

FIGURE 6.5 – Pressure distributions at $\alpha_{3D} = 6°$ obtained with VSPAero and XFoil.

though it appears that there is an issue with the implementation of the Kutta condition in VSPAero, as the flow velocity does not go to zero at the rear stagnation point. Furthermore, the leading edge stagnation point is not always a stagnation point either in VSPAero.

6.2 Stall Models

VSPAero is at its core incapable to model any viscous effects, including stall behavior. However, if desired, two correction methods are available to the limit the lift at large angles of attack to mimic stall behavior and limit. It should be emphasized that the models included in VSPAero are not true viscous stall models and only post-process the inviscid lift results. The two stall models included in VSPAero are the 2D CLmax model and Carlson's Pressure Correlation (CPC). The 2D CLmax model requires the user to specify a maximum lift coefficient, based on a 2D section of the lifting body, which is used to 'clamp' the lift coefficient for high angles of attack. This is straightforward for simple geometries, such as straight wings with a constant cross-section.

However, for any geometry with more than one airfoil type, such as a wing-propeller model, or even a wing model with different airfoil sections over the span, defining a single maximum lift coefficient for the whole geometry already becomes difficult, and it is up to the judgment of the user to determine the most relevant maximum lift coefficient in these cases.
The CPC model predicts stall occurrence based on the local Mach number and pressure coefficient and requires no additional user inputs, though it is important that the Mach number is specified accurately, as the CPC model is very sensitive to Mach number changes. The CPC model does not work for completely incompressible flows, meaning that a linear compressibility correction must be used in VSPAero to use this stall model.

To evaluate the stall models, an angle of attack sweep from zero to thirty degrees in one degree intervals, was performed using the same geometry and flow conditions as in Section 5.1, except the Kárman-Tsien compressibility correction was applied and the Mach number was set to $M = 0.3$. As a reference, wind tunnel measurements performed on a NACA0018 section and RFOIL simulations will be used to compare the lift curves, drag polars and pressure distributions obtained with the stall models (TIMMER, 2008). As the wind tunnel measurements were obtained using pressure taps around the midspan of the model, the same will be done for the numerical results.

Figure 6.6 shows the lift curves obtained with VSPAero, overlaid on top of the experimental results. Based on the experimental results discussed by (TIMMER, 2008), a maximum lift coefficient of $C_{l,max} = 1.096$ was used as an input for the 2D CLmax stall model. It can be seen that in the linear-aerodynamic region, there is no difference between the stall models in VSPAero. Furthermore, the numerical and experimental results agree very well in the linear region, though it can be seen that there is a small dip in the experimental results, which (TIMMER, 2008) attributes to a small laminar separation bubble, which cannot be present in the VSPAero results. Additionally, it must be noted that the results from (TIMMER, 2008) show a stall hysteresis loop, as the flow detachment and reattachment behaviors are different for an increasing and decreasing angle of attack sweeps, which in not accounted for in the relatively simple models included with VSPAero, as these can only predict a single point where the stall behavior begins to occur.

In the experimental results, it can be seen that the linear lift slope ends at approximately $\alpha = 9.5°$, with the maximum lift coefficient being reached at $\alpha = 15.1°$. For the numerical results, both stall models predict divergence from the linear lift slope at higher angles of attack than the experiment, which is $\alpha = 12°$ and $\alpha = 13°$ for the 2D CLmax and Carlson models, respectively. For the 2D CLmax model, it can be seen that beyond the linear lift region, the lift coefficient almost asymptotically approaches $C_l = 1.25$, showing little variation at large angles of attack. The CPC model on the other hand, predicts a lift collapse after the linear lift regime, showing very sudden lift decay between $\alpha = 13°$ and $\alpha = 18°$. Interestingly, the difference between the two stall models almost mimics the two different paths on the lift hysteresis curve, as the 2D CLmax model more closely mimics the gentle stalling behavior for increasing angles of attack, whereas the CPC model is more similar to the sharper lift drop observed for the decreas-

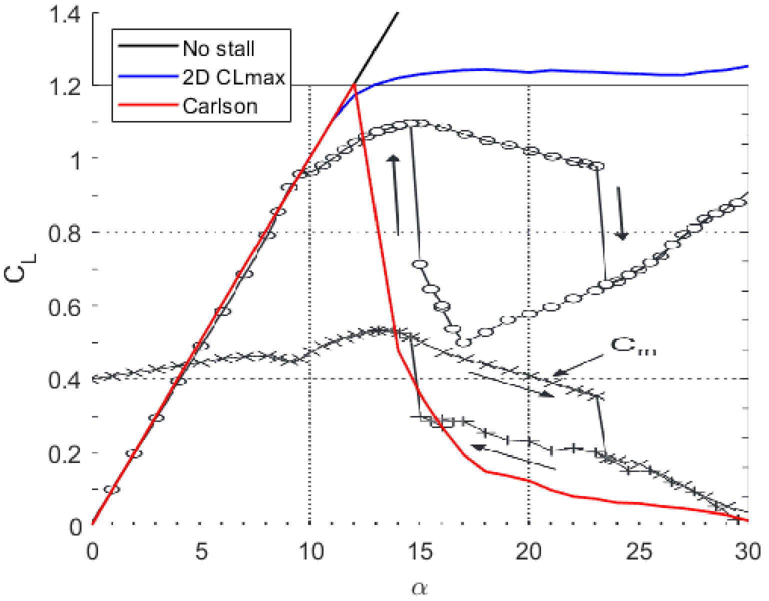

FIGURE 6.6 – Lift curves obtained with VSPAero plotted against experimental results. Both numerical and experimental results were obtained at $Re_c = 700000$. Original figure taken from the work by (TIMMER, 2008), with VSPAero results superimposed on top.

ing angle of attack part of the curve. While this is likely a coincidence, this observation could be taken into account if using VSPAero for modeling cases where highly different stalling behavior are expected. An oddity that can be observed is the fact that the maximum lift coefficient reached with the 2D CLmax model is noticeably larger than the specified CLmax, $C_l = 1.25$ versus $C_l = 1.096$, respectively. Coincidentally, at $\alpha = 11°$, the last angle of attack in the linear lift range obtained with the 2D CLmax model, the lift coefficient found equals $C_l = 1.106$, which is very close to the specified lift coefficient limit. Although this likely a coincidence, as the limited documentation of VSPAero states that the maximum lift coefficient of the whole lift curve should be used as an input, rather than the largest lift coefficient from the linear range. Table 6.3 summarizes the findings regarding the stall behavior in this section.

TABLE 6.3 – Difference between the stalling behaviors from measurements and both stall models available in OpenVSP.

	$\alpha_{max,lin}(°)$	$C_{l,max,lin}$	$\alpha_{C_l,max}(°)$	$C_{l,max}$
Measurements	9.5	0.955	15.1	1.096
2D CLmax	12	1.106	30	1.253
Carlson	13	1.204	13	1.204

Although it has already been established that the drag model in OpenVSP is rather crude, it is interesting to take a look at the difference between the drag polars obtained with the simulations and the experimental results. A comparison between the drag polars is shown in Figure 6.7. For the VSPAero results, only C_{D0} is plotted as opposed to the complete drag, since the wind tunnel set-up from (TIMMER, 2008) has the airfoil spanning from wall to wall in the test section, meaning no tip vortices can form, thus the lift induced drag is zero. Interestingly, up to $C_l \approx 1.0$, the zero-lift drag obtained with OpenVSP is larger than what was found in the measurements, which is typically the other way around. When comparing the difference between the polar

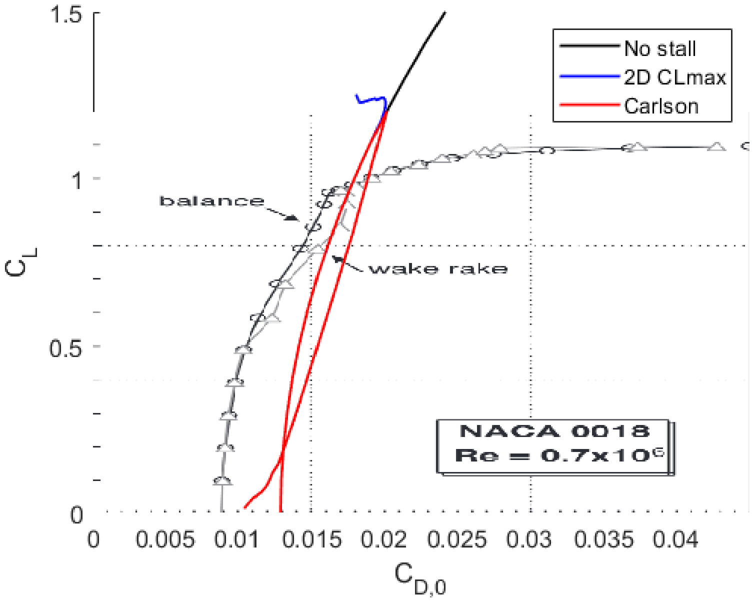

FIGURE 6.7 – Drag polars obtained with VSPAero plotted against experimental results. Original figure taken from the work by (TIMMER, 2008), with VSPAero results superimposed on top.

beyond this point, which could be described as the (post-)stall behavior, it can be seen that for the real measurements, the lift does not increase significantly, while the drag does, likely due to either the flow transition or separation point moving upstream over the airfoil. As such viscous simulation is not possible in VSPAero, it can be seen that the results without any stall modeling simply continue the curve seen at lower angles of attack. For the 2D CLmax curve, it can be seen that not only the lift coefficient is clamped, but the drag coefficient as well, as described in Section 6.2. The most interesting result can be seen for the CPC model, as it suggests a collapse of the profile drag, similar to the lift. As it was already established that the drag model in OpenVSP is rather simplistic, it is not surprising that its assumptions become less valid when mimicing stalling conditions.

Lastly, the pressure distributions obtained with the different models will be compared. As Section 6.1 discussed the disparity between the pressure distributions obtained with OpenVSP and XFoil already, this section will mainly cover the difference due to the different stall models.

When comparing the results for the 2D CLmax model with the uncorrected pressure distribution, it can be seen that these are identical. Furthermore, both are similar to the pressure distribution obtained with RFoil, though it can be seen that in the RFoil results, flow transition occurs on the suction side around $x \approx 0.15m$, which is not modeled in VSPAero. However, the results obtained with the CPC model are quite puzzling, as a very large part of the suction peak is cut-off compared to the other results, while still having the same lift and drag coefficients as the other VSPAero results. This strongly suggests that the CPC model applies rather odd post-processing steps to modify the pressure distribution. Because of this, the CPC model will not be investigated further in this research and the author highly recommends further parametric study be performed with this model, as it is unclear whether the observed behavior is set to

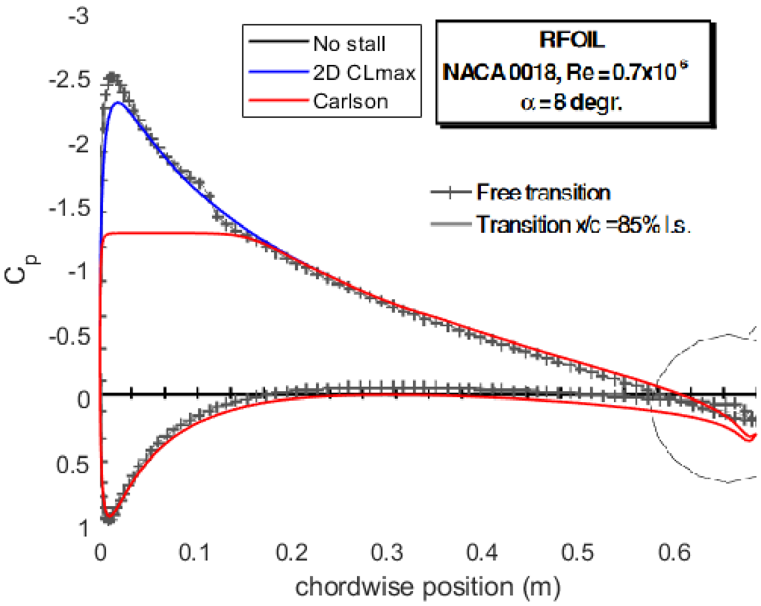

FIGURE 6.8 – Pressure distributions obtained with VSPAero plotted against RFOIL results. Original figure taken from the work by (TIMMER, 2008), with VSPAero results superimposed on top.

inherently occur with the CPC model, or whether an unlucky test case has been used. For cases where adding a stall correction is deemed useful, the 2D CLmax model will be used.

6.3 Propeller Performance Comparison

Since the propeller geometry was modified, it was necessary to quantify the performance difference between the original and modified geometries. For these simulations, the same grid settings were used for both geometries to make the simulations as similar as possible. Unfortunately, this meant that a grid of consisting of 24 chordwise and 48 spanwise panels per propeller blade had to be used (denoted as 4x 24c48s), as this was the finest spatial grid that was able to converge for the original geometry. While this is a rather crude grid in the chordwise direction, the differences between both propellers, were still sufficiently distinguishable in terms of the discretized geometry and performance.

To compare the two geometries, the same analysis types, flow conditions, propeller settings and timestep settings were used as discussed in Section 5.2.1.

6.3.1 Time History Global Coefficients

Figure 6.9 shows the time history of the thrust coefficient for all timesteps tested for both geometries. For the complete time history shown in Figure 6.9a, it can be seen that both geometries produce mostly similar results, with the propellers initially having a brief thrust peak on start up, after which a steady state is gradually reached. However, even on the C_T scale plotted in Figure 6.9a, it can be seen that during the steady state, there are spikes in the thrust of the original geometry for the finest timestep tested, which is already an indication that there problems with this geometry.

When looking a the zoomed-in view shown in Figure 6.9b, which only shows the last two rotations, the difference between both geometries can be more clearly seen. If ignoring the outliers, it seems that the modified geometry settles reaches $C_T \approx 0.08$ in the steady state, whereas the original geometry settles at a slightly higher value of $C_T \approx 0.085$. This seems to suggest that either, the original geometry produced too much thrust near the tip, or the modified geometry produced too little thrust near the tip, which will be determined when analyzing the radial load distributions. Furthermore, Figure 6.9b shows some interesting behavior regarding the 'spread' in the steady state when different timesteps are used: For both geometries, the largest timestep $dt = 0.01s$ is a clear outlier as expected. Aside from this, the steady states for all other timesteps seem to cluster rather nicely, with a slightly tighter grouping being observed for the original geometry than for the modified geometry. A clear exception to this is the result obtained for $dt = 0.0025s$, which strangely predicts consistently higher thrust than all other timesteps for both geometries. Lastly, it can be seen that there are large spikes in the thurst for $dt = 0.000625s$, and to a lesser extent for $dt = 0.00125s$ for the original geometry, whereas the results for the modified geometry are significantly smoother. As the propellers are under a steady axi-symmetrical inflow, there is no reasonable physical explanation for these spikes, meaning that they are an artifact from the numerical solution process. Since no finer grid could be successfully simulated on the original geometry, it seems plausible that the solver is on the brink of numerical stability for the used grid, which could be the cause of the peaks.

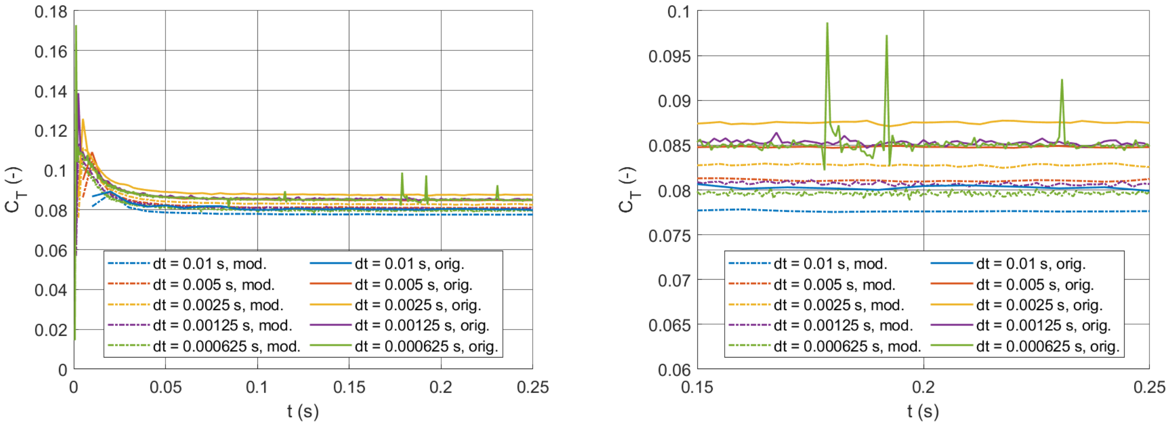

(a) Time history for five complete rotations.

(b) Time history for the last two rotations.

FIGURE 6.9 – Time histories of C_T for both geometries for all timesteps tested.

For further comparison of the global performance between both geometries, the average thrust coefficient, power coefficient and efficiency were computed over the last rotation for all cases. These are shown in Figure 6.10 and Table 6.4. Interestingly, it can be seen that the original geometry consistently produces more thrust at the expense of a greater power draw, compared to the modified geometry, whereas the modified geometry has a consistently better efficiency than the original. This is not unexpected, as the efficiency is defined as $\eta_P = \frac{JC_T}{C_P}$, thus a proportionally greater decrease in the power coefficient than the thrust coefficient at the same propeller operating conditions results in greater efficiency.

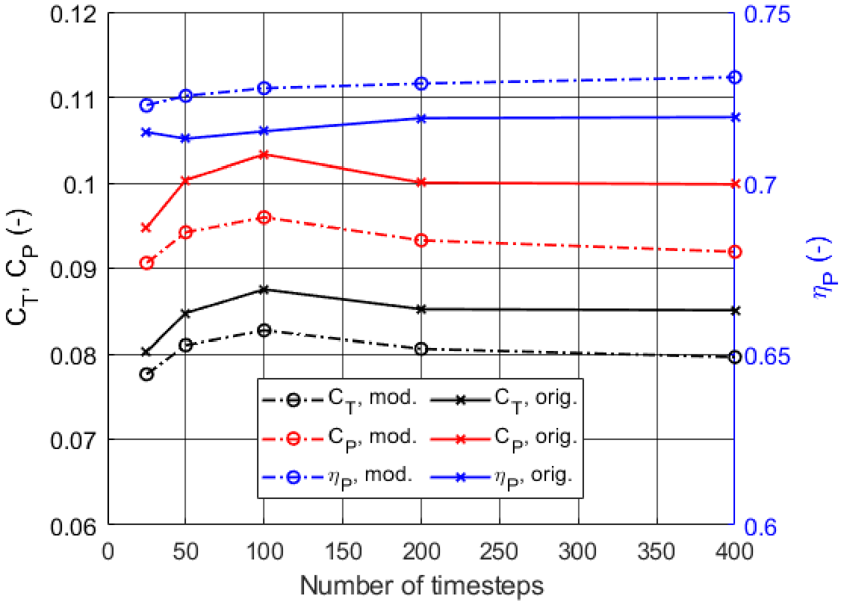

FIGURE 6.10 – Evolution of the global performance parameters for both propeller geometries.

TABLE 6.4 – Comparison between the global C_T, C_P and η_P for both geometries.

dt	0.01 s	0.005 s	0.0025 s	0.00125 s	0.000625 s
C_T, modified	0.0776	0.0810	0.0827	0.0806	0.0796
C_T, original	0.0803	0.0848	0.0876	0.0852	0.0851
C_P, modified	0.0906	0.0942	0.0959	0.0933	0.0919
C_P, original	0.0948	0.1003	0.1033	0.1000	0.0998
η_P, modified	0.7227	0.7254	0.7277	0.7290	0.7309
η_P, original	0.7148	0.7129	0.7151	0.7190	0.7193

6.3.2 Radial Load Distribution

To get a better understanding of the difference between the geometries, the time-averaged radial load distribution over the last rotation was analyzed for both cases. As the geometries have slightly different tips, it is expected that decomposing the thrust generated along the radius of the propeller will explain the observed difference in the global performance from results seen in Section 6.3.1.

Figure 6.11 shows the radial load distribution for both geometries and all timesteps. Two different visualizations of this distribution are shown: Figure 6.11a shows the thrust coefficient per radial station, whereas Figure 6.11b shows the thrust coefficient per radial station, divided by the normalized station area. The normalized station area is defined as the area of the station, divided by the total propeller blade area. In essence, Figure 6.11a shows a nondimensionalized force distribution and Figure 6.11b shows a nondimensionalized pressure distribution.

In Figure 6.11a, it can be seen that most of the thrust is produced around 0.75 r/R, which is typical for propellers under normal operating conditions. Furthermore, in Figure 6.11b, it can be seen that for most of the radius, the nondimensionalized pressure is approximately linear with the radial coordinate, except for the region near the root and tip, which matches expectations as well (VERHOEFF, 2005). When comparing the different geometries, two clear differences stand out: the modified geometry produces noticeably more thrust around the r/R = 0.45 region compared to the original geometry. As both geometries are actually identical around this radial locations, this difference cannot be explained. The other difference between the geometries makes a bit more sense, and can be seen at the tip of the propeller blade: for the original geometry, there is a spike in the thrust coefficient, which is absent in the modified geometry. It can be stated with certainty that the spike in the distribution of the original geometry is physically wrong, as around the tip, it is possible for the high-pressure fluid of the bottom surface of a three-dimensional lifting surface is able to move over the tip to the area of low-pressure, which would result a loss of lifting force near the tips and the generation of tip vortices. Therefore, it should be expected that the thrust coefficient should be going to zero near $r/R = 1$, which is not true for the original geometry. It should be noted that the thrust for the modified geometry does not exactly go down to zero at the tip either, though this is more likely due to the fact that the thrust distribution data is taken from the control points in the center of the panels, rather than at the edges, hence the data corresponding outer station is an averaged value over the panels near the tip.

Lastly, it can be seen that the influence of the timestep size is similar to the observations made for the global thrust coefficient for Figure 6.9: An underprediction for the thrust coefficient is seen for the largest timestep, and the other timestep sizes are clustered closer together. Interestingly, the largest difference along the radius between the different timesteps can be observed for $r/R > 0.6$, which suggests that the outer portion of the propeller is particularly sensitive to changes in the wake geometry. Since this is the part of the propeller containing the area where the peak thrust is generated, it makes sense that this results in noticeable changes in the global thrust output as well.

To get a clearer view of the difference in the radial load, Figure 6.12 shows the radial C_T distribution for the finest timestep only. Aside from the clear difference at the tip, more subtle differences between the exact radial load distribution for both geometries become apparent. It can be seen that for approximately $0.6 < r/R < 0.8$, the original geometry produces slightly more thrust than the modified geometry, whereas this trend reverses for $0.8 < r/R < 1$, with the obvious exception of the tip load. While the load appears to be slightly more spread out for the modified geometry, the differences between the regions for both cases seem to approximately cancel each other out, suggesting that the primary reason for the greater C_T observed for the original geometry is due to the physically incorrect spike at the tip. Figure 6.12b shows a zoomed-in view of the radial loads close to the tip.

For $0.148 < r/R < 0.6$, there appears to be no significant difference in the load distribution for both geometries, aside from the aforementioned bump near $r/R = 0.45$ seen in the result of

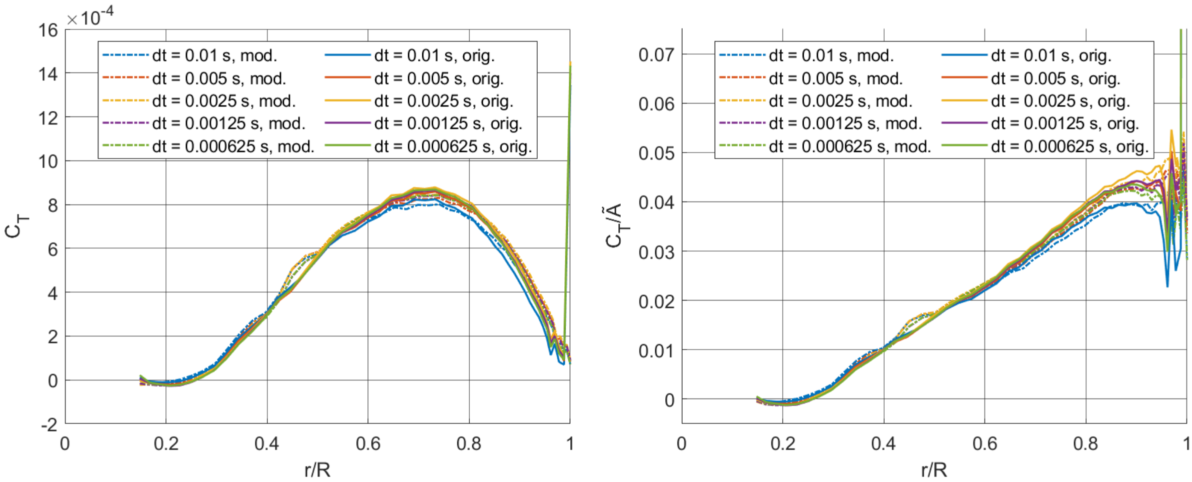

(a) Thrust coefficient per radial station.

(b) Thrust coefficient per radial station, normalized by the relative area of the radial station with respect to the complete blade area.

FIGURE 6.11 – Comparison between the radial C_T distribution for both propeller geometries for all timesteps tested.

the modified geometry.

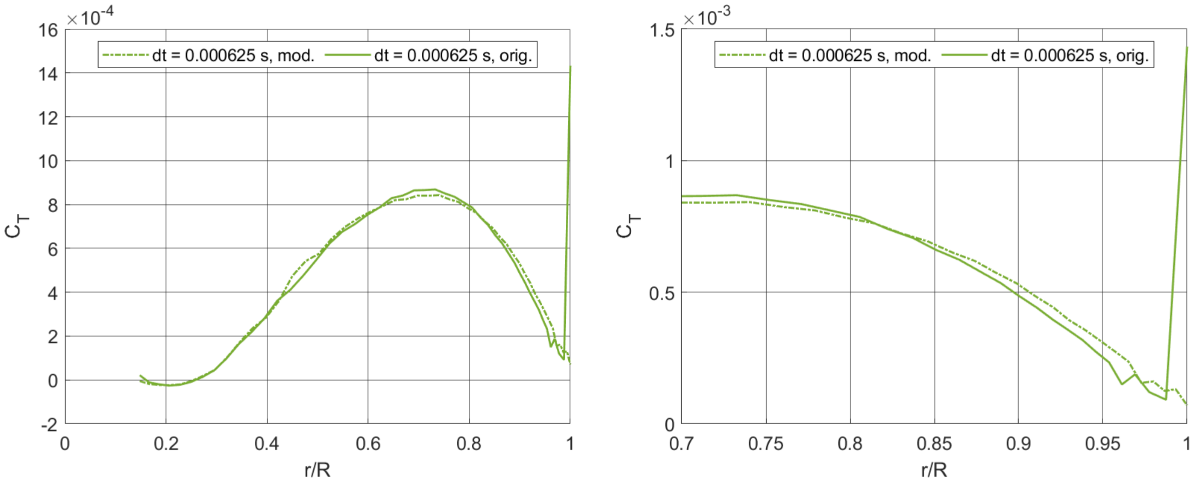

(a) Thrust coefficient per radial station.

(b) Thrust coefficient per radial station, zoomed in onto the outer 30% of the radius.

FIGURE 6.12 – Comparison between the radial C_T distribution for both geometries for $dt = 0.000625s$.

Judging by the results discussed in this section, the modification of the tip geometry is justified. Aside from the clear computational benefit of surpassing the grid resolution limitations that were observed on the original geometry, the results observed for the modified geometry seem to make more physical sense as well. However, it is rather strange that the tip modification was required to obtain these results indicating that OpenVSP may contain a bug or otherwise ill-posed condition near the tips of lifting surfaces for relatively small panel sizes.

6.4 Propeller Under Nonzero Angle of Attack

Up to this point, only axi-symmetric inflow conditions have been used for all propeller simulations. However, the propeller-wing aerodynamic interference will result in highly non-uniform inflow, it should be verified whether VSPAero is able to simulate non-uniform inflow conditions correctly. To this end, the simplest possible non-uniform flow was created by pitching the propeller 10 degrees up and comparing the results against a propeller aligned with the freestream. All other conditions will be kept the same across the tests, which are the same as discussed in Section 5.2. For the grid and timestep settings, the 4x 80c48s grid was used, in combination with a timestep of $\Delta\theta_t = 4.5^\circ$, or $dt = 0.000625s$.

Figure 6.13 shows the comparison between the changes in the load for a single blade over a full rotation for the two angles of attack. For the $\alpha = 0^\circ$ case shown in Figure 6.13a, it can be seen that the load is axisymmetric as expected, whereas for the $\alpha = 10^\circ$ case, there is an increase in the thrust generated when the propeller blade is between $\theta = 135^\circ - 250^\circ$. This makes sense, as the blade will be advancing between $\theta = 90^\circ$ and $\theta = 270^\circ$, and retreating on the remaining angles, which correspond to the left and right halves of the figures, respectively. During the blade advance, the effective inflow velocity is greater, as the blade is moving against the freestream flow, whereas during the retreat, the blade moves with the freestream, reducing the effective velocity. Additionally, the geometric angle of attack is also modified, as at the $\theta = 180^\circ$ and $\theta = 0^\circ$, the whole propeller blade receives an effective additional twist of $+10^\circ$ and -10°, respectively, which contributes to the difference in the loads as well.

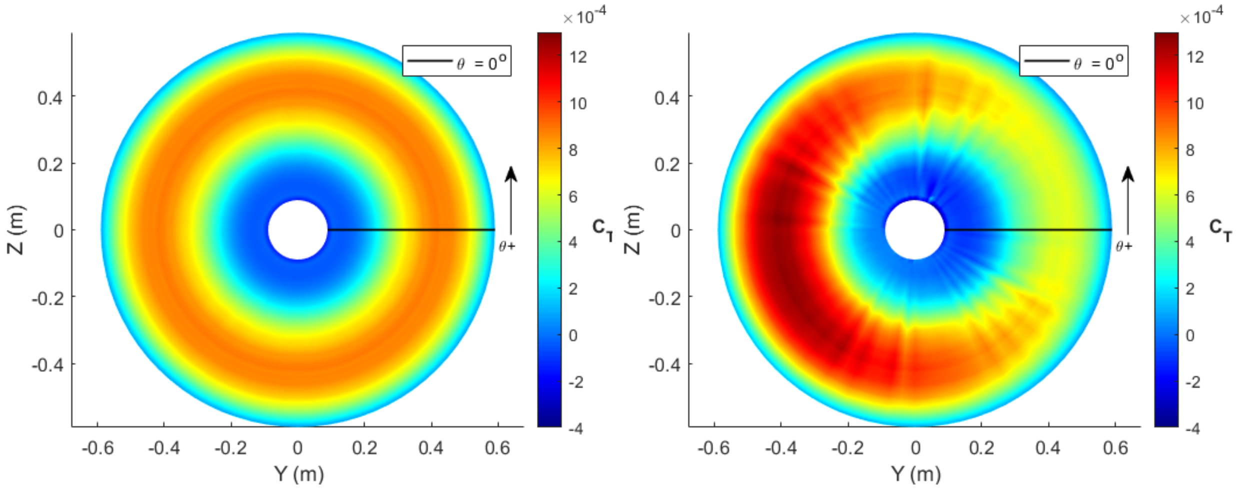

(a) $\alpha = 0^\circ$.

(b) $\alpha = 10^\circ$.

FIGURE 6.13 – Thrust distribution over a full rotation, shown from the front (upstream) of the propeller. Propeller rotates counterclockwise. Black line indicates $\theta = 0^\circ$.

To get a clearer view of the load changes over a full rotation, the C_T at four radial stations will be plotted against θ: $r/R = 0.25$, 0.50, 0.75 and 0.95. For sake of clarity, the locations of the radial stations has been marked on Figure 6.14.

In Figure 6.15, the thrust over a full rotation is shown for the four radial stations shown in Figure 6.14. For $\alpha = 0^\circ$ shown in Figure 6.15a, it can be seen that the load is basically constant

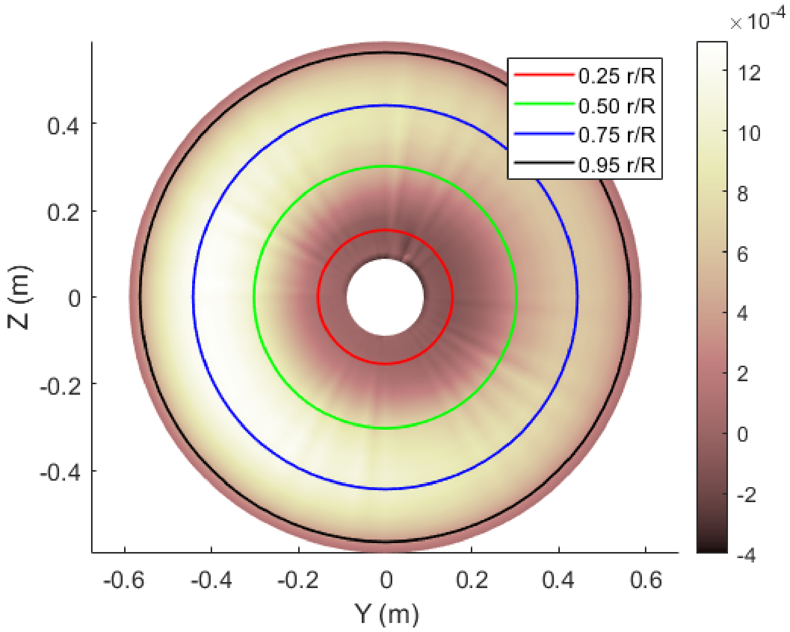

FIGURE 6.14 – Locations of the four radial stations used for further analysis.

at all four radial stations, with the fluctuations being at most 0.5% with respect to the mean at the mean value at the station. Furthermore, the relative amplitudes of every radial section is as expected as well, with the largest being found for $r/R = 0.75$, followed by $r/R = 0.5$ and $r/R = 0.95$. The least amount of thrust is produced at $r/R = 0.25$, as expected.

For the $\alpha = 10°$ results shown in Figure 6.15b, the almost sinusoidal behavior of the loading can be seen. Interestingly, the amplitude of the sinusoid is greater for the radial stations where more thrust is produced. An oddity that can very clearly be seen is the fact that the curves are all very jagged. This is likely a result of the very small timestep, causing the convected wake segments to travel only a small distance from the Kutta nodes and inducing a relatively large unsteady velocity which affects the circulation of the complete propeller blade. As these wiggles have a period of approximately two timesteps, another possibility is that this is the result of the wakes not quite reaching a steady state on every timestep, causing a small continuous over- and undershoot over the loading. This is corroborated by the fact that in the unsteady mode, VSPAero limits the amount of wake iterations to only one per timestep.

To be able directly compare the radial loads, the results from Figure 6.15, are plotted together in Figure 6.16. Unsurprisingly, it can be seen that the largest differences occur for the radial stations where the most load is produced. In Figure 6.16b, it can be seen that for the two stations at $r/R = 0.50$ and $r/R = 0.75$, the difference between the two angles of attack is nearly identical. Furthermore, it can be seen that during the blade advance, the thrust increase compared to $\alpha = 0°$ is greater than the thrust decrease during the blade retreat. For the $r/R = 0.25$ station, similar behavior can be observed, albeit with a smaller magnitude. The results for $r/R = 0.95$ show slightly different results, as the increased thrust during the advance is actually smaller than the decrease during the retreat, which is an interesting reversal of the trend, and it is somewhat unclear why this behavior occurs.

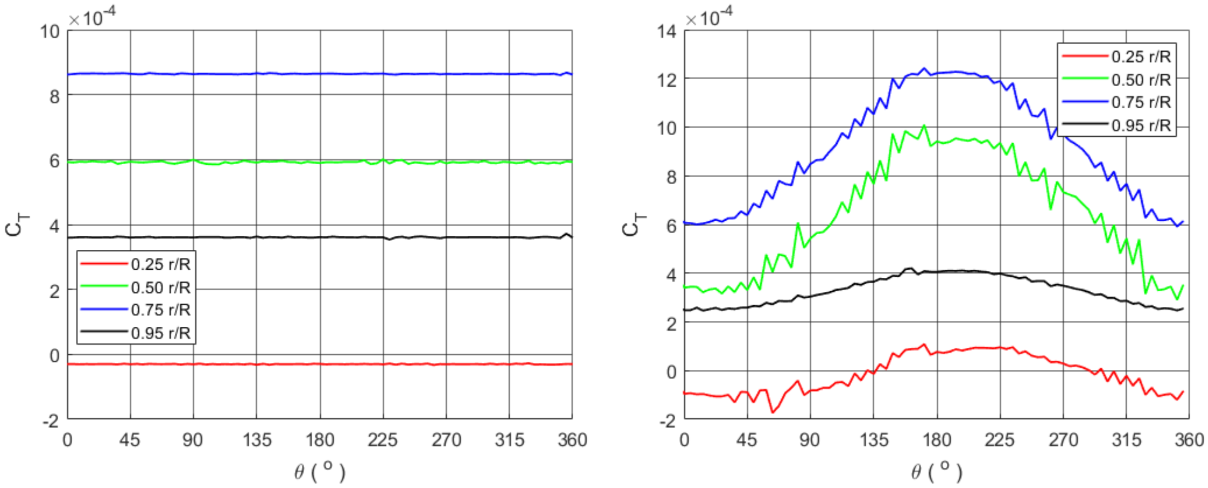

(a) $\alpha = 0°$.

(b) $\alpha = 10°$.

FIGURE 6.15 – Thrust evolution over a full rotation for four radial stations.

It has been shown that VSPAero can simulate non-uniform propeller inflows, and the observed trends do match with the physical expectations. The remaining question is whether the magnitudes of the difference due to the non-uniform inflow are correct as well, which will be discussed in Section 7.

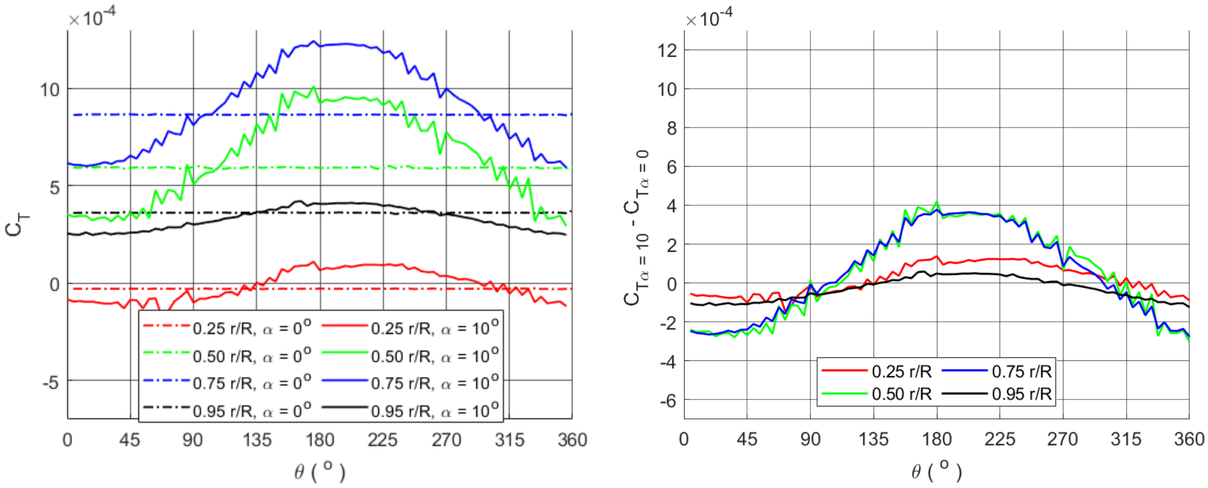

(a) Thrust comparison.

(b) Thrust differences.

FIGURE 6.16 – Comparison between the thrust at four radial stations between the two propeller angles of attack.

7 VSPAero Propeller-Wing Aerodynamic Interference Study

In this section, the main results of the simulations will be discussed and compared to the experimental results of (SINNIGE *et al.*, 2019) and the VSPAero VLM results of (GONÇALVES, 2024).

7.1 Test Case Description

As for all three phases of the simulations, the same procedure and settings were used, these will be discussed beforehand. The results will be grouped in a similar fashion as shown in sections 5 and 6: First, the global performance parameters of the propeller and wing will be discussed and compared to the other available datasets. Then, the local load distribution for the propeller blades and wing will be discussed, though without comparing it to other sources as this data is not available.

To get the most use out of the simulations, the experiments described by (SINNIGE *et al.*, 2019) were replicated as closely as possible in VSPAero, which consisted primarily of an advance ratio sweep at an angle of attack of $\alpha = -0.2°$ (table E.1), and an angle of attack sweep from $\alpha = -0.2°$ to $\alpha = 19.8°$ at four advance ratios, namely: $J = 0.7, 0.8, 0.9, 1.0$. However, as the amount of time to perform simulations and process the results was limited, only $J = 0.7$ and $J = 1.0$ were simulated, and larger intervals between the angles of attack in the sweep were made (table E.2 and E.3). Additionally, for the cases where both the propeller and wing were simulated, the tip-mounted and conventional configurations were tested. While the experimental results for both IU and OU rotation are available, mainly the IU rotating propeller has been simulated. For the conventional layout, there is very little difference between the IU and OU rotations for a wing of sufficiently large aspect ratio (VELDHUIS, 2005), thus simulating both is not very interesting. For the tip-mounted layout, whether the propeller rotation direction influences whether the tip vortex of the wing gets diminished or augmented, which has more significant effect on the wing performance. As there is no apparent benefit to increasing the strength of the tip vortex, the OU rotation case makes little practical sense to simulate.

In addition to replicating the experiments, all simulations were performed with and without the compressibility and viscosity corrections (table E.4). Originally, it was planned to perform an additional set of simulations where the 2D CLmax stall model was enabled, to verify whether this would yield good results for the cases where stall was predicted to occur. The stall point was estimated by calculating the velocity triangles at several radial stations on the propeller to compute the local angle of attack, which was compared to XFoil predictions to obtain both $C_{L,max}$ and the approximate stall angle of attack. Unfortunately, this was completely ineffective as including the 2D CLmax stall model with this procedure did not change the results at all. Even reducing the specified $C_{L,max}$ value by a factor of ten still did not affect the results. As a last resort, the CPC model was tested, though that did not work either. So, in the end, the simulations including a stall model were scrapped.

7.2 Isolated Propeller Results

First, the global performance characteristics of the isolated propeller will be discussed, starting the advance ratio sweep. In Figure 7.1, the results obtained for the advance ratio sweep are shown for experimental measurements, as well as VLM and panel mode simulation results. Generally, the trends observed in the experimental results can be reproduced with VSPAero. However, it can be seen that both set of numerical results overpredict the thrust and power coefficients over the entire range of advance ratios considered, though interestingly, these effects nearly cancel out, resulting in very comparable efficiencies, as seen in Figure 7.1b.

In the experimental results, it can be observed that the measured thrust and power coefficients scale mostly linearly with respect to the advance ratio, though towards the lower end of the range, it can be seen that the slope of the power coefficient in particular seems to taper down somewhat. For the numerical results, the quasi-linear dependence on the advance ratio is captured well, though it can be seen that the slopes of the thrust and power coefficients differ between the VLM and panel results: for both the thrust and power coefficient, the slopes found for the panel mode are higher than VLM. Interestingly, the intersection points are different, as the same thrust coefficient is achieved for the highest advance ratio considered, whereas the same power coefficient is achieved for lowest advance ratio. The difference in the thrust slope between both numerical methods can likely be attributed to the fact the for the VLM results, the maximum lift slope is 2π per the lifting line theory, whereas this is not necessarily the case for the panel mode, which can have larger lift slopes than 2π. Since the thrust produced by the propeller is closely related to the sectional lift production, this might be the underlying cause for the difference in the thrust slopes. The difference in the power slope could be attributed to the differences in the drag calculation between VLM and panel mode in VSPAero, as the power coefficient represents the amount of power required to spin the propeller. However, it is not clear why the VLM mode predicts a larger power coefficient at lower advance ratios compared to the panel mode results.

When comparing the propeller efficiency for all three datasets shown, it can be seen that for the advance ratios considered, both numerical methods and the experimental results show good agreement for the trend behavior. However, the experimental results show a large drop in efficiency for advance ratios above $J = 0.95$, which is partially captured by the numerical methods as well, though to a significantly lesser degree. This behavior makes sense as well, since the numerical results show a mostly-constant increase in the value of C_T and C_P over the range of advance ratios tested, and since $\eta_P = JC_T/C_P$ by definition, it follows that the largest difference between the numerical and experimental results is observed whenever C_T is low to begin with, such as for larger advance ratios.

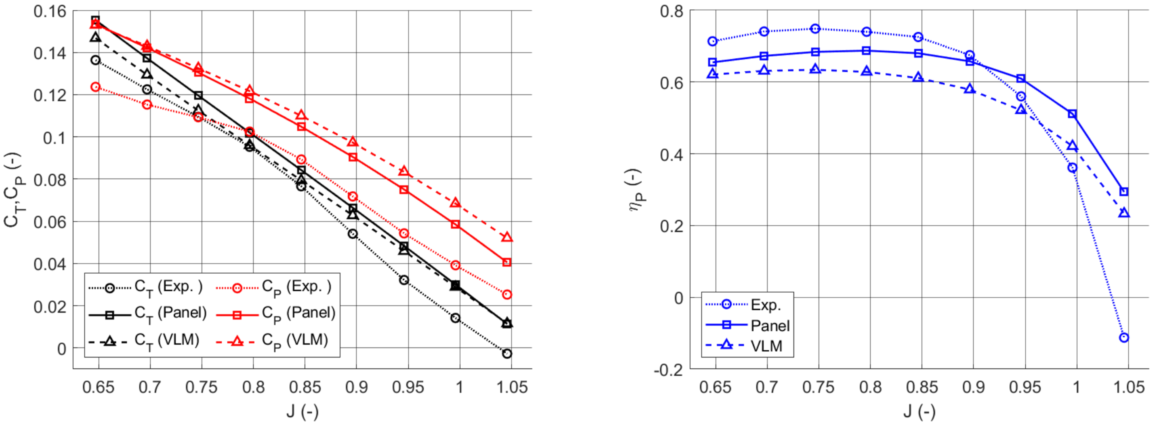

(a) Thrust and power coefficients.

(b) Propeller efficiency.

FIGURE 7.1 – Comparison of the global performance characteristics of the propeller between experimental, VLM and panel mode results.

As Figure 7.1 shows the numerical results where a viscous and compressibility have been applied, an additional comparison will be made with a 'pure' potential flow solution, without viscous and compressibility corrections, shown in Figure 7.2. A very remarkable observation that can be made right away is the fact that the power coefficient of the potential flow solution is unexpectedly close to the experimental measurements. This could be yet another indication that the viscous drag correction is overpredicting the magnitude of the viscous losses, as already shown in Section 6.2. When looking at the thrust coefficient, it can be seen that the slope found for the potential flow simulation is slightly less steep than for the corrected panel method, which can be attributed to the compressibility correction. With these two observations in mind, it is unsurprising that the potential flow results predict the largest propeller efficiency. Interestingly, the most efficient operating condition predicted by the potential flow is significantly different from the experiments, as the efficiency is the maximum for the former at $J = 0.9459$, compared to $J = 0.7466$ for the latter. The panel mode results on the other hand, which overpredicts both C_T and C_P, has peak efficiency at $J = 0.7963$, which is significantly closer to the experimental data.

The blade load distribution for all advance ratios has been investigated as well, and is shown in Figure 7.3. As there are no experimental or VLM results for comparison, the discussion of the radial load distribution will be kept brief. It can be seen that the shape of the load distribution is very consistent across all advance ratios and that the main difference is in the magnitude of the thrust peak in the distribution. Interestingly, it can be seen that the location of the thrust peaks seems to shift slightly outwards for increasing advance ratios, as for the lower advance ratios considered, the peak is located around $r/R \approx 0.75$, whereas for the higher advance ratios,

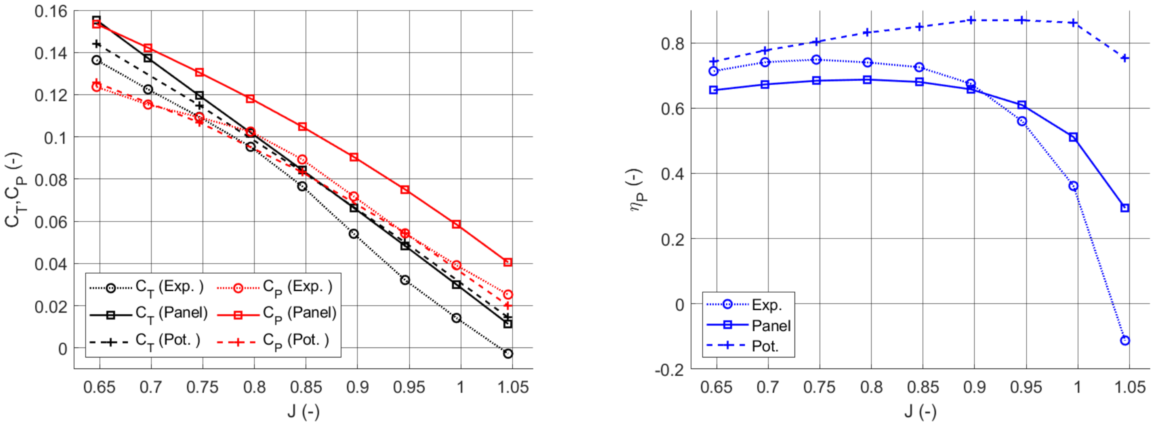

(a) Thrust and power coefficients.

(b) Propeller efficiency.

FIGURE 7.2 – Comparison between the experimental and the panel method results with and without viscous and compressibility corrections.

it is closer to $r/R \approx 0.8$.

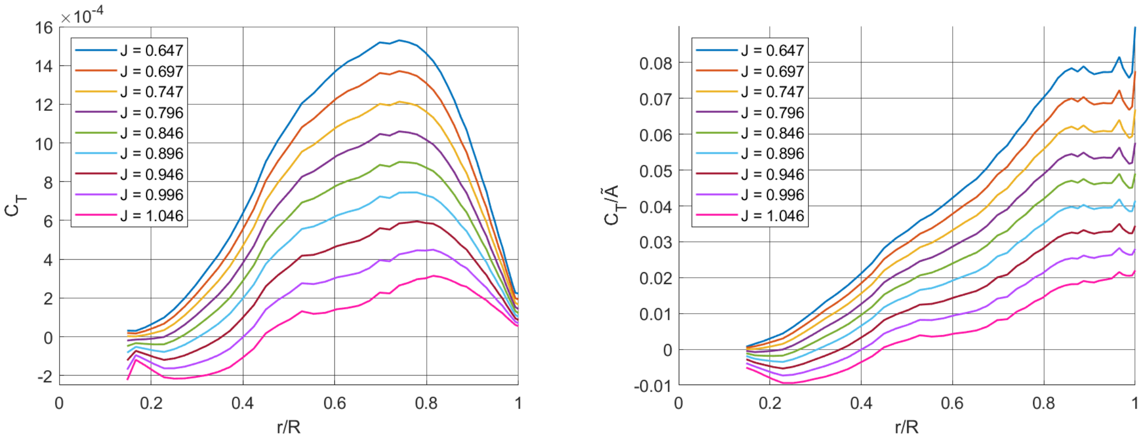

(a) Load distribution.

(b) Area-normalized load distribution.

FIGURE 7.3 – Radial thrust distribution for a single blade for all advance ratios considered. Results are including viscous and compressibility correction.

Next, the results for the angle of attack sweep will be discussed, which are shown in Figure 7.4a. It the experimental results for $J = 0.7$, the thrust coefficient is nearly completely independent of the angle of attack, whereas for $J = 1.0$, a gradual thrust increase is obtained for increasing angles of attack. This difference has a few causes: for $J = 0.7$, it was remarked that local flow separation started to occur, even at an angle of attack of $\alpha = -0.2$ (SINNIGE *et al.*, 2019) (STOKKERMANS *et al.*, 2019), thus it seems that increasing the propeller angle of attack under these operating conditions would worsen the blade stall on the downgoing stroke, which seems to be compensated by the upgoing stroke. A crude analysis was performed by computing the velocity triangles and angles of attack for a few radial stations, which were compared to C_l-α plots in XFoil. It was indeed found that for $J = 0.7$, a significant amount of blade sections was operating at a local angle of attack very close or slightly exceeding the stall angle of attack predicted by XFoil. Thus it is not surprising that the local stall behavior would worsen if the

propeller was placed under an angle of attack.
For $J = 1.0$, every local blade section operates at an effective angle of attack significantly below the stall angle. Thus, pitching the entire propeller upwards will still result in a local speed and angle of attack increase on the downgoing blade, which is a slightly stronger effect than the effective speed and angle decrease on the upgoing blade, yielding a net thrust increase that is not negated due to flow separation effects.

When comparing the experimental results to the numerical results, it can be seen that for both $J = 0.7$ and $J = 1.0$, the thrust increases with increasing angle of attack, which is only correct behavior for $J = 1.0$. As the numerical results do not account for thrust loss due to stall, it is likely that this is indeed the reason for the disparity between the simulations and experiments at $J = 0.7$. For $J = 1.0$, it can be seen that the numerical results overpredict the thrust coefficient compared to the experiments, though the overall trend is predicted very well.

In order to demonstrate the ineffectiveness of the stall model on the propeller, Figure 7.4b shows the results obtained with the 2D CLmax stall model turned on, compared to the panel mode solution without stall and the experiments. The 2D CLmax value was chosen by taking the propeller blade cross-section at $r/R = 0.75$ and performing an angle-of-attack sweep in XFoil using the local Reynolds and Mach numbers to determine the maximum lift coefficient. However, as can be seen in Figure 7.4b, the inclusion of the stall model unexpectedly seems to do nothing. In Section 6.2, it was already shown that the stall models in VSPAero do show different results compared to the potential flow solution on a wing, making it puzzling as to why the propeller seems to be unaffected. As a last-ditch measure, the CPC model was tried as well, to no avail.

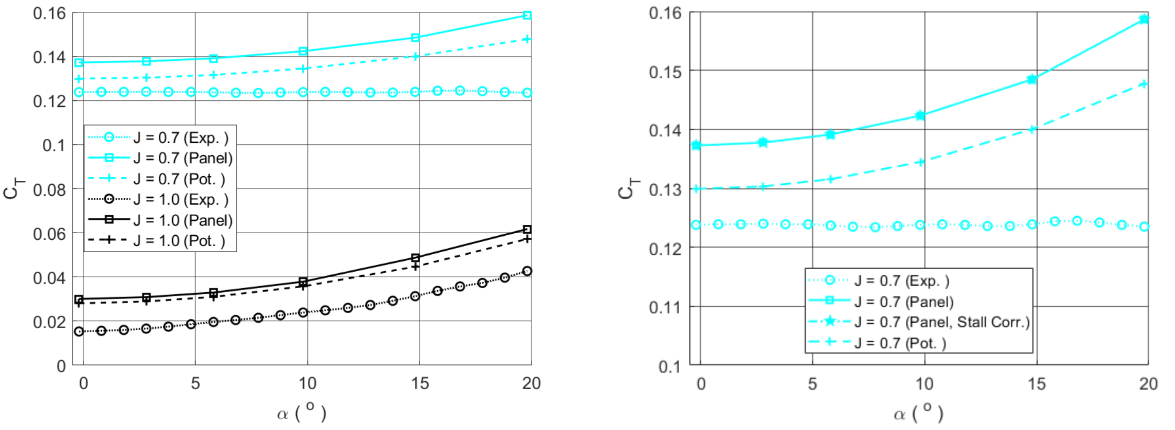

(a) Comparison numerical and experimental results for $J = 0.7$ and $J = 1.0$.

(b) Closeup of the $J = 0.7$ sweep, as well as the comparison with the stall model.

FIGURE 7.4 – Angle of attack sweep results for the isolated propeller.

The blade load distribution for the angle of attack sweep was investigated as well. However, as for any nonzero angle of attack the blade load varies with blade angle θ, it is interesting to investigate these variations in addition to the average blade load. In Figure 7.5, it can be seen that the average blade load increases for increasing angle of attack. Furthermore, the shape of the load distribution does not seem dependent on the angle of attack. Interestingly, it can be seen that for $J = 0.7$, every blade section is producing positive thrust, whereas for $J = 1.0$, large parts near the root produce, on average, negative thrust for all angles of attack except $\alpha = 19.8°$.

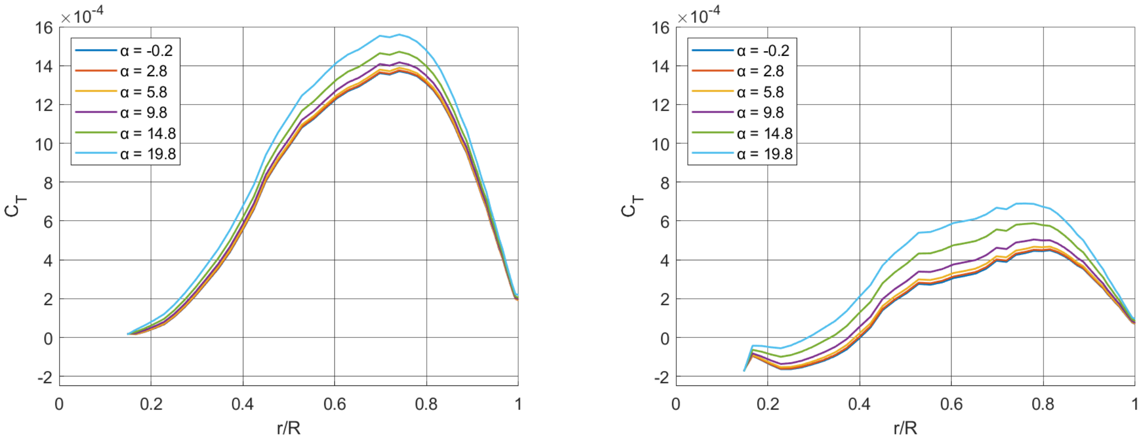

(a) $J = 0.7$ (b) $J = 1.0$

FIGURE 7.5 – Radial thrust distribution for a single blade under different angles of attack for two advance ratios. All results include viscous and compressibility correction.

To get a better understanding of the non-uniform propeller loading, the complete propeller load of the last rotation has been plotted for both $J = 0.7$ and $J = 1.0$, as can be seen in figures 7.6 and 7.7. The radial stations shown in these figures are the same as shown in Figure 6.14. For both cases, the results for $\alpha = 19.8°$ are shown, as this yielded the most non-uniform inflow. In both cases, it can be seen that the peak thrust is achieved at approximately $\theta \approx 180°$, which corresponds to the point of the rotation where the effective inflow speed of the propeller blade is the smallest. While no directly comparable experimental data is available, the load distributions seem to correspond to the pressure rise downstream of the propeller blade measured by (SINNIGE *et al.*, 2019). Furthermore, when looking at figures 7.6b and 7.7b, the difference in the shape of the load distributions seen in Figure 7.5 becomes apparent: for $J = 0.7$, it can be seen that the thrust coefficient at $r/R = 0.50$ and $r/R = 0.75$ is always greater than at $r/R = 0.25$ and $r/R = 0.95$, meaning that the overall shape of the thrust distribution is more or less consistent for the full rotation. However, for $J = 1.0$, it can be seen that for $\theta \approx 0°$ the local load for all radial stations is similar, yielding a relatively flat load distribution. By contrast, at $\theta \approx 180°$, the radial differences are similar to those observed for $J = 0.7$. Thus, for $J = 1.0$ a flatter load distribution is obtained.

Additionally, it can be seen that the thrust curves shown in figures 7.6b and 7.7b are very smooth, compared to the jagged curves seen in Figure 6.15b. This is likely due to the difference in timestep size and grid spacing, as the results shown in Figure 6.15b were obtained using a four times smaller timestep and grid almost twice as fine compared to figures 7.6b and 7.7b. Thus, the ratio between the trailing edge panels and shed wake segments is different, which has been shown by (HSIN, 1990) to affect the circulation for constant-strength vortex wake elements.

To summarize this section: the baseline performance of the isolated propeller has been established. It has been observed that generally, VSPAero overpredicts both C_T and C_P, though sim-

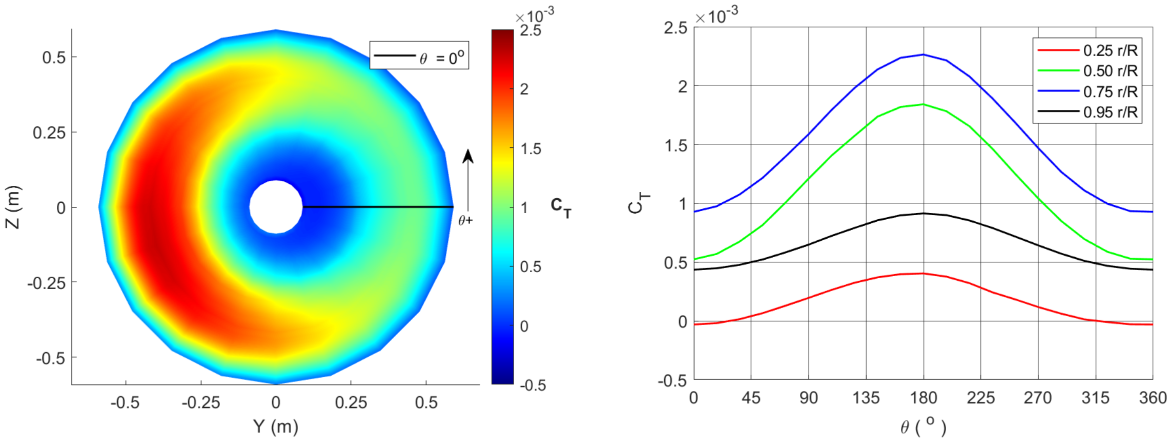

(a) Thrust distribution for the complete propeller disk. Front of disk shown.

(b) Thrust evolution for four radial stations.

FIGURE 7.6 – Radial thrust distribution for the isolated propeller operating at $J = 0.7$ and $\alpha = 19.8°$

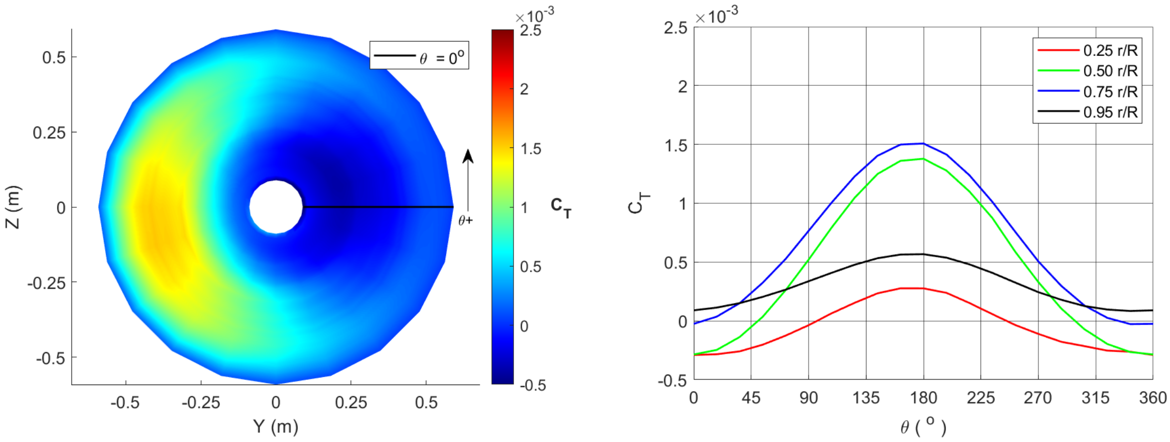

(a) Thrust distribution for the complete propeller disk. Front of disk shown.

(b) Thrust evolution for four radial stations.

FIGURE 7.7 – Radial thrust distribution for the isolated propeller operating at $J = 1.0$ and $\alpha = 19.8°$

ilar efficiencies as the experiments have been found. Interestingly, whenever running VSPAero in 'pure' potential mode, the power coefficient matched surprisingly well with experimental results, though a significant overprediction in the propeller efficiency was seen. Disappointingly, it has been seen that VSPAero was unable to capture stall-effects on the propeller. Lastly, the blade loads under non-uniform inflow conditions were found to be consistent with experimental observations.

7.3 Propeller-Wing Parametric Study

In this section, the results the propeller-wing simulations will be discussed, starting with the performance map of the propeller, shown 7.8, where the global performance parameters of the isolated propeller will be compared to three cases: the conventional layout of the propeller-wing model and the tip-mounted layout with the propeller spinning OU and IU. For both the pure potential (Figure 7.8c) and panel (Figure 7.8a) results, it is observed that there is basically no significant difference in the power coefficient between any of the simulated cases, except that power coefficient is lower for the potential results as already observed for the isolated propeller case in Section 7.2. Figure 7.8a) shows that the propeller thrust coefficient is increased whenever there is a wing in its slipstream, with a slightly larger thrust increase being observed for the conventional layout than for the tip-mounted configuration. For the latter case, it can be seen that the propeller rotation direction has no influence on the produced thrust. This increase in thrust observed for the propeller-wing geometry seems to suggest that the enhanced dynamic pressure due to the wing blockage effect seems to be captured (VELDHUIS, 2004), though it is not possible to say whether the magnitude of this effect is correct. When comparing the efficiencies for the different configurations, it can be seen that for lower advance ratios, there is essentially no difference in the results obtained for the conventional and tip-mounted layout, though it can be seen that for higher advance ratios, that the propeller efficiency is slightly higher for the conventional layout. It is particularly remarkable that for the panel mode results in Figure 7.8b, the efficiency for the propeller-wing cases is extremely close to the experimental results for advance ratios below $J = 0.75$, though this is very likely coincidental, as the magnitude of the interference effect of the experimental results is likely significantly lower compared to the simulations, as the isolated propeller in the experiments was mounted on an elongated nacelle (SINNIGE *et al.*, 2019). For higher advance ratios it can be seen that the propeller-wing interference effect seems to cause the propeller to behave as if it was operating at a lower effective advance ratio, as the downward curve in the efficiency seems to be less steep for the propeller-wing results than the isolated propeller results.

In Figure 7.9, the time-series of the thrust coefficient is shown for the last three rotations for all geometries at three different advance ratios. It can be seen that for the conventional layout, a clear oscillation at four times the rotation frequency can be seen as expected. For the tip-mounted results, this oscillation can very vaguely be recognized as well, despite the ‘messier’ time history. However, the same oscillation can be seen in the thrust output of the isolated propeller. This is unexpected: a propeller under an axisymmetric inflow should produce a steady thrust output as the flow is essentially steady from the perspective of the propeller blades (VALAREZO, 1991). Furthermore, the magnitude of these oscillations for the isolated propeller seems to decrease for increasing advance ratios, whereas for the propeller-wing simulations, it can be seen that the oscillation magnitude seems to be independent of the advance ratio. This observation for the isolated propeller seems to indicate an issue in the Kutta condition, as the wakes segments are convected further for larger advance ratios.

The average load distribution was compared for all cases and are shown in Figure 7.10. Compared to the isolated propeller, it can be seen that for both the conventional and tip-mounted layout, the load distribution is mostly unchanged near the tips, with the main load increase being observed between approximately $r/R = 0.5$ and $r/R = 0.8$, though the overall shape of the load distribution is mostly unchanged. The load is increased slightly more for the conventional layout than for the tip-mounted layout, as already observed for the global performance parameters.

The results for the angle of attack sweeps for the propeller-wing geometries at $J = 0.7$ and $J = 1.0$ are shown in Figure 7.11. Generally, very similar trends arise to those observed for the

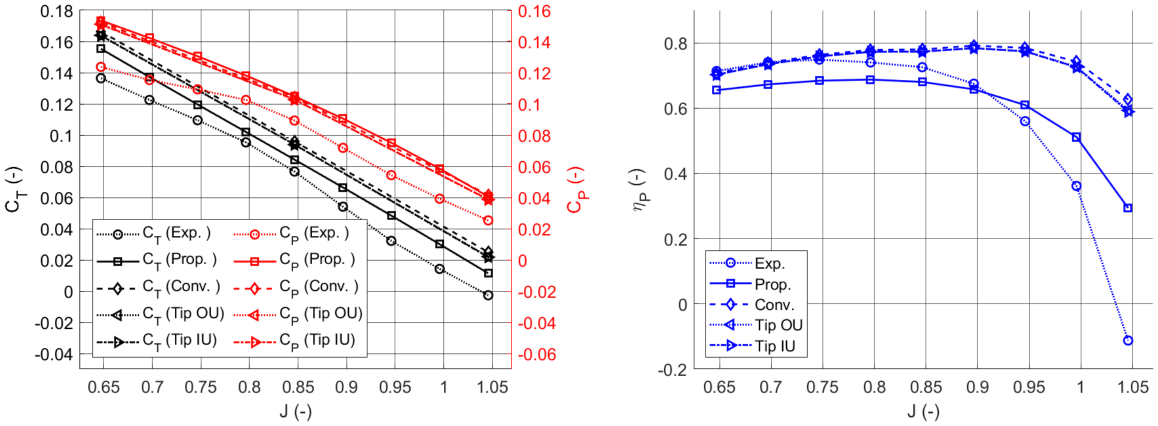

(a) Thrust and power coefficients.

(b) Propeller efficiency.

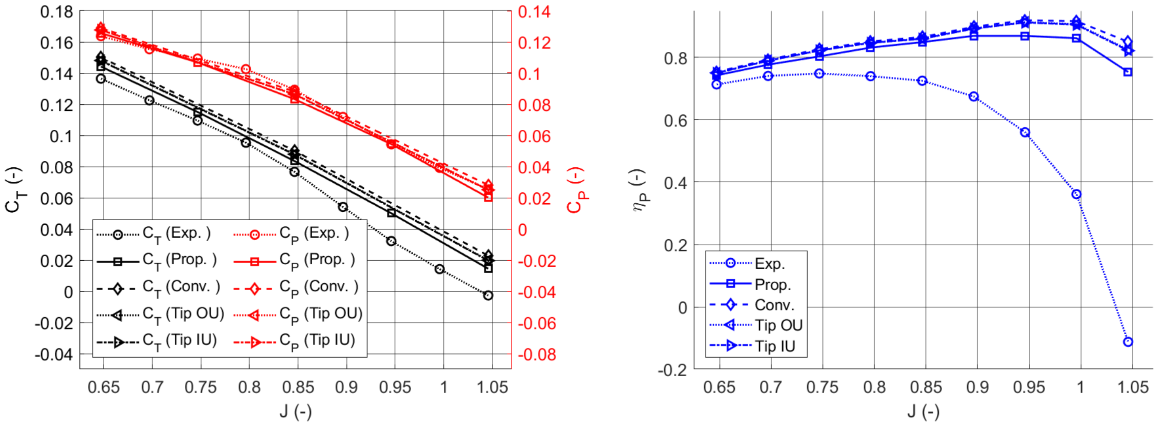

(c) Thrust and power coefficients.

(d) Propeller efficiency.

FIGURE 7.8 – Comparison between experiments, isolated propeller simulations and three configurations for the propeller-wing simulations. The simulation results in subfigures (a) and (b) include viscous and compressibility corrections, whereas (c) and (d) do not.

isolated propeller: for $J = 0.7$, it can be seen that all simulations incorrectly predict an increasing thrust coefficient for increasing angles of attack. However, for $J = 1.0$, the trend observed in the experiments is predicted correctly. Regarding the differences between the propeller-wing layouts: for $J = 0.7$ more propeller thrust is produced with the conventional layout than the tip-mounted configuration for all angles of attack. This is not the case for $J = 1.0$, as it can be seen in Figure 7.11b that for $\alpha = 14.8°$, the tip-mounted IU layout results in a greater thrust instead. Due to the limited amount of results it is not clear whether this is a fluke or a consistent trend at higher angles of attack. In the very limited amount of tip OU results, it can be seen that the thrust increase with angle of attack is slightly greater than for tip IU, though there is again too little data to draw a definitive conclusion.

Some data points for high angles of attack are missing from the numerical results of the propeller-wing cases. This was not intentional, as it was found that for higher angles of attack, the wakes in the propeller-wing simulations had the tendency to turn into 'tumbleweeds' or explode. Unfortunately, no clear pattern in these failed simulations has been observed, other than an increased chance of failure for larger angles of attack. However, it could be argued that the results for these

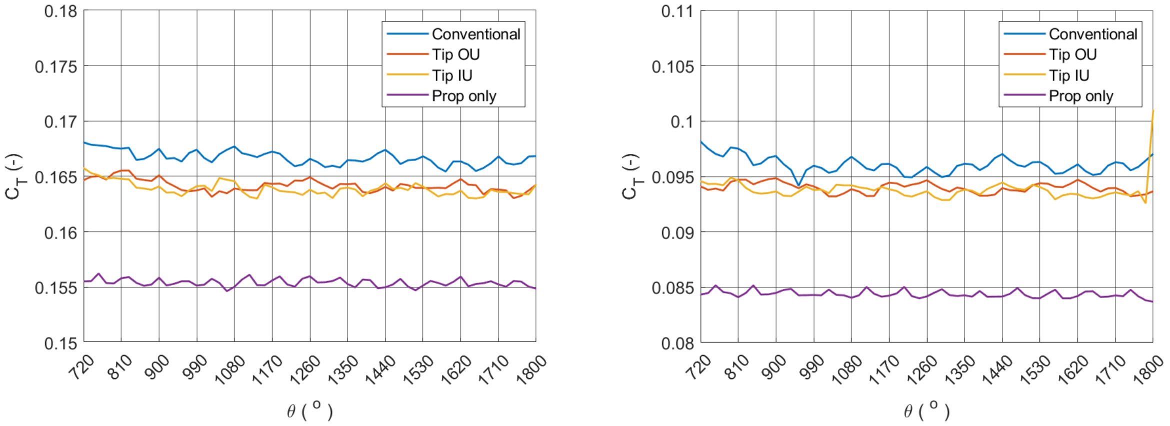

(a) $J = 0.647$ (b) $J = 0.846$

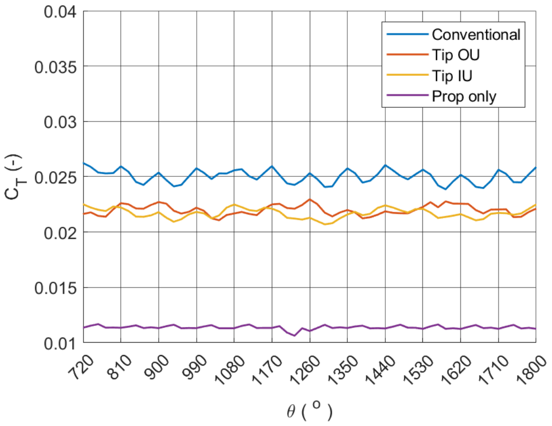

(c) $J = 1.046$

FIGURE 7.9 – Time history of the thrust coefficient for all configurations, shown for the last three rotations.

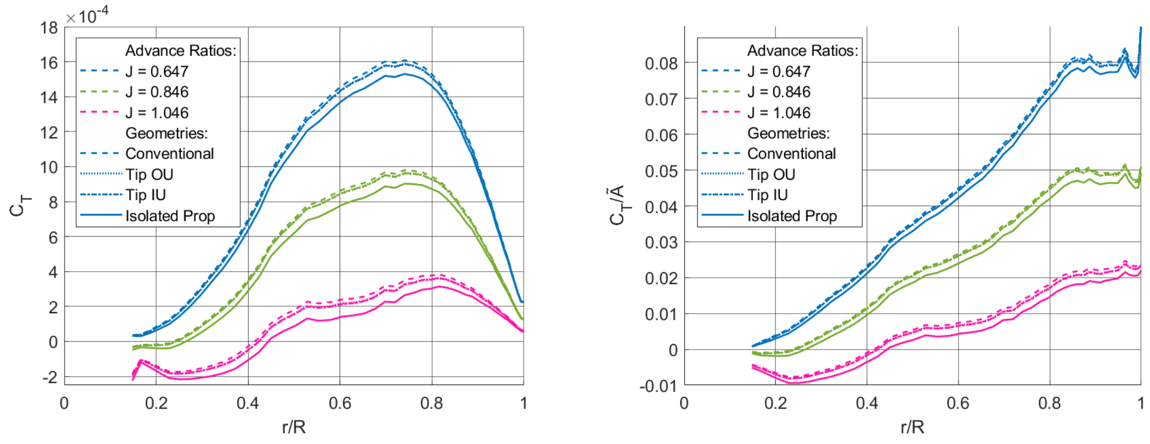

(a) Load distribution. (b) Area-normalized load distribution.

FIGURE 7.10 – Radial thrust distribution for a single blade for all advance ratios considered. Results are including viscous and compressibility correction.

large angles of attack already have questionable validity due to the potential flow assumptions, but this discussion is outside of the scope of this research.

The average blade load is shown for $\alpha = 6°$ and $\alpha = 15°$ in Figure 7.12. It can be seen that the

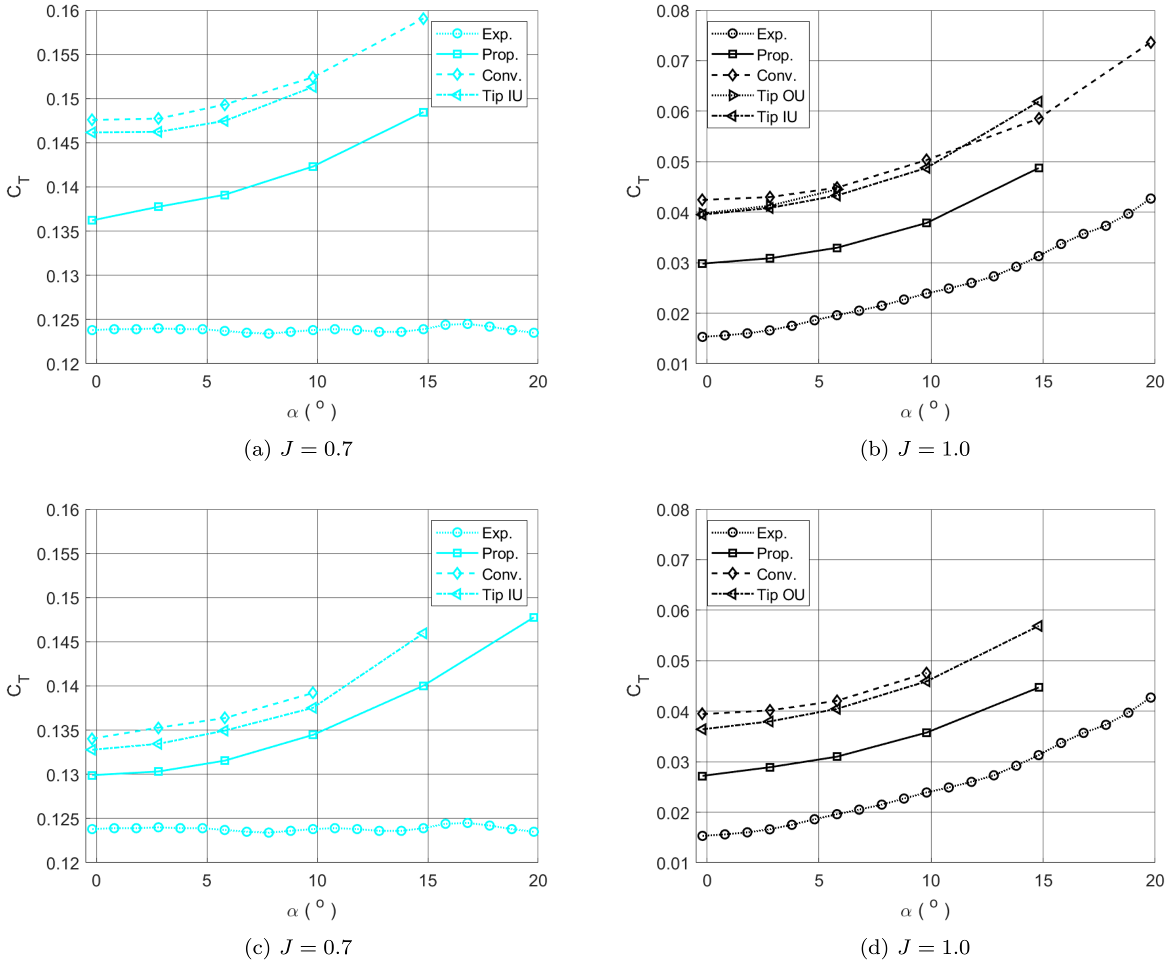

(a) $J = 0.7$

(b) $J = 1.0$

(c) $J = 0.7$

(d) $J = 1.0$

FIGURE 7.11 – Angle of attack sweep results for the experiments, isolated propeller and the different propeller-wing configurations. The simulation results in subfigures (a) and (b) include viscous and compressibility corrections, whereas (c) and (d) do not.

trends observed in Figure 7.10 are all recognizable and will not be elaborated upon. There are some differences in the shape of the load distribution between the two layouts for $J = 1$ seen in Figure 7.12b: up to approximately $r/R = 0.4$, the propeller load in the conventional layout is slightly greater, but beyond this point, the load on the tip-mounted propeller is greater, possibly due to the wing tip vortex inducing a greater tangential velocity in the propeller plane.

To further analyze the difference between the load distributions observed for the conventional and tip-mounted layouts, the load distribution for a full rotation has been compared for $J = 0.7$ and $J = 1.0$, as shown in figures 7.13 and 7.14, respectively. Additionally, the isolated propeller result is shown as well as a reference.

Starting with the results for $J = 0.7$, a few observations can be in Figure 7.13d: Firstly, it can be seen that for the cases where a propeller-wing configuration was simulated, the amplitude of the load differences, both positive and negative with respect to the baseline, is greater than for the isolated propeller. However, it can be seen that for more than half of the rotation (approximately $200 - 250°$, depending on which station is considered), the propeller-wing load is greater than for the isolated propeller, thus it is not surprising that for the propeller-wing

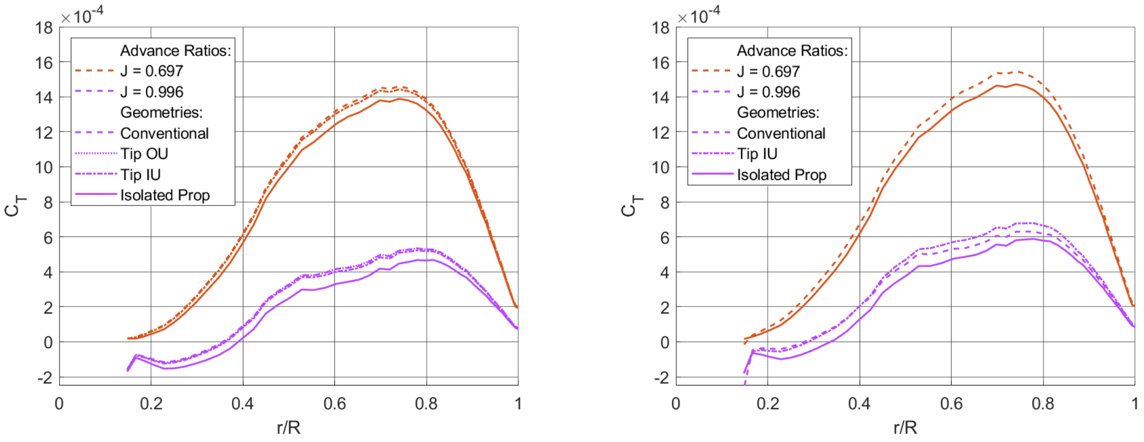

(a) $\alpha = 6°$

(b) $\alpha = 15°$

FIGURE 7.12 – Radial thrust distribution for a single blade under different angles of attack for two advance ratios. All results include viscous and compressibility correction.

cases, an overall larger thrust production is observed compared to the isolated propeller. Secondly, when comparing the conventional and tip-mounted layouts, it can be seen that for is that for the conventional layout, the load peak around $\theta = 180°$ is significantly greater than for the tip-mounted layout. This makes sense, as for the conventional layout, the propeller blades encounter the wing at $\theta = 0°$ and $\theta = 180°$, whereas for the tip-mounted layout, the wing is only encountered at $\theta = 0°$. Thus, for the conventional layout, the enhanced dynamic pressure in the rotor plane due to the wing is experienced twice as often, resulting in more propeller thrust. Additionally, it can be seen that the overall shape of the load curve between the two layouts is slightly different, which is the most clearly visible for $0° \leq \theta \leq 90°$ for $r/R = 0.75$. This difference is possible related to the influence of the tip vortex on the wing behind the propeller, though that is only conjectured. The results for $J = 1.0$ shown in Figure 7.14d are globally similar to those seen for $J = 0.7$, though the differences between the configurations are a bit larger. Aside from that, all remarks made for $J = 0.7$ apply here as well.

Lastly, the results obtained for the wing will briefly be discussed as well. Although this research focuses on the performance of the propeller, the propeller-wing aerodynamic interference is a two-way relationship, thus the influence of this effect on the wing should be validated as well.

Up to this point in the analysis of the results, it could be argued that overall, the results obtained with VSPAero seem decent, even if there are a few shortcomings in the solver. However, from the results obtained for the wing, all prior conclusions become somewhat more questionable. Figure 7.15 shows the lift distribution on the wing for the three configurations tested, compared to the isolated wing under the same conditions. The best results have been obtained for the conventional layout shown in Figure 7.15a. Compared to the ‘Veldhuis-curve’ from Figure 2.1 and the experimental results from (SINNIGE *et al.*, 2019), the same overall shape can very vaguely be recognized for $J = 0.647$, though that cannot be said for the other two advance ratios. It can be seen that on the inboard section of the wing, there is indeed a lift increase predicted, though there seems to be no relation between the increase and propeller advance ratio, while theory

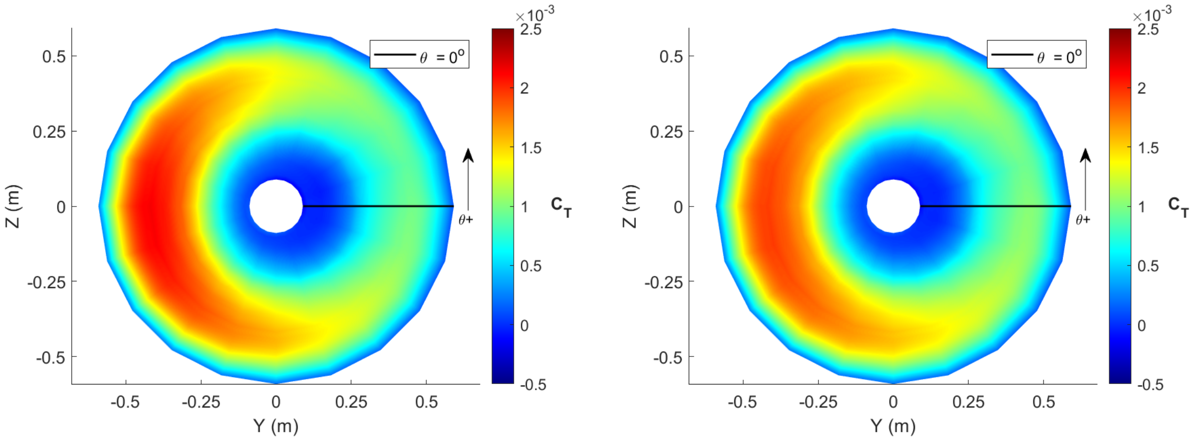

(a) Conventional layout.

(b) Tip-mounted layout.

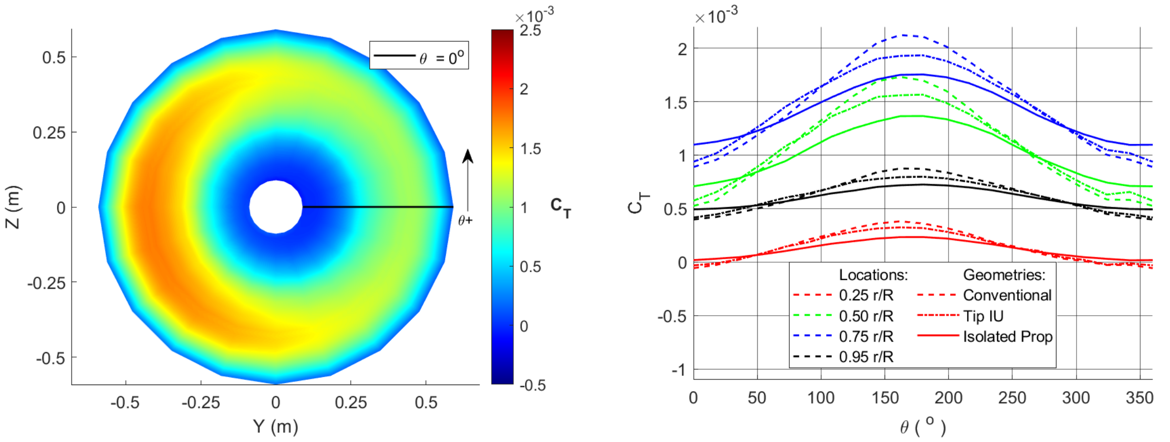

(c) Isolated propeller.

(d) Thrust evolution for four radial stations.

FIGURE 7.13 – Radial thrust distribution comparison between the conventional layout, tip-mounted layout and isolated propeller operating at $J = 0.7$ and $\alpha = 9.8°$. Results shown include viscous and compressibility correction.

(VELDHUIS, 2005) and experiments (SINNIGE *et al.*, 2019) clearly show that the lift increases with increasing propeller thrust (decreasing J) in this section. The opposite effect applies to the outboard section, which cannot be observed in the numerical results either.

For the tip-mounted configuration, the lift distributions make so little sense that there is no point in attempting to explain the results. The results for $\alpha = 2.8°$ are very similar as well and are shown in Figure F.1 in appendix F.

Although the lift distributions make little sense, it is possible that insights may be obtained from the lift polars instead, which are shown in Figure 7.16. Strangely, it can be seen that even for the isolated wing, the lift is significantly overpredicted in the VSPAero compared to the experiments, though a similar lift slope can be observed. For the blown wing cases, the simulations show no consistent behavior. It was expected that there could be some oscillations, as (GONÇALVES, 2024) observed similar results for the VLM mode of VSPAero, though the trend behavior of those results agreed decently with the experimental. However, for the panel mode results shown in this work, no clear trend can be observed.

The results obtained for the propeller-wing geometry could be briefly summarized as follows: for the propeller, the trends in the global results seem to align with theoretical predictions,

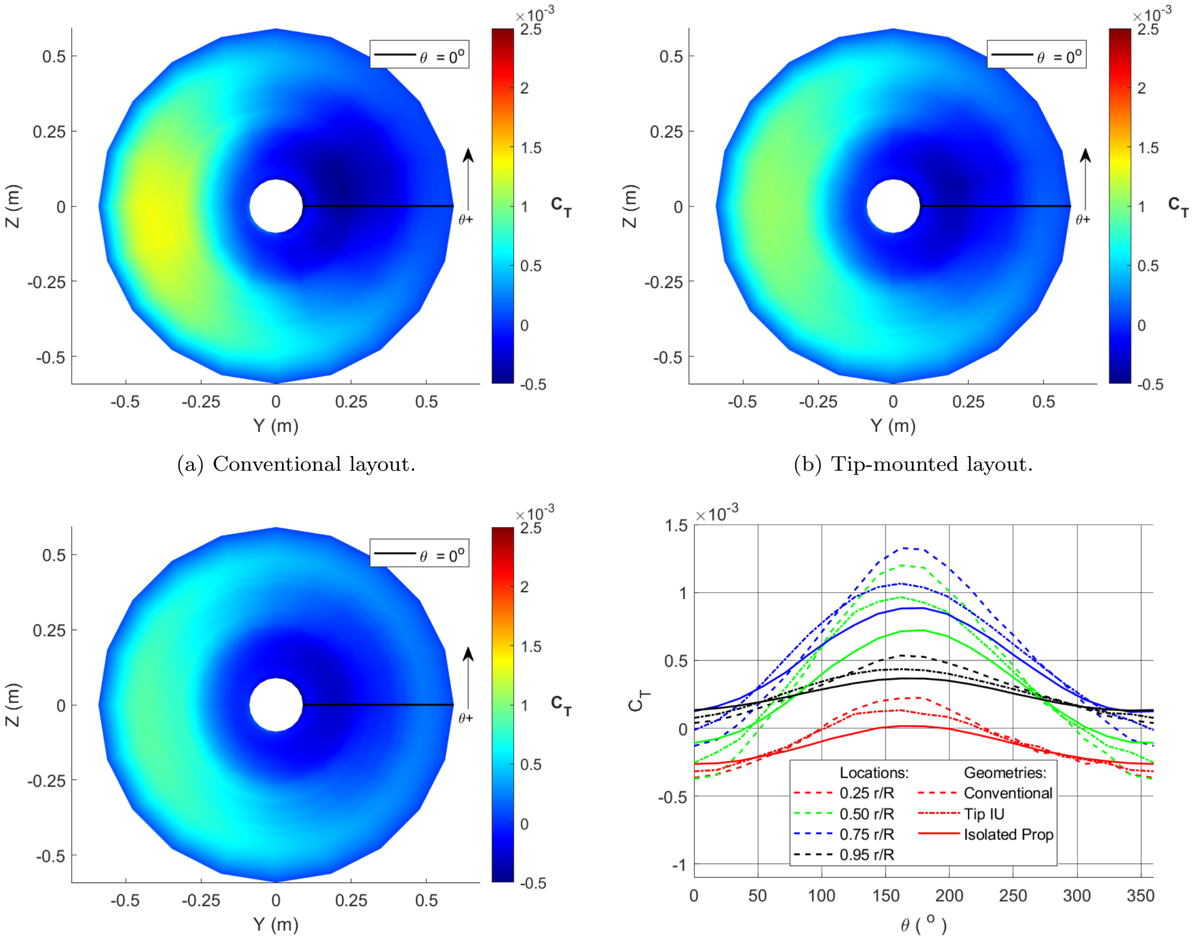

(a) Conventional layout.

(b) Tip-mounted layout.

(c) Isolated propeller.

(d) Thrust evolution for four radial stations.

FIGURE 7.14 – Radial thrust distribution comparison between the conventional layout, tip-mounted layout and isolated propeller operating at $J = 1.0$ and $\alpha = 9.8°$. Results shown include viscous and compressibility correction.

though it seems that the isolated propeller results have unexpected oscillatory behavior that should not be present. Additionally, some differences were observed in the loading of the propeller depending on whether it is mounted on the midspan or wingtip, with a few hints pointing at a possible trend reversal for higher angles of attack, which could be interesting for future studies. Unfortunately, the results found for the blown wing are unusable, which casts doubt on the validity of the propeller results as well. A frustrating aspect about the very poor wing results is that there seems to be no obvious cause: great effort has been put into the meshing procedure and all best practices outlined by (LITHERLAND, 2021) have been followed where possible.

The most likely cause of the poor wing results is the fact that the propeller wakes pass through the wing, such an intersection occurs near a panel control point, which will very heavily affect the results if a wake node ends up in nearly the same position. This is supported by the fact that in the animation of the results, it was consistently observed that the pressure on the part of the wing directly in the wake of the propeller fluctuated by orders of magnitude between timesteps on certain panels, which does not make physical sense. Another possibility is that a mistake was made while setting up the simulation or in the basic methodology, though other studies with similar test cases did better, making it very unlikely that the applied methodology is completely

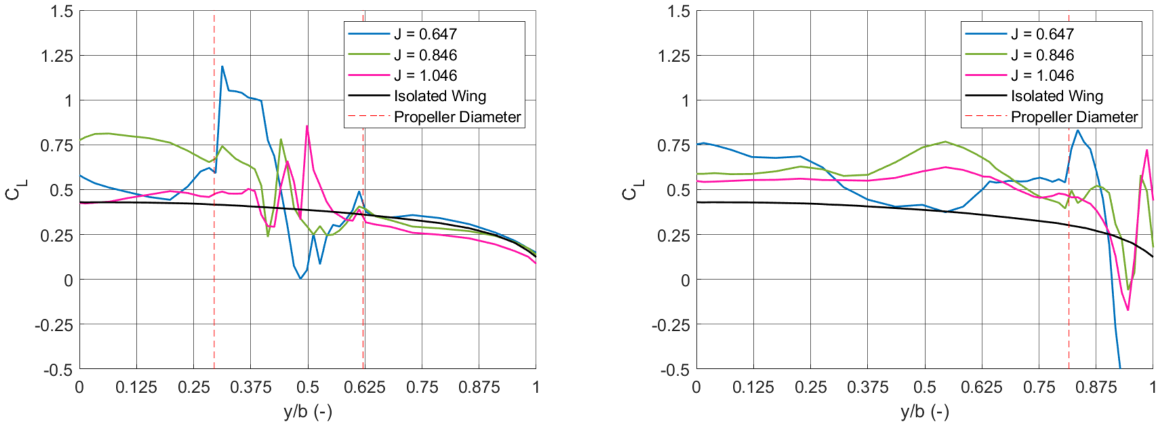

(a) Conventional layout.

(b) Tip-mounted layout, spinning OU.

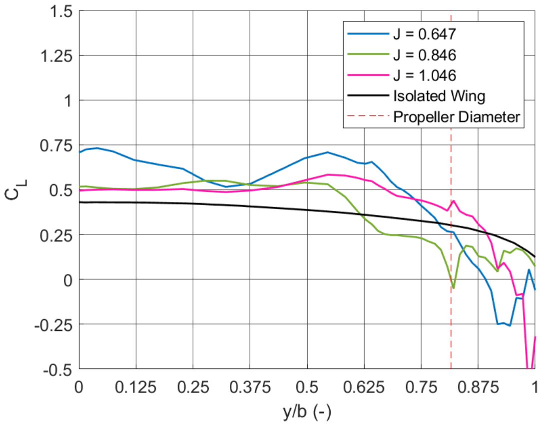

(c) Tip-mounted layout, spinning IU.

FIGURE 7.15 – Lift distribution comparison for different layouts and advance ratios at $\alpha = -0.2°$.

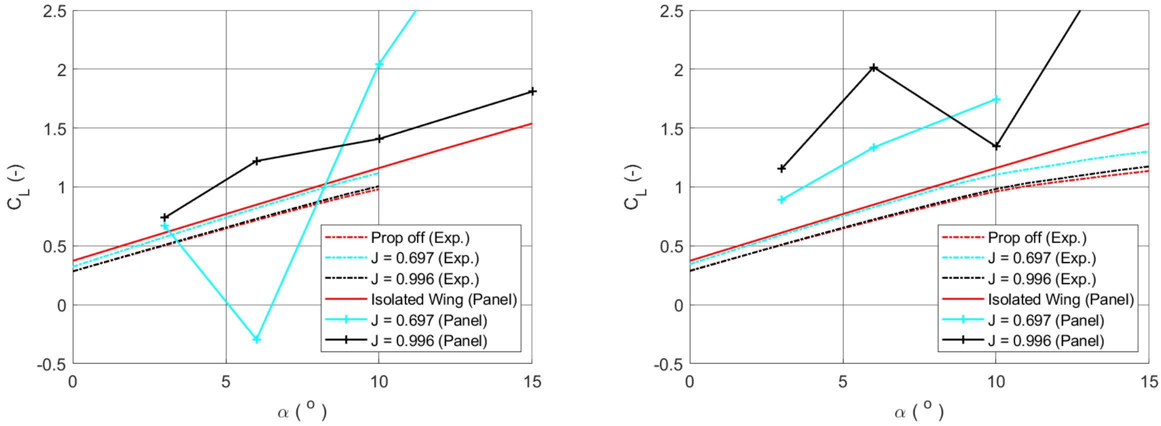

(a) Conventional layout.

(b) Tip-mounted layout, spinning IU.

FIGURE 7.16 – Lift polar comparison between experimental and numerical results for both configurations.

flawed.

7.4 Complete Model Comparison

In this section, the results for the complete geometry will be discussed. It should be noted that for all cases, the propeller was spinning IU. Figures 7.17 and 7.18 show the propeller performance map for the conventional and tip-mounted configurations, respectively. For both configurations, there is very little difference in the numerical results for power coefficients, showing that the aerodynamic interference effect does not seem to impact the power draw of the propeller in a significant way. For both layouts, it can be seen that the addition of the nacelle and spinner resulted in a thrust increase compared to the propeller-wing model. The overall efficiency of the full geometry is very similar to the prop-wing model, though the former is slightly higher, especially for the higher advance ratios considered.

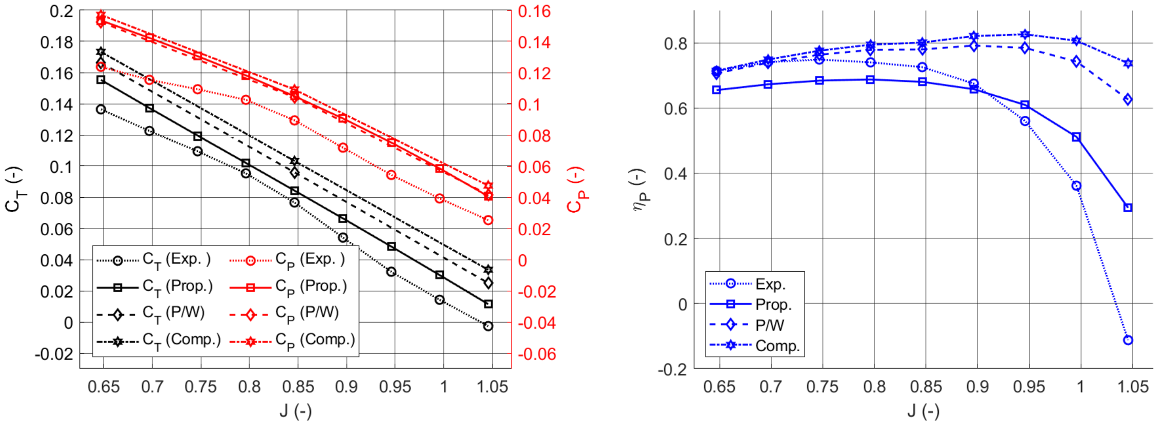

(a) Thrust and power coefficients.

(b) Propeller efficiency.

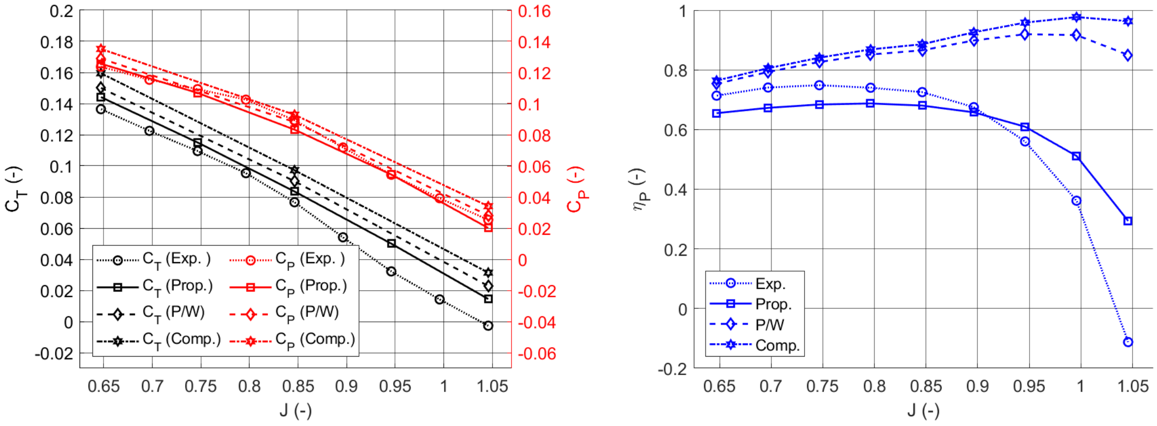

(c) Thrust and power coefficients.

(d) Propeller efficiency.

FIGURE 7.17 – Comparison between experiments, the simulations of the isolated propeller, propeller-wing model and complete geometry for the conventional layout. The simulation results in subfigures (a) and (b) include viscous and compressibility corrections, whereas (c) and (d) do not.

To investigate the possible causes in the performance difference observed between the complete geometry and propeller-wing model, the time history and local load distribution will be analyzed, starting the time history shown in Figure 7.18. It can be seen that for the two different advance ratios considered, the time histories of the complete models are quite different: for $J = 0.647$, there appear to be two oscillation frequencies present, corresponding to the rotation frequency

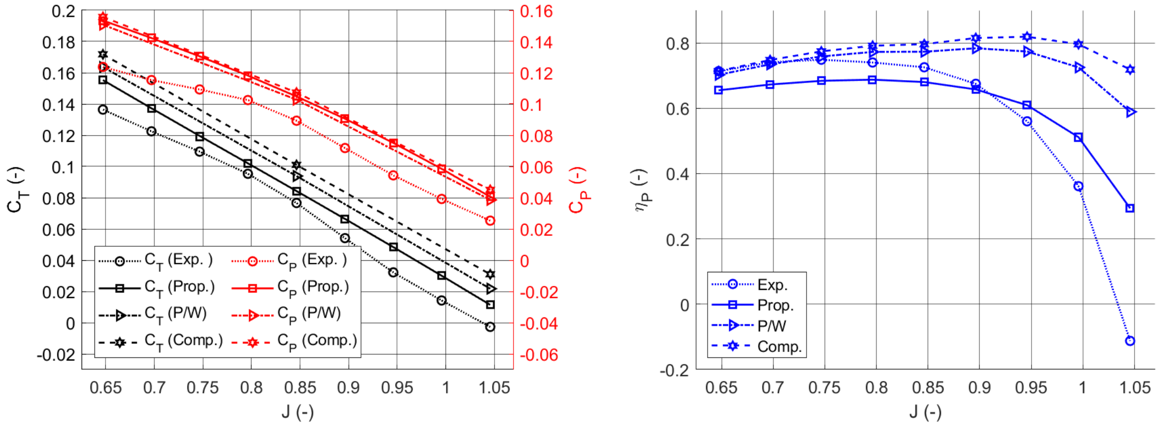

(a) Thrust and power coefficients.

(b) Propeller efficiency.

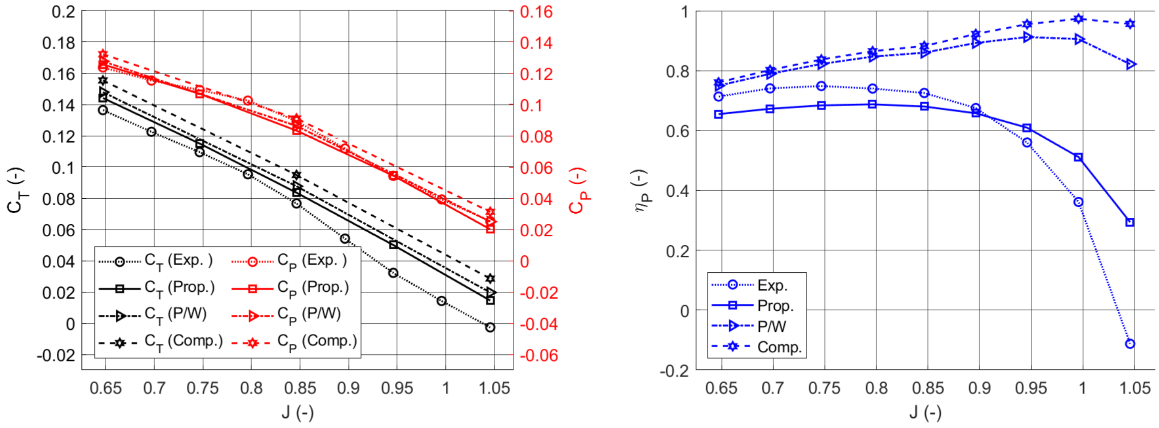

(c) Thrust and power coefficients.

(d) Propeller efficiency.

FIGURE 7.18 – Comparison between experiments, the simulations of the isolated propeller, propeller-wing model and complete geometry for the tip-mounted layout. The simulation results in subfigures (a) and (b) include viscous and compressibility corrections, whereas (c) and (d) do not.

and four times the rotation frequency, whereas for the propeller-wing model, only the latter frequency could be observed. On the other hand, for $J = 1.046$, it can be seen that the load history for the complete geometry does not appear to have any particularly consistent oscillation in the loading, though this could be observed for the propeller-wing model as well. Strangely, it seems that the complete model has not quite reached a steady state yet, as evidenced by the general downward trend of the thrust coefficient, which is rather puzzling, as for the isolated propeller and propeller-wing geometries, it can be seen that a quasi-steady state is reached.

In addition to the time history, the load distribution was analyzed as well, shown in Figure 7.20. It can be seen that load distribution has the same shape for all geometries, with one very clear difference: from the blade root up to approximately $r/R = 0.4$, the local thrust is greater for the complete geometry compared to the other cases for all advance ratios. Interestingly, at the blade root, the same sectional thrust is obtained independent of advance ratio for the complete geometry. While (VELDHUIS, 2004) pointed out that aerodynamic interference between the propeller and nacelle could result in a slight increase in propeller axial velocity, and therefore thrust, this effect is very small. In this case, it is more likely that the distorted flow field due to the spinner is the cause of the thrust increase near the root, as it is already modeled incorrectly

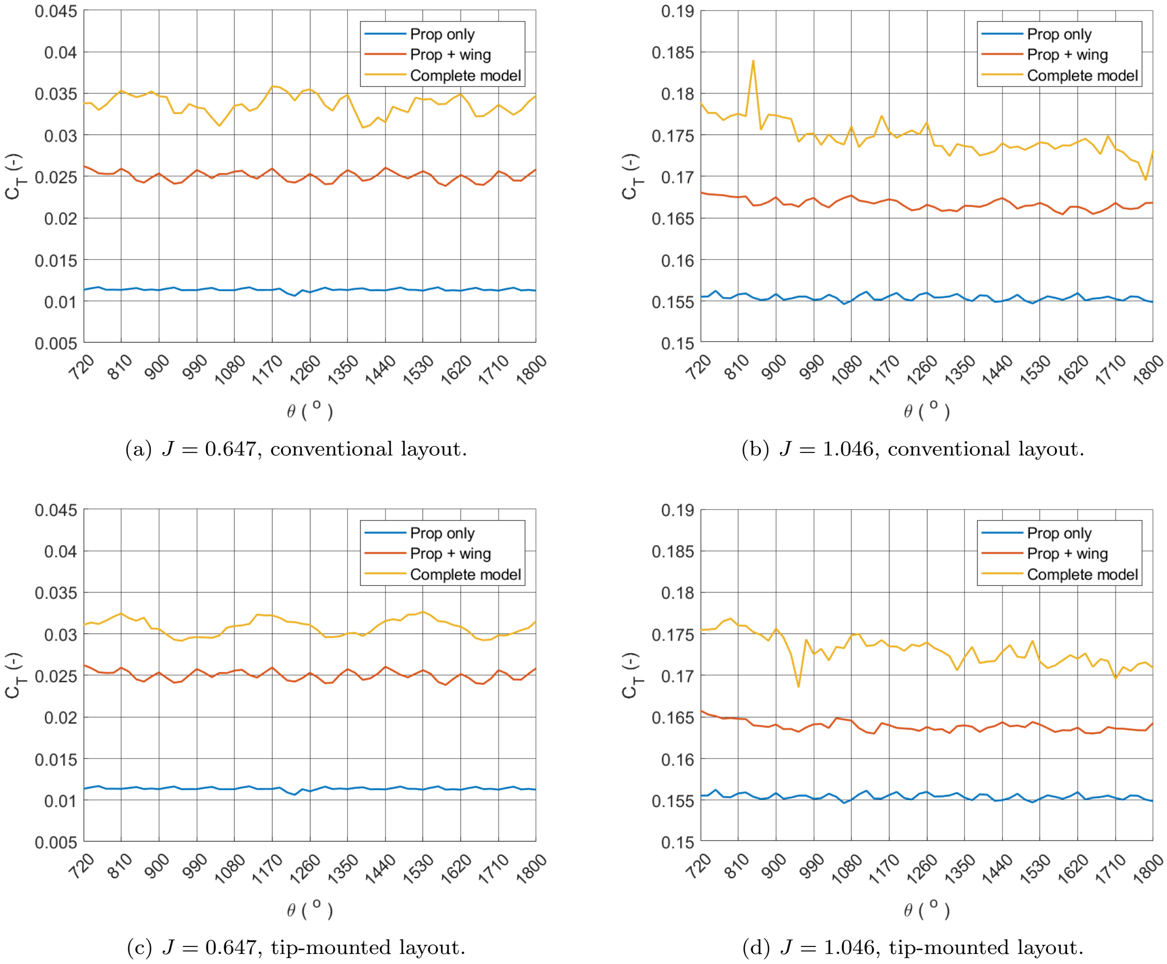

(a) $J = 0.647$, conventional layout.

(b) $J = 1.046$, conventional layout.

(c) $J = 0.647$, tip-mounted layout.

(d) $J = 1.046$, tip-mounted layout.

FIGURE 7.19 – Time history of the thrust coefficient. Results shown for the last three rotations.

as a stationary part and it has been observed that placing the blade root closer to the spinner yielded extremely large pressure gradients near the root. Thus, it is very likely that the thrust increase observed at the root in Figure 7.20 is an artifact of the numerical solution. Even if a the observed behavior is physically correct, it is still unlikely that a thrust increase of this magnitude would occur.

An angle of attack sweep was performed for the full geometry only for $J = 1.0$, as it has already been shown that the simulation results for $J = 0.7$ are inaccurate. For the complete geometry, the simulations became unstable at lower angles of attack than the propeller-wing model, hence little data is available. In Figure 7.21, it can be seen that for the angles tested, the thrust coefficient for the full geometry is greater compared to the other cases. However, the trend in the thrust coefficient for increasing angles of attack is completely wrong for the full geometry, as it can be seen that it either remains mostly constant (figures 7.21b and 7.21d) or even decreases for increasing angles of attack (Figure 7.21a. The only exception is the trend seen in Figure 7.21c, where the thrust coefficient does increase with increasing angle of attack, though it still appears that compared to the other simulations and experiments, that this increase is lower than it should be. To find a possible explanation for the unexpected trends in the thrust coefficient seen in Figure 7.21, the radial load distribution at $\alpha = 5.8°$ will be investigated, which is shown

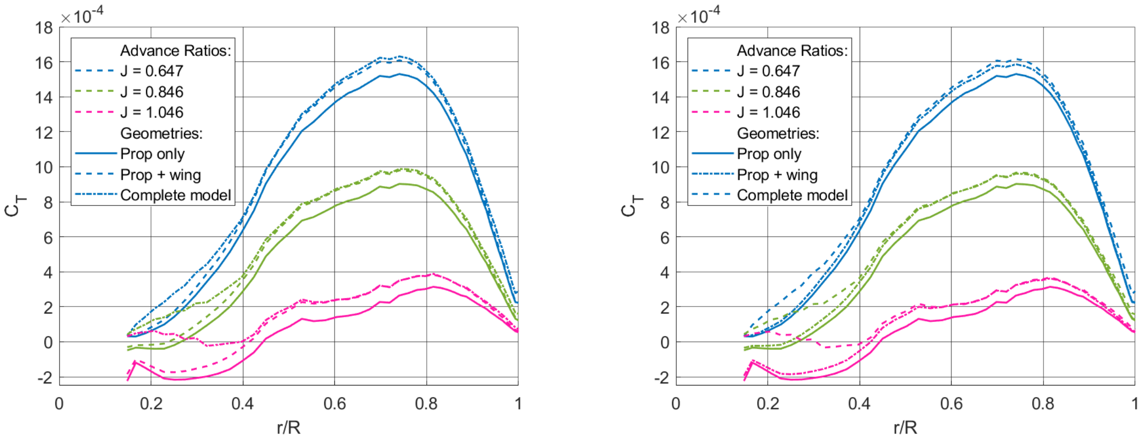

(a) Conventional layout.

(b) Tip-mounted layout.

FIGURE 7.20 – Radial thrust distribution for a single blade for all advance ratios considered for both configurations. Results are including viscous and compressibility correction.

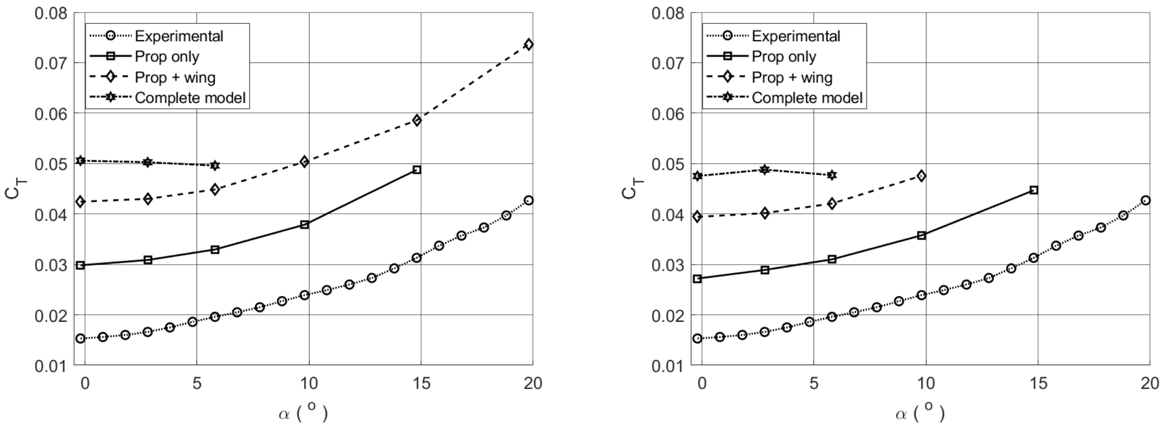

(a) Conventional layout, viscous and compressible.

(b) Conventional layout, inviscid and incompressible.

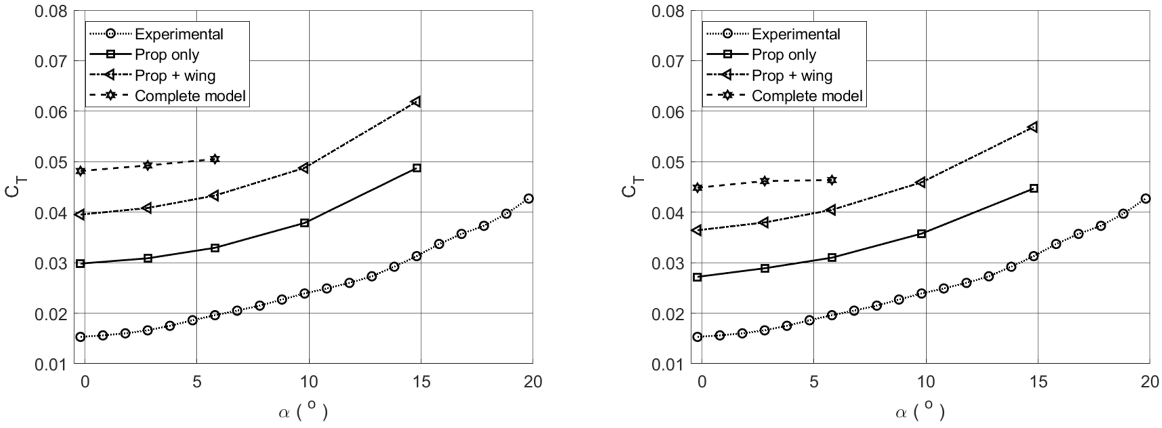

(c) Tip-mounted layout, viscous and compressible.

(d) Tip-mounted layout, inviscid and incompressible.

FIGURE 7.21 – Angle of attack sweep results for the experiments, and the simulations of the isolated propeller, propeller-wing model and complete geometry for $J = 1.0$.

in Figure 7.22. For the complete geometry, the increased thrust at the blade root up to $r/R = 0.4$ persists for non-zero angles as well. For $0.4 < r/R < 0.5$ and $r/R > 0.9$, it can be seen that there is essentially no difference between the full geometry and the propeller-wing model, but for the region in-between, the load is greater for the propeller-wing model compared to the full geometry, especially for the conventional layout. Combined with the load distribution for $\alpha = -0.2^\circ$ shown in Figure 7.20, it seem that for the complete geometry, the increase in thrust near the root is balanced out by a reduction in thrust around the middle section of the blade.

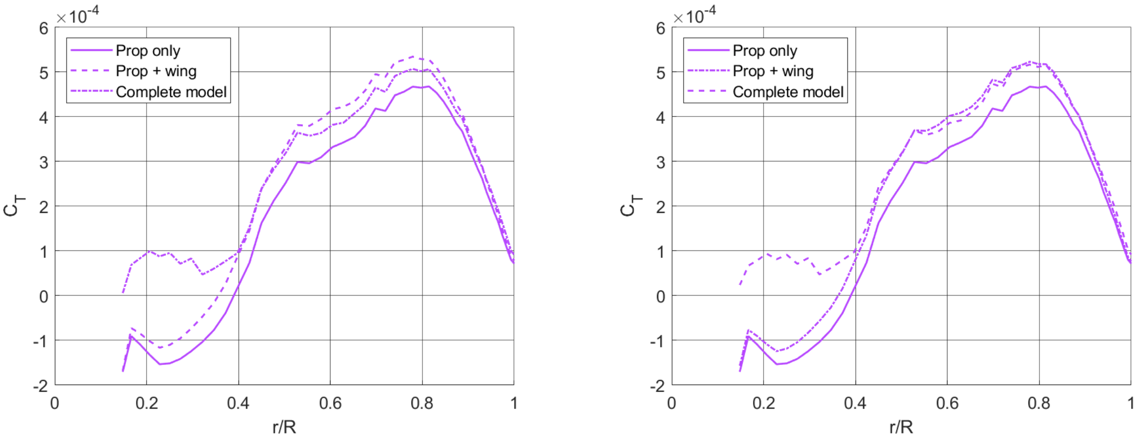

(a) Conventional layout.

(b) Tip-mounted layout.

FIGURE 7.22 – Radial thrust distribution for a single blade under for $J = 1.0$ and $\alpha = 5.8^\circ$. All results include viscous and compressibility correction.

The blade load over a full rotation is shown for the conventional layout in Figure 7.23 and for the tip-mounted layout in Figure 7.24. However, as the overall behavior of both cases is rather similar, they will not be discussed separately. Unsurprisingly, it can be seen that at the $0.25r/R$ station, the thrust level is greater for the complete model than the other two geometries for the whole rotation. However, for the other stations, there seems to be little difference in the load magnitude between the full geometry and propeller-wing models. Additionally, it can be seen that in the full geometry, there seems to be an inexplicable lag present in the thrust of approximately $\theta \approx 45^\circ$ compared to the other geometries.

As the results for the lift distribution are of similar quality to those shown in Section 7.3, these will not be discussed in detail and can be found in appendix F.

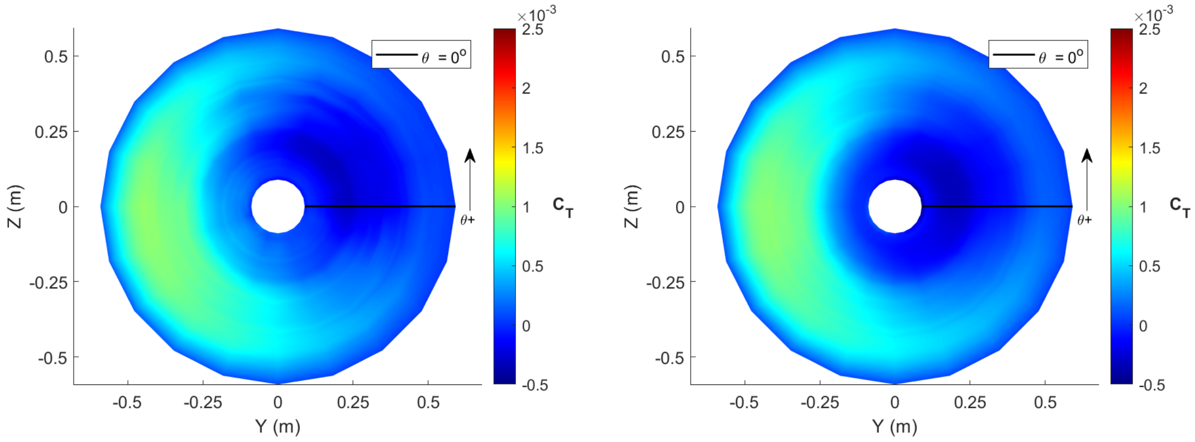

(a) Complete geometry.

(b) Propeller-wing model.

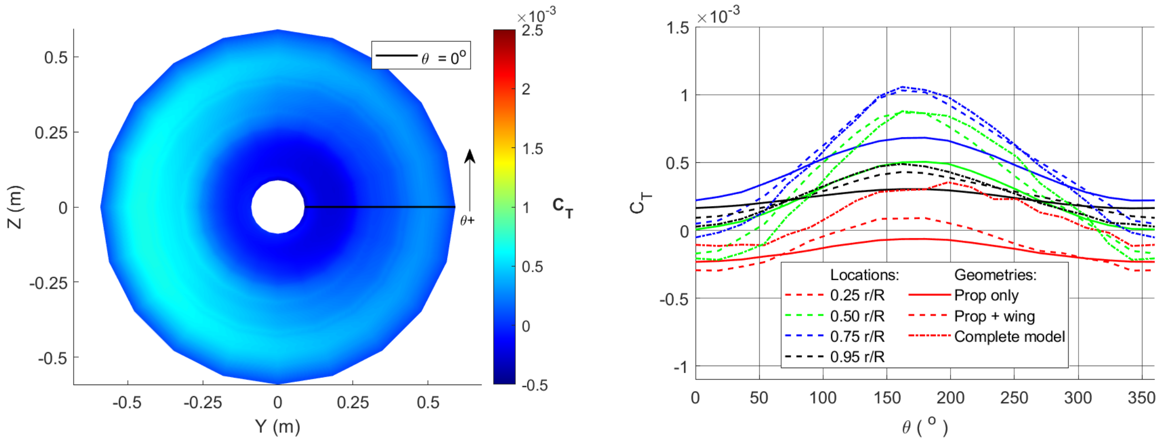

(c) Isolated propeller.

(d) Thrust evolution for four radial stations.

FIGURE 7.23 – Radial thrust distribution comparison between the isolated propeller, propeller-wing model and complete geometry in the conventional layout, operating at $J = 1.0$ and $\alpha = 5.8°$. Results shown include viscous and compressibility correction.

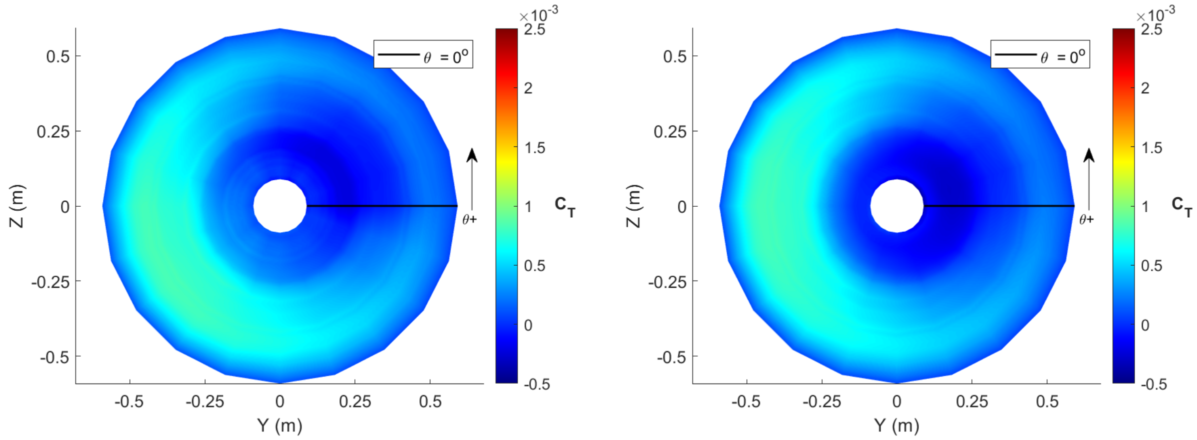

(a) Complete geometry.

(b) Propeller-wing model.

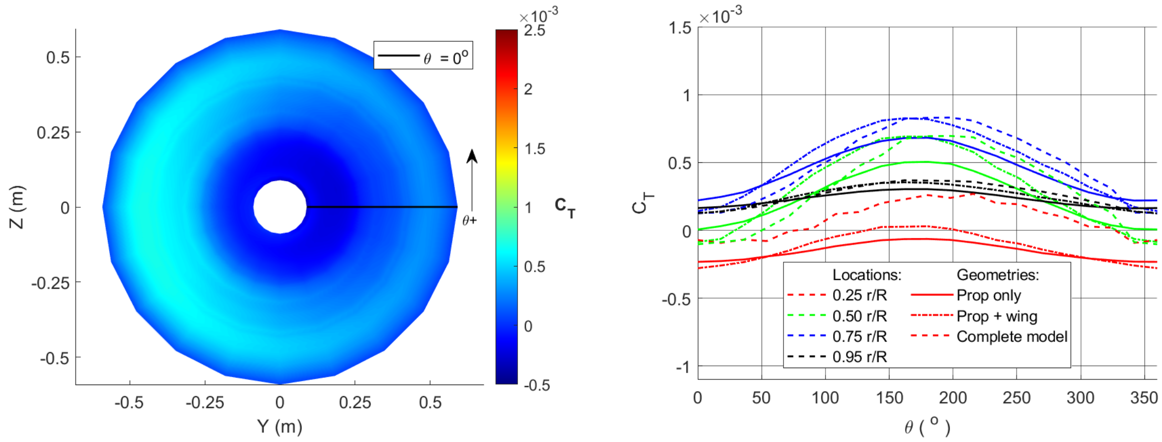

(c) Isolated propeller.

(d) Thrust evolution for four radial stations.

FIGURE 7.24 – Radial thrust distribution comparison between the isolated propeller, propeller-wing model and complete geometry in the tip-mounted layout, operating at $J = 1.0$ and $\alpha = 5.8°$. Results shown include viscous and compressibility correction.

8 Conclusions, Recommendations and Discussion

8.1 Conclusions

Throughout this research, it became increasingly apparent that the VSPAero panel method is not yet suitable for modeling propeller-wing interference effects, despite suggestions from literature to the contrary. As most studies using VSPAero used the VLM solver, rather than the panel mode, it may be that the VLM mode in VSPAero is more mature. Another possibility that cannot be ruled out is that the methodology of this research is flawed and that the main in propeller-wing aerodynamic interference should have been captured with VSPAero, as historically similar panel methods have been employed successfully.

A great hurdle during this research was the accessibility of knowledge regarding the solution process of governing equations and the implementation in VSPAero specifically. While some limited information was available, it was all too often either lacking in detail, only applicable to older versions of OpenVSP, or not verifiable, which meant that a lot of details regarding the implementation of the solver had to be obtained by scouring through the source code. This lack of detailed information is affecting many open source flow solvers, especially those with a high update frequency such as OpenVSP. In the end, the limited documentation in combination with a review of the source code yielded the description of the VSPAero solver shown in this report. The capabilities of VSPAero were established by means of a grid sensitivity study and a small series of verification tests. The grid sensitivity study showed that the default simulation settings in VSPAero are not adequate if a consistent numerical solution process is desired. In particular, it was observed that panel clustering near high gradients, more wake nodes, more wake iterations and a larger far-field distance were required to obtain consistent error reductions.
For unsteady simulations it was observed that the differences between simulations would decrease for increasingly finer timesteps, though with diminishing returns. For the finest temporal resolution considered during the grid sensitivity study, it became apparent that the solution started to exhibit oscillatory behavior, which was clearly an artifact of the numerical solution process. Furthermore, no truly timestep-independent solution could be obtained with VSPAero, likely due to the specific implementation of the wake shedding. In addition to quantifying the numerical error during the grid sensitivity study, the simulation time was tracked as well. It was found that the simulation time would grow proportional to approximately $\mathcal{O}(n^{1.5})$ with either

the panel or timestep count. In the end, a set of settings was obtained, which attempted to strike a balance between simulation accuracy and required computation time.

During the grid sensitivity study and verification process, the limitations of VSPAero which were not directly related to the assumptions taken for the governing equations became apparent. A clear weakness of the solver seems to be the wake calculation process: firstly, comparisons with XFoil showed an apparent issue with the implementation of the Kutta condition in VSPAero, as the flow behavior near both leading- and trailing-edge stagnation points physically questionable. Secondly, the solver is not particularly robust, as it was found to be easy to create a simulation that would cause ‘exploding’ wakes. Thirdly, it was found that at the points where a wake would intersect lifting geometries, physically unrealistic load fluctuations in time would occur, giving an indication that (strong) wake vortices near panel collocation points could potentially spoil the result. Another difficulty was found to be related to the paneling of the tips of lifting surfaces, as it seemed that having too many small panels in this region would often cause catastrophic errors without a clear cause for this behavior. Lastly, due to lacking the capabilities to model a rotating spinner, this part of the geometry resulted in some difficulties during the simulations, requiring the spinner to be shrunk as a result.

Despite the limitations of VSPAero, there are still some merits to using the software for relatively simple analyses. For isolated wings or propellers, it was found that generally, results of acceptable accuracy could be obtained, assuming appropriate settings are used. The predicted lift slope for an isolated wing showed reasonable agreement with XFoil and experimental measurements, up to the stall point. For an isolated propeller, it was found that the efficiency showed decent agreements with experimental measurements, though VSPAero overpredicted both the thrust and power coefficients compared to the experiments. For the cases where a propeller and wing were simulated together, the propeller results seemed reasonable, while the lift distribution on the wing was very questionable in most cases. Since the aerodynamic interference is a two-way interaction, this cast significant doubt on the validity of the propeller results in these cases. Thus, if it is desirable to capture the aerodynamic interference effects, it appears that VSPAero is not yet an adequate tool. For simpler cases, especially for those without interactions between lifting bodies and wakes, VSPAero can provide a reasonably accurate flow field solution for a preliminary design phase. In the end, the main strength of the OpenVSP suite is the fact it is possible to relatively quickly and easily create a geometry, and not necessarily the quality of the included solvers.

8.2 Recommendations

The recommendations will be split into two categories: recommendations for using OpenVSP and VSPAero from a user perspective and recommendations for the development team to improve their program and user experience.

Recommendations for using OpenVSP and VSPAero

- Chordwise panel count should be prioritized over spanwise panel count to improve the accuracy of the pressure integration.
- Increasing the amount of wake nodes and wake iterations, and increasing the far-field distance compared to the default settings is recommended to increase the quality of the results relatively efficiently, provided no wakes intersect a lifting body.
- The default time integration setting leading to $\Delta\theta_t = 18^\circ$ was found to strike a good balance between geometric accuracy of the shed wake strips and the quality of the results for the cases tested.
- Ensure that the panels at the tips of lifting surfaces are not too small and are not slivers, as it was observed that the geometry and meshing of tips can result in significantly different results, or even prevent the simulation from working.
- If it is absolutely necessary to include a stall correction, the 2D CLmax model could provide a crude approximation for simple wings. The Carlson Pressure Correlation model is not recommended.
- OpenVSP is recommended for the design of the geometry and the export of the model or mesh.

Recommendations for the OpenVSP Development Team

- Provide a reference document containing the governing equations, the solution algorithms and their implementation.
- Implement a method for simulating rotating spinners, which could for example be achieved by adding the propeller rotation code for a pod element.
- Add the advanced blade controls available for propellers to wings, to make it easier to create non-trapezoidal wings.
- Make it possible to completely disable the friction drag and compressibility corrections to run the solver in a pure potential flow mode.
- Make the raw pressure data for each panel available to the user.
- Investigate and resolve the root cause of the possible bug in the tip paneling code.
- Regarding the implementation of the trailing wakes, a few different recommendations can be made:
    1. Verify the implementation of the Kutta condition, as it seems that the flow accelerates near the rear stagnation point.
    2. Add a viscous vortex modification to the wakes to prevent massive pressure fluctuations whenever wakes intersect solid bodies.

3. Consider implementing prescribed (analytical) wakes, similar to the method described by (HESS; VALAREZO, 1985), or use the same wake shedding model as for the actuator disks to alleviate wake instabilities and potentially reduce computation time.
4. Investigate the convergence of the unsteady results for different ratios of trailing edge panels and shed vortex panel lengths to verify whether this is the cause of the observed timestep dependency of the unsteady solutions and investigate shed wake segments with streamwise linear vorticity distributions to alleviate this timestep dependency.

8.3 Discussion

The performance of VSPAero raises the question as to why the results are as poor as shown in this research. Unfortunately, no fully satisfactory answer can be provided to this question. Due to a lack of any detailed theoretical description, it is only possible for us to speculate based on the source code and to reverse engineer the choices made in the model and its implementation as best as possible.

Assuming that the theoretical description of VSPAero shown in Section 3.2 is correct, several flaws can be pointed out in the solver: In Section 3.2.1, the difference in enforcing the no-penetration condition with the Dirichlet and Neumann boundary condition is discussed. While these are similar, and even equivalent in certain cases, not all formulations of these boundary conditions result in a well-posed problem. In VSPAero, a Neumann boundary condition is used in combination with constant-strength vortex loops and no source elements. For this configuration, (MASKEW, 1982) pointed out that an ill-posed problem is obtained, affecting the solution near the trailing edge. To be exact, (MASKEW, 1979) showed that for two vortex loops placed on close parallel panels, such as near the trailing edge, the average vortex strength of the two panels has diminishing influence. It was pointed out that this type of ill-conditioning of the boundary conditions is particularly bad for iterative solution schemes. While (MASKEW, 1979) acknowledges that this exact situation rarely occurs in practice, it is approached for sharp, small opening angle trailing edges. VSPAero requires sharp trailing edges in panel mode and iteratively solves for the strengths of the vortex loops, thus it is suspected that the odd behavior seen near the trailing edge is caused by the ill-posedness of the problem.

The vortex loop agglomeration scheme discussed briefly in Section 3.2.4, referred to as a multipole method by the developers (KINNEY, 2020) (KINNEY, 2023), only takes an area-weighted average of the vortex strengths when merging vortex loops. It is unclear why exactly this scheme is referred to as a multipole method, as no polynomial expansion of the vortex integral kernels seems to be made. In VSPAero, it is unclear what the order of the error introduced for every agglomeration step is. This could be a possible cause for the poor convergence behavior.

The wake calculation was discussed in Section 3.2.5. It was suggested by (HSIN, 1990) and (KINNAS; HSIN, 1992) that the choice of constant-strength vortex segments causes the timestep dependency observed in the results and that a streamwise higher order vorticity distribution for the wake panels attached to the trailing edge could reduce this dependency significantly.

It appears that in the VSPAero codebase, several odd choices have been made for numerical schemes. Since VSPAero originally only featured the VLM mode, it is suspected that the panel mode was built upon the same code as the VLM mode, causing ill-conditioning in the panel mode as a result. This could be the underlying reason why in most documented use-cases of VSPAero, the VLM mode is used instead of the panel mode, as the former produces better results by the virtue of being based on a well-established theoretical foundation.

Bibliography

ABE, H.; KAWAMURA, H.; MATSUO, Y. Direct numerical simulation of a fully developed turbulent channel flow with respect to the reynolds number dependence. **Journal of Fluids Engineering**, v. 123, n. 2, p. 382–393, 2001. Available at: https://doi.org/10.1115/1.1366680.

AIRBUS. **Vahana - Our Single-Seat eVTOL Demonstrator**. 2024. Www.airbus.com. Accessed: 24/09/2024. Available at: https://www.airbus.com/en/innovation/energy-transition/hybrid-and-electric-flight/cityairbus-nextgen/vahana.

ANDERSON, J. D. **Introduction to Flight**. 8th. ed. New York: McGraw-Hill, 2016. ISBN 978-981-4636-18-6.

BUTCHER, J. **Numerical Methods for Ordinary Differential Equations**. 2nd. ed. Chichester, England: Wiley, 2003. ISBN 0-471-96758-0.

CELLSIUS. **Project e-Sling**. 2024. Accessed: 24/09/2024. Available at: https://cellsius.aero/en_gb/project-esling/.

DRELA, M. **Xfoil, Version 6.99**. December 2013. Accessed: 10/10/2024. Available at: https://web.mit.edu/drela/Public/web/xfoil/.

DRELA, M. **Flight Vehicle Aerodynamics**. Cambridge, Massachusetts/London, England: The MIT Press, 2014. ISBN 978-0-262-52644-9.

ERICKSON, L. L. **Panel Methods - An Introduction**. [*S.l.*], 1990. Accessed: 2024-11-02. Available at: https://ntrs.nasa.gov/api/citations/19910009745/downloads/19910009745.pdf.

EVIATION. **Alice - The All-Electric Game Changer**. 2024. Accessed: 24/09/2024. Available at: https://www.eviation.com/aircraft/.

FEI, X.; GERMAN, B. J.; PATTERSON, M. D. **Exploring the Effects of Installation Geometry in High-Lift Propeller Systems**. [*S.l.*], 2018. Available at: https://ntrs.nasa.gov/api/citations/20190000432/downloads/20190000432.pdf.

FERNÁNDEZ, M. B. **CFD Tool VSPAERO: Actuator Disk and Flow Visualization**. Dissertation (Master's thesis) — HAW Hamburg, Hamburg, Germany, October 2023. Available at: https://doi.org/10.7910/DVN/HFCSQZ.

GLOUDEMANS, J. R.; DAVIS, P. C.; GELHAUSEN, P. A. A rapid geometry modeler for conceptual aircraft. *In*: **34th Aerospace Sciences Meeting and Exhibit**. **Proceedings** [...]. Reno, NV: American Institute of Aeronautics and Astronautics, 1996. AIAA 1996-52.

GONÇALVES, L. E. B. **Análise Aerodinâmica dos Efeitos de Interação Hélice-Asa em Veículos Aéreos Não Tripulados**. São José dos Campos, São Paulo state, Brazil: [*s.n.*], October 1 2024. Final report regarding educational research activities.

HAGMEIJER, R. **Numerical Methods in Mechanical Engineering - Part I: Continuum Mechanics, Related Equations and Discretization Methods**. June 2008. Lecture notes for Numerical Methods in Mechanical Engineering (115771) - University of Twente.

HAHN, A. Vehicle sketch pad: Parametric geometry for conceptual aircraft design. *In*: **48th AIAA Aerospace Sciences Meeting**. **Proceedings** [...]. Orlando, FL: American Institute of Aeronautics and Astronautics, 2010. AIAA 2010-657.

HASS, J.; HEIL, C.; WEIR, M. D.; THOMAS, G. B. **Thomas' Calculus**. 14th. ed. [United States]: Pearson, 2018. ISBN 9780134438986.

HESS, J. L.; VALAREZO, W. O. Calculation of steady flow about propellers using a surface panel method. **Journal of Propulsion**, v. 1, n. 6, p. 470–476, November 1985. Available at: https://doi.org/10.2514/3.22830.

HOEIJMAKERS, H. W. M. **Panel Methods for Aerodynamic Analysis and Design**. Amsterdam, The Netherlands, 1992.

HOEIJMAKERS, H. W. M. **Gasdynamics - Lecture Notes - Part I**. 2022. Lecture notes for Gasdynamics, course code: 115434 - University of Twente. Master Course.

HSIN, C.-Y. **Development and Analysis of Panel Methods for Propellers in Unsteady Flow**. Thesis (PhD Thesis) — Massachusetts Institute of Technology, Boston, Massachusetts, USA, September 1990.

JOHNSON, W. **Helicopter Theory**. Dover edition. New York, USA: Dover Publications Inc., 1980. ISBN 0-486-68230-7.

KATZ, J.; PLOTKIN, A. **Low Speed Aerodynamics**. Second edition. New York, USA: Cambridge University Press, 2001. ISBN 978-0-521-66219-2.

KINNAS, S. A.; HSIN, C.-Y. Boundary element method for the analysis of the unsteady flow around extreme propeller geometries. **AIAA Journal**, v. 30, n. 3, p. 688–696, March 1992. Available at: https://doi.org/10.2514/3.10973.

KINNEY, D. **2020 VSP WS: VSPAERO Theory, Validation, and Features**. December 17 2020. YouTube Video. Accessed: 2024-08-15. Available at: https://www.youtube.com/watch?v=-zQEmmrb6ck.

KINNEY, D. **VSPAERO Theory**. August 2023. Presentation Slides. Presented at The 2023 OpenVSP Workshop, Wright Brothers Institute (WBI), Dayton, Ohio. Accessed: 2024-08-15. Available at: https://openvsp.org/wiki/lib/exe/fetch.php?media=workshop23:2023_workshop_-_theory.pdf.

KUETHE, A. M.; SCHETZER, J. D. **Foundations of Aerodynamics**. 2nd. ed. [*S.l.*]: John Wiley & Sons, 1959. ISBN 0-471-50952-3.

KUROPATWA, M.; KOZUBA, J.; WEGRZYN, N. Turbofan engines efficiency, historical trends, and future prediction – a review. **Safety & Defense**, v. 8, n. 2, p. 82–90, December 2022. Available at: https://doi.org/10.37105/sd.186.

LAWLESS, A.; LEWIS, G.; NORTON, B.; HRELOV, D.; ARNEY, S.; MINOR, J.; KIDMAN, D.; MOULDER, C.; STEVENS, C. **Flight Test Engineering Reference Handbook**. 3rd. ed. Lancaster, California, USA: Society of Flight Test Engineers, 2013. `https://society-of-flight-test-engineers.github.io/handbook-2013/index.html`.

LENOVO. **Thinkpad P51 User Guide**. 6th. ed. [*S.l.*], September 2018. Accessed: 12/09/2024. Available at: https://download.lenovo.com/pccbbs/mobiles_pdf/p51_ug_en.pdf.

LENOVO. **ThinkPad P16v Gen 2 User Guide**. Second edition. [*S.l.*], July 2024. Accessed: 30/09/2024. Available at: https://download.lenovo.com/pccbbs/mobiles_pdf/p16v_gen2_ug_en.pdf.

LILIUM. **The Lilium Jet**. 2024. Accessed: 24/09/2024. Available at: https://jet.lilium.com/.

LITHERLAND, B. **Modeling Best-Practices for VSPAERO**. October 2021. Slides presented at the 2021 OpenVSP Workshop. Accessed: 2024-09-05, NASA Langley Research Center. Available at: https://openvsp.org/wiki/lib/exe/fetch.php?media=workshop21:2021_vspws_-_modeling_best-practices_for_vspaero.pdf.

MACDONALD, R.; LITHERLAND, B.; GRAVETT, J. **Get the Latest OpenVSP from the Links Below**. 2024. `https://openvsp.org/download.php`. Accessed: 2024-06-24.

MARIËN, F. **Software Testing: VSPAERO**. 137 p. Dissertation (Mestrado) — Hamburg University of Applied Sciences, Hamburg, 2021. URN: `https://nbn-resolving.org/urn:nbn:de:gbv:18302-aero2021-07-16.018`.

MASKEW, B. **Modifications to the Potential Flow Code to Allow Part-Span, High-Life Devices and Close-Interference Calculations**. Moffett Field, California, USA, March 1979.

MASKEW, B. Prediction of subsonic aerodynamic characteristics: A case for low-order panel methods. **Journal of Aircraft**, v. 19, n. 2, p. 157–163, February 1982. Available at: https://doi.org/10.2514/3.57369.

MCDONALD, R. **OpenVSP**. June 2024. GitHub repository, version 3.39. Accessed: June 24, 2024. Available at: https://github.com/OpenVSP/OpenVSP.

MCDONALD, R.; LITHERLAND, B.; GRAVETT, J. **About OpenVSP**. January 2012. `https://openvsp.org/learn.shtml`. Accessed: 2024-08-26.

MCDONALD, R. A.; GLOUDEMANS, J. R. Open vehicle sketch pad: An open source parametric geometry and analysis tool for conceptual aircraft design. *In*: **AIAA SCITECH 2022 Forum**. **Proceedings** [...]. San Diego, CA: American Institute of Aeronautics and Astronautics, 2022. AIAA 2022-0004.

NASA. **X-57 Maxwell**. February 2024. Accessed: 24/09/2024. Available at: https://www.nasa.gov/wp-content/uploads/2020/10/afrc-fs-109-10-28-19.pdf?emrc=574ff8.

OpenVSP Google Group. **OpenVSP Discussion Forum**. 2024. `https://groups.google.com/g/openvsp`. Accessed: September 11, 2024.

PERDOLT, D.; THIELE, M.; MILZ, D.; MAY, M.; KUCHAR, R.; HORNUNG, M. Comparison of multi-fidelity rotor analysis tools for transitional and low speed flight regimes. *In*: **Deutscher Luft- und Raumfahrtkongress 2021**. **Proceedings** [...]. [*S.l.*]: Deutsche Gesellschaft für Luft- und Raumfahrt - Lilienthal-Oberth e.V., 2021. p. 1–13.

PIPISTREL. **Technical Data Velis Electro**. 2024. Accessed: 24/09/2024. Available at: https://www.pipistrel-aircraft.com/wp-content/uploads/2024/07/VelisElectro_2024.pdf.

PRESS, W. H.; TEUKOLSKY, S. A.; VETTERLING, W. T.; FLANNERY, B. P. **Numerical Recipes in C: The Art of Scientific Computing**. Second edition. New York, NY, USA: Cambridge University Press, 1992. 46–47 p. ISBN 0-521-43108-5.

REDDY, P. **Unconventional Swept Rotor Design using Open Vehicle Sketch Pad (OpenVSP)**. Dissertation (Mestrado) — Virginia Polytechnic Institute and State University, May 2023. Http://hdl.handle.net/10919/115574, Master's thesis.

RUBBERT, P.; SAARIS, G. Review and evaluation of a three-dimensional lifting potential flow computational method for arbitrary configurations. *In*: **Proceedings of the 10th Aerospace Sciences Meeting**. **Proceedings** [...]. San Diego, California, USA: AIAA, 1972. p. 1–15. Available at: https://doi.org/10.2514/6.1972-188.

SAAD, Y.; SCHULTZ, M. GMRES: A Generalized Minimal Residual Algorithm for Solving Nonsymmetric Linear Systems. **SIAM Journal on Scientific and Statistical Computing**, v. 7, n. 3, p. 856–869, http://dx.doi.org/10.1137/0907058, 1986.

SCHIPHOLT, G. J.; VOOGT, N.; VAN HENGST, J. Investigation of methods for modeling propeller-induced flow fields. *In*: **31st Aerospace Sciences Meeting & Exhibit**. **Proceedings** [...]. Reno, Nevada, USA: AIAA, 1993. (AIAA report, 93-0874), p. 1–12.

SCHLICHTING, H.; GERSTEN, K. **Boundary Layer Theory**. 9th. ed. Berlin, Heidelberg: Springer, 2017. ISBN 978-3-662-52919-5.

SEO, Y.; HONG, Y.; YEE, K. Numerical investigation of wing–multiple propeller aerodynamic interaction using actuator disk method. **International Journal of Aeronautical and Space Sciences**, v. 23, p. 805–822, abr. 2022. Available at: https://doi.org/10.1007/s42405-022-00446-7.

SHERIDAN, C. N.; PHAM, D. D.; WHITESIDE, S. Evaluation of vspaero analysis capabilities for conceptual design of aircraft with propeller-blown wings. *In*: **Proceedings of the AIAA AVIATION 2021 Forum**. **Proceedings** [...]. American Institute of Aeronautics and Astronautics, 2021. p. 1–21. Available at: https://doi.org/10.2514/6.2021-2510.

SINNIGE, T.; VAN ARNHEM, N.; STOKKERMANS, T.; DE VRIES, R.; CORTE, B. D. **TUD Data Sets on Propeller Integration**. June 2020. Presentation, Delft, The Netherlands. Accessed: 30/09/2024. Available at: https://filelist.tudelft.nl/Websections-/Propeller%20Aerodynamics/TUD_propIntegrationResearch_Overview.pdf.

SINNIGE, T.; VAN ARNHEM, N.; STOKKERMANS, T. C. A.; EITELBERG, G.; VELDHUIS, L. L. M. Wingtip-mounted propellers: Aerodynamic analysis of interaction effects and comparison with conventional layout. **Journal of Aircraft**, v. 56, n. 1, p. 295–312, 2019. Available at: https://doi.org/10.2514/1.C034978.

SINNIGE, T.; VELDHUIS, L.; EITELBERG, G.; RAO, A. G. **Propeller models**. June 2020. Accessed: 30/09/2024. Available at: https://www.tudelft.nl/lr/organisatie/afdelingen/flow-physics-and-technology/flight-performance-propulsion/flight-performance/propeller-aerodynamics/facilities/propeller-models.

SINNIGE, T.; VRIES, R. de; CORTE, B. D.; AVALLONE, F.; RAGNI, D.; EITELBERG, G.; VELDHUIS, L. L. M. Unsteady pylon loading caused by propeller-slipstream impingement for tip-mounted propellers. **Journal of Aircraft**, v. 55, n. 4, p. 1605–1618, 2018. Available at: https://doi.org/10.2514/1.C034696.

STOKKERMANS, T. C. A.; VAN ARNHEM, N.; SINNIGE, T.; VELDHUIS, L. L. M. Validation and comparison of rans propeller modeling methods for tip-mounted applications. **AIAA Journal**, v. 57, n. 2, p. 566–580, 2019. Available at: https://doi.org/10.2514/1.J057398.

sUAS News. Vahana has come to an end. but a new chapter at airbus has just begun. **sUAS News**, accessed: 24/09/2024, December 2019. Available at: https://www.suasnews.com/2019-/12/vahana-has-come-to-an-end-but-a-new-chapter-at-airbus-has-just-begun/.

THOMPSON, J. F.; WARSI, Z. U. A.; MASTIN, C. W. **Numerical Grid Generation**. New York: North-Holland, 1985. 307–308 p.

TIMMER, W. A. Two-dimensional low-reynolds number wind tunnel results for airfoil naca 0018. **Wind Engineering**, v. 32, n. 6, p. 525–537, 2008. Available at: https://www.researchgate.net/publication/27342064_Two-Dimensional_Low-Reynolds_Number_Wind_Tunnel_Results_for_Airfoil_NACA_0018.

VALAREZO, W. O. Surface panel method for installed multiple rotor flows. **Journal of Aircraft**, v. 28, n. 8, p. 496–501, August 1991. Available at: https://doi.org/10.2514/3.46054.

VALAREZO, W. O.; CHIN, V. D. Method for the prediction of wing maximum lift. **Journal of Aircraft**, v. 31, n. 1, p. 103–109, https://doi.org/10.2514/3.46461, January 1994.

VAN DER WEIDE, E. T. A. **Discretization Schemes for Hyperbolic Partial Differential Equations**. 2021. Lecture notes for Computational Fluid Dynamics (191154731) - University of Twente.

VAN GARREL, A. **Development of a Wind Turbine Aerodynamics Simulation Module**. The Netherlands, August 2003. Accessed: April 22, 2024.

VAN GARREL, A. **Multilevel Panel Method for Wind Turbine Rotor Flow Simulations**. Thesis (Doutorado) — University of Twente, Enschede, The Netherlands, December 14 2016. Http://dx.doi.org/10.3990/1.9789036542241.

VELDHUIS, L. L. M. Review of propeller-wing aerodynamic interference. *In*: **24th International Congress of the Aeronautical Sciences**. **Proceedings** [...]. [*S.l.: s.n.*], 2004. Available at: https://www.icas.org/ICAS_ARCHIVE/ICAS2004/PAPERS/065.PDF.

VELDHUIS, L. L. M. **Propeller Wing Aerodynamic Interference**. Thesis (PhD Thesis) — Technische Universiteit Delft, Delft, The Netherlands, June 2005. Available at: https://repository.tudelft.nl/file/File_126267d1-d9f1-464b-acb8-d37f2b1cc159?preview=1.

VENNER, C. H.; LUBRECHT, A. A. (Ed.). **Multi-Level Methods in Lubrication**. 1st. ed. [*S.l.*]: Elsevier, 2000. (Tribology Series, v. 37). ISBN 9780080537092.

VERHOEFF, A. J. J. **Aerodynamics of Wind Turbine Rotors**. Thesis (PhD Thesis) — Universiteit Twente, Enschede, The Netherlands, December 1 2005.

VINOKUR, M. On one-dimensional stretching functions for finite difference calculations. **Journal of Computational Physics**, v. 50, p. 215–234, 1983.

Appendix A - Rewriting the Navier-Stokes Equations to the Potential Flow Equation.

The Navier-Stokes equations, shown in equations A.1-A.3, are the governing equations describing the flow of a fluid, as long as the continuity assumption is true (HOEIJMAKERS, 2022). However, it is nearly impossible to solve them directly due to the closure problem, as there are seven unknown terms and only five equations, making the system underdetermined. Even if the closure problem is resolved by, for example, adding two equations of state to have an equal number of equations and unknowns, it would still be rather computationally expensive to solve the Navier-Stokes equations directly.

$$\frac{\partial \rho}{\partial t} + \nabla \cdot (\rho \vec{u}) = 0 \tag{A.1}$$

$$\frac{\partial}{\partial t}(\rho \vec{u}) + \nabla \cdot (\rho \vec{u}\vec{u}) = \rho \vec{f} - \nabla p + \nabla \cdot \bar{\bar{\tau}} \tag{A.2}$$

$$\frac{\partial}{\partial t}(\rho E) + \nabla \cdot (\rho \vec{u} E) = \rho \vec{u} \cdot \vec{f} - \nabla \cdot (p \vec{u}) + \nabla \cdot (\bar{\bar{\tau}} \cdot \vec{u}) + \dot{Q} - \nabla \cdot \dot{\vec{q}} \tag{A.3}$$

Thankfully, the complete set of Navier-Stokes equations is seldom needed to have a flow field description of acceptable accuracy. In typical aerodynamics calculations, the relevant flow Reynold number is sufficiently high that the effects of viscosity are negligible in most of the flow field, with the exception of the boundary layer. If it would be assumed that the complete flow field is inviscid, the Navier-Stokes equations can be simplified into the Euler equations (HOEIJMAKERS, 2022):

$$\frac{\partial \rho}{\partial t} + \nabla \cdot (\rho \vec{u}) = 0 \tag{A.4}$$

$$\frac{\partial}{\partial t}(\rho \vec{u}) + \nabla \cdot (\rho \vec{u}\vec{u}) = \rho \vec{f} - \nabla p \tag{A.5}$$

$$\frac{\partial}{\partial t}(\rho E) + \nabla \cdot (\rho \vec{u} H) = \rho \vec{u} \cdot \vec{f} + \dot{Q} - \nabla \cdot \dot{\vec{q}} \tag{A.6}$$

While the Euler equations are simplified compared to the Navier-Stokes equations, there are still two additional equations required to close the problem and the Euler equations are still computationally expensive to solve. Therefore, it is possible to simplify the governing equations even further: In addition to assuming an inviscid flow, it is usually possible to assume that heat generation and transfer effects are negligible for aerodynamic calculations. The amount of heat generated or transferred is typically neglegible unless transonic or supersonic flow speeds are reached, hence the energy balance (equation A.6 can be neglected. Furthermore, if assuming that the flow is incompressible (ρ is assumed to be constant everywhere), irrotational and not subject to external forces, the Euler equations can be simplified even further to yield the following equations:

$$\nabla \cdot \vec{u} = 0 \tag{A.7}$$

$$\frac{\partial \vec{u}}{\partial t} + \frac{1}{2}\nabla(\vec{u} \cdot \vec{u}) = -\frac{1}{\rho}\nabla p \tag{A.8}$$

Equations A.7 and A.8 are known as the incompressiblility condition and the unsteady Bernoulli equation, respectively. To solve quation A.7, a velocity potential function of the following form is introduced (DRELA, 2014):

$$\vec{u} = \nabla \phi \tag{A.9}$$

Being able to describe a flow field in terms of a velocity potential has many benefits, which are outlined in section 3.2.

Appendix B - Definition of Dimensionless Numbers in Different Contexts

In the fluid dynamics field, it is very common to work with dimensionless numbers instead of variables with a physical dimension. This is very practical for a multitude of reasons: it reduces the problem down to the independent variables, allows for easier comparisons between different results, and allows for the identification of dominant and negligible contributions in problems. While these are all great benefits, there are cases where there exist different definitions for the same dimensionless number.

B.1 Thrust, Power and Torque Coefficients

When analyzing a propeller or rotor in VSPAero, the results for the global thrust, power and torque coefficients over time are scaled using the definition for propeller and rotors separately, however, for the radial load distribution, only the definition for rotors is used. Due to this omission, it is necessary to convert between the two conventions. Since this seemingly has not been documented yet, this report will provide the relations between the two conventions. In table B.1, the typical definitions for the thrust, power and torque coefficients used for propellers and rotors are listed. A clear distinction that is that the propeller coefficients are scaled using the propeller disk diameter and the rotation speed in rotations per minute, whereas the rotor coefficients are scaled using the rotor disk area and tip speed instead.

TABLE B.1 – Definitions for the typical performance coefficients used for propellers and (helicopter) rotors (LAWLESS *et al.*, 2013) (JOHNSON, 1980).

	Propeller	Rotor
C_T	$\frac{T}{\rho n^2 D^4}$	$\frac{T}{\rho A V_{tip}^2}$
C_P	$\frac{P}{\rho n^3 D^5}$	$\frac{P}{\rho A V_{tip}^3}$
C_Q	$\frac{Q}{\rho n^2 D^5}$	$\frac{Q}{\rho A R V_{tip}^2}$

To compute the conversion factors (C), the two different definitions will be divided and simplified. As an example, the calculation will be shown for the thrust coefficient, though all factors will be provided. As a starting point, the thrust coefficient of a propeller will be divided by the thrust coefficient of a rotor:

$$C_{T,prop}\,C_{T,rotor}^{-1} = C \tag{B.1}$$

$$\frac{T}{\rho n^2 D^4}\frac{\rho A V_{tip}^2}{T} = C \tag{B.2}$$

From equation B.2, The thrust and density can be canceled out, resulting in the following expression:

$$\frac{A V_{tip}^2}{n^2 D^4} = C \tag{B.3}$$

To simplify equation B.3 further, certain definition substitutions need to be made. First of all, the area of a rotor disk is related to the diameter by $A = \frac{\pi D^2}{4}$. Secondly, the tip velocity is defined as $V_{tip} = \Omega R$, which can be rewritten using $\Omega = 2\pi n$ as: $V_{tip} = \pi n D$. Applying these substitutions to equation B.3, results in equation B.4, which can be simplified by grouping and canceling out equal terms:

$$\frac{\pi D^2 (\pi n D)^2}{4 n^2 D^4} = C \tag{B.4}$$

$$\frac{\pi^3 n^2 D^4}{4 n^2 D^4} = C \tag{B.5}$$

$$\frac{\pi^3}{4} = C \tag{B.6}$$

This results in equation B.6, which shows that the conversion factor between the propeller and helicopter thrust coefficients is equal to $\frac{\pi^3}{4}$, which matches difference between the thrust coefficient evolution outputted by VSPAero. A similar calculation was performed for the power and torque coefficient as well to obtain their respective conversion factors, with the result being shown in equation B.7 and B.8, respectively.

$$C_{P,prop}\,C_{P,rotor}^{-1} = \frac{\pi^4}{4} \tag{B.7}$$

$$C_{Q,prop}\,C_{Q,rotor}^{-1} = \frac{\pi^3}{8} \tag{B.8}$$

B.2 Advance and Tip Speed Ratio Relation

The relation between the axial flow velocity through a rotor plane and the radial velocity is an important parameter in various aerodynamics communities. However, similarly to the performance coefficients discussed earlier, different conventions exist for describing this parameter. Both the propeller and helicopter/rotorcraft communities refer to this parameter as the advance ratio, which is described as the ratio of the freestream velocity to the rotation velocity of the rotor. However, as different conventions are used for propellers and rotors, these advance ratios differ by a factor of π.

Additionally, in the wind energy community, it is convention to take the reciprocal of the advance ratio, known as the tip speed ratio. This difference makes sense considering the typical operating conditions for both propellers and wind turbines, as for the former, the inflow velocity and tip velocity are typically within the same order of magnitude, whereas for wind turbines, the tip speed is often one to orders of magnitude greater than the freestream velocity, making the tip speed ratio more appropriate in that case. The definition for the propeller advance ratio (J), and the conversion to the rotor advance ratio (μ) and tip speed ratio (λ) is shown in equation B.9.

$$J = \frac{V_\infty}{nD} = \frac{\mu}{\pi} = \frac{\pi}{\lambda} \tag{B.9}$$

Appendix C - Propeller Geometry Tables

This appendix provides the raw geometry data of the PROWIM for those interested in recreating the geometry. The blade cross-sections and technical drawings are available in the works of (SINNIGE *et al.*, 2019) and (SINNIGE *et al.*, 2018).

TABLE C.1 – Twist and thickness distribution of the PROWIM.

r/R	0.15	0.30	0.45	0.55	0.65	0.75	0.85	0.95	1.00
β (°)	45.4	36.8	32.6	29.2	26.1	23.9	22.1	20.7	20.3
t/c	1.0000	0.4692	0.1670	0.1112	0.0937	0.0809	0.0751	0.0632	0.0632

TABLE C.2 – Chord distribution of the PROWIM. *Linearly interpolated values.

r/R	0.15	0.30	0.45	0.55	0.65	0.75	0.85	0.95	0.96	0.97	0.98	0.99	0.995	1.00
c/R, original	0.084	0.110	0.146	0.162	0.163	0.156	0.142	0.118	0.113	0.104	0.091	0.068	0.049	0.02
c/R, modified	0.084	0.110	0.146	0.162	0.163	0.156	0.142	0.118	0.113	0.102*	0.091	0.077*	0.07	0.059

Appendix D - Hardware Description

During the grid refinement study, the computational time required for every simulation was kept track of as well, to study how the computational time scales with the model complexity. Although the computational time is not strictly necessarily the topic of this study, it is an important consideration for the hardware to run the simulations on. Since every computer has different computational power, the specifications for the two machines used for simulations, a Lenovo Thinkpad P51 and P16v Gen2, are listed in table D.1 to provide context to the results. Further details can be found in the user guides provided by the manufacturer (LENOVO, 2018) (LENOVO, 2024). It should be noted that the P51 was not running a clean installation of Windows 10 and that other programs may have been running in the background, likely impacting the computation time. The P16v was running a clean installation of Windows 11, with no other programs running concurrently with the simulations. Only a single run of every simulation was performed, meaning that no run-to-run variation was accounted for.

TABLE D.1 – Overview of the key specifications of the computers used for running the simulations.

Machine	Lenovo Thinkpad P51	Lenovo Thinkpad P16v Gen 2
CPU	Intel Core i7-7700HQ	Intel Core Ultra 7 155H
RAM	32 GB DDR4	32 GB DDR5
GPU	Nvidia Quadro M1200	Nvidia RTX A1000
Operating System	Windows 10 Home, version 22H2	Windows 11 Home, version 23H2

Appendix E - Test Case Description Details

This appendix provides an overview of the simulation settings used in section 7.

TABLE E.1 – Table with the parameters of the advance ratio sweep, indicating which reference data is available and which simulations were performed in this study.

Advance ratio $J\,[-]$	0.6471	0.6970	0.7466	0.7963	0.8463	0.8962	0.9459	0.9957	1.0457
Rotation speed $[RPM]$	3129.835	2905.762	2712.7196	2543.409	2393.142	2259.893	2141.1528	2034.063	1936.804
Fluid density $\rho\,[kg/m^3]$	1.2074	1.2068	1.2077	1.2073	1.2072	1.2073	1.2071	1.2071	1.2080
Experiments (SINNIGE *et al.*, 2019)	All cases tested								
VLM (GONÇALVES, 2024)	All cases simulated								
Phase 1: Isolated prop	All cases simulated								
Phase 2: Prop and wing	Yes	No, linearly interpolated			Yes	No, linearly interpolated			Yes
Phase 3: Full geometry	Yes	No, linearly interpolated			Yes	No, linearly interpolated			Yes

TABLE E.2 – Angles of attack simulated for an advance ratio of $J = 0.6970$ (referred to as $J = 0.7$ in literature).

Angle of attack $\alpha\,[°]$	-0.2	2.8	5.8	9.8	14.8	19.8
Fluid density $\rho\,[kg/m^3]$	1.1991	1.1994	1.1993	1.1991	1.1990	1.1988
Phase 1: Isolated prop	Yes					
Phase 2: Prop and wing	No, interpolated	Yes		Incomplete, convergence issues		
Phase 3: Full geometry	No					

TABLE E.3 – Angles of attack simulated for an advance ratio of $J = 0.9957$ (referred to as $J = 1.0$ in literature).

Angle of attack $\alpha\,[°]$	-0.2	2.8	5.8	9.8	14.8	19.8
Fluid density $\rho\,[kg/m^3]$	1.1982	1.1983	1.1984	1.1984	1.1984	1.1983
Phase 1: Isolated prop	Yes					
Phase 2: Prop and wing	No, interpolated	Yes		Incomplete, convergence issues		
Phase 3: Full geometry	No, interpolated	Yes		Incomplete, convergence issues		

TABLE E.4 – Reference values used for all simulations.

	$M_\infty\,[-]$	$Re_{c,ref}\,[-]$	$V_\infty\,[m/s]$
Phase 1: Isolated prop Viscous/Compressible	0.116	$\rho \pi n D c_{tip}/\mu$	40
Phase 1: Isolated prop Inviscid/Incompressible	0	$1 \cdot 10^{12}$	40
Phase 2: Prop and wing Viscous/Compressible	0.116	650000	40
Phase 2: Prop and wing Inviscid/Incompressible	0	$1 \cdot 10^{12}$	40
Phase 3: Full geometry Viscous/Compressible	0.116	650000	40
Phase 3: Full geometry Inviscid/Incompressible	0	$1 \cdot 10^{12}$	40

Appendix F - Wing Loading Results

This appendix contains results for the wing loading from sections 7.3 and 7.4 omitted from the main discussion.

F.1 Propeller-Wing

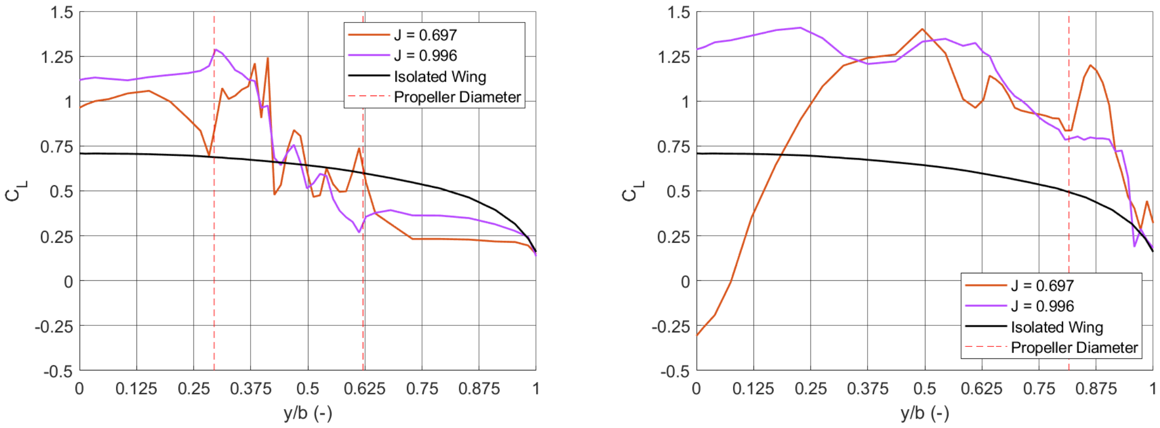

(a) Conventional layout.

(b) Tip-mounted layout, spinning IU.

FIGURE F.1 – Lift distribution comparison for different layouts and advance ratios at $\alpha = 2.8°$.

F.2 Complete Geometry

Annoyingly, VSPAero does not output the lift at the location of the nacelle, hence the lift distributions contain gaps. Figure F.2 shows the lift distribution for both configurations for three advance ratios. For the conventional layout shown in figure F.2b, the relation between wing lift coefficient and propeller advance ratio is completely incorrect, and the distributions do not correspond to the Veldhuis-curve. For the tip-mounted layout in figure F.2a, the obtained distributions make slightly more sense than those of the conventional layout, but there is again no clear trend. For $\alpha = 2.8°$, shown in figure F.3, it can be seen that for the conventional layout, the distribution makes slightly more physical sense than what was observed for $\alpha = -0.2°$, though the result is still quite poor. The lift distribution for the tip-mounted layout at $\alpha = 2.8°$ is of equal quality as the equivalent at $\alpha = -0.2°$.

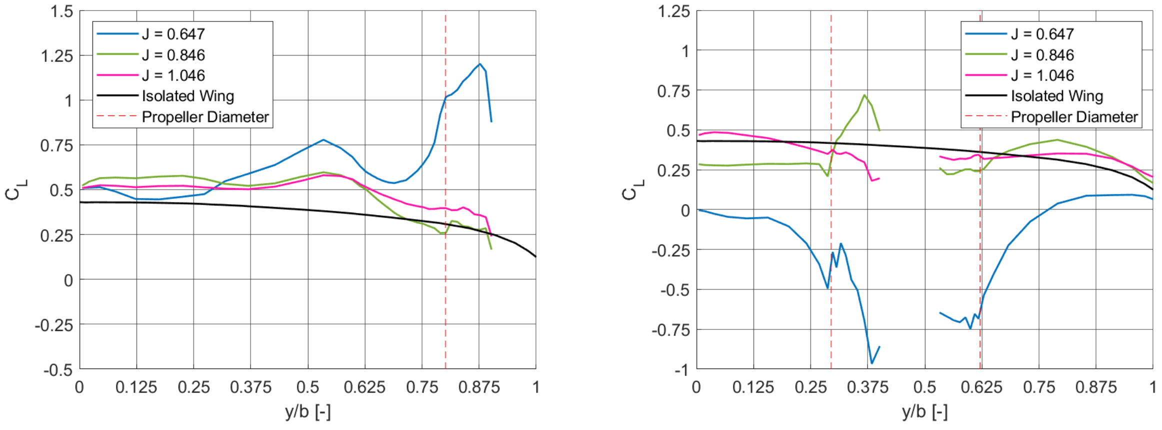

(a) Tip-mounted layout.

(b) Conventional layout.

FIGURE F.2 – Lift distribution comparison for different layouts and advance ratios at $\alpha = -0.2°$.

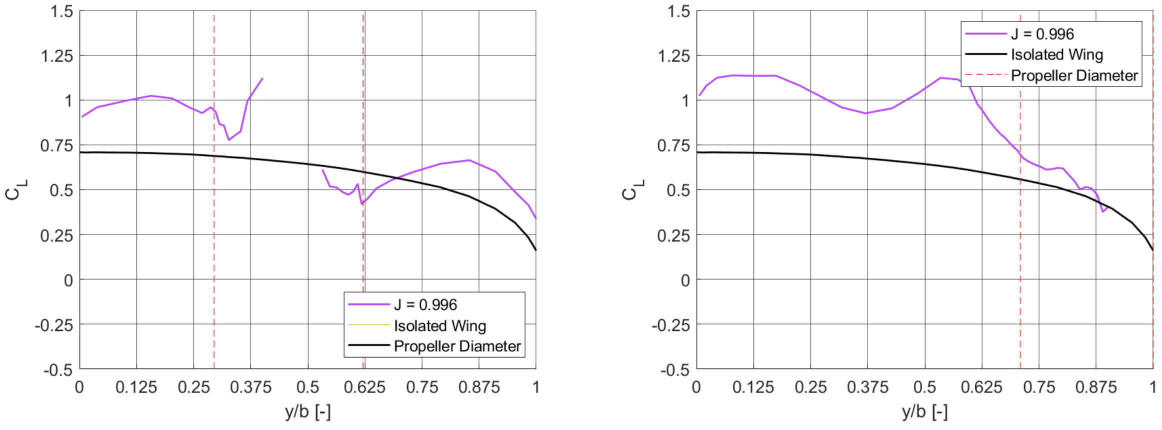

(a) Conventional layout.

(b) Tip-mounted layout.

FIGURE F.3 – Lift distribution comparison for different layouts at $\alpha = 2.8°$.

For sake of completion, the lift polars have been plotted as well, shown in figure F.4, but these are so meaningless that no comment will be made.

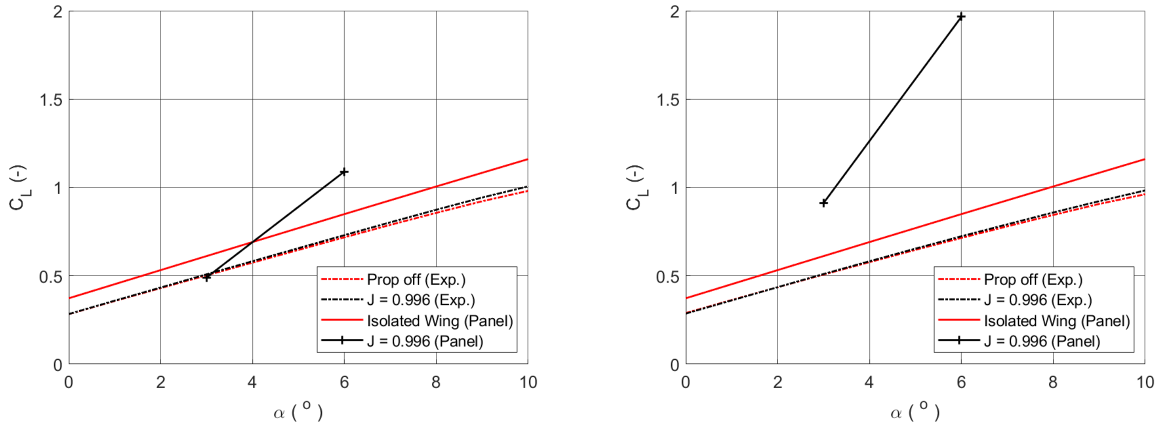

(a) Conventional layout.

(b) Tip-mounted layout.

FIGURE F.4 – Lift polar comparison between experimental and numerical results for both configurations.

Appendix G - Simulation Failure Example

Throughout this thesis, the term ‘exploding wake’ is mentioned several times in the context of failed simulations. To provide some context, Figure G.1 shows four timesteps from a failed simulation. At timestep 45, a disturbance starts at the trailing edge of the wingtip, which grows uncontrollably. The disturbance eventually starts to distort the rest of the shed propeller and wing wakes, as can be seen for timesteps 50 and 55. Eventually all wakes become completely unstable and are convected in all directions like an explosion, which occurs at timestep 60.

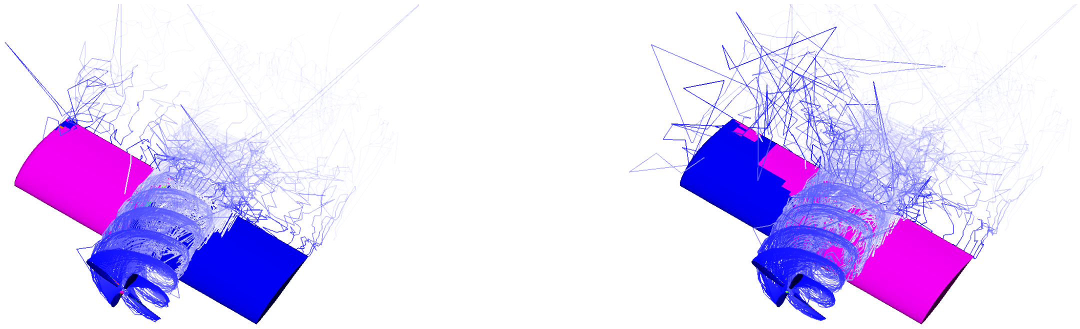

(a) Timestep 45. (b) Timestep 50.

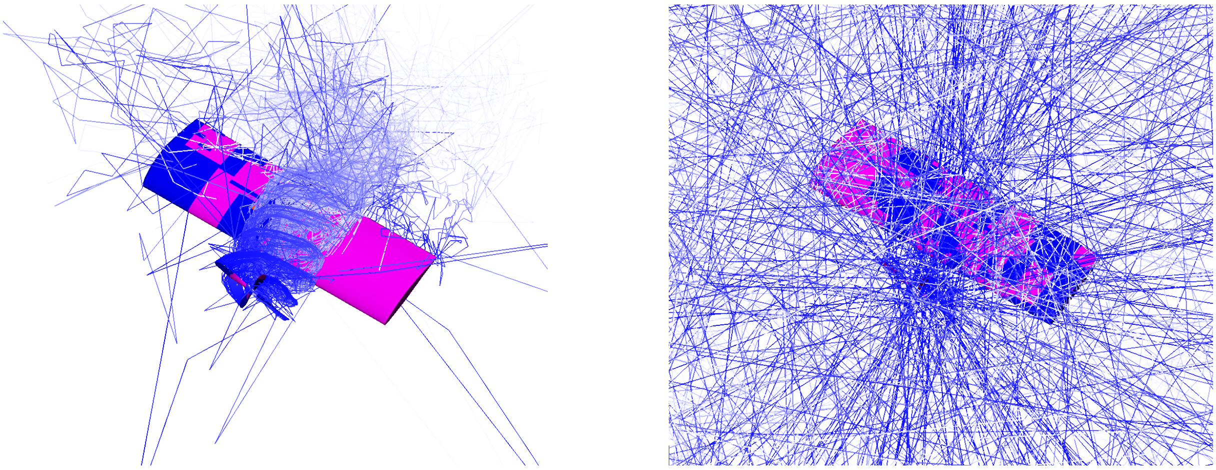

(c) Timestep 55. (d) Timestep 60.

FIGURE G.1 – Example of an ‘exploding’ wake. Simulation was performed at $J = 0.7$ and $\alpha = 19.8^\circ$ for the propeller-wing model. Shading represents pressure coefficient.

FOLHA DE REGISTRO DO DOCUMENTO

1. CLASSIFICAÇÃO/TIPO DM	2. DATA November 27, 2024	3. DOCUMENTO Nº DCTA/ITA/DM-018/2015	4. Nº DE PÁGINAS 149

5. TÍTULO E SUBTÍTULO:
Parametric study of aerodynamic interference on global propeller performance using OpenVSP

6. AUTOR(ES):
Nikolaj Angel Peter Even

7. INSTITUIÇÃO(ÕES)/ÓRGÃO(S) INTERNO(S)/DIVISÃO(ÕES):
Instituto Tecnológico de Aeronáutica – ITA e Universiteit Twente – UT

8. PALAVRAS-CHAVE SUGERIDAS PELO AUTOR:
Propeller; Panel Method; Aerodynamic Interference

9. PALAVRAS-CHAVE RESULTANTES DE INDEXAÇÃO:

10. APRESENTAÇÃO: ( ) **Nacional** (**X**) **Internacional**
ITA/UT, São José dos Campos/Enschede. Curso de Mestrado. Programa de Pós-Graduação em Engenharia Aeronáutica e Mecânica.

11. RESUMO:

As tecnologias de motores elétricos e baterias avançaram a ponto de viabilizar aeronaves elétricas com carga útil da ordem de centenas de quilogramas. Em comparação com os motores de turbina a gás, a eficiência dos motores elétricos é menos dependente do tamanho da unidade de potência, o que oferece maior flexibilidade para o layout da integração aeropropulsiva de um conceito de aeronave elétrica. Para descartar rapidamente conceitos de projeto preliminares com baixo potencial, e concentrar-se em conceitos com características de desempenho aeropropulsivo promissoras, é altamente desejável ter ferramentas de análise de média fidelidade que possam avaliar com relativa rapidez a viabilidade de uma ampla gama de configurações diferentes. Em um estágio posterior do processo de projeto, apenas o projeto mais viável passará a ser analisado detalhadamente com métodos computacionais e/ou experimentais de alta fidelidade o que implica em alto custo computacional. O presente trabalho concentra-se na interferência aeropropulsiva, sob o aspecto aerodinâmico, entre hélices e asas. Estes aspectos físicos relacionado às interferências serão estudados empregando um método de painéis implementado no software VSPAero, um código de solução aerodinâmica potencial que faz parte do software OpenVSP.

Para a hélice ou asa isolada, foi possível obter resultados que concordaram razoavelmente bem com a literatura, embora tenham sido observadas algumas deficiências claras nos resultados obtido por VSPAero. Embora algumas dessas deficiências fossem esperadas devido às suposições e simplificações subjacentes às equações governantes, também houve algumas limitações com causas associadas e aspectos não identificados neste trabalho. Quando a geometria combinada hélice e asa foi simulada, verificou-se que, embora os resultados para a hélice fossem plausíveis, os resultados para a asa eram, às vezes, altamente irregulares, lançando dúvidas significativas sobre a precisão dos resultados da hélice também devido à interação mútua entre as geometrias.

12. GRAU DE SIGILO:
(**X**) **OSTENSIVO** ( ) **RESERVADO** ( ) **SECRETO**